All Sciences Academy

TREND AND INNOVATIVE RESEARCH IN ENGINEERING

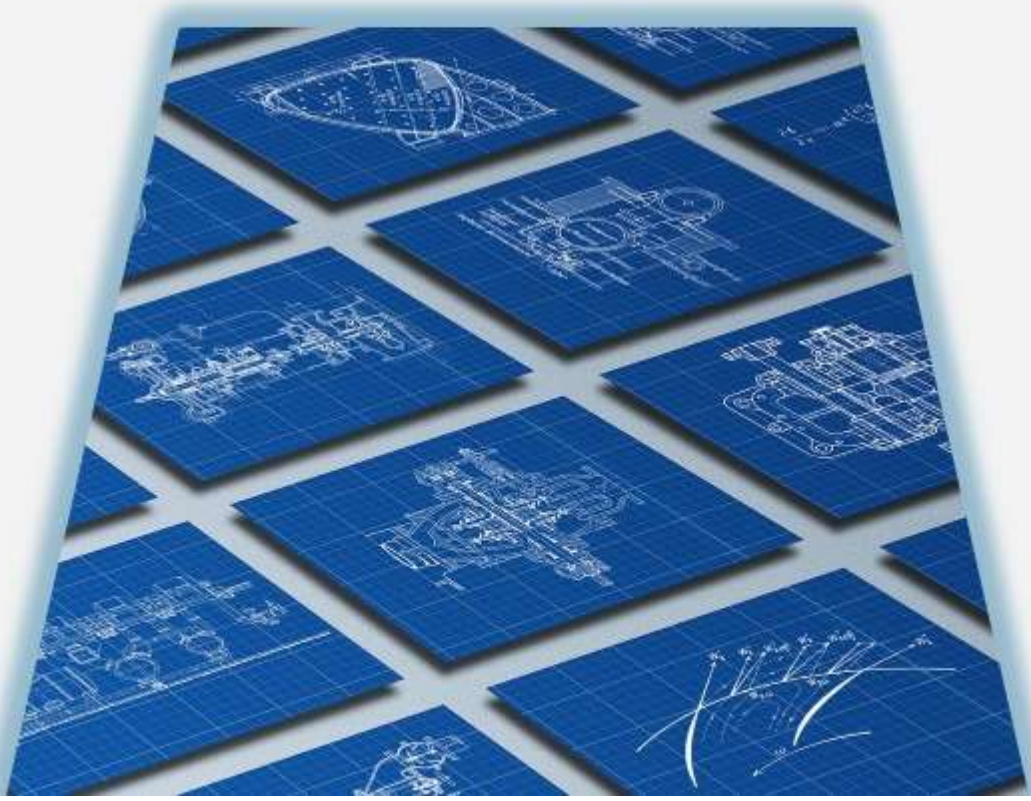

TREND AND INNOVATIVE RESEARCH IN ENGINEERING

Editor
Asst. Prof. Dr. Umut ÖZKAYA

Trend and Innovative Research in Engineering
Editor: Asst. Prof. Dr. Umut ÖZKAYA

Design: All Sciences Academy Design
Published Date: February 2026
Publisher's Certification Number: 72273
ISBN: 978-625-8676-63-1

www.allsciencesacademy.com
allsciencesacademy@gmail.com

CONTENT

Solar Panel Installation on Batman Kıra Mountain Road to Prevent Icing

Furkan KINAY[1]

Abdulrezzak BAKIŞ[2]

1- Dr.; Batman University, Graduate Education Institute, Department of Civil Engineering, Transportation, kinayfurkan@hotmail.com ORCID No: 0000-0002-8525-8072

2- Assoc. Prof.; Batman University, Faculty of Engineering and Architecture, Department of Civil Engineering, Transportation, abdulrezzak.bakis@batman.edu.tr ORCID No: 0000-0002-7487-884X

ABSTRACT

Solar panels, thanks to the photovoltaic cells they contain, absorb and convert sunlight into energy. Solar panels prevent environmental pollution and produce energy very efficiently. Kıra Mountain is located between Batman Province and Beşiri District. This situation also brings with it transportation problems. Due to snowfall, icing and similar reasons cause disruptions in transportation on Kıra Mountain. Due to the altitude of 885 meters, vehicles skid on the icy roads during ascent and descent of Kıra Mountain. This causes traffic flow to stop and reduces travel time. The increase in travel time is one of the factors that negatively affect the national economy. By applying a similar study in South Korea to the Kıra Mountain pass, the transportation problem of the region, which is negatively affected by adverse weather conditions, will be solved. Therefore, road traffic flow on the Kıra Mountain road, which is prone to icing and heavy snowfall, will be safer and accidents will be minimized. In addition, the energy obtained from solar energy will be converted into electricity, contributing to the economy of Batman Province and the country. The use of solar panels on the highway, a highly significant example of making transportation sustainable, will also have sufficient capacity to charge electric vehicles and power the highway lighting system. The study proposes placing the solar panels on the median of the 4-lane D370 state road, approximately 5 km long, to be constructed at the Kıra Mountain road. The energy generated from these solar panels is intended to power the lighting of the highway and the Kıra Mountain recreational areas.

Keywords–Solar panel, Solar energy, Transportation, Highway, Road Icing

INTRODUCTION

Electricity can be generated from solar energy. Solar panels, thanks to the photovoltaic cells they contain, absorb and convert sunlight into energy. Solar panels prevent environmental pollution and produce energy very efficiently. Solar panels come in different types. Not all types may be equally efficient. However, solar panels are quite efficient when installed on the ground. These panels contain regulators, batteries, and inverters. Inverters enable the electricity obtained from solar photons to become usable. Solar panels obtain direct current from the rays hitting the photovoltaic cells. When the incoming rays hit the panels, a voltage is generated, and this voltage is released as direct current. However, since it is not possible to transmit direct current to the grid and use it directly, inverters must be present in solar panels. Alternating current is 220 Volts in our country. The direct current (DC) in the panels is converted to alternating current (AC) with the help of inverters. Inverters enable the conversion of

the direct current obtained from sunlight into alternating current, thus allowing us to use electricity. There are three types of inverters. Off-grid inverters, also known as stand-alone inverters, are not connected to the grid. They are used to provide the stored electricity we use in our homes, which operates regularly thanks to batteries; they regulate not only the voltage but also the current. On-grid inverters, also known as grid-tie inverters, are a grid-connected system. The electricity to be used comes only from photovoltaic cells and is stored for later use. Solar inverters use the energy of photovoltaic cells to provide more power to the batteries when we have enough energy. When there is no sun, the inverter uses the energy in the battery or the energy from the grid.

Solar panels contain many systems within them. Additionally, devices working in conjunction with the panels increase their efficiency. These include components such as regulators, batteries, and inverters. Regulators balance the voltage obtained from the solar panels, thus preventing overcharging of the battery, which is one of the most important components. The DC voltage obtained from solar panels is not sufficient for us to use electricity. Therefore, inverters convert the direct current to 220V alternating current. Directly sending this voltage to the batteries would damage them. For this reason, regulators are essential in a solar panel system.

Inverters provide speed adjustment from 0.5 Hz to 2000 Hz. They can also convert direct current between 12 V, 24 V, and 48 V to 220V alternating current. They are not only used to generate alternating current. Electric current is generated by the movement of electrons and can lead to certain interruptions. The resulting voltage needs to be maintained at a specific frequency. If this is not done, various leakages or interruptions can occur. Rectifiers are needed to obtain electricity at a specific frequency. Inverters rectify and maintain the current obtained from solar panels. In addition to performing all these functions, inverters also have storage capabilities. Thanks to their off-grid operation, they enable the storage and conversion of energy in areas without a grid connection, instead of incurring costs. On-grid, they can be used in place of batteries when necessary. Thanks to inverters, electricity is both regulated and stored. Many studies have been conducted on electricity generation from solar energy (Şimşek and Uncu, 2025:42; Demirel, 2025:19; Polat, 2025:19; Özay vd., 2026:12).

Solar panels are highly efficient energy sources in themselves. Energy can be produced with much less carbon emissions thanks to solar panels. The use of solar panels has become quite widespread in recent years. In our country, larger power plants are being built day by day, and thanks to this, the heating and electricity needs of many building areas can be met (Tureco Enerji, 2026).

MATERIALS AND METHODS

Kıra Mountain is located within the borders of Beşiri District in Batman Province. It is bordered by Kurtalan to the east, Hasankeyf and Gercüş to the south, Kozluk District to the north, and Batman city center to the west. Kıra Mountain lies between Batman Province and Beşiri District. The climate is characterized by rainy, harsh, and cold winters, short springs, and dry, very hot summers. The Kıra Mountain Recreation Area, established by the Provincial Administration with agency support, is the most popular resting and picnic area in the province. With an altitude of 885 meters, Kıra Mountain experiences heavy snowfall during the winter months. This situation also brings about transportation problems. Due to snowfall, icing and similar reasons cause disruptions in transportation on Kıra Mountain. Because of its altitude of 885 meters, vehicles skid on the icy roads during ascents and descents. This leads to traffic stoppages and reduced travel times. The lengthening of the travel time is one of the factors that negatively affect the country's economy. The view of the Kıra Mountain route is shown in Figure 1 (Beşiri-Der, 2026).

Figure 1. Batman Kıra Mountain Road

Satellite view of Batman Kıra Mountain is given in Figure 2 (Google maps, 2026).

Figure 2. Satellite view of Mount Kira in Batman.

The distance between Batman and the beginning of Kıra Mountain is approximately 12 km. The Kıra Mountain road is approximately 5 km long. Figure 3 shows the starting (A) and ending points (B) of Kıra Mountain (Google maps, 2026).

Figure 3. Route for Installing Solar Panels at Kıra Mountain Road

Considering previous studies, an application related to the study was carried out in South Korea as shown in Figure 4 (Salehi, 2015).

Figure 4. Application of Solar Panel Bicycle Path in South Korea


Figure 5. Solar Panels Proposed for Implementation at the Kıra Mountain Road (South Korea Example)

The aerial view of the bicycle path between Daejeon and Sejong cities is shown in Figure 5 (Salehi, 2015). Both cities are located 2-3 hours south of Seoul. The solar panels installed on the road not only generate electricity but also the road under the panels is used as a bicycle path.

By applying a similar study in South Korea to the Kıra Mountain road, the transportation problem of the region, which is negatively affected by adverse weather conditions, will be solved.

The energy obtained from solar panels on the road's top layer should be converted into electricity and laid beneath the road surface at 5-meter intervals. This will improve road traffic flow and minimize accidents on the Kıra Mountain road, which experiences icing and heavy snowfall. Furthermore, converting solar energy into electricity will contribute to the economy of Batman province and the country as a whole.

The use of solar panels on highways, a remarkable example of making transportation more sustainable, will also have sufficient capacity to charge electric vehicles and power the highway lighting system.

Perovskite solar cells are attracting significant interest in the renewable energy sector due to their high efficiency and low production costs. However, concerns exist regarding the recycling and environmental impact of these cells. A recent study has developed an environmentally friendly and low-cost method that enables the complete recycling of perovskite solar cells. In this new method, environmentally harmless solvents such as isopropyl alcohol and ethyl acetate are used to dissolve the perovskite layer. This allows the components of the device—glass, electrodes, and perovskite material—to be effectively separated and reused. Researchers state that this approach is both economically and environmentally sustainable. A study conducted at the Julich Research Center revealed that perovskites can be recovered efficiently and cost-effectively. The study suggests that if this method proves to be effective and economically applicable to complete modules, it will contribute to making perovskite solar energy technology truly sustainable and effective. In previous studies on solar cells, researchers at the Institute of Chemical Technologies achieved an efficiency level of approximately 18 percent in solar panels thanks to perovskite material, which is cheap and abundant. This means that approximately 18 percent of the reflected sunlight can be converted into energy. A team from various universities and institutes in the Netherlands increased the energy conversion efficiency of silicon-based cells, which have approximately 22 percent, to 30 percent using perovskite. Obtaining heat and electrical energy from sunlight has been a system used for many years and is considered the most important alternative energy source. However, despite its great importance, not all of the reflected sunlight can be converted into energy (Temiz Enerji, 2026). Researchers are still continuing their work to increase efficiency using new materials.

RESULTS AND DISCUSSION

In the study, it is planned to place solar panels on the median of the 4-lane D370 state road, which will be constructed for approximately 5 km in

the Kıra Mountain road. The energy obtained from the solar panels will provide lighting energy for the highway and the Kıra Mountain picnic areas as seen in Figures 6 and 7 (Batman Özel İdare, 2026).

Figure 6. Batman Kıra Mountain Recreation Area-1

Figure 7. Batman Kıra Mountain Recreation Area-2

In addition, the lower sections of the solar panels (median area) will serve entirely as a bicycle path, as in the South Korean example (Figure 8). This will alleviate traffic congestion in the area and minimize carbon emissions. Since the bicycle path is covered with solar panels, cyclists will also be protected from rain and snow.

Figure 8. Proposed Solar Panel Installation on the Median Strip and Bicycle Path Below the Panels.

Another benefit of solar panels built on the road is to prevent the road from icing up in winter months, as shown in Figure 9 (İlke Haber Ajansı, 2026). With the energy obtained from solar panels, the systems that will be laid under the road surface will prevent the road from icing up and closing.

Figure 9. Kıra Mountain Road Starting Point (Batman Organized Industrial Zone Junction)

Cost Calculation

The study proposes placing solar panels on the median of the 4-lane D370 state road, which will be constructed for approximately 5 km at the Kıra Mountain road. Cost calculations (for the year 2026) are as follows:

5 km of median strip area = 8750 m²

Solar Panel Dimensions = 1646 x 992 x 35 mm (250 Watt)

Number of solar panels within a 5 km radius = 5000 units.

Total Energy = 1250 kW

Solar Panel Cost = 5000 x $106 = $530.000 = 23.007.300

(28.01.2026 as of that date - 1 $ = 43.41 TL)

Solar Inverter Cost = 1.250.000 watts $ 0.14=$175.000=7.596.750 TL

Solar Construction Cost = 1,250,000 watts = $ 0.14 **$** 175,000 = 7.596.750 TL

Cable Trays for Solar Panels = 5000 meters x 164 TL = 820.000 TL

Solar Cable (Photovoltaic Cable) Cost = 10,000 meters x 25 TL = 250.000 TL

Lightning Rod (Lightning Protection) Cost = 31 x 82.000 TL = 2.542.000 TL

Cost of Power Transmission Line and Transformer Station = 3.809.994 TL

Security Camera System Cost = 200 Cameras x 4200 TL= 840.000 TL

Road Heating System Cost=70.000 m² x 175 TL=12.250.000 TL (4 lanes)

Total Cost = 58.712.794 TL

REFERENCES

Batman Özel İdare. (2026). https://www.instagram.com/p/DKZcEgoMOJH adresinden 12 Ocak 2026 tarihinde alınmıştır.

Beşiri-Der. (2026). *Yeşil Kuşak Kıra Dağı Projesi*. https://www.facebook.com/share/v/1ExC7WTeEu adresinden 5 Ocak 2026 tarihinde alınmıştır.

Demirel, A. (2025). Üniversitelerde Sürdürülebilirlik Uygulamaları: Yeşil Denetim ve Green Metric Çerçevesinden Bakış. *Sürdürülebilir Çevre Dergisi*, *5*(1), 19-38.

Google, maps. (2026). https://www.google.com/maps adresinden 8 Ocak 2026 tarihinde alınmıştır.

İlke Haber Ajansı. (2025). https://www.youtube.com/watch?v=G3uxBiLo4Xs adresinden 10 Aralık 2025 tarihinde alınmıştır.

Özay, K., Kaya, H., ve Yücel, İ. (2026). Techno-Economic Assessment of Photovoltaic, Wind, and Hybrid Systems in Residential-Scale Islanded Microgrids Using HOMER Pro: A Comparative Study Based on HOMER Pro Simulations.

Polat, M. (2025). Sürdürülebilirlik Bağlamında Yeşil Bina ve Yeşil Güçlendirme: Kamu Binalarında Yeşil Güçlendirme. *Fiscaoeconomia*, *9*(2), 950-969.

Salehi, J. (2015). *Travel from Daejeon to Sejong by bike*. https://www.youtube.com/watch?v=LuYsYLqjUtU adresinden 12 Ocak 2026 tarihinde alınmıştır.

Şimşek, H., ve Uncu, D. Y. (2025). Sürdürülebilir kent içi ulaşımda mikromobilite incelemesi ve güzergâh planlaması: Manisa örneği. *İDEALKENT*, (49), 67-95.

Temiz Enerji. (2026). *Perovskit güneş hücreleri çevre dostu ve düşük maliyetli olarak nasıl geri dönüştürülebilir.* https://temizenerji.org adresinden 12 Ocak 2026 tarihinde alınmıştır.

Tureco Enerji (2026). *Enerji Depolama*. https://tureco.com.tr adresinden 17 Ocak 2026 tarihinde alınmıştır.

Investigation of Inorganic Halogen-Free Flame Retardant Additives in Thermoplastics

Aslıhan AVŞAR[1*]

İlyas KARTAL[2]

[1]Marmara University, Institute of Pure and Applied Sciences, Metallurgical and Materials Engineering Department, 34722, Istanbul-TURKEY, ORCID:0009-0008-1601-4593
[2]Marmara University, Faculty of Technology, Metallurgical and Materials Engineering Department, 34722, Istanbul-TURKEY, ORCID: 0000-0001-9677-477X
*Corresponding author. e-mail: aslihanavsar96@gmail.com

INTRODUCTION

Flame-retardant (FR) systems are typically formulated to achieve a defined level of resistance against ignition or flame propagation, as determined through standard small- or large-scale testing methods. Their primary purpose is to prevent or at least delay the transition of minor ignition events into fully developed fires. Because any fire can pose a serious toxic threat to occupants, FR systems generally contribute to lowering toxic risk within the range of ignition conditions they are designed to address. Even when combustion occurs, these systems can still help mitigate the development of toxic hazards by slowing down flame spread and overall fire growth, a behavior commonly observed in practice (Horrocks et al., 2001). FRs are typically incorporated into commodity thermoplastics during processing to improve fire safety and, secondarily, to meet regulatory requirements or customer demands. Early FRs were mostly halogen-based and operated in the gas phase by replacing the high-energy free radicals that drive flame propagation with more stable species like Cl(–) and Br(–), thereby inhibiting combustion. These additives were chosen based on their suitability for the host polymer and their appropriate decomposition temperature ranges. The selection of FRs are straightforward and typically based on increasing thermal stability to match the polymer's thermal degradation range. Due to their interaction with flames through chemical reactions, combustion often remains incomplete. While carbon oxidizes easily to carbon monoxide (CO), the full conversion to carbon dioxide (CO_2) is frequently inhibited, leading to the release of smoke and highly toxic fire effluents containing partially combusted products. For instance, during the combustion of plasticized PVC, approximately 20% of its mass is lost, generating various chlorine-containing compounds. More than 70 different compounds have been identified in the emissions. Many of these substances pose significant toxicological risks, with hydrogen chloride (HCl) being particularly hazardous, surpassing even CO in criticality. Additionally, the leaching of halogenated FRs from polymers is a major concern, as some have been confirmed as endocrine disruptors. Due to these safety and environmental challenges, extensive research has focused on developing halogen-free alternatives. These include metal hydroxides, carbonate fillers, phosphorus-based compounds, low-melting-point glasses, and advanced materials. Recent studies primarily explore novel halogen-free FR systems that, when combined with traditional FR additives, demonstrate enhanced efficiency through synergistic effects. However, stricter regulations and evolving safety standards are leading to the gradual phase-out of many widely used halogenated additives. For decades, there has been a strong trend toward halogen-free FR solutions, particularly in response to regulatory directives and consumer demand for environmentally friendly materials. Brominated FRs remain widely used due to their balance of performance, cost-effectiveness, properties, and ease of processing (Olabisi et al., 2016)(Hull et

al., 2011). An examination of three residential fire incidents involving television housings that contained brominated FRs revealed surface residues of brominated dioxins at concentrations reaching up to 14.9 ppm. It has been further suggested that, even under normal operating temperatures, televisions may emit small amounts of these compounds. More recent studies conducted in Sweden reported that the concentration of polybrominated ethers in human breast milk has risen more than fiftyfold over the past twenty-five years, having doubled since 1992. In addition, workers exposed to brominated FRs were found to have blood concentrations approximately fifty times higher than those of the general population. These findings have raised concerns regarding the potential neurotoxic effects of brominated FRs, and Sweden has reportedly considered implementing a ban on their use (Horrocks et al., 2001).

However, the additive industry is actively researching alternatives for electrical and electronic applications, aiming to replace brominated and chlorinated additives. Halogen-free FRs are highly polymer-specific, with some, like volatile phosphorus compounds, acting in the gas phase to inhibit combustion similarly to halogens. However, most halogen-free FRs function in the condensed phase, forming protective barriers such as charring, inorganic residues, or intumescent layers that insulate the material. Despite their advantages, halogen-free FRs are generally less efficient than their halogenated counterparts, often requiring higher loadings—sometimes up to 70% by weight—to meet flammability standards. This presents challenges in commercial adoption, as their effective incorporation into polymers requires compatibilizers for uniform dispersion and specialized processing equipment, to handle the increased melt viscosity associated with higher filler concentrations (Olabisi et al., 2016)(Hull et al., 2011).

Halogen-Free Flame Retardant Additives (HFFR) and Their Properties in Thermoplastics

HFFR additives encompass a variety of chemicals commonly classified as inorganic FRs, phosphorus-based FRs, and nitrogen-based FRs (Yılmaz, 2011). Inorganic FRs provide multiple benefits compared to their organic counterparts, such as enhanced thermal stability, long-lasting performance, non-toxicity, lower smoke production, and cost-effectiveness (Gupta et al., 2024). Various inorganic compounds are employed as FRs, interfering with the combustion process through different physical mechanisms: the emission of water or non-combustible gases that dilute flammable vapors, the absorption of heat energy during gas release reactions to lower the fire temperature, and the creation of a fire-resistant protective layer on the material's surface. However, the efficiency of these mechanisms in inorganic compounds is relatively low, necessitating their use at high concentrations or in combination with other types of FRs. Specific application

methods, such as incorporating them into organic coatings, allow high concentrations of these additives to be used in plastics without altering their performance characteristics. Among the commonly used inorganic FRs are aluminum trihydrate, magnesium hydroxide, boron compounds, phosphorus-containing compounds, and nitrogen-containing compounds (Rothon et al., 2014). It can be seen that some flame retardant materials in Table 1 cover a wide decomposition temperature range and include the release of carbon dioxide and water (Atay, 2019).

Table 1: Principle candidate flame-retardant fillers

Material	Onset of decomposition (^oC)[a]	Enthalpy of decomposition ($kJ.kg^{-1}$)	Content of volatile substances (% w/w)		
			H_2O	CO_2	Total
Nesquehonite ($MgCO_3 3H_2O$)	70-100	1750	39	32	71
Calcium sulfate dihydrate, gypsum ($CaSO_4 2H_2O$)	60–130	Not available	21	0	21
Magnesium phosphate octahydrate, ($Mg_3(PO_4)_2 8H_2O$)	140–150	Not available	35.5	0	35.5
Alumina trihydrate, aluminum hydroxide, ($Al(OH)_3$)	180–200	1,300	34.5	0	34.5
Basic magnesium carbonate, hydromagnesite ($4MgCO_3 Mg(OH)_2 4H_2O$)	180–200	1,300	19	38	57
Dawsonite (sodium form) ($NaAl(OH)_2CO_3$)	240–260	Not available	12.5	30.5	43
Magnesium hydroxide, ($Mg(OH)_2$)	300–320	1,450	31	0	31
Magnesium carbonate sub-hydrate, ($MgOCO_2(0.96)H_2O(0.30)$)	340–350	Not available	9	47	56
Boehmite, (AlO(OH))	340–350	560	15	0	15
Calcium hydroxide, ($Ca(OH)_2$)	430–450	1,150	24	0	24

[a]The reported decomposition temperatures are approximate values since they are typically measured under dynamic conditions and can vary with factors such as heating rate and sample characteristics.
Source: Atay, 2019

Aluminum Trihydrate (ATH)

This simple inorganic additive functions through all three of the mechanisms outlined above. At approximately 200°C, ATH decomposes into aluminum oxide and water. The water vapor forms a barrier of non-combustible gas near the material's surface, suppressing flames. ATH serves as an effective FR and smoke suppressant when incorporated at high concentrations, typically ranging from 40% to 60% by weight. To achieve adequate flame retardancy, filler levels often need to exceed 60% by weight. The reaction is endothermic, absorbing heat and reducing the material's temperature, which slows combustion. Since its initial commercial introduction, ATH has dominated the market and continues to do so today due to its comparable flame retardancy and smoke suppression performance to other candidates (primarily magnesium hydroxide) and its significantly lower production cost in a usable form (Rothon et al., 2014)(Zakut, 2012).

Xu et al. (2016) investigated the combined FR effects of ATH and HFFR in HDPE composites. The results indicated significant cooperative FR effects of ATH and halogen-free substances. FRs such as expandable graphite (EG) and RP. Tirri et al. (2019) explored the synergistic potential of sulfenamides with conventional HFFRs. Five distinct sulfenamides were individually mixed with phosphorus-based FRs or ATH, and their effect on the flammability of polypropylene (PP) was evaluated. Compared to the sulfenamide-free reference, the modified PP exhibited improved char stability, along with reductions in peak heat release rate (HRR), CO and CO_2 emissions, and total smoke production. Liang et al. (2014) investigated the flame-retardant performance and mechanical behavior of PP composites formulated with microencapsulated red phosphorus (MRP) and MH/ATH fillers. As the proportion of MRP increased, both the limiting oxygen index (LOI) and smoke density ratings rose in a non-linear manner, whereas the horizontal burning rate declined non-linearly. Young's modulus and elongation at break increased, as the MRP weight ratio increased, there was a slight decrease in both tensile yield strength and tensile breaking strength. Shah et al. (2014) examined the impact of ATH concentration on the strength of PP/ATH composites. The tensile strength, flexural strength (Figure 1), and fracture toughness of the composites decreased with increasing ATH content. Conversely, a slight increase in elastic modulus was observed with higher ATH content.

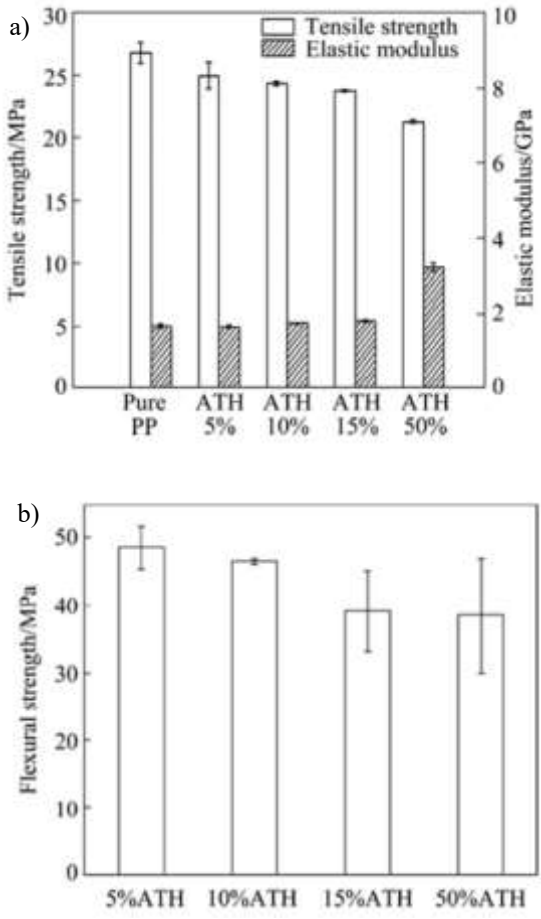

Figure 1: Variation in a) tensile strength, elastic modulus and b) flexural strength among different blends of PP/ATH (Shah et al., 2014)

Magnesium Hydroxide (MH)

MH exhibits all the essential properties required for a FR filler. It can be synthetically produced with high purity in various advantageous morphologies, responds well to surface modifiers, and undergoes endothermic decomposition at elevated temperatures, releasing water in alignment with polymer decomposition. As the second most commonly used FR filler, MH is costlier than ATH but provides a higher decomposition temperature (~300°C), making it especially suitable for thermoplastics that undergo processing at elevated temperatures. Unlike ATH, MH is compatible with polymers such as PP and engineering plastics, which require elevated processing conditions. Research has shown that when incorporated at appropriate levels, MH

effectively enhances fire resistance in materials, while also significantly reducing smoke emissions during combustion. Furthermore, the negative impact on mechanical properties, particularly impact strength, observed at high filler loadings can be minimized or even eliminated through proper filler modification techniques (Zakut, 2012)(Xu et al., 2006)(Hornsby et al., 1990).

Sener and Demirhan (2008) investigated the use of MH as a FR in cable insulation materials containing cross-linked low-density polyethylene (PE) prepared via silane grafting. Their test results analyzed the optimal MH content for cable insulation materials, showing that appropriate levels of MH provided good material properties that met insulation standards. Wang et al. (2003) produced HFFR and silane-cross-linkable PE composites by melt processing with MH as the FR. Their investigation showed that increasing the MH content led to lower heat release and smoke emission rates, while the LOI, ignition time, and char residue after combustion increased accordingly. In another study, Liu and Zhang (2011) prepared HFFR blends of linear low-density polyethylene (LLDPE) and ethylene–acrylic acid copolymer (EAA) using MH as a FR through melt processing. They examined how EAA affected the flame resistance and overall performance of LLDPE/EAA/MH composites. The addition of EAA raised the LOI value from 28% to 39% and decreased both the HRR and smoke production rate (SPR), as verified by cone calorimeter tests. These improvements were attributed to the uniform distribution of MH within the matrix, promoted by hydrogen bonding and acid–base interactions between MH and EAA. Shen et al. (2011) investigated two types of MH as fillers in PP. The inclusion of MH enhanced the flame retardancy of PP but led to a decline in mechanical strength due to poor interfacial adhesion between the filler and the polymer matrix, as revealed by scanning electron microscopy (SEM). Similarly, Shen et al. (2012) incorporated lanthanum oxide (La_2O_3) as a catalytic synergist to improve the FR performance of MH in PP composites. The study demonstrated that an optimal amount of La_2O_3 significantly enhanced the flame retardancy of MH-filled PP. Hao et al. (2011) also reported that combining MH and HMOS in PP improved its FR behavior, although the mechanical properties decreased because of weak bonding at the filler–matrix interface, consistent with SEM observations. Liang examined how incorporating varying amounts (5–60%) of the high-performance flame retardant magnesium hydroxide (FMX) influences the tensile and flexural behavior of PP composites. The results indicated that both Young's modulus and flexural modulus increased in an almost linear manner, whereas the tensile yield and tensile breaking strengths showed slight reductions with higher FMX loading. Hornsby et al. (1996) studied four different types of MH. At high addition levels (around 60% by weight), it was shown that MH acted effectively as a FR in polyamide (PA6) and to a lesser extent in PA6,6. Nevertheless, the UL 94 ratings fluctuated

based on the viscosity of the formulations. Balakrishnan et al. (2012) prepared MH-containing FR PA6/PP composites with various MH contents (20-50% by weight). Figure 2 shows the UL-94 tests also demonstrated increased flame retardancy with higher MH content.

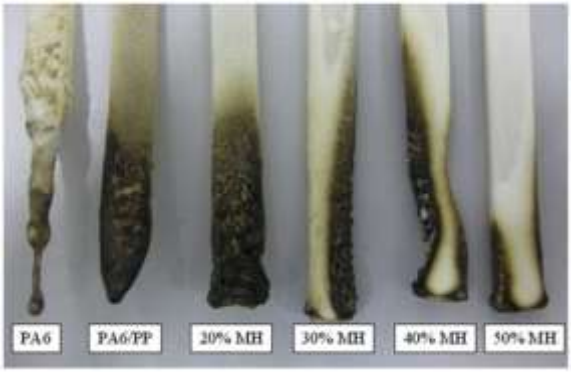

Figure 2: The appearance of the burned UL-94 samples (Balakrishnan et al., 2012)

Huntite/Hydromagnesite (H/HM)

The H/HM mineral is incorporated into polymer applications because of its FR capabilities, enhancing fire resistance in the material. Hydromagnesite, also referred to as basic magnesium carbonate, and huntite, a compound of calcium and magnesium carbonate. Currently, commercial deposits are located in Greece and Turkey. These deposits typically consist of physical mixtures of the two minerals, with proportions ranging between 40%-30% huntite and 60%-70% hydromagnesite. The impurity content is minimal, with the primary ones being other white carbonate minerals. The density of huntite ($Mg3Ca(CO3)4$) is 2.70 g/cm³, while hydromagnesite ($Mg4(OH)2(CO3)3·3H2O$) has a density of 2.24 g/cm³. The advantages of this mineral include non-abrasiveness to processing equipment, low smoke formation, absence of acid gas emissions, halogen-free composition, environmental safety, recyclability, absence of combustion gas corrosion, unlimited coloring options, and low combustion rates. Additionally, H/HM offers a good cost/performance ratio in FR applications (Zakut, 2012)(Hollingbery et al., 2010)(Shah et al., 2014).

Yurddaskal and Çelik (2018) produced PP composite materials reinforced with H/HM, antimony trioxide, bentonite, and ZB for HFFR applications using extrusion and injection molding techniques. Figure 3 shows that SEM analysis confirmed uniform distribution of additives within the PP matrix. H/HM-reinforced composites demonstrated superior FR performance compared to other composites with the same additive ratio.

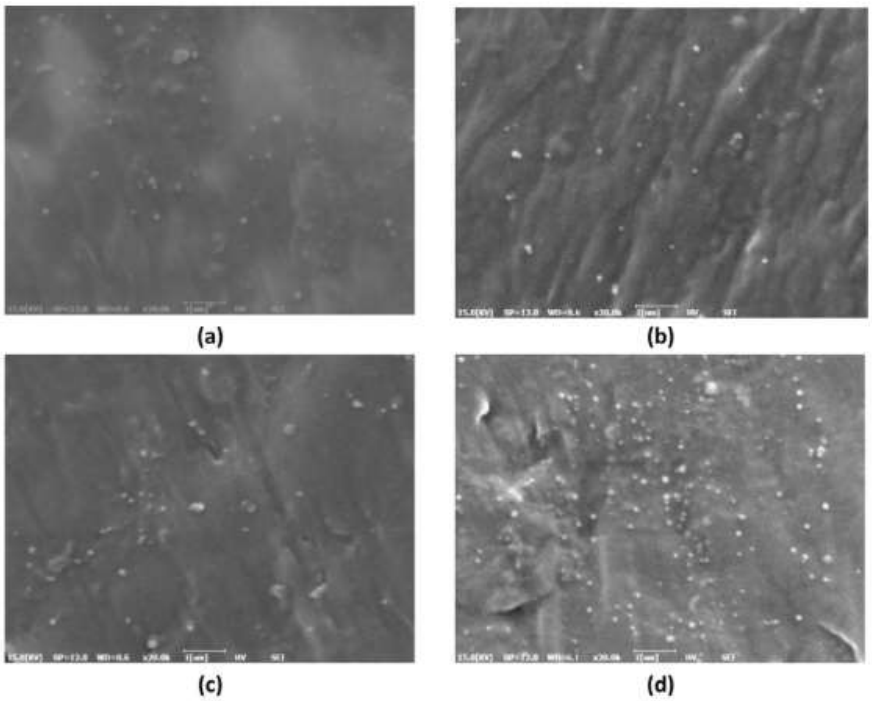

Figure 3: SEM micrographs of (a) PP/30A(Antimony trioxide), (b) PP/30B(Bentonite), (c) PP/30Z(Zinc borate) and (d) PP/30H(H/HM) composites (Yurddaskal et al., 2018)

Boron Compounds

Boron, a Group IIIA element with an atomic number of 10, naturally occurs only in the form of oxo compounds. While approximately 230 boron compounds exist in nature, only a few hold commercial significance. The most notable among these are kernite, tincal, ulexite, colemanite, szaibelyite, and probertite. Beyond naturally occurring compounds, a variety of boron-containing compounds can be created through different chemical techniques. Boron compounds are commonly utilized as versatile FR additives in various polymers, displaying distinct FR mechanisms. These mechanisms vary based on the specific boron compound, the type of polymer, and any additional FR additives (Dogan et al., 2021). Boron-based FRs work by releasing water in an endothermic reaction and creating a glass-like protective layer on the material. Boric acid, in particular, promotes dehydration and charring effects in oxygen-containing substrates (Shah et al., 2014). Among the earliest known FRs, boric acid and sodium borate are primarily utilized for cellulosic materials. While they are cost-effective and highly efficient, their application

is restricted to products where non-durable flame retardancy is acceptable due to their water solubility (Zakut, 2012).

Shen and Sprague (1982) have shown that zinc borate (ZB) is an effective FR in rigid PVC by oxygen index tests. In flexible polyvinyl chloride (PVC) formulations, ZB significantly increases char formation, while antimony oxide, a vapor phase FR, has minimal effect on char production. Pi et al. (2003) explored how zinc borate (ZB) and ZB–ATH hybrid fillers influence the flame-retardant behavior and mechanical performance of PVC. The interfacial interaction between PVC and ZB or ZB–ATH was strengthened through high-energy mechanical milling of PVC/ZB and PVC/ZB–ATH blends by forming chemical bonds, resulting in significant increases in LOI, impact strength, yield strength, and elongation at break. The polymer industry is experiencing a rising demand for FR and smoke-suppressed PVC compositions because of the emission of smoke and toxic gases, like HCl, during the dehydrochlorination of PVC when exposed to temperatures above 140°C (Erdoğdu et al., 2009). Erdoğdu et al. (2009) investigated how the combined use of zinc borate (ZB) and zinc phosphate (ZP) influences the thermal stability of PVC, employing various thermal analysis methods. Induction and stability time measurements were conducted at 140°C and 160°C for PVC plastisols. The findings indicated that plastisols containing either ZP or ZB effectively delayed dehydrochlorination compared to unstabilized PVC. In addition, when ZB and ZP were used together, a clear synergistic effect was observed, particularly in promoting char formation within PVC. Ning and Guo (2000) examined how ZB, ATH, and their combinations influenced the FR and smoke-suppressing behavior of PVC. Their results showed that even low loadings of ZB, ATH, or their mixtures noticeably increased the LOI of PVC and reduced smoke density during burning. Thermogravimetric (TGA) and gas chromatography–mass spectrometry (GC–MS) analyses further revealed that these additives facilitated char generation and suppressed the emission of toxic gases throughout the combustion process. In another study, Doğan et al. (2021) explored the synergistic influence of four different boron-containing compounds on the FR performance of a PP-based intumescent system. They reported that the boron compounds improved the efficiency of the intumescent formulation by reinforcing the char structure and enhancing its barrier stability. Likewise, Zhou et al. (2024) designed a FR composite with improved thermal conductivity by incorporating boron nitride (BN) and hexaphenoxycyclotriphosphazene (HPCP) into a polycarbonate matrix. Their work demonstrated the simultaneous enhancement of both flame retardancy and thermal conductivity in the resulting material.

Phosphorus-Containing FRs

Phosphorus-containing FRs primarily function in the condensed phase by forming a non-flammable surface char that shields the underlying material. Their versatility in applications arises from the ability of elemental phosphorus to adopt various oxidation states. Phosphorus-based FRs commonly exist in oxidation states of 0, +3, and +5, available in both organic and inorganic forms, including phosphines, phosphonium compounds, phosphine oxides, phosphonates, elemental red phosphorus (RP), phosphites, and phosphates. Most inorganic phosphorus-based FRs predominantly contain phosphates. Notably, elemental RP has a unique structure and is widely employed as an FR additive in polymers. When stabilized as coated RP, it is particularly effective in oxygen-rich polymers. Similarly, nitrogen-containing FRs play a significant role in HFFR systems and are widely used in the production of FR polymers. Organic nitrogen-based compounds are commonly integrated into various polymer formulations to improve fire resistance. Melamine, a nitrogen-rich heterocyclic compound, exhibits high thermal stability and crystallinity, with a melting point of 345°C. It readily forms stable salts with strong acids, and its derivatives are widely applied in different FR applications. The FR mechanism of melamine salts differs from that of pure melamine. Melamine phosphates, which incorporate phosphorus in their structure, provide specific benefits. At elevated temperatures, melamine decomposes endothermically, serving as a heat sink during combustion while releasing non-flammable ammonia gas. Moreover, it produces heat-resistant condensed-phase species that aid in developing a strong and stable char layer. As a result, most nitrogen-based polymer derivatives demonstrate FR properties by absorbing heat and releasing non-flammable gases into the flame zone, thereby cooling it and reducing the oxygen concentration (Zakut, 2012)(Knights et al., 2022)(Ray et al., 2025). In cable sheathing applications, they emit less corrosive gases during combustion, minimizing damage to electrical installations. Nitrogen-based FRs are environmentally friendly, as they do not introduce new elements into polymers like PU, nylons, and ABS where nitrogen is already present. Compared to metallic hydroxides, they are more effective and have a less adverse impact on the mechanical properties of plastic materials (Horacek et al., 1996). They are commonly combined with phosphorus-based FRs (Yılmaz, 2011).

Yang et al. (2013) combined liquid polysiloxane and ZB for flame retardancy of PC. As a result, the Si and B elements together significantly improved flame retardancy compared to FR systems using only polysiloxane or only ZB, contributing to the integrity of the charred residue layer with better quality. Wu and Lang (2016) produced a flame-retarded PC/ABS composite by melt-extrusion blending, employing aluminum hypophosphite (AHP) as

the flame-retardant additive. The incorporation of 15 wt% AHP significantly improved the flame retardancy. Levchik et al. (1996) examined the effects of HFFRs, such as APP, ammonium pentaborate, RP, potassium nitrate, or melamine and salts, on PA6. It was shown that APP interacted with PA6 to produce alkyl polyphosphoric esters, which act as precursors for swelling char formation. APB forms an inorganic glass layer on the surface of the burning polymer, which acts to protect the char from oxidation and hinder the diffusion of flammable gases. RP interacts with PA6, likely via radical mechanisms that generate phosphorus ester compounds, demonstrating a condensed-phase FR effect. Polyamine nitrate, a potent oxidizer, reacts with the polymer in the condensed phase, enhancing the efficiency of char formation. Meanwhile, melamine and its salts typically induce the flow of PA6, leading to flame suppression. These compounds also promote the cleavage of $H_2C–C(=O)$ bonds in PA6, which encourages crosslinking reactions and increases char formation within the polymer matrix. Braun et al. (2007) investigated how aluminum diethylphosphinate functions as a flame retardant when used together with melamine polyphosphate (MPP) and zinc borate (ZB) in glass-fiber-reinforced PA66. MPP acts mainly through fuel dilution and by providing an effective barrier layer. The cooperative interaction between aluminum phosphinate and MPP enhances char formation and strengthens the protective barrier. The inclusion of ZB further intensifies these effects by facilitating the generation of boron–aluminum phosphates instead of simple aluminum phosphates. In another study, Doğan et al. (2011) explored how ZB, boron phosphate (BPO_4), and boron–silicon-containing oligomers (BSi) influence the flame retardancy of melamine cyanurate (MC) in a PA6 matrix. The incorporation of ZB and BSi led to the development of a glassy surface film and a compact char layer, which reduced melt dripping and melamine sublimation, thereby lowering the LOI. However, thermogravimetric (TGA) analysis indicated that these boron-based additives reduced the decomposition temperatures of both MC and PA6, resulting in early MC degradation and a subsequent decline in FR performance. Liu and Wang (2009) also examined the FR behavior of MC in PA6 and concluded, based on analyses of the melt-dripping, condensed, and gas phases, that MC strongly influences the thermal degradation pathway of PA6. Zhang et al. (2008) examined the flame retardancy of MC and layered silicates in PA6. Their findings indicated that incorporating 13 wt% MC significantly enhanced the flame retardancy of PA6. However, adding more than 0.2 wt% of organically modified layered silicates had a detrimental effect, reducing the overall FR performance. Broadbent and Hirschler (1984) investigated the FR and smoke-suppressing effects of RP on ABS terpolymer in combination with a nitrogenous compound (melamine). While no positive FR interaction was observed between melamine and either DBB or red phosphorus, the systems containing all three components exhibited the lowest flammability values. Wu and Li (2014) prepared AHP-based FR ABS composites via melt mixing. ABS

composites containing 25 wt% AHP exhibited a LOI of 25.0%, and the FR ABS composite passed the UL-94 V-0 test. TGA measurements showed that as the AHP content increased, the char residue yield also increased. Hou et al. (2021) noted that phosphonium sulfonates (PhS), carrying different substituents, exhibited various synergistic FR effects with triphenyl phosphate (TPP) and bisphenol A bis(diphenyl phosphate) (BDP) in PC/ABS blends. Cone calorimeter test results for these composites showed significant reductions in HRR and total heat release (THR). Pawlowski et al. (2010) investigated bisphenol A PC/ABS with bisphenol A bis(diphenyl phosphate) (BDP) and 5 wt% ZB, both with and without BDP. While ZB is generally used as a smoke suppressant, its effect in PC/ABS with BDP was not very pronounced, and 5 wt% ZB in PC/ABS without BDP did not provide any smoke reduction. Yi et al. (2012) developed a new IFR system combining APP and poly(tetramethylene terephthalamide) (PA4T) to improve the flame resistance of ABS. The IFR demonstrated effective flame retardancy, increasing the LOI of the PA4T/APP/ABS (7.5/22.5/70) system from 18.5% to 30% and achieving a UL-94 V-1 rating. Zheng et al. (2019) designed a halogen-free, intumescent flame-retardant system (HECPM) based on cellulose by chemically modifying the cellulose structure with phosphate and melamine groups. Thermal degradation tests revealed that HECPM exhibited significant expansion when exposed to heat and retained a char residue of over 43% at 600°C, demonstrating its excellent char-forming ability. By incorporating 30 wt% of a 1:3 HECPM/EG blend into PP, a LOI of 31.5% and a UL-94 V-0 rating were achieved. Lu et al. (2009) evaluated the FR performance of ABS/PA6/styrene-maleic anhydride (SMA) alloys (80/20/6 ratio) with APP. The findings reveal that PA6 serves as an effective carbonization agent and enhances the intumescent flame retardancy of ABS/PA6/SMA alloys. Braun et al. (2010) explored the pyrolysis behavior and FR performance of glass fiber–reinforced PA6 systems containing aluminum diethylphosphinate (AlPi), MPP, and their combination (AlPi + MPP) to better understand the mechanisms governing fire resistance in such composites. Their findings showed that the materials achieved a V-0 classification and demonstrated an oxygen index (OI) value of 33%. Similarly, Perret et al. (2009) studied the thermal degradation and combustion characteristics of polycarbonate (PC) formulations, both with and without ABS, incorporating or excluding aryl phosphate FRs such as bisphenol A bis(diphenyl phosphate) (BDP), resorcinol bis(diphenyl phosphate) (RDP), and triphenyl phosphate (TPP). They emphasized that effective flame retardancy and enhanced char formation in the condensed phase depend on the alignment between the decomposition temperature range of the aryl phosphates and that of the PC matrix. This relationship highlights an opportunity to fine-tune the FR action of aryl phosphates through controlled thermal compatibility within PC-based materials.

CONCLUSION

This study highlights the growing importance of HFFR thermoplastic materials in meeting the demands for environmental sustainability and safety. The toxic gas emissions, environmental harm, and adverse effects on human health associated with traditional halogen-based FRs have necessitated the development of alternative materials. Inorganic additives, phosphorus-based compounds, nitrogen-containing agents, and nanotechnology-based materials have emerged as prominent solutions in providing halogen-free alternatives. The primary advantages of HFFRs include reduced toxic gas emissions during combustion, eco-friendly properties, and high thermal stability. Incorporating these additives into polymer matrices is particularly favored in industries such as automotive, construction, electronics, and electrical engineering to meet stringent safety standards. The FR performances of inorganic compounds (e.g., ATH and MH), phosphorus-containing systems (e.g., RP, phosphonates), and nitrogen-based additives (e.g., melamine derivatives) have demonstrated remarkable results, especially when synergistic effects are observed. However, the potential adverse impact of these additives on the mechanical properties of polymers remains a significant drawback, particularly in systems requiring high filler loadings. The analysis of various polymer matrices reveals that halogen-free additives exhibit effectiveness through different mechanisms. Although HFFRs offer many advantages, improving their overall efficiency remains a major challenge. The need for high filler content often leads to difficulties during processing, including increased melt viscosity, which limits their broader industrial use. To overcome these limitations, research has increasingly focused on surface treatments and the use of compatibilizing agents that enhance the interaction between the polymer matrix and the additive. Another promising direction is the design of synergistic formulations that can deliver effective flame retardancy at lower additive concentrations, providing both environmental and cost-related benefits. In summary, HFFRs present strong potential as sustainable and safer alternatives for a wide range of applications. Future investigations should aim to minimize their negative influence on mechanical performance, further improve their environmental profile, and refine manufacturing techniques to ensure economic viability. Moreover, exploring synergistic additive systems may enable high FR efficiency even with reduced filler levels. As these advancements continue, the role of HFFR-based thermoplastics is expected to expand, making them increasingly important in future-oriented sustainable manufacturing.

REFERENCES

Horrocks A.R. and Price D. (2001). *Fire Retardant Materials*. Woodhead Publishing Ltd.

Olabisi O., Adewale K. (2016). *Handbook of Thermoplastics*. 2nd Edition, CRC Press.

Hull T.R., Witkowski A. and Hollingbery L. (2011). Fire retardant action of mineral fillers, *Polym Degrad Stab*, vol. 96, no. 8, pp. 1462–1469, doi: 10.1016/j.polymdegradstab.2011.05.006.

Yılmaz M.C. (2011). Production Of Polymeric Composite Cable Sheat Materials Filled With Halogen-Free Flame Retardant, Master Of Science Thesis, Ege University.

Gupta R., Singh M.K., Rangappa S.M., Siengchin S., Dhakal H.N., and Zafar S. (2024). Recent progress in additive inorganic flame retardants polymer composites: Degradation mechanisms, modeling and applications, Nov. 15, Elsevier Ltd., doi: 10.1016/j.heliyon.2024.e39662.

Rothon R. and Hornsby P. (2014). Fire Retardant Fillers for Polymers, Polymer Green Flame Retardants, Elsevier Inc., pp. 289–321, doi: 10.1016/B978-0-444-53808-6.00009-3.

Atay H.Y. (2019). Halogen-free flame retardant plastics, *Handbook of Ecomaterials*, vol. 5, Springer International Publishing, pp. 3057–3079, doi: 10.1007/978-3-319-68255-6_156.

Zakut M. (2012). Effects Of Huntite/Hydromagneite On Capacity Of Flame Retardancy, Mechanical And Physical Properties Of Polypropylene, Istanbul Technical University.

Xu Z.S., Yan L., and Chen L. (2016). Synergistic Flame Retardant Effects between Aluminum Hydroxide and Halogen-free Flame Retardants in High Density Polyethylene Composites, *Procedia Engineering*, Elsevier Ltd, pp. 631–636, doi: 10.1016/j.proeng.2016.01.130.

Tirri T., Aubert M., Aziz H., Brusentsev Y., Pawelec W., and Wilén C.E. (2019). Sulfenamides in synergistic combination with halogen free flame retardants in polypropylene, *Polym Degrad Stab*, vol. 164, pp. 75–89, doi: 10.1016/j.polymdegradstab.2019.03.021.

Liang J.Z. et al. (2014). Mechanical properties and flame-retardant of PP/MRP/Mg(OH)2/Al(OH)3 composites, *Compos B Eng*, vol. 71, pp. 74–81, 2015, doi: 10.1016/j.compositesb.2014.10.054.

Shah A.U.R. et al. (2014). Effect of concentration of ATH on mechanical properties of polypropylene/aluminium trihydrate (PP/ATH) composite, *Transactions of Nonferrous Metals Society of China (English Edition)*, vol. 24, no. SUPPL. 1, doi: 10.1016/S1003-6326(14)63292-1.

Xu H. and Deng X.R. (2006). Preparation and properties of superfine Mg(OH)2 flame retardant, *Transactions of Nonferrous Metals Society of China*, Volume 16, Issue 2, Pages 488-492, https://doi.org/10.1016/S1003-6326(06)60084-8.

Hornsby P.R. and Watson C.L. (1990). A Study of the Mechanism of Flame Retardance and Smoke Suppression in Polymers Filled with Magnesium Hydroxide.

Sener A.A. and Demirhan E. (2008). The investigation of using magnesium hydroxide as a flame retardant in the cable insulation material by cross-linked polyethylene, *Mater Des*, vol. 29, no. 7, pp. 1376–1379, doi: 10.1016/j.matdes.2007.05.008.

Wang Z., Hu Y., Gui Z., and Zong R. (2003). Halogen-free flame retardation and silane crosslinking of polyethylenes, *Polym Test*, vol. 22, no. 5, pp. 533–538, 2003, doi: 10.1016/S0142-9418(02)00149-6.

Liu J. and Zhang Y. (2011). Effect of ethylene-acrylic acid copolymer on flame retardancy and properties of LLDPE/EAA/MH composites, *Polym Degrad Stab*, vol. 96, no. 12, pp. 2215–2220, doi: 10.1016/j.polymdegradstab.2011.09.010.

Shen H., Wang Y.H., Liang D., and Mai K.C. (2011). Research and preparation of halogen-free flame-retardant polypropylene, *Procedia Engineering*, Elsevier Ltd, pp. 394–400, doi: 10.1016/j.proeng.2011.04.674.

Shen L., Chen Y., and Li P. (2012). Synergistic catalysis effects of lanthanum oxide in polypropylene/magnesium hydroxide flame retarded system, *Compos Part A Appl Sci Manuf*, vol. 43, no. 8, pp. 1177–1186, doi: 10.1016/j.compositesa.2012.02.014.

Hao S., Yu-hai W., Dong L., and Kan-cheng M. (2011). Research and preparation of halogen-free flame-retardant polypropylene, *Procedia Engineering*, Elsevier Ltd, pp. 394–400, doi: 10.1016/j.proeng.2011.04.674.

Liang J.Z. (2017). Tensile and flexural properties of polypropylene composites filled with highly effective flame retardant magnesium hydroxide, *Polym Test*, vol. 60, pp. 110–116, doi: 10.1016/j.polymertesting.2017.03.014.

Hornsby P.R., Wang J., Rothon R., Jackson G., Wilkinson G., and & Cossick K. (1996). Thermal decomposition behaviour of polyamide fire-retardant compositions containing magnesium hydroxide filler, *Polymer Degradation and Stability,*1996, https://doi.org/10.1016/0141-3910(95)00181-6.

Balakrishnan H., Hassan A., Isitman N.A., and Kaynak C. (2012). On the use of magnesium hydroxide towards halogen-free flame-retarded polyamide-6/polypropylene blends, *Polym Degrad Stab*, vol. 97, no. 8, pp. 1447–1457, doi: 10.1016/j.polymdegradstab.2012.05.011.

Hollingbery L.A. and Hull T.R. (2010). The fire retardant behaviour of huntite and hydromagnesite - A review, doi: 10.1016/j.polymdegradstab.2010.08.019.

Yurddaskal M. and Celik E. (2018). Effect of halogen-free nanoparticles on the mechanical, structural, thermal and flame retardant properties of polymer matrix composite, *Compos Struct*, vol. 183, no. 1, pp. 381–388, doi: 10.1016/j.compstruct.2017.03.093.

Dogan M., Dogan S.D., Savas L.A., Ozcelik G., and Tayfun U. (2021). Flame retardant effect of boron compounds in polymeric materials, Elsevier Ltd., doi: 10.1016/j.compositesb.2021.109088.

Shen K.K. and Sprague R.W. (1982). Recent Studies on the Use of Zinc Borate as a Flame Retardant and Smoke Suppressant in PVC, *Journal of Vinyl Technology*, https://doi.org/10.1002/vnl.730040308.

Pi H., Guo S., and Ning Y. (2003). Mechanochemical Improvement of the Flame-Retardant and Mechanical Properties of Zinc Borate and Zinc Borate-Aluminum Trihydrate-Filled Poly(vinyl chloride), *Journal of Applied Polymer Science*, doi:10.1002/app.12202.

Erdoğdu C.A., Atakul S., Balkose D., and Ulku S. (2009). Development of synergistic heat stabilizers for PVC from zinc borate-zinc phosphate, *Chemical Engineering Communications*, pp. 148–160, doi: 10.1080/00986440802293148.

Ning Y. and Guo S. (2000). Flame-Retardant and Smoke-Suppressant Properties of Zinc Borate and Aluminum Trihydrate-Filled Rigid PVC.

Doğan M., Yılmaz A., and Bayramlı E. (2010). Synergistic effect of boron containing substances on flame retardancy and thermal stability of intumescent polypropylene composites, *Polym Degrad Stab*, vol. 95, no. 12, pp. 2584–2588, doi: 10.1016/j.polymdegradstab.2010.07.033.

Zhou F., Xi W., Qian L., Wang J., Qiu Y., and Chen Y. (2024). Hexaphenoxy cyclotriphosphazene/boron nitride high-efficiency charring system enhancing the flame retardancy and thermal conductivity of polycarbonate, *Polym Degrad Stab*, vol. 219, doi: 10.1016/j.polymdegradstab.2023.110601.

Knights A.W., Nascimento M.A., and Manners I. (2022). An investigation of polyphosphinoboranes as flame-retardant materials, *Polymer (Guildf)*, vol. 247, doi: 10.1016/j.polymer.2022.124795.

Ray S.S. and Kuruma M. (2025). Springer Series in Materials Science 294 Halogen-Free Flame-Retardant Polymers Next-generation Fillers for Polymer Nanocomposite Applications. Accessed: Apr. 17. [Online]. Available: http://www.springer.com/series/856.

Horacek H. and Grabner R. (1996). Advantages of flame retardants based on nitrogen compounds, *Polymer Degradation and Stability*, https://doi.org/10.1016/S0141-3910(96)00045-6.

Yang S., Lv G., Liu Y., and Wang Q. (2013). Synergism of polysiloxane and zinc borate flame retardant polycarbonate, *Polym Degrad Stab*, vol. 98, no. 12, pp. 2795–2800, doi: 10.1016/j.polymdegradstab.2013.10.017.

Wu N. and Lang S. (2016). Flame retardancy and toughness modification of flame retardant polycarbonate/acrylonitrile-butadiene-styrene/AHP composites, *Polym Degrad Stab*, vol. 123, pp. 26–35, doi: 10.1016/j.polymdegradstab.2015.11.007.

Levchik S.V., Levchik G.F., Balabanovich A., Caminob G., and Costab L. (1996). Mechanistic study of combustion performance and thermal decomposition behaviour of nylon 6 with added halogen-free fire retardants, *Polymer Degradation and Stability*, https://doi.org/10.1016/S0141-3910(96)00046-8.

Braun U., Schartel B., Fichera M.A., and Jäger C. (2007). Flame retardancy mechanisms of aluminium phosphinate in combination with melamine polyphosphate and zinc borate in glass-fibre reinforced polyamide 6,6, *Polym Degrad Stab*, vol. 92, no. 8, pp. 1528–1545, doi: 10.1016/j.polymdegradstab.2007.05.007.

Doğan M., Yılmaz A., and Bayramlı E. (2011). Effect of boron containing materials on flammability and thermal degradation of polyamide-6 composites containing melamine cyanurate, *Polym Adv Technol*, vol. 22, no. 5, pp. 560–566, doi: 10.1002/pat.1545.

Liu Y. and Wang Q. (2009). The investigation on the flame retardancy mechanism of nitrogen flame retardant melamine cyanurate in polyamide 6, *Journal of Polymer Research*, vol. 16, no. 5, pp. 583–589, doi: 10.1007/s10965-008-9263-6.

Zhang J., Lewin M., Pearce E., Zammarano M., and Gilman J.W. (2008). Flame retarding polyamide 6 with melamine cyanurate and layered silicates, *Polym Adv Technol*, vol. 19, no. 7, pp. 928–936, doi: 10.1002/pat.1063.

Broadbent J.R.A. and Hirschler M.M. (1984). Red Phosphorus As A Flame Retardant For A Thermoplastic Nitrogen-Containing Polymer, *European Polymer Journal*, https://doi.org/10.1016/0014-3057(84)90134-4.

Wu N. and Li X. (2014). Flame retardancy and synergistic flame retardant mechanisms of acrylonitrile-butadiene-styrene composites based on aluminum hypophosphite, *Polym Degrad Stab*, vol. 105, no. 1, pp. 265–276, doi: 10.1016/j.polymdegradstab.2014.04.011.

Hou S., Li Z., Zhang Y.J., and Jiang P. (2021). Phosphorous-phosphorous synergistic effect on flame retardancy, mechanically reinforce and hydrolytic resistance for PC/ABS blends, *Polym Degrad Stab*, vol. 183, doi: 10.1016/j.polymdegradstab.2020.109442.

Pawlowski K.H., Schartel B., Fichera M.A., and Jäger C. (2010). Flame retardancy mechanisms of bisphenol A bis(diphenyl phosphate) in combination with zinc borate in bisphenol A polycarbonate/acrylonitrile-butadiene-styrene blends, *Thermochim Acta*, vol. 498, no. 1–2, pp. 92–99, doi: 10.1016/j.tca.2009.10.007.

Yi L., Jiangsong Y., and Xufu C. (2012). Application of a novel halogen-free intumescent flame retardant for acrylonitrile-butadiene-styrene, *J Appl Polym Sci*, vol. 124, no. 2, pp. 1475–1482, doi: 10.1002/app.35153.

Zheng Z., Liu Y., Dai B., Meng C., and Guo Z. (2019). Fabrication of cellulose-based halogen-free flame retardant and its synergistic effect with expandable graphite in polypropylene, *Carbohydr Polym*, vol. 213, pp. 257–265, doi: 10.1016/j.carbpol.2019.02.088.

Lu C., Chen T., and Cai X. (2009). Halogen-free intumescent flame retardant for ABS/PA6/SMA alloys, *Journal of Macromolecular Science*, Part B: Physics, vol. 48, no. 4, pp. 651–662, doi: 10.1080/00222340903070342.

Braun U., Bahr H., Schartel B. (2010). Fire retardancy effect of aluminium phosphinate and melamine polyphosphate in glass fibre reinforced polyamide 6, *e-Polymers*, no. 041, doi:10.1515/epoly.2010.10.1.443.

Perret B., Pawlowski K.H., Schartel B. (2009). Fire retardancy mechanisms of arylphosphates in polycarbonate (PC) and PC/acrylonitrile-butadiene-styrene, *J Therm Anal Calorim*, doi:10.1007/s10973-009-0379-7.

Sintered Diamond and Applications

Fehim FINDIK[1,2]

1- Prof. Dr. Metallurgy and Materials Engineering Department, Faculty of Technology, Sakarya Applied Sciences University, Sakarya, Turkey. ORCID No: 0000-0003-2537-1951
2- Prof. Dr. Istanbul Aydın University, Mechanical Eng Dept, Engineering Faculty, Florya Halit Aydın Campus, Istanbul, Turkey
C: Corresponding author; e-mail: findik@subu.edu.tr

ABSTRACT

Diamonds are exceptionally hard materials that, when polished, exhibit attractive optical properties, resulting in a brilliant shine and wear-resistant gemstone. However, their extreme hardness makes them difficult to shape. Due to their high melting temperature, resistance to conventional machining tools, and lack of plasticity, subtractive manufacturing methods—such as fracturing, polishing, or laser machining—are employed in jewelry production. Fracturing techniques take advantage of weaker crystallographic planes to shape diamonds. Beyond gemstones, sintered diamonds find applications in cutting tools, mining and construction, electronics and semiconductors, medical devices, automotive and aerospace industries, and research and development. This study examines sintered diamonds from historical, mechanical, and thermal property perspectives, as well as their diverse applications. The research reveals that sintered diamond hardness ranges from 5,000 HV to 13,000 HV, while diamond composites exhibit hardness values increasing from 0 to 9,000 HV after sintering. The strength of diamond composites remains stable at approximately 1,500 MPa up to 80 wt% diamond contents but rises sharply to 4,500 MPa at 90 wt%. Pure diamond has an elastic modulus of 1,050 GPa and a fracture toughness of around 15 $MPa \cdot m^{0.5}$. Thermally, diamond-graphite composites demonstrate a conductivity of about 400 $W/m \cdot °C$ at 1,400°C, peaking at 1,900°C under 6 GPa pressure.

Keywords – Diamond, sintering, applications, mechanical properties, thermal conductivity

INTRODUCTION

Diamonds are hard, and when polished, the optical properties give an attractive shine and sparkle in a wear-resistant gemstone. Hard materials such as diamonds are difficult to shape. The melting temperature is too high for casting, the hardness resists most machining tools, and the lack of plasticity does not allow for reshaping. Therefore, subtractive manufacturing approaches are used to create jewelry. Diamonds are broken, polished, or laser machined. Fracture exploits the weaker crystallographic planes.

Diamonds are often viewed from a perspective that emphasizes precious stones. However, diamond consumption is dominated by artificial diamonds, which are made into industrial tools using powder metallurgy technologies. These composites are preferred due to their exceptional wear resistance in harsh working conditions.

The production of diamond tools dates back 2,500 years (Sorb et al, 2016:1). The first findings involved hammering diamond grains into a soft metal substrate. Later, the use of diamonds in wire drawing began in 1819,

while diamond glass polishing began in 1824 and stone cutting using diamond tools dates from 1854. The emergence of sintered bonded diamond dates back to the 1930s.

Modern industrial applications for diamonds are based on a composite of diamond grains embedded in a matrix. Usually, the matrix is a metal such as cobalt, cobalt, iron or nickel alloys. Diamond gemstones are faceted along their easy fracture planes. Sintering bonds, the diamonds to a matrix phase or other diamond grains.

Before sintering, the diamond powder is loose and flows like a viscous liquid. The loose diamond powder flows to conform to the shape of the container. After sintering, the diamond grains bond together. The sintered structure is strong and maintains the shape determined by the forming equipment. Furthermore, the particles can no longer flow; they bond together to form grains. In most cases, the diamond grain size is proportional to the initial diamond particle size, but they are held in a rigid three-dimensional structure.

Conceptual sketches of the different structures, involving increased diamond content, are shown in Figure 1. The surface bond has diamond impressed only on one surface. The filled volume has mixed diamond and matrix, but no diamond-diamond sintering. The sinter bonded case is high in diamond with considerable diamond-diamond bonding.

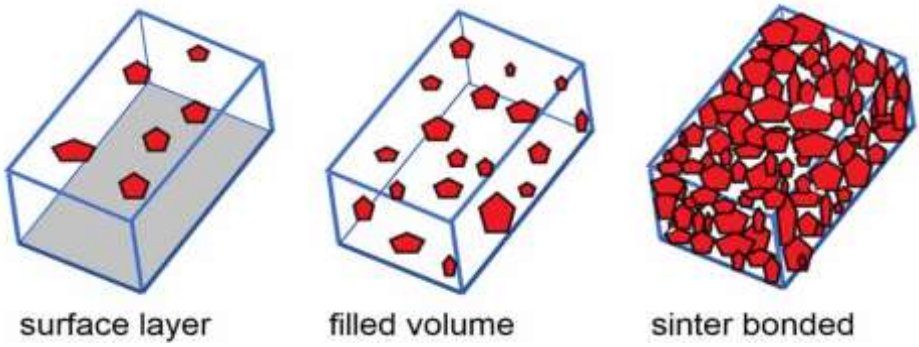

Figure 1. Conceptual sketches of three variants for sintered diamond structures, involving diamond dispersed on the surface (left) mixed diamond and matrix (center) and highly bonded diamond with interstitial matrix (right) (German, 2023:1).

The availability of man-made diamonds has facilitated growth in industrial applications. Early applications were in abrasives, wear components, and cutters. Later, they were also applied to metalworking tools and high-strength bearings. Each uses sintering to produce the desired shapes. Table 1 outlines several examples of diamond dispersion structures.

Table 1. Overview of different sintered diamond structures (German, 2023:1).

diamond vol %	3 to 10	10 to 50	50 to 85	85 to 100
application	polishing, sharpening	drilling, sawing	machining	drawing dies
structure	diamond on substrate	diamond dispersed in metal	diamond bonded with metal	predominantly diamond-diamond bonds
fabrication	electroplating, brazing, spray forming, sintering	sintering, hot pressing, spark sintering	high-pressure high-temperature	high-pressure high-temperature
matrix	copper, silver, nickel	copper, glass, ceramic, cobalt, silicon	cobalt, silicon, nickel alloy	cobalt, cemented carbide

Conceptual drawings of different structures containing increased diamond content are shown in Figure 1. The surface bond has diamonds printed on only one surface. There is mixed diamond and matrix in the filled volume, but no diamond-diamond sintering. The sinter bond case contains a high percentage of diamonds with significant diamond-diamond bonding.

Cutting and machining tools such as wire saws, stone cutters, and cement saws rely on a three-dimensional distribution of diamonds. Similarly, heat sinks are predominantly metal in a diamond distribution throughout the body. Each diamond grain is completely surrounded by matrix. As wear occurs, new diamonds are exposed. These tools are up to about 50% volume diamond, which makes them more difficult to manufacture, relying on a combination of temperature and pressure using hot pressing or similar pressure-assisted sintering ideas.

The first step for diamond sintering is to pressurize the powder while simultaneously applying heat. The transition to the stable region of the diamond occurs during heating. At low temperatures, the kinetics are very slow, but the kinetics of graphite formation increase with temperature. Therefore, the processing scheme is drawn in Figure 2.

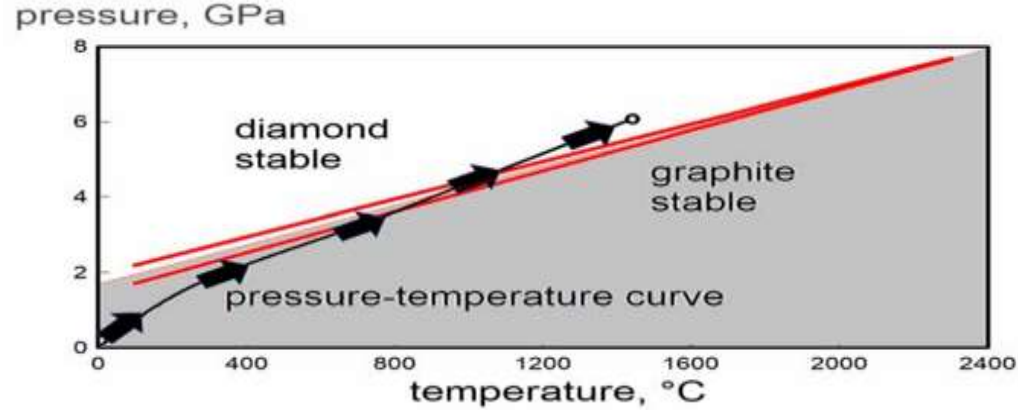

Figure 2. The process sequence for forming sintered diamond relies on pressurization to stabilize diamond and heating to increase the transformation

kinetics. For a selected pressure, an upper limit temperature is set by the diamond reversion to graphite (indicated by the two models shown as red lines) (German, 2023:1).

The black curved path indicates that pressurization begins early and that as the temperature increases, the pressure should pass into the stable region of the diamond. Below about 800 to 1000°C, diamond is metastable and can withstand short-term heating in the stable region of the graphite. As the peak temperature is approached, the pressure should exceed the boundary lines.

During heating, the brittle diamond particles break due to the high pressure applied, but eventually the diamond softens. The final or peak temperature and pressure are in the stable region of the diamond with a holding time sufficient to ensure dissolution of any graphite and precipitation of diamond in the intergranular bonds. Initially, the structure is under pressure to cool to prevent graphite formation while hot.

This HPHT process produces polycrystalline diamond (PCD) that provides significant gains in cutter life, as desired for oil well drilling (Che et al, 2012:134).

The typical diamond cutter is bonded to cemented carbide. This combination is called polycrystalline diamond compacts, or PDC. The structure is layered, with sintered diamond on top and sintered cemented carbide on the bottom. The diamond layer is called the diamond table because it is a flat disk on top of the compact, as shown in Figure 3. The diamond-carbide interface is often corrugated or otherwise wavy to increase the bond area (Lancaster et al, 2007:1), (Frushour & Torbet, 2001:1).

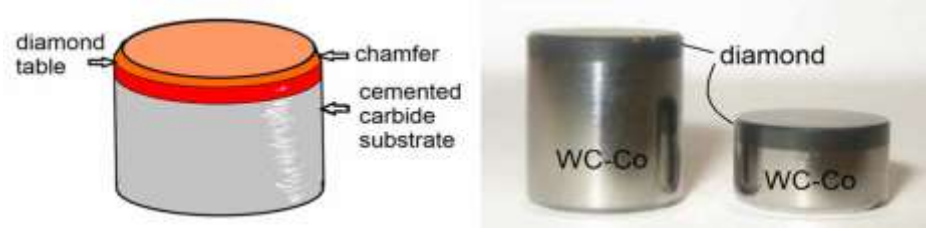

Figure 3. Sketch and photograph of polycrystalline diamond compacts, consisting of a sintered diamond layer or table located on a cemented carbide substrate (Lancaster et al, 2007:1), (Frushour & Torbet, 2001:1).

PHASE DIAGRAMS

A significant limit corresponds to the solid-liquid eutectic temperatures for solvent metals saturated with carbon. The carbon-cobalt phase diagram in Figure 4 helps you understand the sintering ranges. At one atmospheric pressure, liquid cobalt forms a eutectic at 1320°C with 2.6 wt% carbon. Various estimates are available for eutectic systems under pressure, as follows (Belnap, 2010:389), (Boland et al, 2010:1390), (Li et al, 1990:4150):

- 1320°C at atmospheric pressure

- 1336°C at 5.6 GPa
- 1375°C at 4 GPa
- 1400 to 1570°C at 7 GPa.

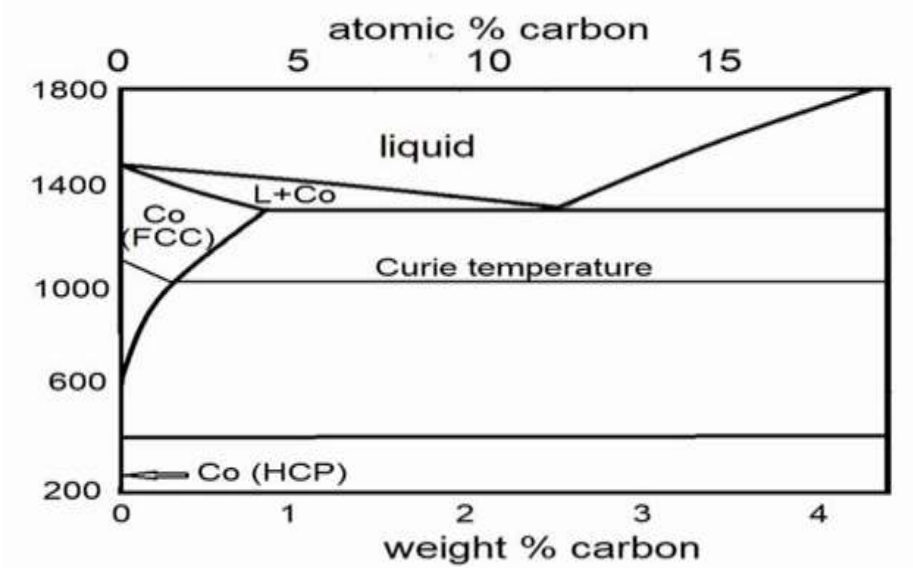

Figure 4. The carbon-cobalt binary phase diagram of temperature (°C) and composition at one atmosphere pressure, showing eutectic melting at 2.6 wt % carbon and 1320°C. The high temperature form of cobalt is the face-centered cubic crystal structure (with some carbon solubility) versus the low temperature hexagonal close-packed phase is devoid of solubility (Li et al, 1990:4150).

If WC deviates slightly from stoichiometry, a small shift in the initial liquid formation occurs, dropping to 1298°C. This liquid is cobalt-carbon with some dissolved tungsten. Pressure stabilizes the denser phases. For carbon this means diamond, for cobalt it means solid. Therefore, pressure delays sintering to higher temperatures, estimated at 1512°C at 5.7 GPa (Li et al, 1990:4150), (Sung, 2000:6041).

This seems excessive, since several reports have found liquid formation and sintering at 1400°C. The disagreement in these studies reflects the difficulty of obtaining accurate temperature and pressure readings.

Diamond becomes ductile when heated. Initial pressure fractures the diamond to melt at 1000°C, but plastic flow occurs at higher levels. The onset of plasticity allows grain change during diamond heating. Thus, three distinct phases are now evident - diamond softening, matrix fracture, and diamond stabilization. Figure 5 solidifies the boundaries of these three transitions to show that the range of diamond sintering can occur. In practice, some steps can be followed as follows (DeVries, 1975:1193).

- 5.8 GPa and 1500°C,
- 8.0 GPa and 1600°C,
- 7.5 GPa and 1900°C.

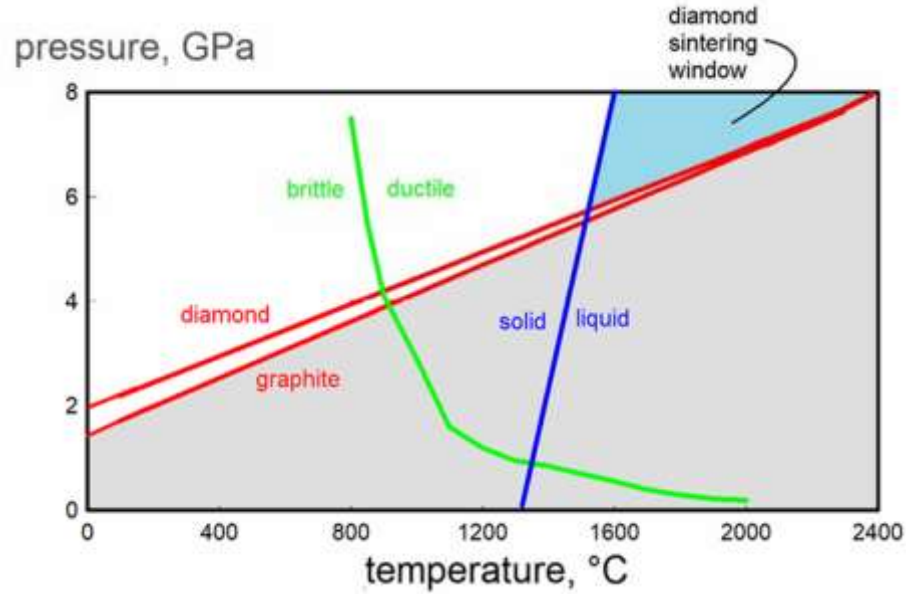

Figure 5. The concept of a sintering window arises by considering significant behavior changes (red = diamond-graphite stability, blue = solvent metal catalyst melting, and green = diamond ductility onset). The upper right corner defines the conditions for diamond sintering with a solvent metal catalyst (DeVries, 1975:1193).

These are equilibrium events. Normally, supercooling and overheating are required to nucleate a new phase, so the diamond sintering window is not sensitive and varies with various processes such as heating or cooling rate.

To avoid difficulties with higher pressures and temperatures, the normal diamond sintering conditions are around 5.8 GPa and 1500°C. The short times in the process, on the order of a few chambers, are sufficient to minimize the solution-redeposition phenomena responsible for diamond bonding.

An important aspect of the phase diagram is the splashing of carbon formations that occur in the liquid initial formations. We then estimate the sintering events. Initial pressurization allows the diamond elements to fracture and heat, allowing graphite pockets to grow. The diamond, which is not in contact with the cemented carbide substrate, pushes the molten cobalt-rich melt into the diamond spaced assembly. The newly formed liquid rapidly fluidizes. The transport obtained by carbon dissolution reduces the solid-liquid surface energy. This leads to rapid liquid phase sintering (German, 1996:1193).

After liquid phase sintering and the formation of diamond-diamond bonds, polycrystalline diamond has high strength, fracture and breakage resistance. It is also bonded to the cemented carbide substrate. High strength, impact resistance and wear resistance are significant properties after sintering. Its characteristic is generally a grain system close to 5 µm and the best overall performance varies according to its size. This allows the distribution, emergence and fracture of a media typically 10 to 20 µm from the initial pressurization.

Unlike graphite, diamond has lower temperatures in liquid cobalt. This provides a driving force for carbon solution from graphite and redeposition as diamond. The binary phase diagram shows that at 1320°C eutectic, 1 wt% graphite dissolves in solid cobalt and 2.6 wt% carbon dissolves in liquid cobalt. In contrast, below the eutectic temperature, diamond loss is about 0.015 wt%. The reduction of cobalt from graphite and diamond is applied in Figure 6 relative to temperature at one atmospheric pressure (Tian et al, 2020:110). Carbon loss increases after the eutectic liquid has formed. However, below 1320°C, diamond depletion is a small fraction of the graffiti release (into solid cobalt) (Kanda, 2000:482).

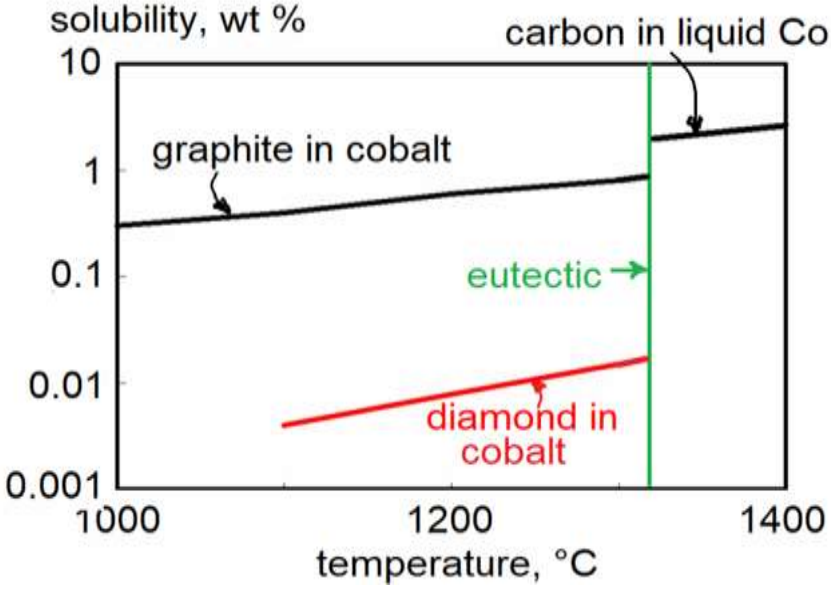

Figure 6. Contrast of the solubility (log scale) of graphite and diamond in cobalt versus temperature (Tian et al, 2020:110).

The formation of the liquid allows the carbon from the graphite to dissolve into the newly formed liquid cobalt. In these suits, the diffusion of cobalt is nominally $3x10^{-9}$ m^2/s. The measured liquid cobalt rates on diamond are 10 sensors 200 µm. In other words, a 2 mm diamond table is completely inoculated with cobalt in less than two minutes. The dissolved carbon from the graphite sources precipitates as diamond. Heterogeneous nucleation occurs and perfect diamond bonds are formed at surface defects.

The driving force for the dissolution of graphite and the precipitation of diamond is the change in its distribution and products. The higher density of diamond (3.51 g/cm^3) compared to graffiti (2.26 g/cm^3) causes a rapid reaction initially when formed as liquid solvent metals. Pressure also shows the effects of diamond and graphite loss. The transition from graphite to diamond and diamond growth slows down significantly after the initial rush (Kanda, 2000:482).

APPLICATIONS

Applications for sintered diamonds are generally in the form of metal-bonded composites fabricated into relatively simple geometric shapes. In addition to metallic matrix phases, there are several examples of ceramic-glass and resin bonds in abrasives. Sintered polycrystalline diamonds, where diamond-diamond bonds are formed, require HPHT conditions to precipitate diamond at grain contact points. This provides impressive performance, but at a high cost.

Figure 7 provides a conceptual outline of consolidation options ranging from dispersed surface layers to sintered polycrystalline diamonds. Products range from substrates with surface layers to three-dimensional systems with little matrix content. The difficulty of creating these structures increases as the diamond content increases, from a few wt% for surface layers to 100% diamond for sintered diamonds without additives.

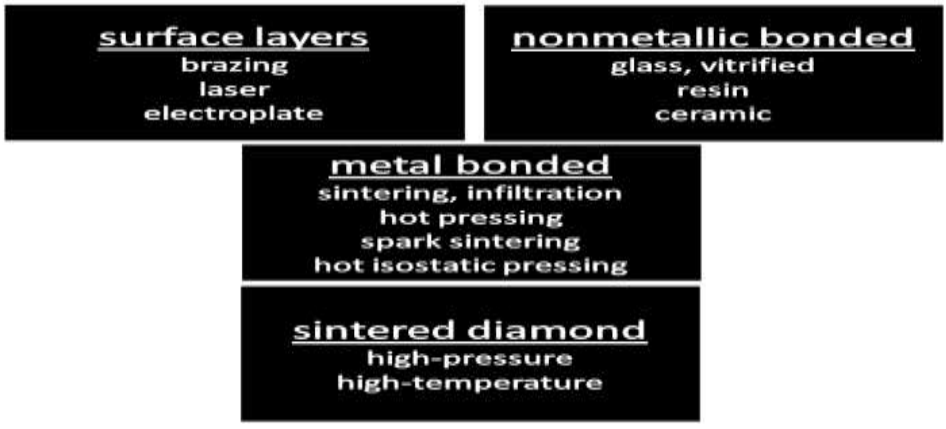

Figure 7. Examples of the different types, bonds, and consolidation processes for sintered diamond composites (German, 2023:1).

Variants may include diamond powder captured as a two-dimensional coating or a three-dimensional structure via one of the following manufacturing routes (Hsieh & Lin, 2001:121), (Huang et al, 2021:34059):

- electroplated metal (nickel) layer
- sintered layers with discrete surface diamond protrusions,
- metal, glass or ceramic bonded diamonds,
- resin bonded diamonds,

- polycrystalline sintered diamond with 3% to 10% metal matrix,
- pure polycrystalline sintered diamond (no matrix phase)

Metal bonds include cobalt, copper-titanium, copper-chromium, cemented carbides (WC-Co), bronze (copper-tin) iron-copper alloys, nickel alloys, copper-cobalt and mixtures thereof (Schubert et al, 2008:263), (Bobrovnitchii et al, 2010:182).

Copper provides high thermal conductivity but has lower strength compared to other metals. Cobalt is much stronger, but has lower thermal conductivity. For this reason, copper is preferred for heat sinks, and cobalt is preferred for applications requiring wear resistance. Tin additions help bond the matrix to the diamond. Titanium and chromium are similar and react when heated to form carbides. This chemical affinity improves wetting and bonding when formed as surface layers on the diamond.

Pressure-assisted sintering supplements the capillary pressure from the wetting fluid with an external force. The capillary pressure is 1 to 10 MPa, pulling the particles together. It is inversely proportional to particle size. For larger particles, an external compressive pressure is added to the capillary pressure, resulting in faster sintering density and higher final densities. The initial applied stress is amplified by the point contacts between the particles, so for example, an applied pressure of 50 MPa will reach a local stress of 1500 MPa at the beginning of sintering. The stress concentration relaxes as the density increases. The greater the pressure, the faster the sintering densification.

Common pressure-assisted sintering approaches are hot pressing and spark sintering (Cavaliere, 2019:1). The cycles compress the metal particles in a short holding time. Full density without graphite formation requires a low peak temperature and a short holding time. However, as shown in the Raman spectra in Figure 8, graphite formation is difficult to prevent.

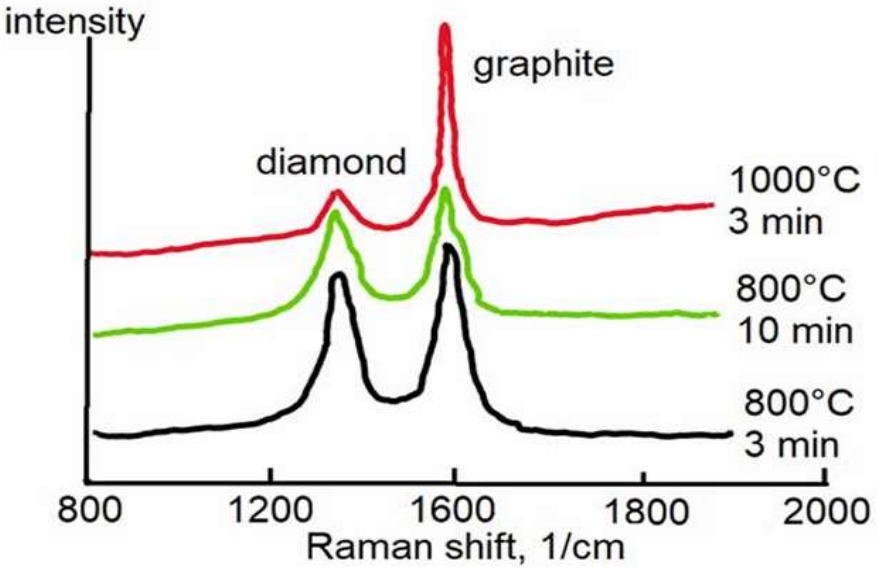

Figure 8. Normalized Raman spectra showing graphite and diamond relative intensities for nickel-diamond mixtures spark sintered at 40 MPa; the red upper curve corresponds to 1000°C for 3 min, and lower two curves correspond to 800°C for 10 min (green) or 3 min (black) (Cavaliere, 2019:1).

Higher temperatures and longer holding times result in more graphite formation. If graphite is formed, the PDC properties are deteriorated.

Hot isostatic pressing is occasionally mentioned as a manufacturing technique, but is rarely used because it is slow and costly. Furthermore, typical component sizes and shapes do not justify hot isostatic pressing, which is best applied to large, three-dimensional geometries.

On the other hand, high-pressure high-temperature consolidation borrows equipment design and operating conditions from the field of diamond synthesis. The target geometries are relatively simple, right-circular cylinders. Here the diamonds are bonded together.

Various consolidation approaches support many applications for sintered diamonds (Munro et al, 1984:783), (Konstanty, 2003:1).

- grinding wheels or diamond-metal composites for grinding wheels,
- glass cutting, polishing and finishing tools,
- plate cutting wire saws for cutting marble, granite and stone,
- machining tools for nonferrous materials such as titanium, wood, aluminum, composites,
- wire drawing dies for nonferrous materials,
- high conductivity electrical contacts,
- semiconductor disk polishing re-polishers,
- mining and cement drills, drilling tools, cutting tools,
- highway cut-off saws,

- wear-resistant jet engine thrust bearings,
- computer heat sinks,
- rigid assemblies for precision laser, radar and electronic devices,
- scratch-resistant watch cases (Sexton & Cooley, 2009:1041).

An illustration is included in Figure 9 to illustrate a specific device.

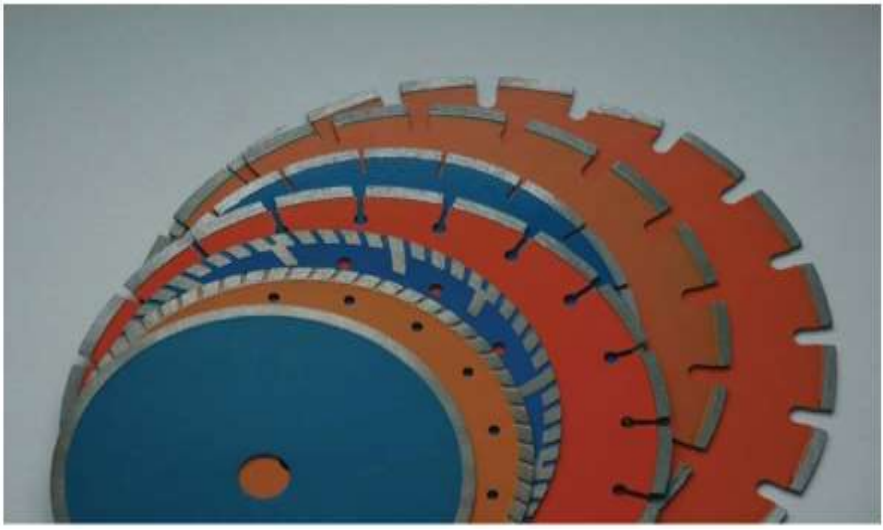

Figure 9. Saw blades with diamond-metal composite tips as the cutting segments (German, 2023:1).

PROPERTIES

In this part three properties of diamond will be investigated. These properties are hardness, mechanical properties as well as thermal properties are criticized as follows:

Hardness

Hardness testing on sintered diamond is difficult because the material is very hard. Hardness readings are more reliable as the diamond content decreases.

Figure 10 is a scatter plot of diamond volume fraction as the independent variable and the hardness reported from the above data compilation. The plot is instructive to see the dominant role of diamond volume fraction. An upper limit line has been added to show the peak hardness that can be achieved. The cases at zero diamond correspond to cemented carbides with no diamond added.

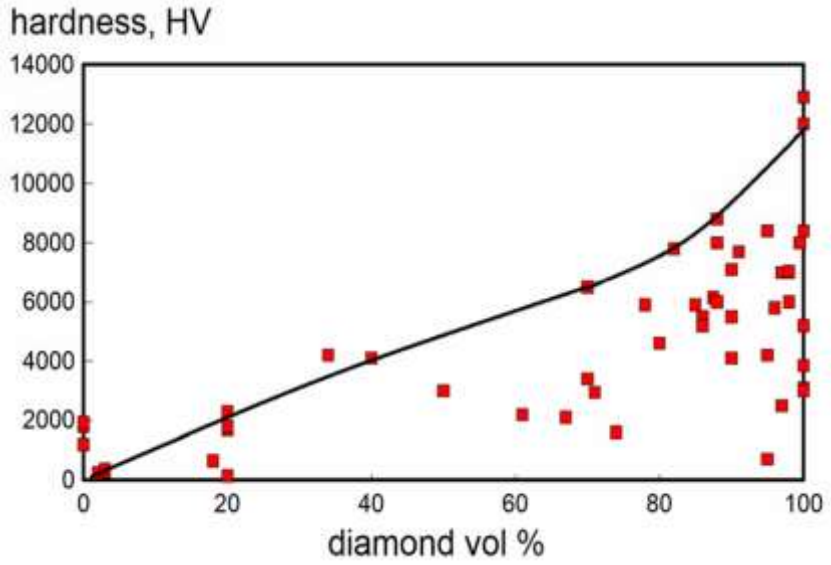

Figure 10. Scatter plot of harness determinations for 51 diamond composites and 3 cemented carbides without diamond, showing how the upper limit hardness is dictated by the diamond content (German, 2023:1).

Hardness is also affected by consolidation temperature and pressure factors. These two parameters determine particle fracture, cobalt infiltration, and the degree of diamond-diamond bonding. An example plot of peak HPHT sintering temperature versus sintered hardness is given in Figure 11. The results are for compacts produced with the same particle size, pressure, and holding time.

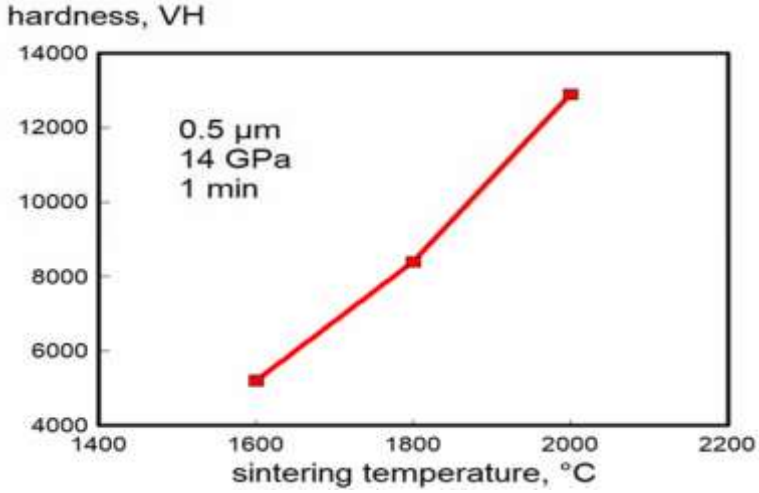

Figure 11. Plot of Vickers hardness versus consolidation temperature for 0.5 µm diamond powder held for 1 min at 14 GPa and temperatures from 1600 to 2000°C (German, 2023:1).

Mechanical properties

Sintered diamond composites are often used in high-stress situations. Consequently, mechanical properties are studied in detail and predictors of good performance are sought. At full density, attributes such as strength depend on composition and microstructure, especially grain size. Single-crystal diamond fails at a compressive stress of 9 GPa for 400 μm particles and decreases to 5.3 GPa for 1000 μm particles (Field, 1992:1). An important factor is the defect structure.

As a measure of mechanical properties, two extremes are noted. At one extreme is polycrystalline diamond, which contains no intercalated metals. This is a hard, strong material with a flexural strength ranging from 800 to 3000 MPa. However, it is brittle. The change in strength reflects the defects. At the other extreme are composites consisting of a metal matrix with a low diamond concentration in the 5 vol.% range. Here, the strength depends on the matrix alloy and the interface between the diamond and the matrix. Example values for this dispersed diamond case are as follows (Yang et al, 2013:2366).

Fe-43Cu-2Sn-3Zn 570 MPa tensile strength, 11% elongation,
Co 565 MPa tensile strength, 1% elongation,
Fe-30Cu-2P 510 MPa tensile strength, 1% elongation.

The matrix phase and diamond mixtures fall between the two. Below about 20 vol% diamond, the matrix-diamond interface strength is the controlling factor. At a weak interface, the strength decreases as more diamond is added. For example, a WC-Ni-Co-Mn-Cu-Sn matrix hot-pressed at 28.5 MPa for 5 min at 880°C has a compressive strength of 1650 MPa, but when 20 wt% (54 vol%) diamond is used, the strength drops to 1407 MPa.

- temperature – heating path and peak temperature are not measured, only electrical power is monitored, errors and deviations are possible but not detected,
- pressure – cell pressure is not measured; only hydraulic pressure is monitored with significant potential variations between compacts.

Because of the brittle character, most strength tests are performed under compression. Test types include compression on flat circular surfaces of a cylinder, compression on the diameter of a thin disk-shaped cylinder, bending of a rectangular geometry, shearing in a clamped fixture, and occasionally tensile fracture.

Smaller grain sizes provide higher strengths. For diamond contents of 77 to 94 wt%, PCD strength ranges from 650 to 1815 MPa (Scott, 2018:161). The highest strengths (approximately 1700 to 1800 MPa) come with grain sizes of 3 to 5 μm and 20 to 24 wt% matrix. The lowest reports (444 and 650 MPa) have grain sizes of 30 to 125 μm and 7 to 12 wt% binder. Table 31 compares the strengths according to different test conditions. For most matrix phases, at densities close to 8 g/cm3, the volume % diamond is about

2.2 times the weight %, so 20 weight % diamond gives about 45 volumes %. Pure PCD samples provide strengths of about 2800 MPa. At low diamond contents, the strength reflects the bonding of the matrix and diamonds. As shown in Figure 12, the strength peaks at about 90 weights % diamond. Otherwise, the upper range, close to 1500 MPa, is achieved over a wide range of diamond contents.

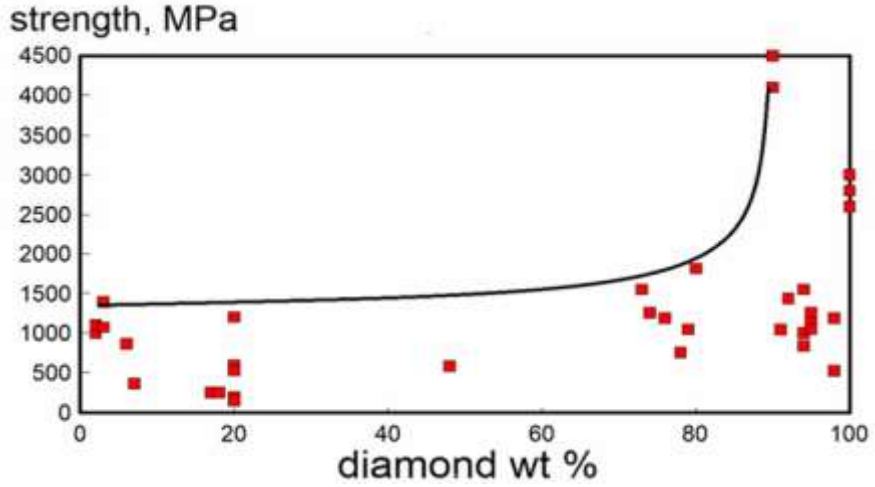

Figure 12. A comparison of strength reports for diamond composites versus the wt % of diamond. For the most part the upper strength is independent of the diamond content, with an upturn near 90 wt % diamond (Scott, 2018:161).

Several post-sintering treatments are being investigated to improve properties such as strength and wear resistance. For example, the solvent metal catalyst on the outer surface is removed by leaching. The remaining graphite is removed by immersion in a boiling mixture of 50% H_2SO_4, 40% $HClO_4$, and 10% HNO_3. An alternative is immersion in a mixture of sulfuric acid and chromic acid. Immersion in a mixture of HF, HNO_3, and water at 160°C is effective for removing cobalt (Belnap, 2010:2424). These treatments increase thermal stability but do not increase strength.

The elastic modulus (Youngs modulus) is highest with low cobalt contents (Lammer, 1988:949). Various reports have been collected for 13% to 100% diamond and are listed in Table 2.

Table 2. Elastic modulus (Youngs modulus) for sintered diamond composites (Lammer, 1988:949).

diamond wt %	value GPa
13	32
39	166
80	543
80	892
94	750
94	800
95	890
96	890
98	900
98	920
100	1050

Resistance to crack propagation is measured by fracture toughness. For brittle materials, hardness is captured by indentation techniques. Single crystal diamonds have a fracture toughness of 3 to 5 MPa√m. For sintered diamond, fracture toughness is generally below 12 MPa√m (Moriguchi, 2007:237). Several determinations are collected in Table 3.

Table 3. Fracture toughness for sintered diamond composites (McNamara, 2016:1).

diamond wt %	value MPa√m
70	3
78	8.5
80	6
81	10
82	5.5
83	9.5
86	10
87	7
90	6
90	8.5
94	7
95	9
95	8
95	14

In this total, the average value is 8 MPa√m. There is no static correlation between diamond content and fracture toughness. This is probably due to the high variability in the test. Furthermore, there are technical sensitivities in the results. For example, an increase in the loading rate reduces fracture toughness (Petrovic, 2011:153).

Some results, especially for small grain sizes, are low in the range of 2 to 6 MPa√m, with 9 MPa√m reported for a grain size of 30 µm and 7

MPa√m for a grain size of 150 μm. The typical flaw size is estimated to be 20 μm. This is the suggested reason for the shift in fracture toughness near a grain size of 20 to 30 μm (Scott, 2018:161).

Thermal properties

The high thermal conductivity of pure diamond is the basis for considering diamond composites in thermal management applications. These use high conductivity matrix metals of copper, silver or aluminum. For example, 50 vol% diamond and 50 vol% silver results in a thermal conductivity of 717 W/(m°C). While high conductivity is possible, realized values are often significantly lower than expected. This problem extends to the diamond-metal interfaces. Each interface contributes to scattering to reduce phonon conductivity. Residual porosity is a similar problem. An illustration of the porosity effect is shown below for a copper composite containing 30 vol% diamond consolidated by spark sintering;

- The thermal conductivity of 87% density is 150 W/O m °CO
- The thermal conductivity of 91% density is 340 W/O m °CO
-The thermal conductivity of 100% density is 657 W/O m °CO

The model for the effect of porosity on thermal conductivity is as follows:

$$K = Ko\ (1 - a\ (1 - f))$$

Where K is the thermal conductivity of the porous composite, Ko is the full density thermal conductivity, and f is the fractional density (f is the fractional porosity). For the copper diamond case mentioned above, the "a" parameter is 5.7. The low diamond content and low density further reduce the thermal conductivity to 240 W/(m °C) at 20 vol diamond and 98% density.

The above data show that a diamond composite with high thermal conductivity should be fully dense. Appropriate consolidation is achieved by pressure-assisted sintering after diamond surface treatments to enhance the (Hayat, 2022:949) interface. A high interfacial area (associated with a small diamond particle size) results in increased phonon scattering with a loss in thermal conductivity (Every, 1992:123). For example, a spark-sintered diamond-copper composite shows a 73% thermal conductivity gain with an increase in diamond size from 20 to 135 μm. Adding chromium as a coating to the diamond powder slightly improves thermal conductivity.

The copper-diamond composite interface incurs a significant conductivity penalty. Nanoscale diamond with a large interfacial area results in a thermal conductivity of only 50 W/(m °C) (Kidalov, 2008:844). Modest gains are achieved from pure diamond compaction, but porosity due to incomplete densification limits conductivity to less than 270 W/(m °C) (Semchinova, 1999:2140). Consolidation with μm diamond powder at a higher temperature (C) and pressure (GPa) results in a peak thermal conductivity of 385 W/(m °C) less than that possible with pure copper. The peak thermal conductivity for a nanoscale diamond is only 50 W/(m °C),

while when micrometer-sized diamond is consolidated at 6 GPa for less than 30 seconds at 1800°C, the peak thermal conductivity is 500 W/(m °C). Higher or lower temperatures are detrimental. Test data showing this behavior are plotted in Figure 4 (Kidalov, 2008:844).

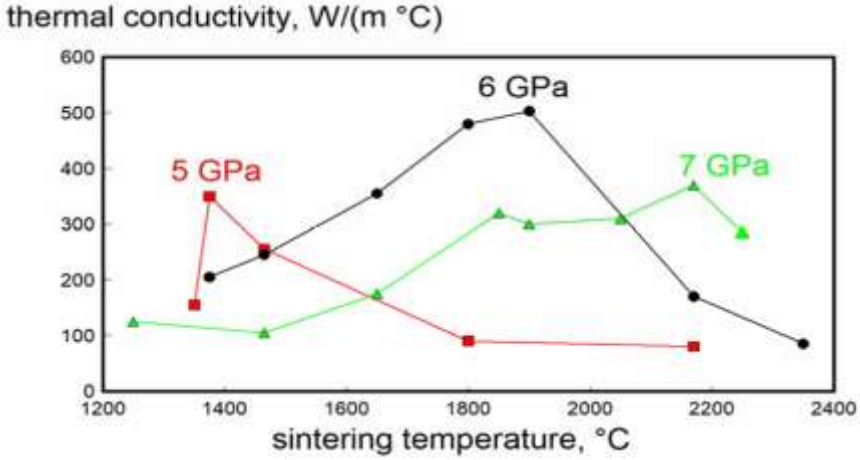

Figure 4. Thermal conductivity of diamond-graphite mixtures after HPHT processing at three pressures (5, 6, or 7 GPa) and various temperatures. Hold times varied from 9 to 25 s (Kidalov, 2008:844).

Copper-diamond composites are particularly applicable to thermal management in electronics. The large difference in strength, hardness, flexibility, and other properties prevents the achievement of high thermal conductivity. Extruded composites of 50 vol% coated diamond mixed with copper achieve a conductivity of 487 W/(m °C). The 75 vol% diamond combinations reach 645 W/(m °C) when condensed using 1200°C and 4.5 GPa (Yoshida & Morigami, 2004:303). Some summary thermal properties are collected in Table 5.

Table 5. Summary thermal properties of diamond-copper, most are consolidated by high pressure high-temperature cycles (GPa and 1200°C) (Yoshida & Morigami, 2004:303).

diamond vol %	diamond particle size µm	density g/cm³	specific heat J/(kg °C)	thermal conductivity W/(m °C)
20	100	7.82	---	263
50	135	6.20*	411	487
50	25	6.24	421	226
70	25	5.14	446	293
70	50	5.14	446	518
70	100	5.14	446	742
75	50	4.87	454	645
80	25	4.61	463	448

* hot extruded

When comparing the results at 70 vol% diamond contents, it is seen that the larger diamond particles are beneficial to thermal conductivity but do not have a significant effect on density or specific heat. At this diamond content, the coefficient of thermal expansion is 6 to 7 ppm/°C. In another study, a 50 vol% copper diamond mixture using 177 to 200 µm diamonds reaches a thermal conductivity of 640 W/(m °C). This formulation is based on an interface wetting agent of 0.8 wt% chromium (Ciupinski et al, 2009:120).

Similar to the improved wetting with chromium, the addition of titanium is an effective surface treatment. When it is added to copper at about the 0.2 wt % concentration, titanium improves bonding, leading to a thermal conductivity, 529 W/(m °C) for 50 vol O wt %O diamond O Aluminum as the matrix results in similar behavior at 445 to 491. W/(m °C) for 40 to 50 vol % diamond with a titanium coating (Liang et al, 2011:1127). Without the titanium coating, the thermal conductivity is lower, in the 320 W/O m °C range. Hot pressed variants reach a slightly higher thermal conductivity of 567 W/(m °C) (14). Some reports of thermal conductivity are summarized in Table 6. In some cases, the values are low due to residual porosity.

Table 6. Example thermal conductivity reports for diamond composites (HPHT = hig pressure high-temperature, HIP = hot isostatic pressing, spark = spark sintering) (Liang et al, 2011:1127).

diamond vol %	diamond D50, µm	matrix	process	T °C	P MPa	t min	thermal conductivity W/(m °C)
10	1.6	Al_2O_3	hot press	1250	32	---	36
20	100	Cu-Cr	sinter	950	0	120	280
30	50	Cu	spark	1200	---	---	352
40	100	Cu	extrude	1040	50	5	475
40	50	Cu	spark	600	---	30	134
40	200	Al	hot press	650	67	90	475
45	100	Cu	hot press	920	30	5	304
45	100	Cu-Ni-W	hot press	920	30	5	661
45	165	Al	spark	540	50	5	403
≈ 50	25	Ag	HPHT	1200	5300	10	690
50	310	Ag-Si	spark	915	80	1	717
50	150	Ag-Ti	sinter	980	0	30	701
50	62	Al	hot press	605	60	25	321
≈ 50	25	Co	HPHT	1200	5300	10	678
≈ 50	25	Cu	HPHT	1200	5300	10	730
≈ 50	25	Cu-Cr	HPHT	1200	5300	10	926
50	195	Cu-Ti	spark	925	40	10	529
50	---	Cu-Ti	sinter	980	0	30	719
50	40	Al	hot press	700	50	120	237
50	200	Cu-Cr	spark	900	60	20	640
50	310	Ag-Si	spark	910	80	1	717
50	65	Al	hot press	605	60	25	321
55	200	Al	hot press	650	67	90	567
55	100	Si-7Al	spark	1370	50	5	346
60	195/40	Ag-Si	spark	820	31	30	680
66	135	Si	HIP	1450	196	30	486
70	100	Cu	HPHT	1200	4500	15	742
70	100	Cu	HPHT	1200	4500	---	742
75	25	Cu	HPHT	1200	4500	15	427
75	50	Cu	HPHT	1200	4500	15	645
100	1	none	HPHT	1800	6000	0.5	500
100	12	none	HPHT	2100	7000	---	385

Table 7 compiles some examples of the thermal expansion coefficient for diamond composites over a range of diamond contents. Largely the values reflect the volumetric rule of mixtures, with a degrading effect from residual porosity.

Table 7. Thermal expansion coefficient for various diamond composites (German, 2023:1).

diamond vol %	matrix	processing	thermal expansion coefficient, ppm/°C
10	Al_2O_3	hot press, 1250°C, 32 MPa	5.6
20	Cu	hot press, 850°C, 50 MPa, 15 min	13.5
40	Cu	extrude, 1040°C, 50 MPa, 5 min	10.9
50	Al	hot press, 605°C, 60 MPa, 25 min	11
55	Si-Al	spark sinter, 1370°C, 50 MPa, 5 min	1.5
60	Ag-Si	spark sinter, 820°C, 31 MPa, 30 min	7.7
75	Cu	HPHT, 1200°C, 4.5 GPa, 15 min	5.5

Performance is determined by properties. In turn, applications dictate the required property combinations and best design. For sintered diamonds, the range of factors involved in performance optimization is enormous. Consider the parameters summarized in Table 8, subdivided by composition, design, microstructure, and processing considerations.

Table 8. Summary of factors influencing sintered diamond performance (German, 2023:1).

factor	parameter
composition	added phase (carbide, metal)
	diamond coating
	diamond purity
	matrix composition
	added graphite
	added wetting agent
design	cutter rake angle
	layered diamond
	leached diamond
	overall size and diamond thickness
	taper, chamfer, interface serration
microstructure	diamond contiguity
	diamond grain size
	matrix-diamond wetting, dihedral angle
	mean free path (separation distance)
	matrix connectivity
processing	diamond particle size distribution
	diamond surface pretreatment
	additive type, amount, particle size
	apparent density, diamond density
	heating rate
	hold time
	high pressure cell design
	initial pressure
	pressure cycle, peak pressure
	peak temperature
	press design
	pressure transmission medium
	substrate composition
	cooling rate
	surface treatment

Optimization depends on the target property. Balance is required, as optimization of one parameter may degrade another - strength versus wear resistance for example (Wise et al, 2005:545). Processing parameters are adjusted to deliver the desired property combination. Chemical additives are another variant, such as intentional additions of boron, nitrogen, silicon, or other soluble species. Likewise, surface coatings are used in some situations to improve wetting or increase nucleation sites. Consequently, there are many solutions just as there are many applications with different property demands.

Some selected property values for HPHT sintered diamond compacts are given in Table 9.

Table 9. Selected properties for sintered polycrystalline diamond (German, 2023:1).

property	composition	value
density, g/cm^3	3 wt % Co	3.57
heat capacity, J/(kg °C)	3 wt % Co	790
thermal expansion, ppm/°C	3 wt % Co	2.5
	50 wt % Cu	8
elastic modulus, GPa	3 wt % Co	890
Poisson's ratio	3 wt % Co	0.07
friction coefficient	3 wt % Co	≈ 0.2
transverse strength, MPa	7 wt % Co	1050
fracture toughness, MPa√m	5 wt % Co	10
diamond grain size, μm	7 wt % Co	9
contiguity	7 wt % Co	0.6
thermal conductivity, W/(m °C)	0	400
	3 wt % Co	543
	50 wt % Cu	640

CONCLUSIONS

The following conclusions can be drawn from the present investigation:

a. Phase diagrams are beneficial to understand to find which phases forms in which temperature for different components and compositions. Carbon-cobalt binary diagram demonstrates similar valuable data including Curie temperature.
b. Pressure-temperature relationship bestows changes in solid/liquid phase for graphite and diamond system.
c. Sintered diamonds can be used for cutting tools, mining and construction, electronics and semiconductors, medical applications, automotive industry as well As research and development.
d. Diamond is the hardest material. If diamond sintered its hardness reaches from 5000 HV to 13000 HV. Similarly, after sintering hardness of diamond composites increases from 0 up to 9000 HV.

Strength of diamond composites are about the same as 1500 MPa up to 80 wt% diamond. However, it increases up to 4500 MPa in 90 wt% diamond. Pure diamonds elastic modulus is 1050 GPa and fracture toughness is about 15 $MPa.m^{0.5}$. Thermal conductivity of diamond-graphite is about 400 W//M.ºC) at 1400 ºC and increases to maximum level at 1900 ºC in 6 GPa pressure.

REFERENCE

Sorb, Y., Bundy, F. P., & DeVries, R. C. (2016). Diamond: High pressure synthesis. In *Reference module in materials science and engineering* (pp. 1–8). Elsevier.

German, R. M. (2023). *Sintered diamond: From metal matrix composites to polycrystalline diamond*. German Materials Technology Publishing.

Che, D., Han, P., Guo, P., & Ehmann, K. (2012). Issues in polycrystalline diamond compact cutter–rock interaction from a metal machining point of view—Part I: Temperature, stresses and forces. *Journal of Manufacturing Science and Engineering, 134*, 064001. https://doi.org/10.1115/1.4007564

Lancaster, B., Roberts, B. A., Parker, I., Tank, K., Achilles, R. D., & Van Der Riet, C. D. (2007). *Polycrystalline diamond abrasive elements* (U.S. Patent No. 2007/0181348). U.S. Patent and Trademark Office.

Frushour, R. H., & Torbet, C. J. (2001). *Composite polycrystalline diamond compact with discrete particle size areas* (U.S. Patent No. 6,187,068 B1). U.S. Patent and Trademark Office.

Belnap, J. D. (2010). Sintering of ultrahard materials. In Z. Z. Fang (Ed.), *Sintering of advanced materials* (pp. 389–414). Woodhead Publishing.

Boland, J. N., & Li, X. S. (2010). Microstructural characterization and wear behavior of diamond composite materials. *Materials, 3*, 1390–1419. https://doi.org/10.3390/ma3031390

Li, S. J., Akaishi, M., Ohsawa, T., & Yamaoka, S. (1990). Sintering behavior of the diamond–super Invar alloy system at high temperature and pressure. *Journal of Materials Science, 25*, 4150–4156.

Sung, J. (2000). Graphite–diamond transition under high pressure: A kinetics approach. *Journal of Materials Science, 35*, 6041–6054.

DeVries, R. C. (1975). Plastic deformation and work-hardening of diamond. *Materials Research Bulletin, 10*, 1193–1200.

German, R. M. (1996). *Sintering theory and practice*. Wiley-Interscience.

Tian, Y., Wang, J., Zhang, J., Guan, S., Zhang, L., Wu, B., Su, Y., Huang, M., Zhou, L., & He, D. (2020). Solubility and stability of diamond in cobalt under 5 GPa. *Diamond and Related Materials, 110*, 108158. https://doi.org/10.1016/j.diamond.2020.108158

Kanda, H. (2000). Large diamonds grown at high pressure conditions. *Brazilian Journal of Physics, 30*, 482–489.

Hsieh, Y. Z., & Lin, S. T. (2001). Diamond tool bits with iron alloys as the binding matrices. *Materials Chemistry and Physics, 72*, 121–125.

Huang, J., Lu, J., Wang, Y., & Ma, Z. (2021). Fabrication of porous structure vitrified bond diamond grinding wheel via direct ink writing. *Ceramics International, 47*, 34059–34068.

Schubert, T., Ciupiński, Ł., Zieliński, W., Michalski, A., Weissgarber, T., & Kieback, B. (2008). Interfacial characterization of Cu/diamond composites prepared by powder metallurgy for heat sink applications. *Scripta Materialia, 58*, 263–266.

Bobrovnitchii, G. S., Filgueira, M., Monteiro, S. N., & Tardim, R. C. (2010). Cobalt-based binders and the efficiency of diamond saw blades. *Materials Science Forum, 660*, 182–187.

Cavaliere, P. (2019). *Spark sintering of materials: Advances in processing and applications*. Springer.

Munro, R. G., Block, S., Piermarini, G. J., & Mauer, F. A. (1984). Diamond anvil cell technology for P–T studies of ceramics: ZrO_2 (8 mol% Y_2O_3). In *Emergent process methods for high technology ceramics* (pp. 783–792). Springer.

Konstanty, J. (2003). *Cobalt as a matrix in diamond impregnated tools for stone sawing applications*. Wydawnictwa AGH.

Sexton, T. N., & Cooley, C. H. (2009). Polycrystalline diamond thrust bearings for downhole oil and gas drilling tools. *Wear, 267*, 1041–1045.

Field, J. E. (1992). *The properties of natural and synthetic diamond*. Academic Press.

Yang, J., Huang, Y., & Chen, W. (2013). Study on effect of sintering pressure on the properties of diamond bit. *Advanced Materials Research, 634*, 2366–2372.

Scott, T. A. (2018). The influence of microstructure on the mechanical properties of polycrystalline diamond: A literature review. *Advances in Applied Ceramics, 117*, 161–176.

Belnap, D. (2010). Effect of cobalt on PCD fracture toughness. In *Proceedings of the Materials Science and Technology Conference* (pp. 2424–2434). Houston, TX.

Lammer, A. (1988). Mechanical properties of polycrystalline diamonds. *Materials Science and Technology, 4*, 949–955.

Moriguchi, H., Tsuduki, K., Ikegaya, A., Miyomoto, Y., & Morisada, Y. (2007). Sintering behavior and properties of diamond/cemented carbides. *International Journal of Refractory Metals and Hard Materials, 25*, 237–243.

McNamara, D., Carolan, D., Alveen, P., Murphy, N., & Ivankovic, A. (2016). Effect of loading rate on the fracture toughness and failure mechanisms of polycrystalline diamond (PCD). *International Journal of Refractory Metals and Hard Materials, 60*, 1–10.

Petrovic, M., Carolan, D., Ivankovic, A., & Murphy, N. (2011). Role of rate and temperature on fracture and mechanical properties of PCD. *Key Engineering Materials, 452*, 153–156.

Hayat, M. D., Singh, H., Karumbaiah, K. M., Xu, Y., Wang, X. G., & Cao, P. (2022). Enhanced interfacial bonding in copper/diamond composites via deposition of nano-copper on diamond particles. *JOM, 74*, 949–953.

Every, A. G., Tzou, Y., Hasselman, D. P. H., & Raj, R. (1992). The effect of particle size on the thermal conductivity of ZnS/diamond composites. *Acta Metallurgica et Materialia, 40*, 123–129.

Kidalov, S. V., Shakhov, F. M., & Vul, A. Y. (2008). Thermal conductivity of sintered nanodiamonds and microdiamonds. *Diamond and Related Materials, 17*, 844–847.

Semchinova, O. K., Graul, J., Neff, H., Holzhuter, G., Smirnov, E. P., & Davydov, V. Y. (1999). Synthesis and properties of single-phase diamond ceramics. *Diamond and Related Materials, 8*, 2140–2147.

Yoshida, K., & Morigami, H. (2004). Thermal properties of diamond/copper composite material. *Microelectronics Reliability, 44*, 303–308.

Ciupiński, Ł., Siemiaszko, D., Rosiński, M., Michalski, A., & Kurzydłowski, K. J. (2009). Heat sink materials processing by pulse plasma sintering. *Advanced Materials Research, 59*, 120–124.

Liang, X., Jia, C., Chu, K., Chen, H., Nie, J., & Gao, W. (2011). Thermal conductivity and microstructure of Al/diamond composites with Ti-coated diamond particles consolidated by spark plasma sintering. *Journal of Composite Materials, 46*, 1127–1136.

Wise, J. L., Grossman, J. W., Wright, E. K., Gronewald, P. J., Bertagnolli, K., & Cooley, C. H. (2005). Latest results of parameter studies on PDC drag cutters for hard-rock drilling. *Geothermal Resources Council Transactions, 29*, 545–552.

Consensus Kalman Filter Algorithm for Multisensor Distributed State Estimation

Gökhan KARAÇOBAN[1]

Nurbanu GÜZEY[2]

1- Res. Asst.; Sivas University of Science and Technology, Faculty of Aviation and Space Sciences, Department of Astronautical Engineering, gokhankaracoban@sivas.edu.tr ORCID No: 0000-0001-5155-8360

2- Asst.Prof. Dr.; Sivas University of Science and Technology ,Faculty of Engineering and Natural Sciences, Department of Computer Engineering, nurbanu.guzey@sivas.edu.tr ORCID No: 0000-0002-6587-2489

ABSTRACT

This chapter discusses the concept of state estimation within the framework of Kalman filter-based methods; distributed and consensus-based Kalman filtering approaches, particularly those used in multi-sensor systems, are examined in detail. State estimation is the process of predicting system state variables that cannot be directly measured or are hidden, using system models and measurement data. This process is critically important in many fields such as electric power systems, robotics, autonomous vehicles, target tracking, navigation, and positioning. The chapter first summarizes common state estimation algorithms such as the Kalman Filter (KF), Extended Kalman Filter (EKF), Unscented Kalman Filter (UKF), and particle filter; and explains their applications in linear and nonlinear systems. In centralized state estimation approaches, collecting and processing all sensor data in a single center presents significant limitations such as bandwidth requirements, transmission delay, high computational load, and the risk of single-point failure. Furthermore, when evaluating measurements from heterogeneous sensors with varying accuracy levels, noisy measurements can negatively impact estimation accuracy. Therefore, this chapter highlights the advantages of the distributed state estimation approach, where each sensor makes individual estimations with its local measurements and reaches a common estimation by sharing information with neighboring nodes. In particular, the consensus Kalman filter structure and the decisive role of consensus gain in estimation performance are emphasized. In this context, the information-weighted consensus-based optimal Kalman filter approach and the distributed consensus Kalman filter (MDCKF) approach developed for asynchronous multi-rate sensor networks are examined. Both methods are evaluated as being able to produce more consistent, robust, and accurate estimation results by reducing the impact of unreliable measurements. In conclusion, it is shown that consensus-based distributed Kalman filtering methods offer a more effective alternative to classical centralized approaches in multi-sensor systems.

Keywords – State estimation, distributed Kalman filter, multisensor systems, consensus Kalman filter, consensus gain

INTRODUCTION

State estimation is the process of estimating the hidden or cannot be measured directly state variables of a system from its observable parameters. State estimation aims to determine the past, present and future states of the system using a mathematical model of the system and available measurement data (Zhu et al., 2024.). It is used in many fields such as, electric power systems (Schweppe & Handschin, 1974), robotics (Moore et

al., 2009), autonomous vehicles (Jeon et al., 2021) and defense system technologies such as, target tracking, navigation and localization (Toloei & Niazi, 2014). State estimation techniques can be categorized into centralized and decentralized method (Chandrasekaran et al., 2023). In centralized state estimation, each sensor data is transmitted into central unit. All sensor data are processed together to estimate the system state.

Various algorithms are used for state estimation such as, Kalman filter (KF) algorithm (Tamas et al., 2008), extended Kalman filter (EKF) algorithm (Luo et al., 2013), unscented Kalman filter (UKF) algorithm (Burchett, 2019) and particle filter algorithm (Ullah et al., 2020). Kalman filter algorithm is used to estimate the system states of linear dynamical system using noisy sensor measurements. The Kalman filter algorithm flowchart was given in Figure 1.

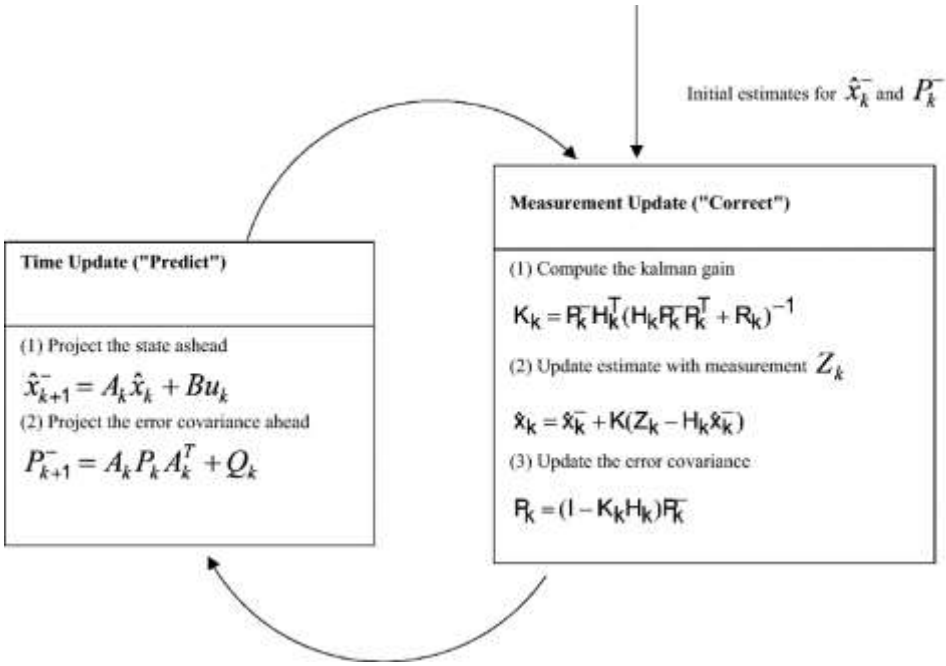

Figure 1: The flowchart of Kalman Filter Algorithm (Khodarahmi et al., 2022)

The system dynamic model and sensor observation equations must be linear to use Kalman filter algorithm (Tamas et al., 2008). On the other hand, most of the systems and sensor measurements are nonlinear in real world applications. Therefore, nonlinear state estimation is very important. EKF and UKF algorithms are used for nonlinear state estimation problems. EKF algorithm is the extended version of the linear KF algorithm and uses Jacobian matrix for linearizing the nonlinear system. The flowchart of EKF algorithm was given in Figure 2.

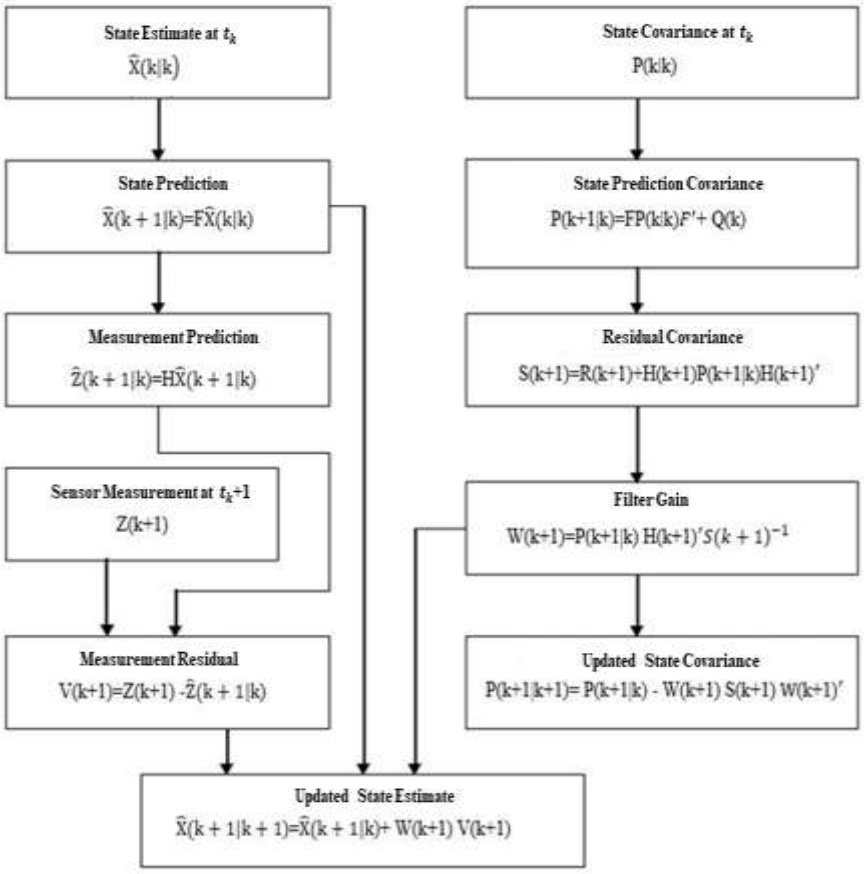

Figure 2: The flowchart of EKF Algorithm (Bar-Shalom et al., 2001)

In EKF algorithm, first order Taylor series expansion is used to calculate Jacobian matrix to linearize the nonlinear system dynamics or sensor measurements (Tamas et al., 2008). However, Taylor series expansion has infinite term and just the first two term is used to calculate Jacobian matrix. Therefore, linearizing errors occur due to the ignoring of higher order terms when calculating Jacobian matrix. This results in high estimation error of EKF algorithm.

UKF algorithm is another state estimation algorithm for nonlinear state estimation. UKF algorithm uses unscented transformation for state estimation. The dynamic system is defined as random variable and the probability density function (PDF) is described. Random variable is represented as mean and covariance. Sigma points are sampled from this PDF and propagated using unscented transformation to estimate system state (Tamas et al., 2008). By propagating sigma points through unscented

transformation and using the formulas of UKF algorithm, the mean and covariance of random variable is estimated. The estimated mean and covariance of random variable represent the estimated state and estimated state covariance of nonlinear system (Li et al., 2019).

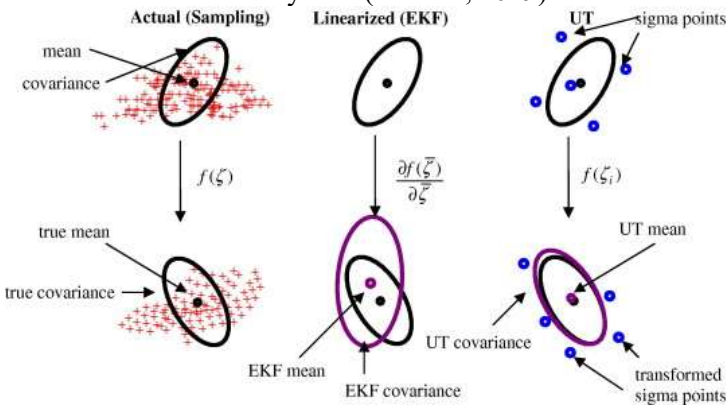

Figure 3: State Estimation via EKF and Unscented Transformation (Ijaz et al., 2008)

Traditional implementations of Kalman filter based algorithms are centralized. That is, all sensor data are transmitted to a single central unit and processed there to estimate the system state. To process sensor measurements, sensor measurements are updated by using sequential or parallel update method in multisensor systems (Willner et al., 1976). However, the centralized approach brings the following problems, especially for the large-scale sensor networks:

Bandwidth and Transmission Restrictions: Due to large data volumes, transmission delays may be experienced.

Single Point of Failure: In case of failure of the central unit, the entire system is affected.

Computational Load: Data processing is distributed to the central unit, which increases the computational load.

Intolerance to Noisy Sensor Measurements: Sensor measurements are fed into a Kalman filter estimator independently. Noisy sensor measurements cannot be tolerated with highly accurate sensor measurements.

Centralized based approaches are not very appropriate for multisensor state estimation due to the issues mentioned above. Therefore, distributed state estimation algorithms are more popular for multisensor state estimation.

The distributed state estimation algorithms have been developed to solve the problems result from centralized state estimation. Distributed sensor network includes numerous interconnected sensor agents, where each agent functions collaboratively by communicating with others in a

decentralized manner (Khan et al., 2023). In distributed estimation methods, each sensor makes an estimation individually by using its local measurements and shares information with neighboring sensors to reach a common agreement.

One of the distributed state estimation algorithms is multisensor distributed consensus Kalman filter algorithm. It is an advanced algorithm for multisensor distributed state estimation. Consensus Kalman filter algorithm was developed to prevent the disadvantages of classical Kalman filter based algorithms for multisensor state estimation. In classical Kalman filter algorithm, noisy sensor measurements cannot be tolerated and result in high estimation errors. However, in consensus Kalman filter algorithm, noisy sensor measurements can be tolerated with highly accurate sensor measurements by using consensus gain.

The estimation of multisensor distributed consensus Kalman filter algorithm was given below (Olfati-Saber, 2009).

$$\hat{x}^i_{k|k} = \hat{x}^i_{k|k-1} + K^i_k\left(z^i_k - H^i_k\hat{x}^i_{k|k-1}\right) + C_i\sum_{j\in N_i}(\hat{x}^j_{k|k-1} - \hat{x}^i_{k|k-1})$$

In the equation given above, $\hat{x}^i_{k|k}$ is the state estimation of multisensor distributed consensus Kalman filter algorithm. Moreover, $K^i_k$and C_i are the Kalman and consensus gains, respectively. Also, $\hat{x}^j_{k|k-1}$ is the state prediction of the Kalman filter algorithm using sensor j and $\hat{x}^i_{k|k-1}$ is the state prediction of the Kalman filter algorithm using i-th neighbor of sensor j. When the equation is examined, it is seen that, the state estimation is obtained by adding consensus term into the classical Kalman filter algorithm. Therefore, each of the individual estimations is reached a consensus by adding consensus term into the equation of state estimation (Olfati-Saber, 2009). For that reason, in distributed consensus Kalman filter algorithm, determining the consensus gain optimally is crucial for the performance of the algorithm. This is because, consensus gain determines how individual sensor estimates are connected for final state estimation.

In this study, different strategies to determine consensus gain have been investigated from several papers.

The first paper to investigate the modelling of consensus gain is “Optimal Kalman filter with information weighted consensus” (Khan et al., 2023). In this study, an information-weighted consensus based Kalman filter (Optimal KCF-WDG) is proposed. The algorithm optimizes the minimum mean square error (MMSE) performance in distributed sensor networks. The proposed algorithm calculates the optimal consensus coefficients for each sensor and applies them over a dynamic directed weighted graph (WDG). In this paper, by using multiple sensors, it is aimed to combine the information from heterogeneous sensors to make a reliable distributed state estimation. This is achieved by providing cooperation between sensors with the

information weighted consensus method. Since the measurement errors of the sensors are different from each other, some sensors provide more reliable measurements, while others are less reliable. With the information weighted consensus approach, less weight is given to the noisy sensor measurements to produce the state estimation in the consensus phase. Therefore, the estimation accuracy increases. Thus, the information weighted consensus approach ensures that reliable information receives more weight in the combination of sensor measurements. Thus, the effect of estimation errors of low reliability sensors is limited. The concept of "information" used here is typically associated with the inverse of the covariance matrix of the estimate. As the output of the Kalman filter, both a state estimate and the estimated state covariance are produced at each node. When the estimated state covariance is low, the information matrix value (P^{-1}) increases. Because, information matrix was modelled as the inverse of estimated state covariance. Therefore, the information content (P^{-1}) of the state estimates of the nodes is taken as the basis, when determining the consensus coefficients. Thus, among all the sensor estimates, more weight is given to the estimations with lower covariance to produce the final estimate. Therefore, the collective estimate of the target object whose location is to be detected has lower uncertainty and higher accuracy.

The working principle of the algorithm are summarized in 6 steps as given below.

- Obtaining the State Estimation and Estimation Covariance of Each Sensor Using the Standard Kalman Filter Algorithm: Each sensor takes measurements to observe the system state and the standard Kalman filter algorithm is run. Thus, each sensor obtains the state estimation and state estimation covariance.
- Sharing information with neighboring sensors: After each sensor obtains its estimation values, it enters the consensus phase. In the consensus phase, each sensor transmits the state estimation and estimation covariance values to its neighbor sensors. In this phase, the neighborhood relationships between sensors are determined by graph theory. In the consensus phase, i-th sensor receives the state estimation and estimation covariance data from its neighboring sensors. The information flow between neighbors is provided through the communication network. In this study, this information flow is provided by using a weighted directed graph structure (WDG).

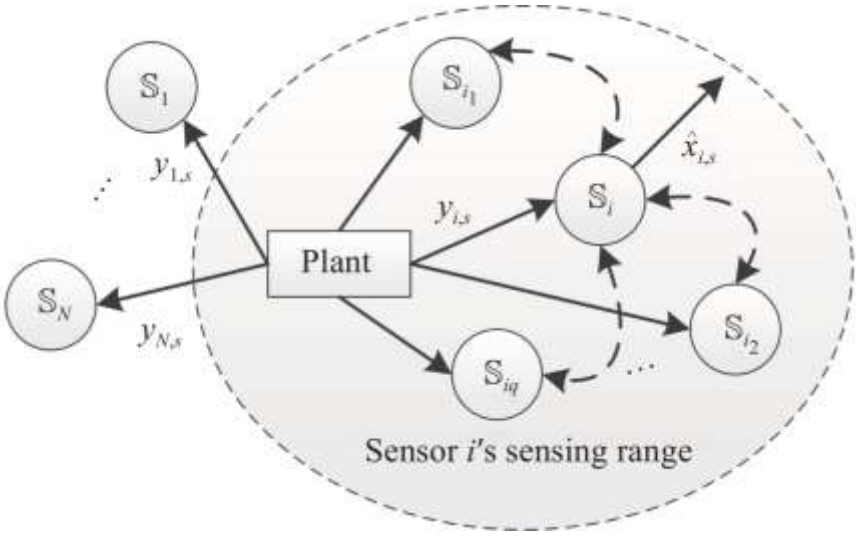

Figure 4: Sensor Neighborhood Relationship (Wang et.al., 2023)

- Calculation of Distributed Information Matrix: The distributed information matrix for the i-th sensor is calculated as follows:

$$F_i = [F_{r,s}] = P_i^{-1}$$

Where P_i is the updated state covariance of the Kalman filer algorithm using the ith sensor.

- Calculation of optimal Kalman and consensus gains: For each sensor, the optimal Kalman gain and consensus gain are calculated. The i expressions in the formulas represent the Kalman and consensus gains of the i-th sensor. The consensus weights are determined to minimize the total error rate MMSE for each sensor.

$$K_i = (\sum_{r\in N_i'}\sum_{s\in N_i'} {F_{r,s}}^i + {H_i}' R_i^{-1} H_i)^{-1} {H_i}' R_i^{-1}$$

$$C_{j,i} = (\sum_{r\in N_i'}\sum_{s\in N_i'} {F_{r,s}}^i + {H_i}' R_i^{-1} H_i)^{-1} \sum_{r\in N_i'} {F_{r,j}}^i$$

- The Final State Estimation of The Consensus Kalman Filter Algorithm: Sensor i combines its own estimation with the information received from its neighbors. Through this process, the consensus Kalman filter algorithm produces the final state estimation. This value represents an optimized result that combines the i-th sensor's own measurement data with the estimates from its neighboring sensors. In this way, all sensors in a distributed sensor network reach a common estimation accuracy.

$$\hat{x_i} = \bar{x_i} + K_i(z_i - H_i\bar{x_i}) + \sum_{r\in N_i} C_{j,i}(\bar{x_j} - \bar{x_i})$$

- Posterior Error Covariance Calculation: Posterior error covariance matrix is calculated as given below.

$$M_{i,j} = \widetilde{C_i} \sum_{r \in N_i'} \sum_{t \in N_j'} ((\sum_{s \in N_i'} {F_{r,s}}^i))P_{r,t}(\sum_{s \in N_j'} {F_{t,s}}^j))\widetilde{C_j'} + K_i R_i K_i' \delta_{i,j}$$

Consensus gain is calculated with the following formula.

$$C_{j,i} = (\sum_{r \in N_i'} \sum_{s \in N_i'} {F_{r,s}}^i + {H_i}' R_i^{-1} H_i)^{-1} \sum_{r \in N_i'} {F_{r,j}}^i$$

${F_{r,s}}^i$: It is an element of the distributed information matrix belonging to the i-th sensor. The distributed information matrix is the inverse of the state estimation covariance. When the state estimation covariance is small, the information value is large. Therefore, estimates from sensors with higher information values are given more weight during the consensus stage.

$\sum_{s \in N_i'} {F_{r,s}}^i$: This expression represents the sum of the information from all neighboring sensors (N_1, N_2, N_3). This sum is used in the normalization of the weighting. Thus, the estimates of the sensors with higher information matrix contribute more to the total weighting when generating the state estimation.

${H_i}' R_i^{-1} H_i$: This term is related to the measurement made by the i-th sensor. H_i is the measurement matrix of the i-th sensor, and R_i is the measurement noise covariance. If the measurement noise is small, more weight is given to this sensor measurement in the consensus phase.

$\sum_{r \in N_i'} {F_{r,j}}^i$: This term expresses the weighting of the information coming from the neighboring sensor j. If the information (state estimation) coming from the sensor j is more reliable, the value of this term increases. Then, more weight is given to the estimation obtained by using the j-th sensor to produce final state estimation. If the information matrix belonging to the j-th sensor is large, this indicates that the error and uncertainty in the estimation made by using sensor j is low.

When the estimation uncertainty is high, the updated state covariance matrix is also high. Because, the updated state covariance matrix represents the uncertainty in the state estimation of the Kalman filter algorithm. In this case, since the information matrix is the inverse of the state estimation covariance matrix, the information matrix will be small. When the information matrix is small, the contribution of the estimation value of that neighboring sensor is kept smaller in the consensus phase.

Another investigated study to examine the modelling of consensus gain is “Distributed consensus Kalman filtering for asynchronous multi rate sensor networks” (Shao, 2024). In this study, Teng Shao et al., developed an optimal distributed consensus Kalman filter (MDCKF) algorithm for sensor

networks with different sampling rates that make asynchronous measurements. This is done to provide higher accuracy and consistency in the algorithms used to estimate the situation across the network when sensors have different sampling rates. Traditional distributed Kalman filtering methods usually work with the assumption that all sensors are synchronous and have the same sampling rate. However, in the real world, sensors usually collect data at different rates, which creates an asynchronous and multi-rate structure. For example, a sensor operating at a low frequency such as GPS can be in the same system with a sensor operating at a high frequency such as inertial navigation. This causes incompatible data exchange between the sensors. Therefore, the case of using asynchronous sensors is investigated in this study. In addition, in the study, the case where all sensors collect data simultaneously ($\lambda_k^i = 1$) and the case where none of the sensors collect data and make measurements ($\lambda_k^i = 0$) are examined separately. Then, the optimal values of different Kalman and consensus gains are calculated for both cases. Thus, it is possible to examine the performance of the algorithm separately for the moments when sensor measurements are available or not. Examining the algorithm's performance with and without constant sensor measurements adds practical value by better reflecting real-world conditions. The performance of the proposed MDCKF algorithm is tested with Monte Carlo simulation. The MDCKF algorithm is compared with the classical Kalman consensus filter (KCF), the classical Kalman filter (KF) algorithm and the Kalman filter algorithm (MKF) used when the sampling rates of the sensors are different in terms of both estimation accuracy and consensus performance. The MDCKF algorithm improves information sharing during consensus, making it more accurate and efficient in distributed systems. It delivers better results than other methods in both estimation accuracy and consensus.
The proposed MDCKF algorithm is summarized below.

- Calculation of state prediction and state prediction covariance values of the classical Kalman filter algorithm for each sensor

$$\hat{x}_{k|k-1}^i = F_{k-1}\hat{x}_{k-1|k-1}^i$$
$$P_{k|k-1}^{ij} = F_{k-1}P_{k-1|k-1}^{ij} + Q_{k-1}$$
$$P_{k|k-1}^i = F_{k-1}P_{k-1|k-1}^i + Q_{k-1}$$

  i: 1, 2, …n (First sensor, second sensor, … n-th sensor)

- Calculating the optimal consensus and Kalman gains

$$C_k^i = (\lambda_k^i P_{k|k-1}^i (H_k^i)' (\Delta_k^i)^{-1} H_k^i - \mathrm{I})(L_k^i)' (D_k^i - \lambda_k^i L_k^i (H_k^i)' (\Delta_k^i)^{-1} H_k^i (L_k^i)')^{-1}$$
$$K_k^i = \lambda_k^i (P_{k|k-1}^i + C_k^i \sum_{s \in N_i} (P_{k|k-1}^{si} - P_{k|k-1}^i)) (H_k^i)' (\Delta_k^i)^{-1}$$

- Calculation of State Estimation and State Estimation Covariances of MDCKF Algorithm

$$\hat{x}_{k|k}^{i} = \hat{x}_{k|k-1}^{i} + K_k^i\left(z_k^i - \lambda_k^i H_k^i \hat{x}_{k|k-1}^{i}\right) + C_k^i \sum_{j\epsilon N_i} (\hat{x}_{k|k-1}^{j} - \hat{x}_{k|k-1}^{i})$$

$$P_{k|k}^{ij} = \left(I - \lambda_k^i K_k^i H_k^i\right) P_{k|k-1}^{ij} \left(I - \lambda_k^i K_k^i H_k^i\right)' + \lambda_k^i \lambda_k^j K_k^i R_k^{ij} (K_k^j)' + C_k^i D_k^{ij} (C_k^j)' + \left(I - \lambda_k^i K_k^i H_k^i\right) \sum_{s\epsilon N_j} (P_{k|k-1}^{is} - P_{k|k-1}^{ij})(C_k^j)' + C_k^i \sum_{r\epsilon N_i} (P_{k|k-1}^{rj} - P_{k|k-1}^{ij})\left(I - \lambda_k^i K_k^i H_k^i\right)'$$

$$P_{k|k}^{i} = \left(I - \lambda_k^i K_k^i H_k^i\right) P_{k|k-1}^{i} \left(I - \lambda_k^i K_k^i H_k^i\right)' + \lambda_k^i K_k^i R_k^i K_k^{i'} + C_k^i D_k^i (C_k^i)' + \left(I - \lambda_k^i K_k^i H_k^i\right) L_k^i (C_k^i)' + C_k^i L_k^i \left(I - \lambda_k^i K_k^i H_k^i\right)'$$

$$\Delta_k^i = H_k^i P_{k|k-1}^i (H_k^i)' + R_k^i$$

$$\mathrm{L}_k^i = \textstyle\sum_{s\epsilon N_i} (P_{k|k-1}^{si} - P_{k|k-1}^{i})$$

$$D_k^{ij} = \sum_{r\epsilon N_i} \sum_{s\epsilon N_j} (P_{k|k-1}^{rs} - P_{k|k-1}^{rj} - P_{k|k-1}^{is} + P_{k|k-1}^{ij})$$

$$D_k^{i} = \sum_{r\epsilon N_i} \sum_{s\epsilon N_i} (P_{k|k-1}^{rs} - P_{k|k-1}^{ri} - P_{k|k-1}^{is} + P_{k|k-1}^{i})$$

Consensus gain is calculated with the following formula.

$$C_k^i = \left(\lambda_k^i P_{k|k-1}^i (H_k^i)' (\Delta_k^i)^{-1} H_k^i - \mathrm{I}\right) (L_k^i)' \left(D_k^i - \lambda_k^i L_k^i (H_k^i)' (\Delta_k^i)^{-1} H_k^i (L_k^i)'\right)^{-1}$$

The whole term in the consensus gain has been explained in detail below.

λ_k^i: It is used as an indicator function that indicates whether the sensor is currently measuring the system states or not. When the sensor is measuring, λ_k^i takes the value as 1, when it is not measuring, it takes the value as 0.

$P_{k|k-1}^i$: Predicted state covariance of Kalman filter algorithm when using sensor i in the update stage of the algorithm.

H_k^i: Measurement matrix for sensor i.

Δ_k^i: Innovation covariance of the Kaman filter algorithm when using sensor i.

L_k^i: It expresses the differences in the predictions of neighboring sensors. The expression $P_{k|k-1}^i$ used in the calculation of L_k^i is the error covariance between the i-th sensor and the j-th neighboring sensor of this sensor. This covariance matrix measures the discrepancy between the prediction of the relevant sensor and the neighboring sensor.

D_k^i: It is the sum of all edge errors between neighboring sensors. This term expresses a total measure of the uncertainty in the estimates of neighboring sensors.

I: Using this matrix, the necessary correction is made to ensure that the sensor estimates match.

$(D_k^i - \lambda_k^i L_k^i (H_k^i)' (\Delta_k^i)^{-1} H_k^i (L_k^i)')^{-1}$: It adjusts the factor used to minimize estimation differences within the sensor network. The physical equivalent of this term is a scaling to make consensus applicable.

The consensus coefficient controls how a sensor combines information from its neighbors and incorporates it into its own estimate. This depends on both the sensor's current measurement and its agreement with neighboring sensors.

Thanks to the consensus, estimate differences from neighboring sensors are minimized and the impact of the noisy sensors on the accuracy of the consensus Kalman filter algorithm is reduced.

RESULTS AND DISCUSSION

In conclusion, classical Kalman filter–based estimation algorithms and the consensus-based distributed Kalman filter (CDKF) algorithm were compared, with particular emphasis on the consensus-based distributed multisensor framework. The analysis showed that a key advantage of the CDKF algorithm lies in its ability to mitigate the adverse effects of highly noisy sensor measurements on state-estimation accuracy through the incorporation of a consensus term. In multisensor systems, heterogeneous sensors with different measurement noise characteristics are commonly employed, which reflects a more realistic scenario in practical applications. During the consensus stage of the distributed Kalman filtering process, sensor measurements are effectively weighted according to their uncertainty levels through consensus weights. Consequently, the CDKF algorithm assigns lower influence to sensors with high measurement noise while generating the overall state estimate. As a result, the consensus-based distributed Kalman filter can maintain reliable and accurate state estimation

performance even in sensor networks that include significantly noisy sensors. For this reason, multisensor distributed state estimation can be performed more accurately using the CDKF framework. Overall, the results indicate that the consensus Kalman filter algorithm outperforms classical Kalman filter–based approaches in multisensor distributed state-estimation applications.

REFERENCE

Bar-Shalom, Y., Li, X. R., & Kirubarajan, T. (2004). Estimation with applications to tracking and navigation: theory algorithms and software. John Wiley & Sons.

Burchett, B. T. (2019). Unscented Kalman filters for range-only cooperative localization of swarms of munitions in three-dimensional flight. Aerospace Science and Technology, 85, 259-269. https://doi.org/10.1016/j.ast.2018.12.015

Chandrasekaran, S., Varadan, V., Krishnan, S. V., Dörfler, F., & Mamduhi, M. H. (2023). Distributed State Estimation for Linear Time-Varying Systems with Sensor Network Delays (No. arXiv:2305.00190). arXiv. https://doi.org/10.48550/arXiv.2305.00190

Ijaz, U. Z., Khambampati, A. K., Lee, J. S., Kim, S., & Kim, K. Y. (2008). Nonstationary phase boundary estimation in electrical impedance tomography using unscented Kalman filter. Journal of Computational Physics, 227(15), 7089-7112. https://doi.org/10.1016/j.jcp.2007.12.025

Jeon, W., Chakrabarty, A., Zemouche, A., & Rajamani, R. (2021). Simultaneous State Estimation and Tire Model Learning for Autonomous Vehicle Applications. IEEE/ASME Transactions on Mechatronics, 26(4), 1941-1950. https://doi.org/10.1109/TMECH.2021.3081035

Khan, S., Deshmukh, R., & Hwang, I. (2023). Optimal Kalman Filter With Information-Weighted Consensus. IEEE Transactions on Automatic Control, 68(9), 5624-5629. https://doi.org/10.1109/TAC.2022.3220528

Khodarahmi, M., & Maihami, V. (2023). A review on Kalman filter models. Archives of Computational Methods in Engineering, 30(1), 727-747.

Li, X., Zhang, P., Huang, G., Zhang, Q., Guo, J., Zhao, Y., & Zhao, Q. (2019). Performance analysis of indoor pseudolite positioning based on the unscented Kalman filter. GPS Solutions, 23(3), 79. https://doi.org/10.1007/s10291-019-0870-y

Luo, C., McClean, S. I., Parr, G., Teacy, L., & De Nardi, R. (2013). UAV Position Estimation and Collision Avoidance Using the Extended Kalman Filter. IEEE Transactions on Vehicular Technology, 62(6), 2749-2762. https://doi.org/10.1109/TVT.2013.2243480

Moore, D. C., Huang, A. S., Walter, M., Olson, E., Fletcher, L., Leonard, J., & Teller, S. (2009). Simultaneous local and global state estimation for robotic navigation. 2009 IEEE International Conference on Robotics and Automation, 3794-3799. https://doi.org/10.1109/ROBOT.2009.5152763

Olfati-Saber, R. (2009). Kalman-Consensus Filter: Optimality, stability, and performance. Proceedings of the 48h IEEE Conference on Decision and Control (CDC) Held Jointly with 2009 28th Chinese Control Conference, 7036-7042. https://doi.org/10.1109/CDC.2009.5399678

Schweppe, F. C., & Handschin, E. J. (1974). Static state estimation in electric power systems. Proceedings of the IEEE, 62(7), 972-982. https://doi.org/10.1109/PROC.1974.9549
Shao, T. (2024). Distributed consensus Kalman filtering for asynchronous multi-rate sensor networks. Signal, Image and Video Processing, 18(8-9), 6419-6429. https://doi.org/10.1007/s11760-024-03326-7
Tamas, L., Lazea, Gh., Robotin, R., Marcu, C., Herle, S., & Szekely, Z. (2008). State estimation based on Kalman filtering techniques in navigation. 2008 IEEE International Conference on Automation, Quality and Testing, Robotics, 147-152. https://doi.org/10.1109/AQTR.2008.4588811
Toloei, A., & Niazi, S. (2014). State Estimation for Target Tracking Problems with Nonlinear Kalman Filter Algorithms. International Journal of Computer Applications, 98(17), 30-36. https://doi.org/10.5120/17277-7708
Ullah, I., Shen, Y., Su, X., Esposito, C., & Choi, C. (2020). A Localization Based on Unscented Kalman Filter and Particle Filter Localization Algorithms. IEEE Access, 8, 2233-2246. https://doi.org/10.1109/ACCESS.2019.2961740
Wang, Y., Shen, B., Zou, B., & Han, Q. (2023). A Survey on Recent Advances in Distributed Filtering over Sensor Networks Subject to Communication Constraints. International Journal of Network Dynamics and Intelligence X (), 100007. https://doi.org/10.53941/ijndi0201007
Willner, D., Chang, C., & Dunn, K. (1976). Kalman filter algorithms for a multi-sensor system. 1976 IEEE Conference on Decision and Control Including the 15th Symposium on Adaptive Processes, 570-574. https://doi.org/10.1109/CDC.1976.267794
Zhu, F., Xu, Z., Zhang, X., Zhang, Y., Chen, W., & Zhang, X. (t.y.). On State Estimation in Multi-Sensor Fusion Navigation: Optimization and Filtering.

Effects of Water or Steam Injection on Performance, Emissions and Combustion Characteristics of Diesel and Gasoline Engines: A Comprehensive Review

Idris CESUR[1]

1- Prof. Dr. Idris CESUR; Sakarya University of Applied Sciences, Faculty of Technology, Department of Mechanical Engineering, icesur@subu.edu.tr ORCID No: 0000-0001-7487-5676

ABSTRACT

Increasing environmental concerns and the progressive tightening of emission regulations have intensified the search for advanced combustion control strategies in internal combustion engines. Among the proposed approaches, water and steam addition has attracted considerable attention for both diesel and gasoline engines due to its capability to lower in-cylinder combustion temperatures, thereby mitigating emissions while potentially influencing engine performance characteristics. In this study, the effects of water and steam addition on the performance and emission characteristics of internal combustion engines are comprehensively reviewed and critically evaluated. The literature is examined separately for diesel and gasoline engines, enabling a structured and comparative assessment. The impacts on NOx, CO, HC, and particulate matter (PM) emissions are analyzed alongside key performance indicators, including brake power, torque, and brake specific fuel consumption (BSFC). The reviewed studies consistently demonstrate that water/steam addition is particularly effective in reducing NOx emissions, primarily due to the suppression of peak combustion temperatures and thermal NOx formation mechanisms. However, the findings also reveal that the optimal water-to-fuel ratio is strongly dependent on engine type, load, speed, injection strategy, and overall operating conditions. While emission reductions are generally achieved, performance responses may vary, highlighting the importance of precise control and system integration. In conclusion, when implemented with appropriate control strategies and optimized operating parameters, water and steam addition represents a technically viable and environmentally promising approach for reducing the environmental footprint of internal combustion engines.

Keywords – Water, Steam, Diesel engine, Gasoline engine, Performance, Emissions.

INTRODUCTION

Internal combustion engines continue to constitute the dominant energy conversion technology in transportation and industrial applications. The increasingly stringent regulations on global greenhouse gas and pollutant emissions have intensified the demand for innovative technologies capable of reducing emissions without compromising engine performance (Heywood, 2018). The mitigation of pollutants such as nitrogen oxides (NOx), carbon monoxide (CO), unburned hydrocarbons (HC), and particulate matter (PM) is being addressed particularly through advanced combustion control strategies. In this context, water and steam addition has emerged as a promising approach, as it modifies the in-cylinder thermal and

chemical environment, thereby offering the potential to improve both performance and emission characteristics.

The use of water injection in internal combustion engines as an anti-knock strategy was first demonstrated in early studies and has regained considerable attention in recent years (Iyer et al., 2017; Psota et al., 1997). Owing to its high latent heat of vaporization and specific heat capacity, water effectively reduces in-cylinder temperatures, thereby contributing to the suppression of thermal NOx formation. The literature indicates that this effect is particularly pronounced under high-load operating conditions or in regions where knock tendency is elevated (Wan et al., 2021). Recent systematic reviews have shown that, especially in spark-ignition (SI) engines, water injection can optimize combustion phasing and increase the knock limit, enabling more advanced ignition timing and, consequently, higher thermal efficiency (Wan et al., 2021). However, the influence of water or steam addition on engine performance parameters varies depending on the injection strategy, injection pressure, timing, and in-cylinder conditions. For instance, direct in-cylinder water injection has been reported to reduce peak cylinder pressure and slow down the combustion rate; nevertheless, these adverse effects can be mitigated through appropriate optimization of injection timing (Li, 2021).

In diesel engines, NOx formation is particularly pronounced due to elevated combustion temperatures and excess oxygen availability. When peak in-cylinder temperatures are reduced through water addition, NOx emission reductions of up to 30–60% have been reported (Boretti, 2013). However, the effects on particulate formation are more complex. While the reduction in combustion temperature may contribute to lower soot formation, improvements in atomization associated with the micro-explosion phenomenon can further decrease particulate emissions. In water–diesel emulsions, the rapid vaporization of water entrapped within fuel droplets induces secondary atomization. This process enhances spray breakup and improves air–fuel mixing, thereby promoting more homogeneous combustion. Nevertheless, excessive water content may increase ignition delay, which in turn can intensify combustion noise and adversely affect overall combustion stability.

In spark-ignition (SI) engines, knock represents one of the primary limiting factors for performance enhancement. Knock is characterized by uncontrolled auto-ignition within the combustion chamber, leading to pressure oscillations that constrain engine efficiency and durability. Water injection mitigates this phenomenon by reducing in-cylinder temperature and the rate of pressure rise, thereby increasing the knock threshold. This enables the application of more advanced ignition timing and higher compression ratios, resulting in improved thermal efficiency (Heywood, 2018). Furthermore, water injection can enhance volumetric efficiency by cooling the intake charge. Particularly in turbocharged engines, the evaporative

cooling effect of water contributes to achieving a denser air–fuel mixture, which may lead to an increase in specific power output. However, at excessive water fractions, the combustion rate may decrease and flame propagation may be delayed. Under low-load operating conditions, this can result in elevated CO and HC emissions. Therefore, precise optimization of the water-to-fuel ratio is of critical importance. In addition to thermal effects, water and steam addition influence the physical and chemical kinetics of combustion. The presence of water vapor may reduce flame propagation speed and prolong combustion duration, thereby affecting both engine performance and emission formation (Pukalskas et al., 2024). Nevertheless, despite the growing body of literature, a comprehensive understanding of the physicochemical mechanisms and detailed combustion chemistry associated with water addition remains insufficiently addressed in existing reviews (Wan et al., 2021).

The influence of water addition on the combustion process can be fundamentally explained through three primary mechanisms:

Thermal Dilution Effect: Owing to its high specific heat capacity and high latent heat of vaporization, water limits the rate of in-cylinder temperature rise. This effect suppresses thermal NOx formation, which is predominantly described by the Zeldovich mechanism. NOx formation accelerates significantly at temperatures above approximately 1800 K (Turns, 2012). By reducing peak in-cylinder temperatures, water injection decreases the NOx formation rate exponentially.

Dilution of Oxygen Concentration: The introduction of water vapor into the combustion chamber reduces the molar fraction of oxygen within the overall gas mixture. This effect is particularly relevant in diesel engines, where it attenuates the intensity of oxidative reactions occurring in locally high-temperature regions.

Modification of Radical Chemistry: Water vapor can influence the formation and concentration of OH radicals during combustion, thereby altering chain-branching and chain-propagation reactions. OH radicals play a critical role in both hydrocarbon oxidation and NO formation pathways (Glassman, Yetter, & Glumac, 2014). Consequently, the impact of water addition extends beyond purely thermal effects and also involves chemical kinetic interactions at the molecular level.

Water and steam addition to internal combustion engines can be implemented through three principal methods: intake manifold injection, direct in-cylinder injection, and water–fuel emulsion applications.

In the intake manifold injection method, water or a water–steam mixture is introduced into the intake air stream and subsequently drawn into the cylinder. This approach can be applied to both diesel and gasoline engines. Injection is typically carried out באמצעות an injector mounted on the intake manifold, allowing water droplets to be transported into the cylinder along with the intake air. The primary advantages of this method include

relative simplicity and ease of integration; however, precise control of in-cylinder distribution may be limited.

In the direct in-cylinder water injection method, water is injected directly into the combustion chamber through a dedicated injector, independent of the fuel injection system. This configuration enables more precise control of injection timing and quantity and can be effectively integrated with modern high-pressure injection systems. In diesel engines, water injection may be scheduled before, during, or after the main fuel injection event, thereby enabling control over combustion phasing and in-cylinder temperature profiles. In gasoline direct-injection engines, particularly under turbocharged operation, direct water injection reduces in-cylinder temperatures, suppresses knock, and contributes to increased specific power output. Although direct injection systems are generally more complex and costly than intake manifold injection systems, they offer superior combustion control capability.

The third approach involves the use of water–fuel emulsions, in which water is mixed with diesel or gasoline at specific ratios to form a quasi-homogeneous emulsion fuel. This emulsion is then supplied to the cylinder through the standard fuel injection system. While this technique eliminates the need for a separate water injection system, challenges related to emulsion stability, phase separation, and long-term storage remain significant technical concerns.

Overall, water and steam injection techniques improve combustion characteristics particularly under high-load and high-temperature operating conditions, thereby contributing to emission control. In diesel engines, these techniques are effective in reducing NOx and particulate emissions, whereas in gasoline engines they provide significant advantages in terms of knock suppression and performance enhancement. Nevertheless, engineering considerations such as system complexity, corrosion risk, lubricant dilution, and the optimization of control strategies directly influence the feasibility and effectiveness of practical implementation. Therefore, water injection systems should be addressed in an integrated manner within the broader framework of engine design and operating strategies.

The present study aims to systematically investigate the effects of water and steam addition on the performance and emission characteristics of internal combustion engines. The scope of the study includes an explanation of the fundamental mechanisms associated with water/steam injection, a comparative evaluation of performance and emission outcomes in diesel and gasoline engines, and the identification of research gaps in the existing literature.

RESULTS AND DISCUSSION

Water or Steam Applications in Diesel Engines

Ayhan (2016) experimentally investigated the effects of different water addition methods—specifically intake manifold water injection—on performance and NOx emissions in a single-cylinder, direct-injection diesel engine. The study measured engine torque, brake specific fuel consumption (BSFC), in-cylinder pressure variations, and exhaust emissions under varying water-to-fuel ratios. The results demonstrated that water addition effectively reduced peak in-cylinder temperatures, leading to a significant decrease in NOx emissions, ranging between 25% and 45%.

Zhang and Li (2018) examined in-cylinder steam injection in a turbocharged diesel engine, simultaneously evaluating waste heat recovery and NOx control. The study analyzed the effects of a steam injection system integrated with a Rankine cycle on combustion characteristics. The findings indicated that steam injection reduced the maximum combustion temperature, achieving NOx reductions of up to 30%, while also providing additional work during the expansion stroke, resulting in a modest improvement in effective thermal efficiency.

Szoollis and Kiss (2024) evaluated water injection technologies in diesel engines from the perspective of Euro 7 emission standards. Their study provided a comparative analysis of direct in-cylinder water injection, intake manifold water injection, and water–fuel emulsion methods. The results indicated that water injection is particularly effective for NOx reduction in heavy-duty diesel engines; however, system complexity and long-term durability issues still require further investigation.

Sun et al. (2022) investigated the effects of direct water injection on combustion and emission characteristics in a large-scale marine diesel engine. Injection timing and water-to-fuel ratio were varied as experimental parameters. The study found that NOx emissions could be reduced by up to 40%, although CO emissions increased under low-load conditions. Additionally, the maximum rate of pressure rise was observed to decrease with water injection.

Nour et al. (2017) compared the effects of water injection into the intake and exhaust manifolds on diesel combustion. Injection into the intake manifold was found to reduce in-cylinder temperatures more effectively and achieve greater NOx reduction, whereas exhaust-side injection had a more limited impact.

Subramanian (2011) compared water–diesel emulsion fuel with timed direct water injection. The micro-explosion effect of the emulsion fuel reduced particulate matter (PM) emissions, while direct water injection was more effective for NOx mitigation. A slight increase in brake specific fuel consumption (BSFC) was also reported.

Tauzia et al. (2010) investigated intake manifold water injection effects on NOx and PM emissions. NOx reductions of up to 50% were achieved, accompanied by a decrease in PM emissions. However, ignition delay increased, resulting in higher hydrocarbon (HC) emissions.

Sandeep et al. (2029) studied the effects of atomized water injection, demonstrating that finer droplet sizes improve combustion homogeneity and effectively reduce NOx emissions. The temperature reduction effect was particularly significant under high-load conditions.

Sencic et al. (2019) conducted a CFD-based study simulating various water injection strategies in a large marine diesel engine. The model results demonstrated that, with optimized injection timing, NOx emissions could be reduced while maintaining combustion efficiency.

Abu-Zaid (2004) experimentally investigated the effects of water–diesel emulsion fuel on performance and combustion characteristics in a single-cylinder, direct-injection diesel engine. Emulsions with varying volumetric water content were tested, and a 20% water fraction was identified as providing optimal results. At this ratio, maximum torque and effective power were achieved, along with an average increase of approximately 3.5% in brake thermal efficiency. Additionally, exhaust gas temperatures decreased with increasing water content, with a reduction of about 5.17% observed for the 20% water emulsion.

Canfield (1999) tested stabilized emulsion fuels containing 30%, 40%, and 45% water in a two-stroke, four-cylinder direct-injection diesel engine under full-load conditions. Increasing water content led to reductions in NOx emissions and exhaust temperature, whereas CO emissions increased. Theoretical analysis indicated that the adiabatic flame temperature decreased by approximately 5.7% when using the 30% water emulsion.

Weibiao et al. (2006) experimentally examined a 30% water–diesel emulsion and suggested that the observed increase in combustion efficiency was primarily due to the finer droplet formation resulting from the higher evaporation rate of water compared to diesel, rather than the micro-explosion mechanism.

These studies collectively highlight that both water injection and water–diesel emulsions can effectively reduce NOx emissions and improve combustion characteristics, with the optimal water fraction and injection strategy being critical for maximizing engine performance and efficiency.

Armas et al. (2005) investigated the effects of a 10% water–diesel emulsion on performance and emissions in a turbocharged, intercooled, direct-injection diesel engine. The study reported an increase in brake thermal efficiency alongside a 46% reduction in NOx emissions. Significant reductions were also observed in soot, HC, CO, and particulate matter (PM) emissions.

Samec et al. (2002) analyzed combustion characteristics both experimentally and numerically in a four-cylinder, air-cooled, direct-injection diesel engine using 10% and 15% water–diesel emulsions. The highest emission improvements were achieved at 10% water content, with NOx reduced by 20%, total hydrocarbons by 52%, and soot by 75%.

Lin and Wang (2004) evaluated the use of 10% and 20% water–diesel emulsions in a four-stroke, water-cooled diesel engine. Increasing water content led to higher brake specific fuel consumption (BSFC), while NOx emissions decreased significantly and CO emissions increased. NOx reduction ranged from 8% at 10% water content to 19–24% at 20% water content.

Selim and Elfeky (2001) investigated the effects of 2–8% water–diesel emulsions on performance, heat transfer, and thermal stresses in a single-cylinder pre-chamber diesel engine. At 8% water content, in-cylinder temperatures decreased by approximately 8%, resulting in lower thermal stresses and a potential increase in engine life.

Wang and Chen (1996) studied changes in droplet size distribution when various hydrocarbon fuels were emulsified with water. They found that combustion rates in emulsion fuels increased significantly compared to pure fuels, primarily due to micro-explosion phenomena that enhanced secondary atomization and reduced ignition delay.

Lif and Holmberg (2006) suggested that during the compression stroke, the evaporating water reduces surface tension, producing smaller fuel droplets. This enhances air–fuel mixing quality and improves combustion.

Nazha et al. (2001) compared fumigation, emulsion fuel, and exhaust gas recirculation (EGR) strategies. Fumigation with a 1:1 water-to-fuel ratio reduced NOx by 60%, though soot emissions slightly increased under high-load conditions. Using a 10% emulsion produced limited NOx reduction with increased soot. EGR at 12% and 16% reduced NOx by 50% but increased soot at high load. Combining full-load EGR with water fumigation reduced NOx by 70% while increasing soot by 60%, whereas EGR combined with emulsion resulted in NOx and soot reductions of 55% and 45%, respectively.

Chadwell and Dingle (2008) developed an electronically controlled water injection system for a heavy-duty diesel engine and reported optimum performance at 30% water content under full load. NOx emissions decreased by 42%, CO and PM emissions dropped significantly, and HC emissions showed a limited increase. Bedford et al. studied direct water injection at 30% and 45% water fractions under varying loads. At 44% load, NOx reductions were 24.1% and 39.4%, and at 86% load, reductions reached 46.1% and 71.1%, respectively.

Hang et al. (1991) used high-speed imaging techniques to demonstrate that emulsion fuels produce finer and more homogeneous spray structures after injection. Christensen and Johanson (1999) applied fumigation in HCCI engines to control combustion rates, showing that the method was effective within limited operating ranges.

Ishida (1994) and Donahue (2000) reported that fumigation under low-load conditions reduces NOx, soot, and specific fuel consumption;

however, at high loads, while NOx decreases, soot and fuel consumption tend to increase.

Sarvi et al. (2009) applied direct water injection in a diesel engine with a common rail system, achieving up to 50% NOx reduction. Slight decreases in HC emissions were observed, while soot and CO emissions increased.

Ayhan & Ece (2020) investigated electronically controlled direct water injection timed during compression. NOx reductions of up to 50% were achieved, although combustion noise increased. Ithnin et al. (2015) studied water–diesel emulsions, reporting decreases in NOx and PM, but increases in CO and HC under low-load conditions.

Gowrishankar & Krishnasamy (2022) compared emulsification and direct injection methods, finding direct injection more effective for NOx reduction. Nour et al. (2016) demonstrated that water injection into the exhaust manifold produced an EGR-like effect, reducing NOx with minor efficiency losses. Sahin et al. (2014) reported that intake water injection reduced the heat release rate; NOx decreased, but specific fuel consumption increased.

Rakopoulos et al. (2008) analyzed combustion and emission mechanisms under water addition using multi-zone modeling, confirming that temperature reduction suppresses NOx formation. Savioli (2015) performed CFD analysis, showing that water injection lowers flame temperature and reduces NOx. Tamma et al. (2009) observed NOx reductions with intake water injection, while PM changes depended on injection ratio. Shah et al. (2009) compared water injection with EGR, finding that water injection reduced NOx without increasing PM. Kang et al. (2023) highlighted that injection timing is critical for NOx reduction, with late injection being more effective.

Mello & Mellor (1999) experimentally demonstrated that water and steam dilution decreases NOx formation kinetics. Prasad et al. (2015) analyzed the micro-explosion phenomenon in detail, exploring the trade-off between PM reduction and NOx increase.

A comprehensive review of the literature indicates that water/steam injection and water–diesel emulsion applications in diesel engines consistently produce the following effects:

- Reduction of peak in-cylinder combustion temperature
- Significant decrease in NOx emissions
- General reduction in particulate matter (PM) and smoke opacity
- Improved atomization due to micro-explosion phenomena
- More controlled heat release rate (HRR)
- Partial increase in the premixed combustion phase, promoting more homogeneous combustion
- Decrease in exhaust gas temperature

- Reduction of thermal loads, providing thermal relief to pistons, valves, and cylinder heads
- Potential improvement in brake specific fuel consumption (BSFC) at optimized water/fuel ratios
- CO emissions: potential increase at low loads, generally decreasing at high loads
- HC emissions: potential increase in low-temperature regions
- CO_2 emissions: indirect reduction proportional to specific fuel consumption
- Decrease in the maximum rate of in-cylinder pressure rise

Water or Steam Applications in Gasoline Engines

The primary objectives of water injection in gasoline engines are knock suppression and specific power enhancement. Water sprayed into the intake manifold or directly into the cylinder lowers the mixture temperature through its high latent heat of vaporization, suppressing the auto-ignition tendency in end-gas regions. This mechanism is particularly critical in turbocharged engines. Hoppe et al. (2016) applied direct water injection in a turbocharged GDI engine and demonstrated that, under full-load conditions, the knock limit was significantly advanced, allowing a specific power increase of approximately 10%. The study also reported reduced exhaust gas temperatures and a decreased requirement for full-load enrichment.

Cordier (2009) experimentally showed that water injection enhances efficiency at high compression ratios and substantially reduces NOx emissions. The authors emphasized that combining water with alcohol fuels further improves thermal efficiency. Similarly, Peters and Stebar (1976) demonstrated early on that water injection effectively suppresses knock, with the reduction in in-cylinder temperature mitigating NO formation.

Dahnz and Spicher (2010) investigated the effects of water injection on in-cylinder heat transfer and irreversibilities, reporting improvements in specific fuel consumption, particularly at high loads. They also noted that water enhances mixture homogeneity, making combustion rates more controllable, and that it affects in-cylinder turbulence and flame propagation, reducing the volume of NO-forming regions. Tornatore (2017) showed that water injection in turbocharged spark-ignition engines reduces the risk of early ignition, enabling safe operation at higher compression ratios.

Wang et al. (2022) focused on GDI engines and experimentally demonstrated that water injection reduces both knock tendency and particulate number (PN) emissions. Direct water spray was particularly effective in reducing fuel film formation, thereby lowering PN emissions. Similarly, Etikyala et al. (2019) reported that water injection suppresses particle formation mechanisms in GDI engines, offering notable advantages in meeting Euro 6 emission standards.

Boretti (2013) indicated that water injection in turbocharged gasoline engines can be optimized for both performance and emissions. The study

highlighted that water injection can eliminate the need for full-load enrichment, reducing CO_2 emissions. Fu et al. (2014) analyzed a steam-injected spark-ignition (SI) engine concept and showed that expansion ratios could be effectively increased, theoretically improving thermal efficiency.

Zembi (2021), using three-dimensional CFD analysis, demonstrated that droplet size and injection timing directly affect combustion rates, with optimum timing yielding maximum NOx reduction. In a 2019 study, Zembi et al. further showed through multi-dimensional simulations that water injection reduces local temperature peaks and limits NO formation at the flame front.

Iacobacci et al. (2017) found that water injection lowers exhaust temperatures, reducing the thermal load on turbocharger components a benefit particularly relevant for high-performance engines. Yuan et al. (2021), using chemical kinetic modeling, indicated that water affects OH radical formation indirectly, with dilution and heat absorption mechanisms dominating the combustion kinetics.

The emission-reducing effect of water injection in gasoline engines is primarily associated with lowering peak in-cylinder temperatures and reducing local rich zones. Because NOx formation is largely governed by the Zeldovich thermal mechanism, the evaporative cooling effect of water significantly reduces NOx emissions. Peters and Stebar (1976) reported early on that water injection could reduce NOx by up to 40%, directly correlating with a drop in peak combustion temperatures.

Chen et al. (2019) noted that water injection effectively reduces NOx at high loads but may increase HC and CO emissions under low-load conditions due to incomplete oxidation in low-temperature regions. Similarly, Li et al. (2021) observed NOx reductions of 30–50% in GDI engines, while some operating points showed slight increases in HC.

Water injection also offers significant benefits in particulate emissions (PN). Zhang et al. (2024) demonstrated that direct water injection reduces wall wetting and suppresses fuel film formation, lowering PN emissions. Zembi et al. (2019) highlighted the critical role of injection timing on particle formation, showing that early-phase water injection optimizes PN reduction.

Boretti (2013) further reported that water injection in turbocharged SI engines eliminates the need for full-load enrichment, reducing CO and HC emissions overall. The study observed more stable flame development under stoichiometric combustion conditions and emphasized that water injection lowers exhaust gas temperatures, potentially affecting the inlet temperature of three-way catalytic converters and highlighting the need for optimized catalytic conversion efficiency.

CFD studies by Yin et al. (2020) have shown that reducing water droplet size leads to more pronounced NOx reduction and suppresses local temperature peaks. Wu et al. (2021) reported that in steam-injected SI

engines, the increased expansion ratio lowers end-of-combustion temperatures, reducing NOx emissions. However, the same study noted that CO emissions tend to increase at high steam fractions.

Shahbakhti and Heywood (2021), using chemical kinetic modeling, demonstrated that water addition indirectly affects OH radical concentrations, potentially slowing CO oxidation reactions. This effect is particularly linked to CO increases under low-load conditions. Cavina et al. (2017) indicated that while water injection reduces both NOx and particulate formation, improper calibration may result in HC increases.

In gasoline engines, the steam injection concept differs from conventional water injection. It not only suppresses knock but also increases the in-cylinder expansion ratio, aiming to enhance cycle efficiency. This approach is often integrated with exhaust heat recovery and supported by micro-Rankine cycles. Wu et al. (2022) conducted a thermodynamic analysis of a steam-injected SI engine, showing that additional work during expansion can improve theoretical cycle efficiency. The study predicted reductions in specific fuel consumption, especially at high loads.

Choi et al. (2019) analyzed steam injection combined with the Miller cycle in turbocharged gasoline engines and noted that the increased expansion ratio allows for more efficient utilization of exhaust enthalpy, offering significant advantages in downsizing applications.

Sun et al. (2023) experimentally investigated steam-assisted combustion, showing that steam increases the mixture's specific heat, lowering maximum combustion temperature and reducing NOx formation. However, at high steam fractions, flame propagation speed decreases and CO emissions can increase.

Endo et al. (2007) developed an SI engine integrated with a system generating steam from exhaust heat. The study reported that using a portion of exhaust energy for steam production can improve cycle efficiency by up to 5%. Similarly, Johansson et al. (2012) confirmed that steam injection effectively prolongs the expansion phase and lowers end-of-combustion temperature.

Wan et al. (2021), in a comprehensive study on advanced SI combustion systems, reported that water injection extends the knock limit in high-compression engines and improves efficiency. They also emphasized the positive effect of steam on thermal efficiency due to increased heat capacity.

Yuan et al. (2021), using chemical kinetic modeling, investigated the effect of steam injection on SI engine combustion. They showed that steam dilutes radical concentrations, particularly reducing NO formation, but the basic combustion mechanism remains governed by hydrocarbon oxidation kinetics. This approach explains the effects of water injection on combustion performance and emissions from thermodynamic and kinetic perspectives.

Li et al. (2019) conducted multi-dimensional numerical simulations on a natural gas SI engine, examining the effects of direct steam injection on performance and emissions. The study showed that steam injection reduces exhaust gas temperature, indirectly affecting turbocharger thermal behavior, and highlighted that optimizing the steam fraction is critical for system efficiency.

Hoppe et al. (2016) reported that in a near-production turbocharged GDI engine, water injection significantly advanced the full-load knock limit, with approximately 10% power increase. Full-load enrichment requirements were eliminated, improving CO_2 emissions. Additionally, NOx emissions decreased significantly, and CO_2 emissions were indirectly reduced.

Tornatore (2017) showed that water injection in SI engines allows for higher compression ratios and reduces specific fuel consumption. The authors emphasized that the charge-cooling effect is particularly pronounced in low-speed, high-torque regions. Dahnz and Spicher (2010) demonstrated that in turbocharged applications, water injection controls the maximum in-cylinder pressure rise rate and improves combustion stability.

Boretti (2013) reported that water injection in turbocharged gasoline engines allows higher boost pressures to be safely used, enabling engine downsizing while maintaining performance. The study also noted reductions in NOx emissions and lower exhaust gas temperatures.

Lanni et al. (2021) compared direct in-cylinder water injection with port water injection and found that direct injection is more effective at suppressing knock, especially at high loads. They also highlighted that direct water injection has the potential to reduce turbo lag.

In general, the literature indicates that water injection in gasoline engines exhibits the following common effects:

- Advances the knock limit
- Increases specific power output
- Improves thermal efficiency
- Reduces the need for rich mixtures at high load
- Lowers exhaust gas temperatures
- Provides potential for additional work via Rankine cycle integration
- Reduces NOx emissions
- PN/PM → generally decreases
- CO → may increase at low load, decreases at full load
- HC → potential increase in low-temperature regions
- CO_2 → can be reduced indirectly

These represent the key consensus findings across multiple studies on water injection in SI engines.

RESULTS

Water and steam injection in internal combustion engines, despite a history spanning nearly a century, has regained prominence in recent years due to increasingly stringent emissions regulations. The literature reviewed herein demonstrates that the implementation of water/steam injection exerts significant, yet parameter-dependent, effects on the performance, emission, and combustion characteristics of both diesel and gasoline engines.

From a performance perspective, it is evident that the effect of water injection is not linear. In diesel engines, low to moderate water addition—particularly in emulsified fuels and direct in-cylinder injection applications—can enhance brake thermal efficiency by improving atomization quality and enabling a more controlled combustion process. However, at higher water fractions, increased ignition delay, excessive reduction in flame temperature, and weakened oxidation reactions can lead to higher specific fuel consumption. In gasoline engines, water injection—especially in turbocharged configurations—extends the knock limit, allowing for higher compression ratios and elevated boost pressures. This, in turn, enables increased specific power and reduced full-load enrichment requirements, indirectly contributing to lower CO_2 emissions.

From an emissions perspective, the most consistent and robust finding in the literature is the reduction of NOx emissions. In both diesel and gasoline engines, the high specific heat capacity and latent heat of vaporization of water lower the in-cylinder peak temperature, thereby suppressing the thermal NO formation mechanism. Studies report NOx reductions ranging from 20% to 70%, depending on engine type and water fraction. However, particulate matter (PM/soot) emissions are more sensitive to the injection strategy. In diesel engines, emulsified fuels can reduce soot formation via micro-explosion mechanisms, whereas intake-port fumigation with excessive water can create local cold zones, potentially increasing PM emissions. In gasoline direct-injection (GDI) engines, water injection can reduce diffusion flame regions, thereby lowering particle number (PN) emissions. The behavior of CO and HC emissions is more complex. At low loads and high water fractions, the reduction in combustion temperature can slow oxidation reactions, leading to increases in CO and HC emissions. However, at optimized water-to-fuel ratios, this increase is generally limited, and some studies report it to be negligible.

From a theoretical perspective, the effects of water/steam injection can be explained through three primary mechanisms: (i) thermal dilution and reduction of adiabatic flame temperature, (ii) enhanced atomization via micro-explosions in emulsion fuels, and (iii) indirect chemical-kinetic effects, including modulation of OH radical formation. In diesel engines, softening of the premixed combustion phase and reduction of the pressure rise rate contribute to lower mechanical loads and reduced combustion noise. In gasoline engines, the knock-suppressing effect emerges as the most pronounced advantage.

When combined with exhaust gas recirculation (EGR), water injection has the potential to improve the classical NOx–PM trade-off. This combination represents a particularly important area of research for heavy-duty diesel engines and post-Euro VI emission standards.

In general, water and steam injection technologies:

- Demonstrate high effectiveness in reducing NOx emissions.
- Serve as a performance-enhancing tool in turbocharged engines.
- Reduce thermal loads by controlling combustion temperatures.
- Exhibit variable effects on PM and CO/HC emissions depending on the injection strategy.
- Require precise calibration and optimal dosing for effective operation.

However, the majority of studies reported in the literature are based on short-duration laboratory experiments. Long-term engine durability, corrosion formation, material wear in cylinder liners and valve mechanisms, potential impacts on lubrication systems, and applicability under real driving conditions have been scarcely addressed. Notably, the potential of water to thin the cylinder wall film and its effect on oil dilution are critical parameters that require detailed investigation for assessing long-term performance and engine life.

Furthermore, research on the energy cost of water injection systems, auxiliary pump requirements, control unit integration, and compatibility with existing engine management systems is limited. Therefore, future studies should focus on long-duration durability tests, full-scale driving simulations, and system integration optimization to establish the commercial viability of water and steam injection technologies.

REFERENCE

Abu-Zaid, M. (2004). Performance of single-cylinder DI diesel engine using water fuel emulsions. Energy Conversion and Management, 45, 697–705.

Armas, O., Ballesteros, R., Martos, F.J., Agudelo, J.R. (2005). Characterization of Light Duty Diesel Engine Pollutant Emissions Using Water-Emulsified Fuel, Fuel 84, 1011-1018.

Ayhan, V. and Ece, Y. M. (2020). Electronic controlled direct water injection at compression stroke for NOx reduction. Applied Energy, 260, 114328.

Ayhan, V. (2016). Investigation of the effects of steam and different water introduction methods to a DI diesel engine on performance and NOx emissions. Sakarya Univ. J. Sci. Eng. 20.3.

Boretti, A. (2013). Water injection in directly injected turbocharged spark ignition engines. Applied Thermal Engineering, 52, 62–68.

Canfield, C.A. (1999). Effects of Diesel-Water Emulsion Combustion on Diesel Engine NOX Emission, Master of Science, University Of Florida.

Cadewll, C.J., Dingle, P.J.G. (2008) Effect of Diesel and Water Co-injection with Real-Time Control on Diesel Engine Performance and Emissions, SAE, Technical Paper Series, 01-1190.

Christensen, M., Johansson, B. (1999). Homogeneous Charge Compression Ignition with Water Injection, SAE paper 1999-01-0182.

Cordier, M., Lecompte, M., Malbec, L., Reveille, B. (2019). Water Injection to Improve Direct Injection Spark Ignition Engine Efficiency. SAE Technical Paper 2019-01-1139.

Chen, B., Zhang, L., Han, J., Chen, X. (2019). Investigating the effect of increasing specific heat and the influence of charge cooling of water injection in a TGDI engine. Appl. Therm. Eng. 149, 1105–1113.

Cavina, N., Rojo, N., Businaro, A., Brusa, A., Corti, E. and De Cesare, M. (2017). Investigation of water injection effects on combustion characteristics of a GDI TC engine. SAE International Journal of Engines, 10(4), 2209–2218.

Choi, M., Kwak, Y., Roth, D. B., Jakiela, D., and Song, J. (2019). Synergies of cooled external EGR, water injection, Miller valve events and cylinder deactivation for the improvement of fuel economy on a turbocharged-GDI engine: Part 1 – Engine simulation. SAE Technical Paper 2019-01-0245.

Donahue, R. (2000). Controlling Combustion Using in Cylinder Mixture Preparation, PhD. Thesis, Mechanical Engineering, UW Madison.

Dahnz, C. and Spicher, U. (2010). Irreversible phenomena in spark ignition engines with water injection. International Journal of Engine Research, 11(6), 477–489.

Etikyala, S., Koopmans, L., and Dahlander, P. (2019). Particulate Emissions in a GDI with an Upstream Fuel Source, SAE Technical Paper 2019-01-1180.

Endo, T., Kawajiri, S., Kojima, Y., Takahashi, K., Baba, T., Ibaraki, S., Takahashi, T. and Shinohara, M. (2007). Study on maximizing exergy in automotive engines. SAE Technical Paper 2007-01-0257.

Fu, J., Ju, J., Deng, B., Feng, R., Yang, J., Zhou, F., Zhao, X. (2014). An approach for exhaust gas energy recovery of internal combustion engine: Steam-assisted turbocharging. Energy Conversion and Management. Volume 85. Pages 234-244.

Glassman, I., Yetter, R. A., Glumac, N. (2014). Combustion (5th ed.). Academic Press.

Gowrishankar, S., Krishnasamy, A. (2022). A relative assessment of emulsification and water injection methods to mitigate higher oxides of nitrogen emissions from biodiesel fueled light-duty diesel engine, Fuel, Volume 308, 121926.

Heywood, J. B. (2018). Internal Combustion Engine Fundamentals (2nd ed.). McGraw-Hill Education.

Hang, X., Yunbia, O.S., Chongji, Z., Yuanji, M. (1991). Proceeding of the 5th International Conference on Liquid Atomization and Spray Systems, Natl Inst of Standards and Technology, Gaithersburg, MD, p. 307, USA.

Hoppe, F., Thewes, M., Baumgarten, H., & Dohmen, J. (2016). Water injection for gasoline engines: Potentials, challenges, and solutions. International Journal of Engine Research, 17(1), 86–96.

Iyer, A., Rane, I.P., Upasani, K.S. (2017). Experimental Study on the Effect of Water Injection in an Internal Combustion Engine. 11(6):379. International Review of Mechanical Engineering (IREME).

Ishida, M., Chen, Z. (1994). An Analysis of the Added Water Effect of NO Formation in D.I. Diesel Engines, SAE Paper No. 941691.

Ithnin, A.M., Noge, H., Kadir, H.A., Jazair, W. (2014). An overview of utilizing water-in-diesel emulsion fuel in diesel engine and its potential research study, Journal of the Energy Institute, Volume 87, Issue 4, Pages 273-288.

Iacobacci, A., Marchitto, L., Valentino, G. (2017). Water Injection to Enhance Performance and Emissions of a Turbocharged Gasoline Engine under High Load Condition. SAE Int. J. Engines. 10, 928–937.

Kang, Z., Bai, Y., Feng, S., Wu, J., Wu, Z. (2023). Effect of direct water injection timing on cycle performance and emissions characteristics within a CI-ICRC engine, Alexandria Engineering Journal, Volume 72,Pages 135-145.

Li, A., Zheng, Z., Song, Y. (2021). A Simulation Study of Water Injection Position and Pressure on the Knock, Combustion, and Emissions of a Direct Injection Gasoline Engine. ACS OmegaVol 6/Issue 28Article.

Lin, C.Y., and Wang, K.H. (2004).Effects of Diesel Engine Speed and Water Content on Emission Characteristics of Three-Phase Emulsions, Journal of Environmental Science and Health, Part A 39, No 5, pp. 1345-1359.

Lif, A., and Holmberg, K. (2006). Water-in-Diesel Emulsions and Related Systems, Advanges in Colloid and Interface Science, 231-239.

Li, A., Zheng, Z. and Song, Y. (2021). Research on the study of water injection control parameters on combustion performance of a spark-ignition engine. Energy, 217, 119346.

Li, L. and Zhang, Z. (2019). Investigation on steam direct injection in a natural gas engine for fuel savings. Energy, 183, 958–970.

Lanni, D., Galloni, E., Fontana, G. and Erme, G. (2021). Experimental and Numerical Analyses of Direct and Port Water Injection in a Turbocharged Spark-Ignition Engine. SAE Technical Paper 2021-24-0035

Mello, J. P. and Mellor, A. M. (1999). NOx emissions with water/steam dilution in DI diesel. SAE Technical Paper 1999-01-0836.

Nour, M., Kosaka, H., Bady, M., Abdel-Rahman, A.K. (2017). Effects of intake/exhaust manifold water injection on DI diesel combustion & emissions. J. Thermal Sci. Technol., 12(1).

Nazha, M. A. A., Rajakaruna, H., Wagstafe, S. A. (2001). The Use of Emulsion, Water Induction and EGR for Controlling Diesel Engine Emission, SAE, Technical Paper Series, 01-1941.

Nour, M., Kosaka, H., Abdel-Rahman, A. K. and Bady, M. (2016). Effect of water injection into exhaust manifold on diesel combustion & emissions. Energy Procedia, 100, 178–187.

Pukalskas, S., Korsakas. V., Stankevičius, T., Kriaučiūnas, D., Mikaliūnas, S. (2024). Effect of Water Injection on Combustion and Emissions Parameters of SI Engine. Energies, 17(9), 2132.

Prasad, S., Gonsalvis, J., Vijay, V.S. (2015). Effect of Introduction of Water into Combustion Chamber of Diesel Engines – A Review. Energy and Power 2015, 5(1A): 28-33.

Peters, B. D. and Stebar, R. F. (1976). Water injection for control of NOx emissions in spark ignition engines. SAE Technical Paper 760547.

Psota, M., Easley, W., Fort, T., and Mellor, A. (2997). Water Injection Effects on NOx Emissions for Engines Utilizing Diffusion Flame Combustion. SAE Technical Paper 971657.

Rakopoulos, C. D., Antonopoulos, K. A., Rakopoulos, D. C., & Hountalas, D. T. (2008). Multi-zone modeling of combustion/emissions in DI diesel. Energy Conversion and Management, 49, 625–643.

Szőllősi, D. and Kiss, P. (2024). Effects of water injection in diesel engine emission systems review in the light of Euro 7. Energies, 17(20), 5107.

Sun, X., Ning, J., Liang, X., Jing, G., Chen, Y., Chen, G. (2022). Effect of direct water injection on combustion and NOx in marine diesel engines. Fuel, 310, 122291.

Subramanian, K. A. (2011). Comparison of water–diesel emulsion and timed water injection for NOx/smoke control. Energy Conversion and Management, 52, 849–857.

Sandeep, S., Kumar, D. S., Krishnan, S. and Pandey, S. K. (2019). Assessment of atomized water injection for NOx reduction. IOP Conf. Ser.: Mater. Sci. Eng. 577, 012186.

Senčić, T., Mrzljak, V., Blecich, P., & Bonefačić, I. (2019). 2D CFD simulation of water injection strategies in large marine diesel engines. J. Mar. Sci. Eng., 7, 296.

Samec, C, N., Kegl, B., Dıbble, R.W. (2002). Numerical and Experimental Study of Water/Oil Emulsified Fuel Combustion in a Diesel Engine, Fuel 81, 2035–44.

Selim, M.Y., Elfeky, S.M.S. (2001). Effects of Diesel/Water Emulsion on Heat Flow and Thermal Loading in a Precombustion Chamber Diesel Engine, Applied Thermal Engineering, Vol. 21, Pages: 1565–1582.

Sarvi, A., Kilinen, P., Zevenhover, R. (2009). Emissions from Large-scale Medium-speed Diesel Engines: 3. Influence of Direct Water Injection and Common rail, Fuel Processing Technology 90, S. 222-231.

Sahin, Z.,Tuti, M. and Durgun, O. (2014). Inlet water injection effects on heat release, fuel consumption, opacity & NOx in DI diesel. Fuel, 115, 884–895.

Savioli, T. (2015). CFD analysis of diesel engines with water injection. Energy Procedia, 81, 723–731.

Shah, S. R., Maiboom, A., Tauzia, X. and Hétet, J.-F. (2009). Inlet manifold WI vs EGR on PM & NOx. SAE Technical Paper 2009-01-1439.

Sun, X., Zhao, P., Liang, X., Jing,G., Zhou, G., Chen, G. (2023). Investigation of thermo-physical and chemical effects of in-cylinder steam injection on gasoline engine performance. Fuel.Volume 334, Part 1.

Shahbakhti, M. and Heywood, J. B. (2021). Kinetic modelling of combustion in a spark ignition engine with water injection. Fuel, 283, 118814.

Turns, S. R. (2012). An Introduction to Combustion: Concepts and Applications (3rd ed.). McGraw-Hill.

Tauzia, X., Maiboom, A. and Shah, S. R. (2010). Inlet manifold water injection study on DI diesel. Energy, 35, 3628–3639.

Tamma, B., Alvarez, J. C. and Simon, A. J. (2009). Water addition in diesel intake for NOx reduction. Internal Combustion Engine Division Fall Technical Conference (ICEF). Paper No: ICEF2003-0749, pp. 245-249; 5 pages.

Tornatore, C. (2017). Water Injection: a Technology to Improve Performance and Emissions of Downsized Turbocharged Spark Ignited Engines. SAE International Journal of Engines. 10(5):2319-2329.

Wan, J., Zhuang,Y., Huang,Y., Qian,Y., Qian, L. (2021). A review of water injection application on spark-ignition engines. Fuel Processing Technology. Volume 221. 2021. 106956,

Weibio, F. U., Gong, J., Hou, L.,(2996). There is No Mixro-Explosion in The Diesel Engines Fueled with Emulsified Fuel, Chinese science Bulletin, No. 10, Vol. 51, Pn. 1261–1265.

Wang, C.H., Chen, J.T. (1996). An Experimental Investigation of the Burning Characteristics of Water-Oil Emulsions, Int. Common Heat Mass Transfer 23(6), p., 823-34.

Wang, J., Yan, F., Yan, D., Zhang, W., Zhang, G., Zhang, J., Chen, Z., Wang, Y. (2022). Effects of Water Injection on Combustion Emission and Knock Characteristics of Turbocharged Direct Injection Gasoline Engine. Int. J Automat. Technol. 23, 899–912.

Wu, Z., Kang, Z., Wu, J., Deng, J., Hu, Z. and Li, L. (2021). A review of water-steam-assist technology in modern internal combustion engines. Energy Reports, 7, 2340–2361.

Wu, J., Kang, Z. and Wu, Z. (2022). Thermodynamic analysis of in-cylinder steam assist technology within an internal combustion engine. Applied Sciences, 12(13), 6818.

Wan, J., Zhuang, Y., Huang, Y., Qian, Y. and Qian, L. (2021). A review of water injection application on spark-ignition engines. Fuel Processing Technology, 221.

Yuan, H., Giles, K., Zhu, S., Howson, S., Lewis, A., Akehurst, S., Turner, N., Harris, J., Fowler, G., Geddes, J. (2021). Kinetic modelling of combustion in a spark ignition engine with water injection, Fuel, Volume 283.

Yin, P., Li, X., Hung, D., Fan, Y. and Xu, M. (2020). Numerical investigation of the effects of port water injection timing on performance and emissions in a gasoline direct injection engine. SAE Technical Paper 2020-01-0287.

Zhang, Z. and Li, L. (2018). Investigation of in-cylinder steam injection in a turbocharged diesel engine for waste heat recovery and NOx control. Energies, 11(4), 936.

Zembi, J., Mariani, F., Battistoni, M. (2021). Numerical Investigation of Water Injection Effects on Flame Wrinkling and Combustion Development in a GDI Spark Ignition Optical Engine. SAE Technical Papers. 01.0465.

Zembi, J., Battistoni, M., Ranuzzi, F., Cavina, N., Cesare, M.D. (2019). CFD Analysis of Port Water Injection in a GDI Engine under Incipient Knock Conditions, 12(18), 3409.

Zhang, Q., Huang, Z., Wang, L., Lin, G. and Pan, J. (2024). Experimental study of port water injection on GDI engine fuel economics and emissions. ACS Omega, 9(8), 8893–8903.

Performance Evaluation and Flow Condition Optimization of Shell and Tube Heat Exchangers Under Varying Operational Parameters

Mahir ŞAHİN[1]

Mustafa KILIÇ[2]

1- Res. Asst.; Adana Alparslan Türkeş Bilim ve Teknoloji Üniversitesi Makine Mühendisliği Bölümü. msahin@atu.edu.tr ORCID No: 0000-0002-9565-9160

2- Prof. Dr.; Adana Alparslan Türkeş Bilim ve Teknoloji Üniversitesi Makine Mühendisliği Bölümü. mkilic@atu.edu.tr ORCID No: 0000-0002-8006-149X

ABSTRACT

This research analyzes the thermal performance of a shell and tube heat exchanger operating under laminar flow circumstances. The study's goal is to evaluate the combined effect of various Reynolds numbers (Re = 200, 400, 800, and 1000) and hot fluid input temperatures (40 °C, 50 °C, 60 °C, and 80 °C) using experimental methods supported by numerical validation. The data indicate that operational parameters significantly influence heat transfer effectiveness. It was observed that increasing the input temperature from 40°C to 80°C leads in a consistent decrease in effectiveness, with an average loss of 4% across the provided flow rangeIn contrast, raising the Reynolds number from 200 to 1000 significantly improves thermal performance, leading in a 14.6% increase in overall effectiveness at constant input temperature. The strong correlation between the experimental data and the numerical model, with a maximum error margin of 8.6%, lends credibility to these conclusions. These findings emphasize the need of adjusting flow parameters in heat exchange systems to improve energy efficiency.

Keywords – Fluid flow, Re number, laminar, boundary layer.

INTRODUCTION

The global escalation in energy demand has shifted significant attention toward improving industrial energy efficiency and minimizing thermal losses. Since more than 70% of global energy exchange is heat-based, the optimization of thermal transfer is a cornerstone of sustainable energy practices. Heat exchangers serve as vital components in these processes, and enhancing their performance directly contributes to reduced energy consumption, lower environmental impact, and the development of more compact, cost-effective systems [1-5]. A fundamental strategy for heat transfer enhancement involves decreasing thermal resistance to enable the design of smaller, more efficient equipment, which is essential for high-flux applications such as nuclear reactors, microelectronics, and advanced energy technologies. Various methodologies, including the use of extended surfaces like fins and baffles, fluid vibration techniques, and the incorporation of porous materials, have been widely investigated [6-8]. Porous media, which range from natural materials like wood and rock to artificial constructions like metal foams and ceramic sponges, provide advantages such as high surface area, low density, and high heat conductivity. These characteristics facilitate intensified heat and mass transfer by altering flow dynamics and thinning boundary layers. When integrated into heat exchanger designs, porous structures can achieve superior thermal performance and space efficiency [9,10]. While porous media are successfully utilized in sectors

like geothermal energy, electronics cooling, and fuel cells, challenges such as fouling and maintenance requirements in shell and tube heat exchangers necessitate the strategic selection of both porous architectures and working fluids [11,12].

Abbasi et al. [13] demonstrated that employing porous baffles can improve the heat exchange rate by 139 %, although this was accompanied by a 247 % increase in pressure drop. Similarly, Tian et al. [14] reported that combining porous baffles with annular fins resulted in a 92.14 % increase in heat transfer performance while simultaneously improving pressure drop performance by 65.0 % compared to traditional solid-baffle designs.

The impact of porous material placement and properties has also been a focal point of research. Naqvi and Wang [15] evaluated various STHE configurations (helical, segmental, and clamping anti-vibration) and observed that the Nusselt number on the shell side decreases as porosity increases from 0.6 to 0.95, with optimal performance occurring at a 0.6 porous radius ratio. These findings were supported by Rad et al. [16], who identified that a porous radius ratio of 0.6 combined with 90 % porosity yielded the highest heat transfer performance ratio on the shell side.

Furthermore, the geometric configuration of baffles significantly influences efficiency. Marzouk et al. [17] investigated various designs, including conventional single segmental (CSS) and circular ring with holes (CRH). Their findings revealed that CRH baffles had a 166% greater efficacy and a 142% higher heat transfer coefficient than CSS baffles due to the elimination of dead zones. Additionally, You et al. [18] found that trefoil-hole baffles (THB-STHE) significantly reduce the temperature boundary layer thickness near the walls, thereby substantially enhancing the overall heat transfer rate.

The study investigates the synergy between a certain range of Reynolds numbers (200 to 1000) and different hot fluid input temperatures (40, 50, 60, and 80 °C). By integrating experimental findings with numerical validation, this work addresses a critical gap in understanding how operational temperature fluctuations impact effectiveness at low flow rates, providing essential insights for the precise optimization of industrial heat exchange processes.

MATERIALS AND METHODS

The heat transfer performance is investigated in detail across the selected parameters by utilizing numerical results validated through experimental data. The systematic procedure adopted for both the experimental and numerical analyses is outlined in the subsequent flowchart.

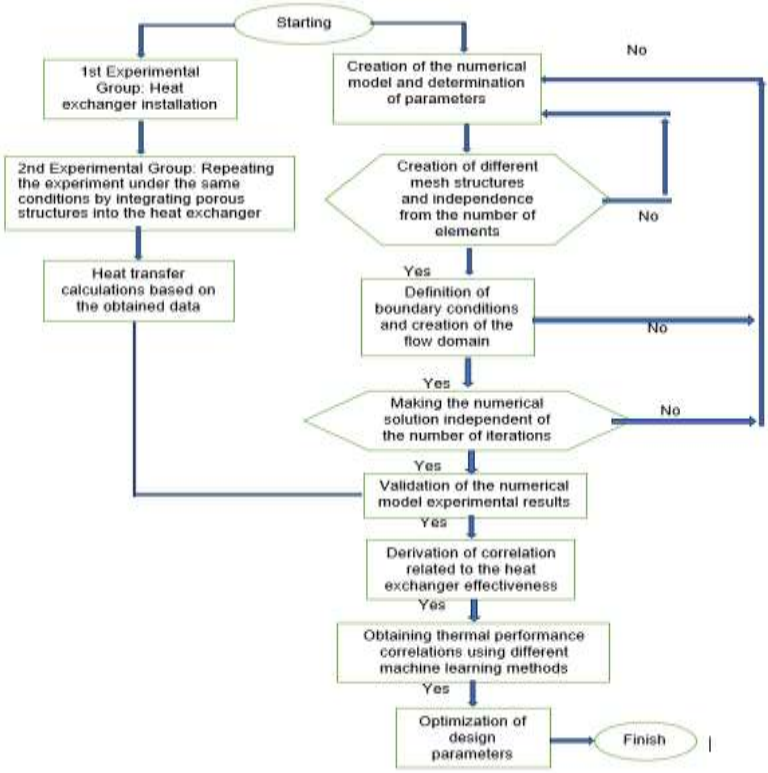

Figure 1: Flowchart for experimental and numerical study

Experimental Setup

STHE employed in this study, as illustrated in Figure 2, features a circular tube arrangement consisting of four baffles, a single shell pass, and six tube passes. The internal tubes have a 7 mm inner diameter, an 8 mm outer diameter, and a total length of 350 mm. While the baffles and tubes are constructed from 304 stainless steel, the shell is fabricated from polycarbonate.

Figure 2: Shell and tube heat exchanger

The constructed experimental setup employed pure water as the hot fluid, which was supplied to the heat exchanger at a defined constant temperature using heater resistances situated within the flow control module. The input temperatures for hot and cold fluids are set at 40°C and 20°C, respectively. In addition, resistors included within the power management unit offer a consistent heat flow.

Figure 3: Flow control unit and data logging computer

Throughout the experimental method, the flow rates of both hot and cold fluids, as well as their respective intake and exit temperatures, were continually monitored and recorded using a customized data logging system, as shown in Figure 3.

Table 1: The parameters to be used in experimental setup

Parameters	**Constant variables**	**Definition**
Re_{hot}=200 =400 =800 =1000	$T_{h,in}$=40°C $T_{c,in}$=20°C Re_{cold}=800	The dimensionless number characterizing the flow.

$T_{h,in}$=40°C =50°C =60°C =80°C	$T_{c,in}$= 20°C Re_{hot}= 400 Re_{cold}= 800	The temperature of the fluid entering a control volume or heat exchanger at the hot side, which serves as the reference temperature for evaluating heat transfer.

Numerical Model

Computational Fluid Dynamics (CFD) is an effective method for assessing complicated heat transport in baffled shell and tube heat exchangers, and ANSYS Fluent is the ideal program for this study. The modeled exchanger features a single shell pass and six tube passes, both 350 mm long, with a 70 mm inner diameter polycarbonate shell and 7 mm inner diameter stainless steel tubes. The simulation evaluates a counter-flow arrangement under laminar conditions at Reynolds numbers of 200, 400, 800, and 1000. This steady state problem, solved in Cartesian coordinates, is governed by Equations 1-5, starting with the continuity equation which defines the conservation of mass within the flow.

$$\frac{\partial u}{\partial x}+\frac{\partial v}{\partial y}+\frac{\partial w}{\partial z}=0 \tag{1}$$

Momentum equation in the x-direction

$$u\frac{\partial u}{\partial x}+v\frac{\partial u}{\partial y}+w\frac{\partial u}{\partial z}=-\frac{1}{\rho}\frac{\partial p}{\partial x}+v\left[\frac{\partial^2 u}{\partial x^2}+\frac{\partial^2 u}{\partial y^2}+\frac{\partial^2 u}{\partial z^2}\right] \tag{2}$$

Momentum equation in the y-direction

$$u\frac{\partial v}{\partial x}+v\frac{\partial v}{\partial y}+w\frac{\partial v}{\partial z}=-\frac{1}{\rho}\frac{\partial p}{\partial y}+v\left[\frac{\partial^2 v}{\partial x^2}+\frac{\partial^2 v}{\partial y^2}+\frac{\partial^2 v}{\partial z^2}\right] \tag{3}$$

Momentum equation in the z-direction

$$u\frac{\partial w}{\partial x}+v\frac{\partial w}{\partial y}+w\frac{\partial w}{\partial z}=-\frac{1}{\rho}\frac{\partial p}{\partial z}+v\left[\frac{\partial^2 w}{\partial x^2}+\frac{\partial^2 w}{\partial y^2}+\frac{\partial^2 w}{\partial z^2}\right] \tag{4}$$

The energy equation:

$$u\frac{\partial T}{\partial x}+v\frac{\partial T}{\partial y}+w\frac{\partial T}{\partial z}=\alpha\left[\frac{\partial^2 T}{\partial x^2}+\frac{\partial^2 T}{\partial y^2}+\frac{\partial^2 T}{\partial z^2}\right] \tag{5}$$

The dimensionless number for Re (Reynolds) are described by the following general equation:

$$Re=\frac{\rho VD}{\mu} \tag{6}$$

The temperature difference which changes logarithmically in the heat exchanger can be determined as:

$$\Delta T_1 = T_{h,in} - T_{c,out} \tag{7}$$

$$\Delta T_2 = T_{h,out} - T_{c,in} \tag{8}$$

$$\Delta T_{lm} = \frac{\Delta T_1 - \Delta T_2}{\ln(\Delta T_1 / \Delta T_2)} \tag{9}$$

Specific heat capacity:

$$C_c = \dot{m}_c c_{pc} \tag{10}$$

$$C_h = \dot{m}_h c_{ph} \tag{11}$$

Maximum temperature difference:

$$\Delta T_{max} = T_{h,in} - T_{c,in} \tag{12}$$

Maximum heat transfer rate:

$$\dot{Q}_{max} = C_{min} \Delta T_{max} \tag{13}$$

Effectiveness of heat exchanger:

$$\varepsilon = \frac{\dot{Q}_{act}}{\dot{Q}_{max}} = \frac{Actual\ heat\ transfer\ amount}{Maximum\ heat\ transfer\ amount} \tag{14}$$

Figure 4 depicts the model geometry, which has a 350 mm shell and tubes length, with the tubes organized in a circular pattern, an 80 mm outer diameter of the shell, a 70 mm inner diameter of the shell, 7 mm inner diameter of tubes, and 8 mm outer diameters of tubes.

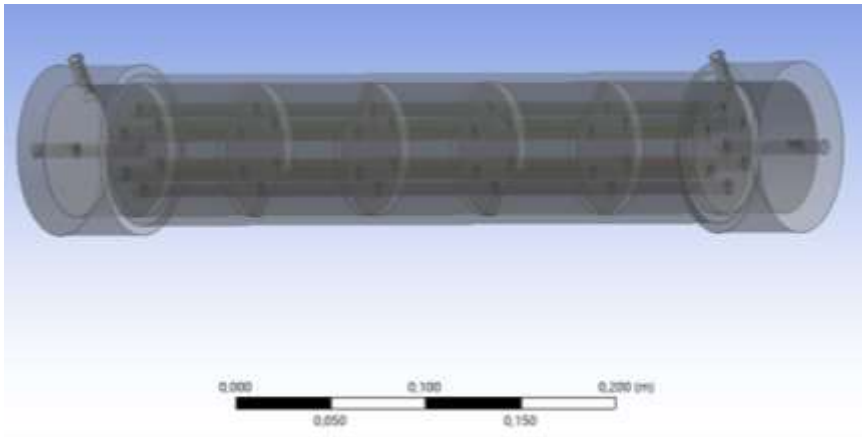

Figure 4: Numerical model geometry generated in SpaceClaim

As shown in Figure 5, the numerical model incorporates three distinct boundary layers. The mesh elements are strategically concentrated at the solid-liquid interfaces to accurately capture the intensified boundary layer effects in these regions, resulting in a higher mesh density where gradients are most significant.

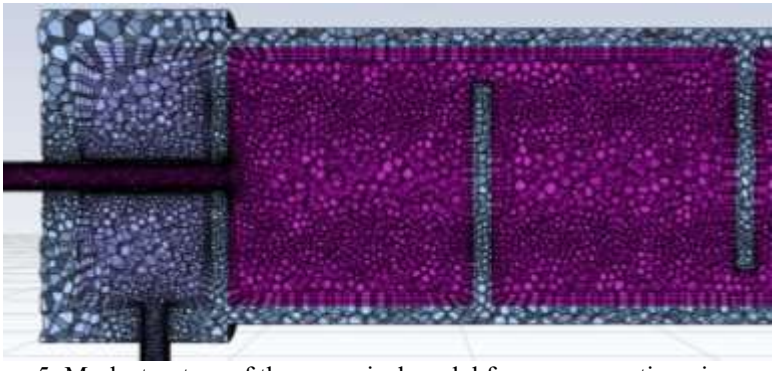
Figure 5: Mesh structure of the numerical model from cross section view

Table 2: The parameters to be used in experimental setup

Parameters	**Constant variables**	**Definition**
Re_{hot} = 200 400 800 1000	$T_{h,in}$=40°C $T_{c,in}$=20°C Re_{cold}=800 L/D =5/80 Φ = 0.2	The dimensionless number characterizing the flow.
$T_{h,in}$= 40°C	$T_{c,in}$=20°C Re_{hot}=400	The temperature of the fluid entering a control

50°C 60°C 80°C	Re_{cold}=800 L/D =5/80 Φ = 0.2	volume or heat exchanger at the hot side, which serves as the reference temperature for evaluating heat transfer.

To ensure accurate and reliable numerical results in ANSYS Fluent, mesh independence was verified by testing various configurations. Simulations were conducted at a hot fluid Re = 200 (40 °C) and a cold fluid Re = 800 (20 °C). Since no significant variation in the hot fluid outlet temperature was observed between Case 6 and Case 7, Case 6 was selected for the subsequent numerical analyses. The mesh independence results are detailed in Table 3 and Figure 6.

Table 3: The parameters to be used in experimental setup

Case No	**Mesh Number**	**Avg. Ort. Quality**	**Avg. Skewness**	**Porous Thickness**	**Porosity Ratio**	**Hot-out**
1	305916	0.740	0.240	5/80	0.5	29.7743
2	424621	0.780	0.205	5/80	0.5	29.7662
3	619793	0.810	0.182	5/80	0.5	29.7587
4	633803	0.830	0.167	5/80	0.5	29.7518
5	741030	0.845	0.158	5/80	0.5	29.7482
6	**891281**	**0.855**	**0.150**	**5/80**	**0.5**	**29.7434**
7	1026722	0.863	0.145	5/80	0.5	29.7414
8	1102365	0.870	0.141	5/80	0.5	29.7425
9	1236887	0.875	0.138	5/80	0.5	29.7425
10	1400255	0.880	0.135	5/80	0.5	29.7425

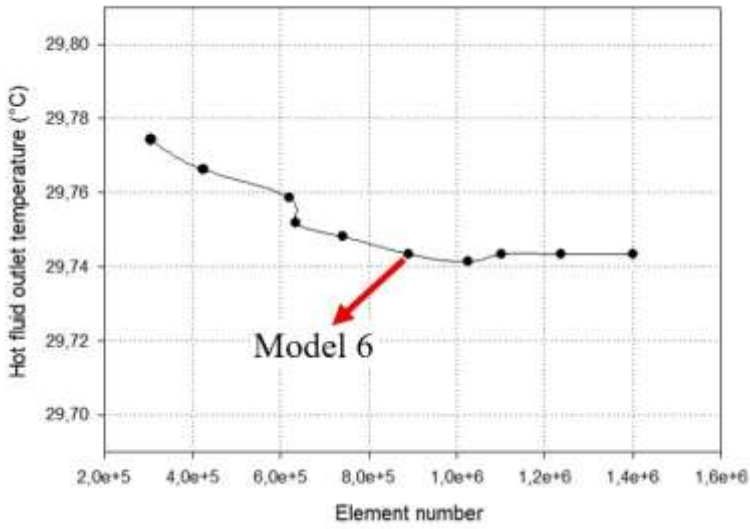

Figure 6: Analyzing of mesh number with respect to outlet temperature of hot fluid

To further ensure numerical accuracy, the mesh-independent model was tested for iteration independence in ANSYS Fluent. Using the Case 6 mesh configuration with a hot fluid Re = 200 (40 °C) and cold fluid Re = 800 (20 °C), various iteration counts were evaluated. Since the hot fluid outlet temperature stabilized after 1200 iterations, this count was selected for all subsequent analyses. The iteration independence results are illustrated in Figure 7.

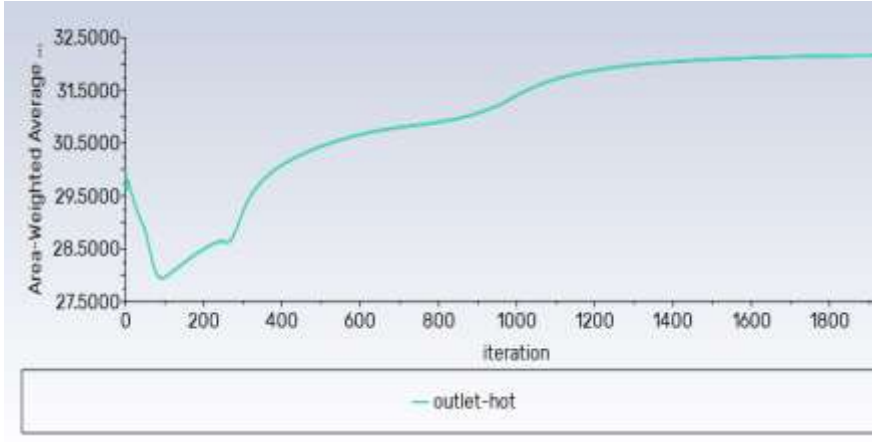

Figure 7: Independence study of iteration number

RESULTS AND DISCUSSION

The analysis focuses on two primary operational parameters: four distinct Reynolds numbers (200, 400, 800, and 1000) and various hot fluid inlet temperatures (40 °C, 50 °C, 60 °C, and 80 °C). Throughout the study, the cold fluid side was maintained at a constant temperature of 20 °C with a fixed Reynolds number of 800. To ensure the reliability of the thermal data, the experimental measurements were compared against a numerical model developed in ANSYS, providing a robust validation of the heat transfer characteristics.

Effect of Reynold Number

The thermal efficacy of the hot fluid at an intake temperature of 40 °C was investigated for various Reynolds numbers (200, 400, 800, and 1000) using both experimental and computational approaches. Experimentally, increasing the Reynolds number from 200 to 400, 400 to 800, and 800 to 1000 enhanced effectiveness by 5.8 %, 6.7 %, and 2.1 %, respectively, resulting in a total increase of 14.6 %. Numerical results showed corresponding enhancements of 3.5 %, 10.1 %, and 4.3 %, totaling a 17.9 % increase across the same range. The experimental data were successfully validated by the numerical findings, as shown in the comparative effectiveness plot in Figure 14. Furthermore, the thermal and flow field developments are visualized through temperature contours in Figure 12 and velocity vector distributions in Figure 13 for Re = 200 and Re = 1000.

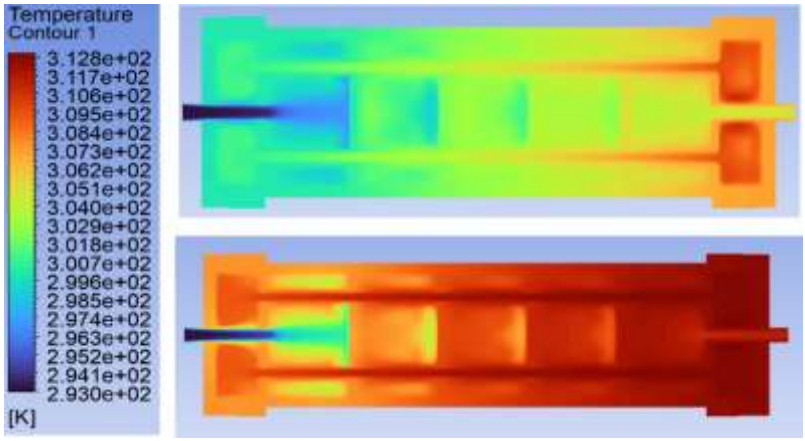

Figure 8: Temperature contours for Re=200 (top) and Re=1000 (bottom)

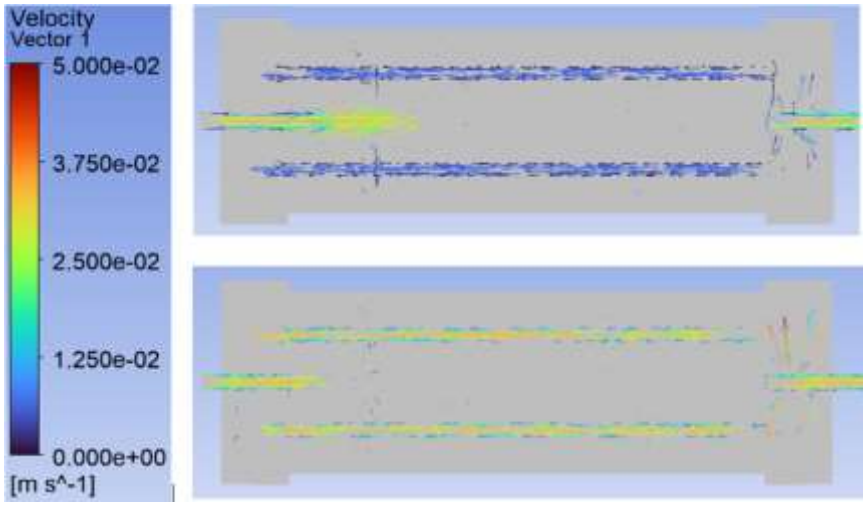

Figure 9: Velocity vector contours for Re=200 (top) and Re=1000 (bottom)

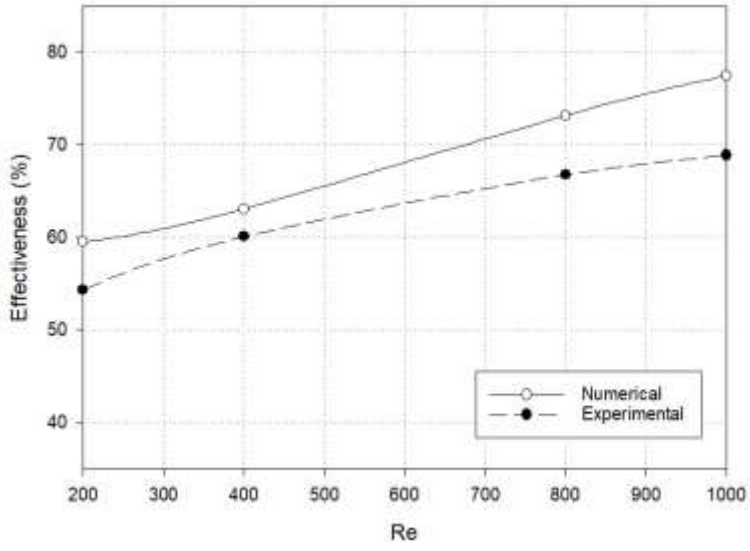

Figure 10: The agreement between experimental and numerical study.

Effect of Inlet Temperature

The thermal efficacy of the hot fluid at Re = 400 was assessed at a variety of input temperatures (40°C, 50°C, 60°C, and 80°C). Increasing the temperature from 40 °C to 50 °C and 50 °C to 60 °C reduced effectiveness by 1.8 % and 1.4 %, respectively, while a further increase to 80 °C resulted in a 0.7 % decrease, leading to a total cumulative reduction of 3.9 %. These trends are illustrated in Figure 13, with corresponding thermal and flow field

developments visualized through temperature contours in Figure 11 and velocity vectors in Figure 12 for the 40°C and 80°C cases.

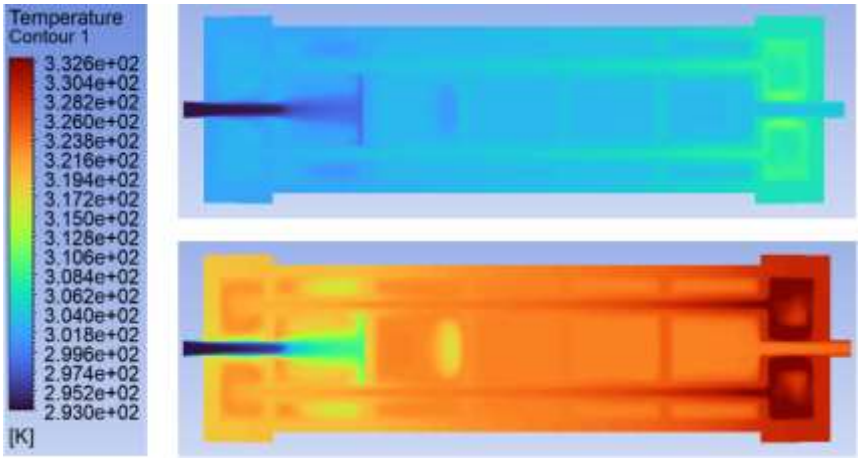

Figure 11: Temperature contours for Th,in=40°C (top) and Th,in=80°C (bottom)

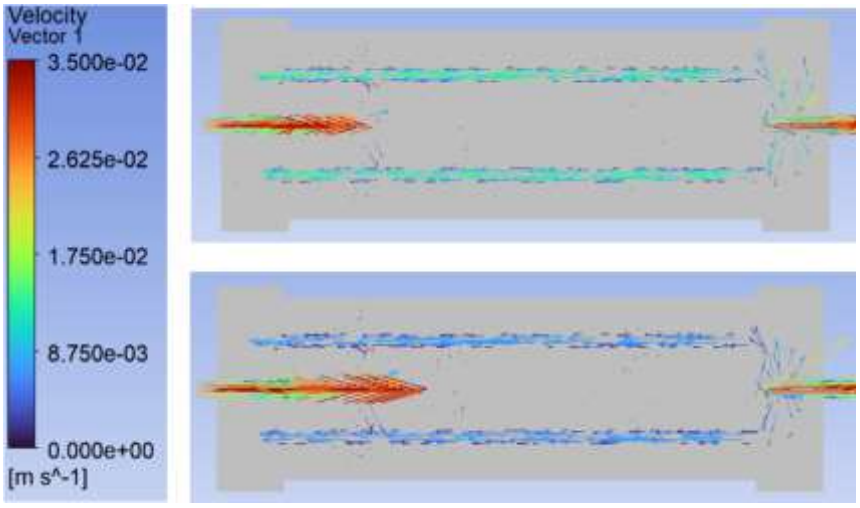

Figure 12: Velocity vector contours for Th,in=40°C (top) and Th,in=80°C (bottom)

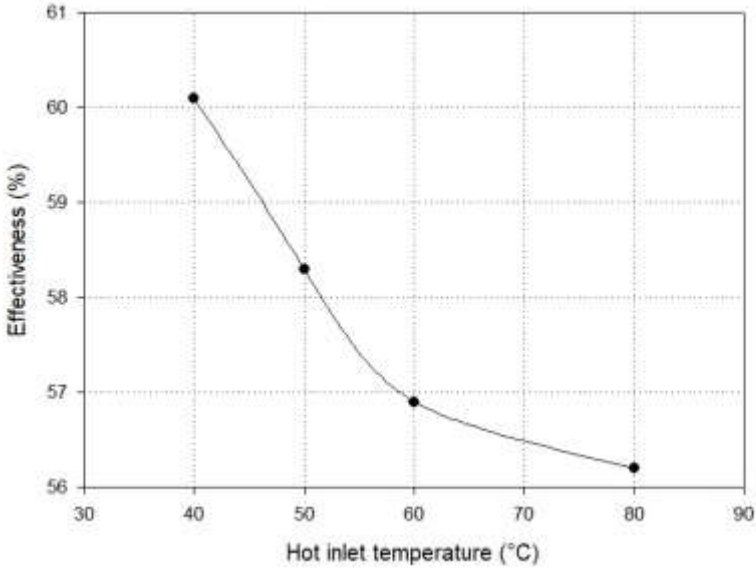

Figure 13: Effect of hot inlet temperature on heat transfer effectiveness

CONCLUSION

This study conducted a numerical assessment of shell and tube heat exchanger performance utilizing intake temperature and Re number as major factors. Using ANSYS Fluent, the study investigated how changes in these factors affect temperature distribution and total heat transfer efficiency. The findings give a complete insight of thermal behavior over the shell side, indicating a strong link between flow conditions and system cooling efficiency. As a result,

1. It was discovered that gradually raising the Reynolds number of the hot fluid from 200 to 1000 while keeping a constant hot intake temperature of 40 °C leads in a 14.6% improvement in total heat transfer efficiency.
2. At a fixed Reynolds number of 400, raising the hot fluid's intake temperature from 40 °C to 80 °C was shown to have a detrimental influence on thermal performance, resulting in a 3.9% drop in total heat transfer efficiency.
3. The numerical model created in this work was tested against experimental data, with a maximum divergence of 8.6%. This close agreement confirms that the numerical results represent the experimental findings with high accuracy and reliability.

4. Optimizing flow conditions improves the heat exchanger's thermal performance. Given that increasing the Reynolds number enhances effectiveness while increasing inlet temperatures only slightly reduces performance, it is argued that determining optimal operating parameters is crucial for enhancing total system efficiency.
5. Future research could focus on investigating the effects of turbulent flow regimes and different tube bundle arrangements to further enhance thermal efficiency. Additionally, the integration of advanced machine learning algorithms for the real-time optimization of operating parameters, such as the Reynolds number and inlet temperature, represents a promising direction for maximizing the sustainable performance of shell and tube heat exchangers.

ABBREVIATIONS

THB	Trefoil-hole baffles
CFD	Plate heat exchangers
CRH	Circular ring with holes baffles
LMTD	Logarithmic mean temperature difference
CSS	Conventional single segmental baffles

REFERENCE

[1] Selbaş, R., Kızılkan, Ö., ve Reppich, M. (2006). A new design approach for shell-and-tube heat exchangers using genetic algorithms from economic point of view. Chemical Engineering and Processing: Process Intensification, 45(4), 268-275.

[2] Sahin, M., Kilic, M., ve Karadag, M. A. (2025). Investigation of heat transfer enhancement using hemispherical turbulators in a double-pipe regenerative heat exchanger with phase change material. Journal of Thermal Analysis and Calorimetry, 150(13), 10249-10265.

[3] Mohammadi, M. H., Abbasi, H. R., Yavarinasab, A., ve Pourrahmani, H. (2020). Thermal optimization of shell and tube heat exchanger using porous baffles. Applied Thermal Engineering, 170, 115005.

[4] Kilic, M., Sahin, M., ve Abdulvahitoglu, A. (2024). A new approach for enhancing the effectiveness of a regenerative heat exchanger by using organic and inorganic phase change material: M. Kilic et al. Journal of Thermal Analysis and Calorimetry, 149(22), 13081-13093.

[5] Arjun, K. S., Gopu, K. B., ve Prasad, S. (2014). Design of shell and tube heat exchanger using computational fluid dynamics tools. Res. J. Eng. Sci.

[6] Hanafi, M. F. I. M., Bahreininejad, A., ve Uddin, N. (2021, Ağustos). Optimization of shell and tube heat exchanger using the water cycle algorithm. In IOP Conference Series: Materials Science and Engineering (Cilt 1173, No. 1, s. 012005). IOP Publishing.

[7] Marzouk, S. A., Abou Al-Sood, M. M., El-Said, E. M., Younes, M. M., ve El-Fakharany, M. K. (2023). A comprehensive review of methods of heat transfer enhancement in shell and tube heat exchangers. Journal of Thermal Analysis and Calorimetry, 148(15), 7539-7578.

[8] Güneş, T., Şahin, M., ve Kılıç, M. (2023). Investigation of the effect of different parameters of phase change materials on heat exchanger performance. Çukurova Üniversitesi Mühendislik Fakültesi Dergisi, 38(4), 1117-1128.

[9] Mukherjee, R. (1998). Effectively design shell-and-tube heat exchangers. Chemical Engineering Progress, 94(2), 21-37.

[10] Ozden, E., ve Tari, I. (2010). Shell side CFD analysis of a small shell-and-tube heat exchanger. Energy conversion and management, 51(5), 1004-1014.

[11] Rashidian, S., ve Tavakoli, M. R. (2017). Using porous media to enhancement of heat transfer in heat exchangers. International Journal of Advanced Engineering, Management and Science, 3(11), 239937.

[12] Dal, A., Şahin, M., ve Kılıç, M. (2023). A thermohydrodynamic performance analysis of a fluid film bearing considering with geometrical parameters. Journal of Thermal Engineering, 9(6), 1604-1617.

[13] Abbasi, H. R., Sedeh, E. S., Pourrahmani, H., ve Mohammadi, M. H. (2020). Shape optimization of segmental porous baffles for enhanced thermo-hydraulic performance of shell-and-tube heat exchanger. Applied Thermal Engineering, 180, 115835.

[14] Tian, H., Zhao, T., Shi, L., Chen, T., Ma, X., Zhang, H., ve Shu, G. (2020). Assessment and optimization of exhaust gas heat exchanger with porous baffles and porous fins. Applied Thermal Engineering, 178, 115446.

[15] Naqvi, S. M. A., ve Wang, Q. (2021). Performance enhancement of shell–tube heat exchanger by clamping anti-vibration baffles with porous media involvement. Heat Transfer Engineering, 42(18), 1523-1538.

[16] Rad, S. E., Afshin, H., ve Farhanieh, B. (2015). Heat transfer enhancement in shell-and-tube heat exchangers using porous media. Heat Transfer Engineering, 36(3), 262-277.

[17] Marzouk, S. A., Abou Al-Sood, M. M., El-Fakharany, M. K., ve El-Said, E. M. (2022). A comparative numerical study of shell and multi-tube heat exchanger performance with different baffles configurations. International Journal of Thermal Sciences, 179, 107655.

[18] You, Y., Fan, A., Lai, X., Huang, S., ve Liu, W. (2013). Experimental and numerical investigations of shell-side thermo-hydraulic performances for shell-and-tube heat exchanger with trefoil-hole baffles. Applied Thermal Engineering, 50(1), 950-956.

Experimental and Numerical Investigation of Porous Structural Parameters and Nanofluid Types on the Thermal Performance of Shell and Tube Heat Exchangers

Mahir ŞAHİN[1]

Mustafa KILIÇ[2]

1- Res. Asst.; Adana Alparslan Türkeş Bilim ve Teknoloji Üniversitesi Makine Mühendisliği Bölümü. msahin@atu.edu.tr ORCID No: 0000-0002-9565-9160

2- Prof. Dr.; Adana Alparslan Türkeş Bilim ve Teknoloji Üniversitesi Makine Mühendisliği Bölümü. mkilic@atu.edu.tr ORCID No: 0000-0002-8006-149X

ABSTRACT

This study assesses the thermal performance improvement of shell and tube heat exchangers by optimizing porous structure features and utilizing different nanofluids for laminar flow conditions. The study explicitly analyzes the effects of porosity ratios ranging from 0.2 to 0.8 and porous layer thicknesses ranging from 5/80 to 20/80 on the heat transmission efficacy of Cu-H_2O, CuO-H_2O, and Al_2O_3-H_2O nanofluids. Experimental data, validated by a numerical model, indicate that structural modifications to the tubes significantly influence efficiency; for instance, at Re = 400, decreasing the porosity from 0.8 to 0.2 and reducing the porous thickness from 20/80 to 5/80 results in effectiveness increases of 0.1 % and 0.6 %, respectively. Furthermore, the comparative analysis of nanofluids reveals that Al_2O_3–H_2O offers the most significant thermal benefits, achieving a 17.1 % increase in effectiveness as the Reynolds number rises to 1000, thereby outperforming Cu–H_2O at 15.9 % and CuO–H_2O at 15.7 %. These results provide critical insights for engineering high-efficiency heat exchange systems by demonstrating that the interactions between porous media and advanced nanofluid compositions leads to superior heat transfer performance.

Keywords – Heat transfer, porous media, porosity ratio, heat exchanger.

INTRODUCTION

Thermal exchange between two separate fluid streams is usually aided by the sturdy construction of heat exchange systems made up of a bundle of internal conduits encased within a cylindrical tank. In this design, the medium traversing the interior of the conduits is designated as the tube-side fluid, whereas the medium occupying the surrounding space within the vessel is identified as the shell-side fluid [1-4]. The inherent structural integrity of this setup makes it exceptionally suitable for demanding industrial environments characterized by high-pressure and high-temperature conditions. Depending on the desired thermal performance, these systems can be configured in parallel-flow or counter-flow arrangements, with the latter often preferred for maximizing the logarithmic mean temperature difference and overall heat transfer effectiveness [5-7]. Owing to their versatility and reliability, these units are indispensable in global industrial sectors, including power plants, petrochemical processing, oil and gas refineries, and large-scale HVAC systems, where they manage critical heating and cooling requirements across diverse thermal cycles [8,9].

The shell, typically fabricated from high-strength, corrosion-resistant materials, is designed to house the shell-side fluid and minimize bypass flow through precise tolerances [10]. Internally, the tube bundle consists of

parallel conduits made of stainless steel, copper, or titanium, which are hermetically sealed to the tube sheets via expansion or welding to prevent leakage. To optimize thermal performance, baffles are strategically positioned within the shell to induce turbulence, increase fluid velocity, and minimize fouling, while simultaneously providing vital structural support against tube vibration and sagging [10,11]. Furthermore, the selection of either bonnet-type or removable-cover heads is dictated by the specific maintenance requirements and the necessity for internal access. Collectively, these components must be carefully engineered to withstand the operational stresses of high-temperature and high-pressure industrial applications [12].

Heat transfer occurs as the warmer medium yields energy to the cooler one, with the shell and tube sections serving as the primary flow domains. For optimal performance, the higher-pressure fluid is typically assigned to the tube side, as the conduits are structurally superior for handling pressure differentials, while the lower-pressure or more viscous fluid occupies the shell volume. This strategic fluid allocation, combined with the orientation of inlets and outlets, ensures maximized conductive heat exchange across the internal surfaces [13,14].

Recent advancements in heat exchanger technology have extensively explored baffle modifications and advanced materials to mitigate pressure drops and amplify thermal efficiency. Studies by Bichkhar et al. [15] and Wen et al. [16] demonstrated that transitioning from segmental to helical or ladder-type fold baffles can reduce pressure loss while increasing heat transfer coefficients by up to 32.6 %. Further innovations, such as the staggered baffle designs proposed by Wang et al. [17] and triple-layer flower baffles by Chen et al. [18], have shown that complex geometries effectively transition flow patterns to favor intensified thermal exchange. Notably, the integration of metal foam baffles has been found to decrease pressure drop by 12.9 % while simultaneously expanding the inlet-outlet temperature differential by 31.0 % [19].

Beyond geometric alterations, the synergy between porous media and nanofluids represents a frontier in high-performance thermal management. Research indicates that porous materials provide a more substantial influence on heat transfer enhancement than simply increasing the Reynolds number [20]. Investigations into nanofluid behavior have shown that Al_2O_3 and CuO particles significantly improve convective heat transfer, with the specific morphology of the nanoparticles—such as platelet shapes—yielding the highest thermal rates [21]. Furthermore, the interplay between the Darcy number and nanoparticle concentration is critical, as higher permeability in porous zones combined with optimized volume fractions can drastically lower heat source temperatures [22]. Collectively, these findings underscore that the strategic combination of porous architectures and specialized nanofluids, such as those evaluated in the present study, is essential for overcoming the limitations of conventional shell and tube designs.

While previous research has extensively documented the general benefits of either porous inserts or nanofluids in thermal systems, there remains a significant gap in understanding their combined impact within the specific architecture of this system. This study distinguishes itself by providing a comprehensive investigation into the synergistic effects of structural porous parameters and advanced fluid thermophysics. Specifically, the research uniquely evaluates the simultaneous influence of varying porosity ratios (0.2 to 0.8) and porous layer thicknesses (5/80 to 20/80) in conjunction with different nanofluid types (Cu-H_2O, CuO-H_2O, and Al_2O_3-H_2O). By systematically comparing these integrated configurations against conventional systems, the present work offers a novel framework for optimizing heat exchanger performance through precise geometric and fluidic adjustments. Consequently, these findings contribute a new perspective to the specialized design of high-flux thermal management systems, filling a critical void in the current literature regarding the optimization of porous-nanofluid interactions.

MATERIALS AND METHODS

The methodology of this study is based on a combined approach using experimental data and numerical simulations to analyze the heat exchanger performance. The experimental setup was configured to measure temperature and flow parameters under laminar conditions, specifically focusing on the integration of porous structures and the use of Al_2O_3-H_2O, Cu-H_2O, and CuO-H_2O nanofluids. This dual-method approach allows for the validation of the thermal results and provides a consistent basis for evaluating how different porosity ratios, porous layer thicknesses, and nanofluid types affect the overall system effectiveness.

Experimental Setup

Figure 1 depicts the structural design of the shell and tube heat exchanger, which has a single shell pass and six tube passes grouped in a circular pattern. The internal tubes are 350 mm long, 7 mm (inner) and 8 mm (outer) in diameter, and made of 304 stainless steel. The shell is composed of polycarbonate, with a 70 mm inner diameter and an 80 mm outer diameter. Inside the shell, four stainless steel baffles with a 20% cut ratio are spaced 70 mm apart to guide fluid flow over the tube bundle.

Figure 1: Shell and tube heat exchanger

The heat exchange process takes place in a counterflow configuration, with the tube side transporting the hot pure water and the shell side handling the cold water flow. To maintain laminar flow conditions, the heated fluid is kept within a 200–1000 Reynolds number range. Thermal conditions are set with an intake temperature of 40°C for the hot fluid and 20°C for the cool fluid. Furthermore, a stable heat supply is maintained by resistors connected to a power control unit, which ensures a constant heat flux throughout the experimental runs.

Figure 2: Flow control unit and data logging computer

Flow rates, as well as intake and output temperatures, were recorded throughout the trials. These operational parameters were tracked and stored using a data logging system, the configuration of which is shown in Figure 2.

Numerical Model

The numerical simulation duplicates the experimental geometry, which includes a 350 mm polycarbonate shell and six stainless steel tubes. Based on mass, momentum, and energy conservation, the solver employs Equations 1-5 in cartesian coordinates, beginning with the continuity equation to assure mass conservation over the flow field.

$$\frac{\partial u}{\partial x}+\frac{\partial v}{\partial y}+\frac{\partial w}{\partial z}=0 \quad (1)$$

The momentum equation:

$$u\frac{\partial u}{\partial x}+v\frac{\partial u}{\partial y}+w\frac{\partial u}{\partial z}=-\frac{1}{\rho}\frac{\partial p}{\partial x}+v\left[\frac{\partial^2 u}{\partial x^2}+\frac{\partial^2 u}{\partial y^2}+\frac{\partial^2 u}{\partial z^2}\right] \quad (2)$$

Momentum equation in the y-direction

$$u\frac{\partial v}{\partial x}+v\frac{\partial v}{\partial y}+w\frac{\partial v}{\partial z}=-\frac{1}{\rho}\frac{\partial p}{\partial y}+v\left[\frac{\partial^2 v}{\partial x^2}+\frac{\partial^2 v}{\partial y^2}+\frac{\partial^2 v}{\partial z^2}\right] \quad (3)$$

Momentum equation in the z-direction

$$u\frac{\partial w}{\partial x}+v\frac{\partial w}{\partial y}+w\frac{\partial w}{\partial z}=-\frac{1}{\rho}\frac{\partial p}{\partial z}+v\left[\frac{\partial^2 w}{\partial x^2}+\frac{\partial^2 w}{\partial y^2}+\frac{\partial^2 w}{\partial z^2}\right] \quad (4)$$

The energy equation:

$$u\frac{\partial T}{\partial x}+v\frac{\partial T}{\partial y}+w\frac{\partial T}{\partial z}=\alpha\left[\frac{\partial^2 T}{\partial x^2}+\frac{\partial^2 T}{\partial y^2}+\frac{\partial^2 T}{\partial z^2}\right] \quad (5)$$

The dimensionless number for Re (Reynolds) are described by the following general equation:

$$Re=\frac{\rho VD}{\mu} \quad (6)$$

The temperature differential that varies logarithmically in the heat exchanger may be calculated as:

$$\Delta T_1=T_{h,in}-T_{c,out} \quad (7)$$

$$\Delta T_2=T_{h,out}-T_{c,in} \quad (8)$$

$$\Delta T_{lm}=\frac{\Delta T_1-\Delta T_2}{\ln(\Delta T_1/\Delta T_2)} \quad (9)$$

Specific heat capacity:

$$C_c=\dot{m}_c c_{pc} \quad (10)$$

$$C_h=\dot{m}_h c_{ph} \quad (11)$$

Maximum temperature;

$$\Delta T_{max} = T_{h,in} - T_{c,in} \tag{12}$$

maximum heat transfer;

$$\dot{Q}_{max} = C_{min} \Delta T_{max} \tag{13}$$

Effectiveness;

$$\varepsilon = \frac{\dot{Q}_{act}}{\dot{Q}_{max}} = \frac{Actual\ heat\ transfer\ amount}{Maximum\ heat\ transfer\ amount} \tag{14}$$

Figure 3 depicts the numerical geometry that duplicates the physical dimensions of the exchanger, which has a 350-mm-long shell and tube. The assembly consists of a shell with an inner diameter of 70 mm and an outer diameter of 80 mm that holds a bundle of circularly arranged tubes. To accommodate the experimental parameters, each tube has an inner diameter of 7 mm and an outside diameter of 8 mm.

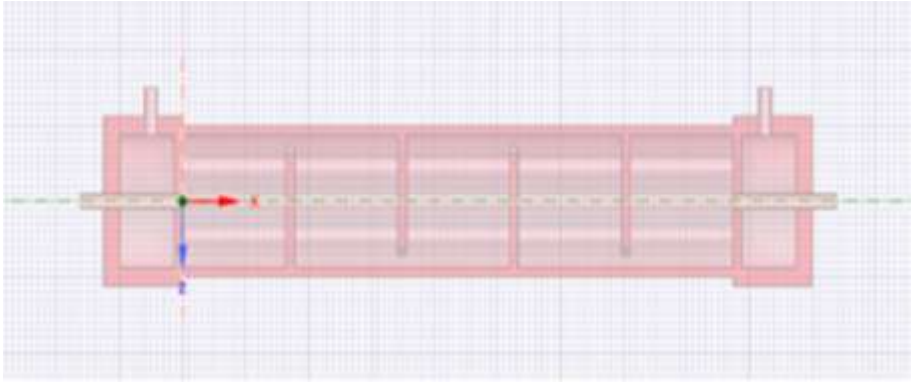

Figure 3: Numerical model geometry generated in SpaceClaim

As illustrated in Figure 4, the numerical domain incorporates three distinct boundary layers to ensure computational accuracy. Mesh elements are strategically concentrated at the solid-liquid interfaces to capture the steep thermal and velocity gradients in these regions. This localized refinement results in a higher mesh density at the interfaces, allowing for a more precise analysis of the boundary layer effects.

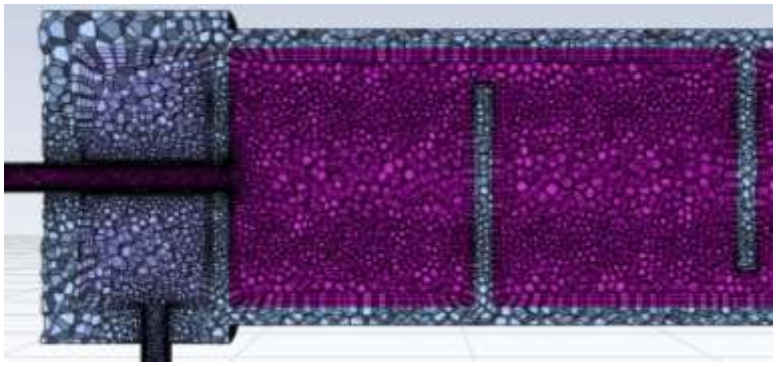

Figure 4: Mesh structure of the numerical model from cross section view

Table 1: The parameters to be used in experimental setup

Parameters	**Constant variables**	**Definition**
L/D = 5/80 10/80 15/80 20/80	$T_{h,in}$=40°C $T_{c,in}$=20°C Re_{hot}=400 Re_{cold}=800 Φ = 0.2	The diameter of the porous structure inside the tube divided by the diameter of the tube itself.
Φ = 0.2 0.4 0.6 0.8	$T_{h,in}$= 40°C $T_{c,in}$= 20°C Re_{hot}= 400 Re_{cold}= 800 L/D =5/80	The ratio of the volume of voids (empty spaces) in a porous medium to its total volume.
Nanofluids: Al_2O_3-H_2O Cu-H_2O CuO-H_2O	$T_{h,in}$=40°C $T_{c,in}$=20°C Re_{cold}=800 L/D =5/80 Φ = 0.2	The fluid containing a modest amount of suspended nanoparticles (usually less than 100 nm in size) used to improve the fluid's thermal characteristics.

The simulations for this validation were performed at a hot fluid Reynolds number of 200 (40 °C) and a cold fluid Reynolds number of 800 (20 °C). Since the hot fluid outlet temperature showed no significant variation between Case 6 and Case 7, Case 6 was selected as the optimal mesh density for all subsequent analyses. Detailed results of the mesh independence study are presented in Table 2 and Figure 5.

Table 2: The parameters to be used in experimental setup

Case No	Mesh Number	Avg. Ort. Quality	Avg. Skewness	Porous Thickness	Porosity Ratio	Hot-out
1	305916	0.740	0.240	5/80	0.5	29.7743
2	424621	0.780	0.205	5/80	0.5	29.7662
3	619793	0.810	0.182	5/80	0.5	29.7587
4	633803	0.830	0.167	5/80	0.5	29.7518
5	741030	0.845	0.158	5/80	0.5	29.7482
6	**891281**	**0.855**	**0.150**	**5/80**	**0.5**	**29.7434**
7	1026722	0.863	0.145	5/80	0.5	29.7414
8	1102365	0.870	0.141	5/80	0.5	29.7425
9	1236887	0.875	0.138	5/80	0.5	29.7425
10	1400255	0.880	0.135	5/80	0.5	29.7425

Verify mesh independence was followed by an iteration independence test within ANSYS Fluent to ensure numerical precision. Using the Case 6 mesh configuration at a hot fluid Reynolds number of 200 (40 °C) and a cold fluid Reynolds number of 800 (20 °C), different iteration counts were evaluated.

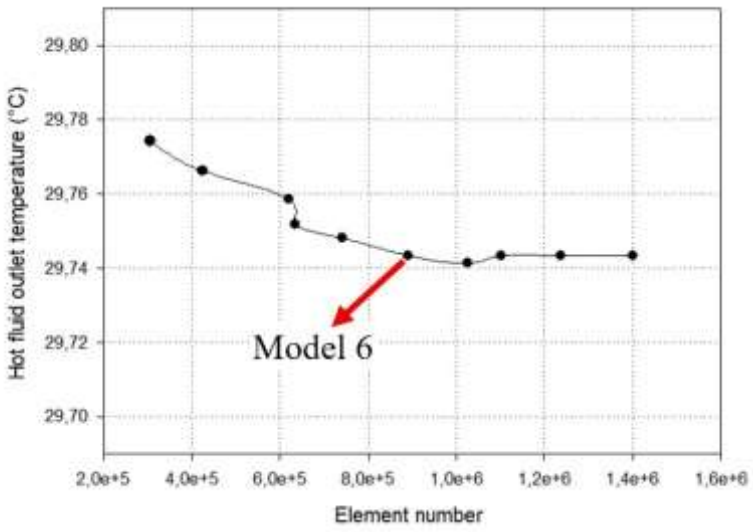

Figure 5: Analyzing of element number

The hot fluid outlet temperature stabilized after 1200 iterations, and this value was used for all further simulations. Figure 6 shows the results from the iteration independence research.

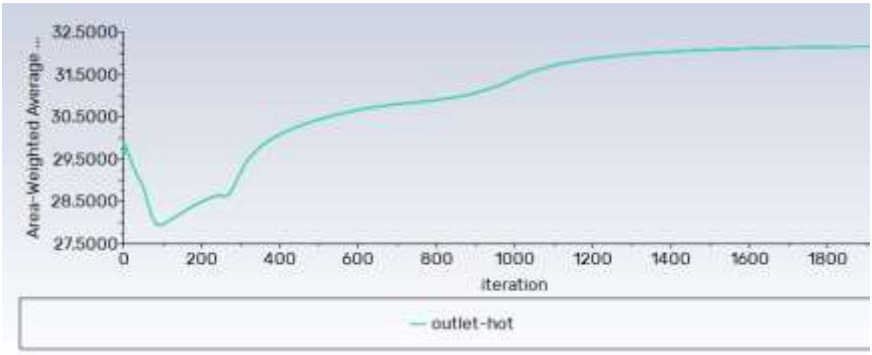

Figure 6: Independence study of iteration number

RESULTS AND DISCUSSION

This study looks at the effects of porous layer integration and the use of Al_2O_3, Cu, and CuO nanofluids on the thermal performance of a shell and tube heat exchanger. The analysis focuses on key parameters such as temperature distribution, heat transfer rates, and overall system effectiveness. The influence of porous media thickness and porosity ratios on flow behavior and thermal enhancement is evaluated by comparing experimental data with numerical simulations. These results demonstrate how the combination of modified surface structures and advanced cooling fluids determines the final efficiency of the heat exchanger.

Effect of Porosity Ratio

The thermal effectiveness of the hot fluid at 40 °C and Re = 400 was analyzed across different porosity ratios (0.2, 0.4, 0.6, and 0.8). An increase in porosity from 0.2 to 0.4 resulted in a 0.1% drop in efficacy, but subsequent increases to 0.8 produced no meaningful difference. This minimal overall reduction of 0.1 % is illustrated in Figure 7, with corresponding temperature and velocity vector contours for $\Phi = 0.2$ and $\Phi = 0.8$ provided in Figures 8 and 9.

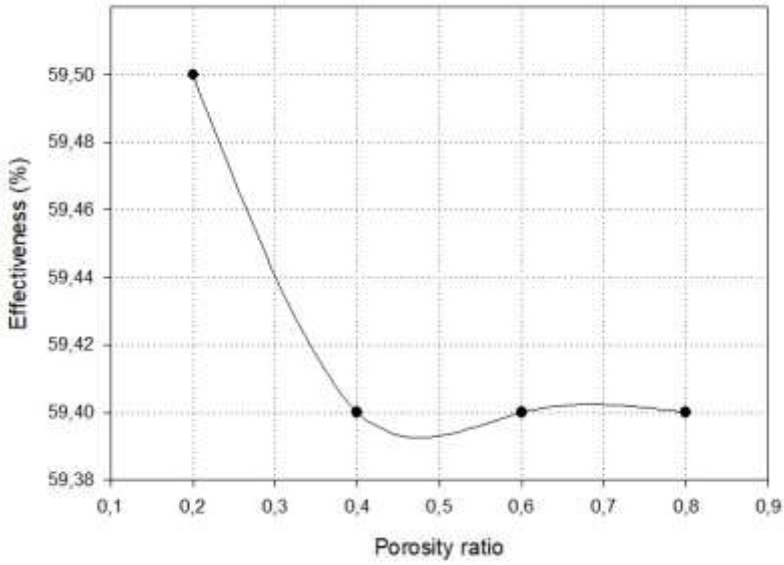

Figure 7: Effect of Porosity ratio on heat transfer effectiveness

Figure 15 shows temperature contours for Φ = 0.2 (top) and Φ = 0.8 (bottom), indicating that raising the porosity ratio has minimal influence on the system's thermal distribution. Lower porosity (Φ = 0.2) boosts heat conduction but also increases flow resistance, thickening the velocity boundary layer while maintaining thermal boundary layer resistance. The nearly identical spatial progression from the cold inlet to the heated zones in both cases suggests that convective heat transfer mechanisms become dominant beyond a certain threshold, causing the thermal resistance contribution of the porous matrix to reach a plateau.

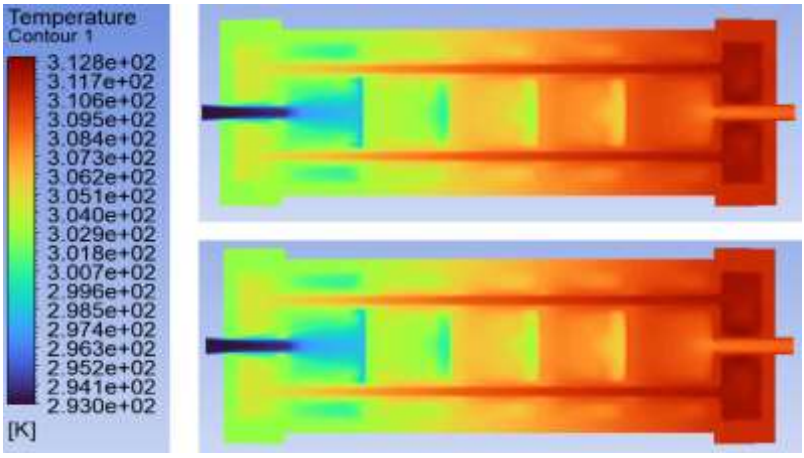

Figure 8: Temperature contours for Φ=0.2 (top) and Φ=0.8 (bottom)

The velocity vectors in Figure 16 show nearly identical flow patterns for both Φ = 0.2 and Φ = 0.8, confirming that the porosity ratio has a negligible effect on the primary flow field. The fluid maintains a consistent velocity profile near the tube surfaces, indicating that the velocity boundary layer thickness remains unchanged despite the varying void fraction.

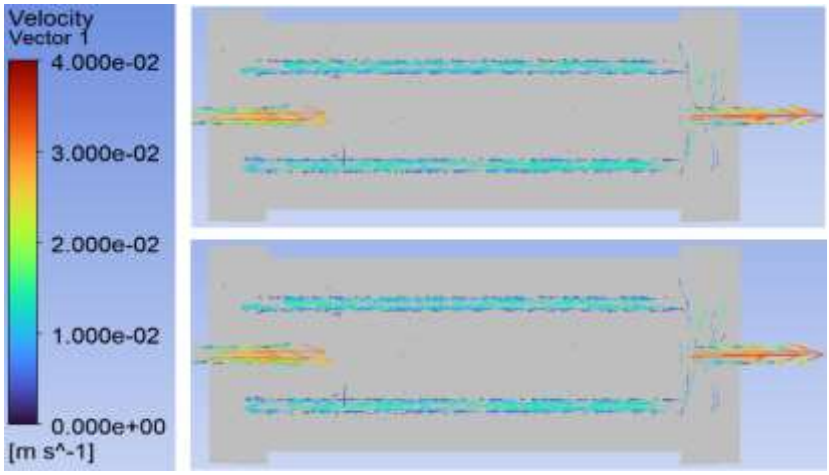

Figure 9: Velocity vector contours for Φ=0.2 (top) and Φ=0.8 (bottom)

This stability in the flow dynamics explains the marginal 0.1% change in effectiveness, as the convective transport capacity is primarily dictated by the shell geometry rather than the porous matrix density.

Effect of Porous Thickness

The heat transfer effectiveness of the hot fluid at an inlet temperature of 40 °C and Re = 400 was evaluated for a range of porous thicknesses, specifically 5/80, 10/80, 15/80, and 20/80. The findings suggest that increasing the porosity thickness from 5/80 to 10/80 decreased effectiveness by 0.3%, while increasing from 10/80 to 15/80 resulted in a 0.1% decrease. Continuing this trend, an increase from 15/80 to 20/80 further diminished the effectiveness by 0.2 %. Consequently, the heat transfer effectiveness consistently declined as the porous thickness rose from 5/80 to 20/80, culminating in a total observed decrease of 0.6 %. The thermal profiles for the L/D = 5/80 and L/D = 20/80 cases are visualized through the temperature contours in Figure 10, while the corresponding flow field characteristics are shown via velocity vector contours in Figure 11.

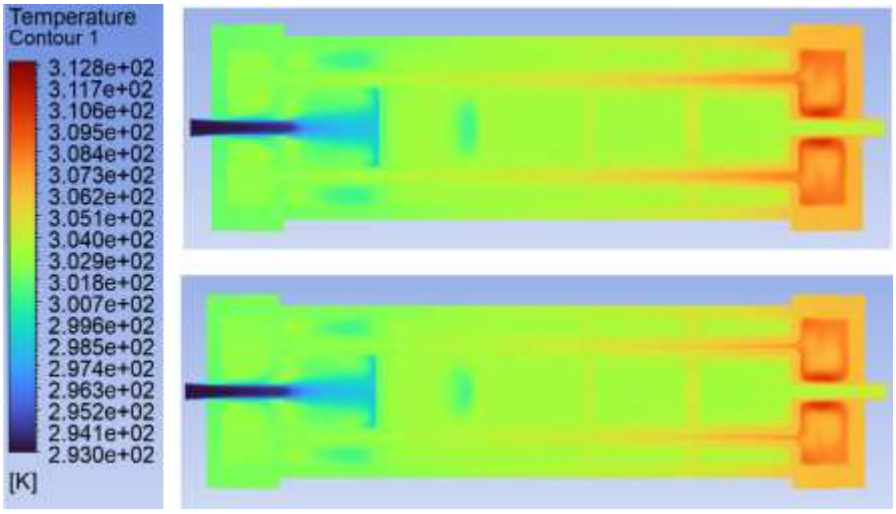

Figure 10: Temperature contours for L/D=5/80 (top) and L/D=20/80 (bottom)

The temperature contours for L/D = 5/80 (top) and L/D = 20/80 (bottom) in Figure 10 show that increasing the porous layer thickness promotes a more uniform temperature distribution. The larger porous matrix forces the fluid to make longer contact with the increased surface area, thus thinning the thermal boundary layer and lowering localized thermal resistance. This leads to improved heat extraction from the tubes, as evidenced by the broader expansion of heated zones toward the outlet in the L/D = 20/80 configuration.

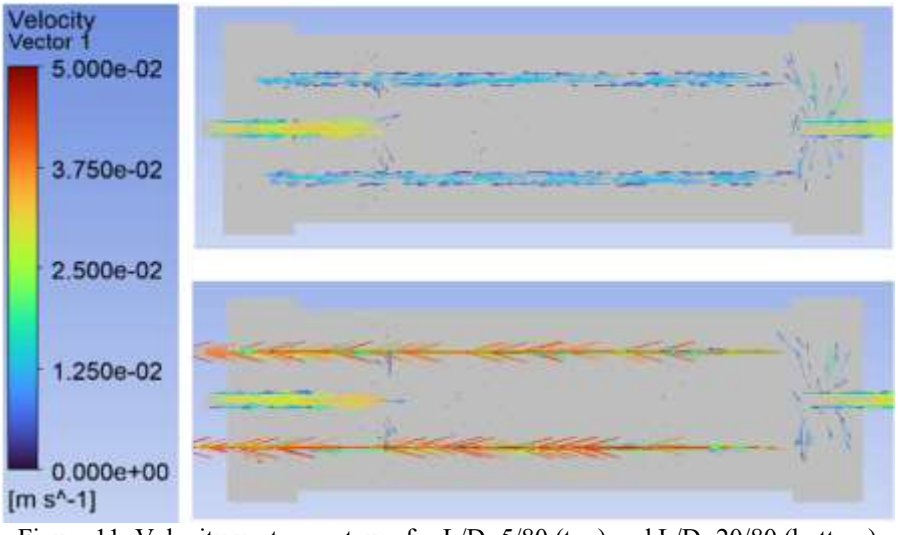

Figure 11: Velocity vector contours for L/D=5/80 (top) and L/D=20/80 (bottom)

The velocity vectors in Figure 11 show that increasing the porous layer thickness to L/D = 20/80 leads to higher velocity magnitudes near the tube surfaces. This acceleration within the thicker porous matrix promotes more intense fluid-solid interaction and thins the velocity boundary layer. The resulting enhancement in convective transport explains the improved thermal effectiveness, as the fluid is forced to interact more thoroughly with the expanded surface area.

Effect of Nanofluid Types

The thermal performance of various nanofluid types, specifically Cu–H_2O, CuO–H_2O, and Al_2O_3–H_2O with a 0.02 particle volume fraction, was analyzed at 40 °C across Reynolds numbers ranging from 200 to 1000 and compared against pure water as the reference fluid. Increasing the Reynolds number from 200 to 1000 enhanced heat transfer efficacy by 15.9% for Cu-H_2O, 15.7% for CuO-H_2O, and 17.1% for Al_2O_3-H_2O (Figure 13).

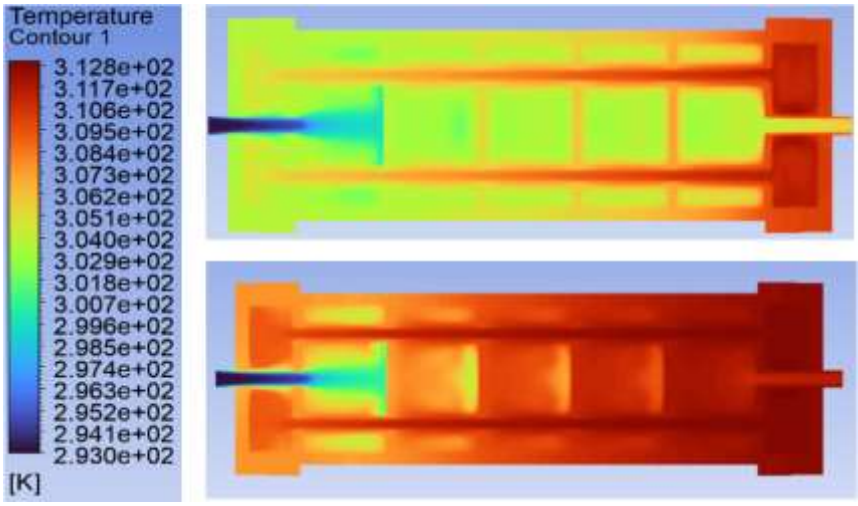

Figure 12: The temperature contours at Re=1000 for Cu-H_2O and H_2O

Reynolds number of 200, the nanofluids showed enhanced effectiveness relative to pure water by 3.5 % for CuO–H_2O, 3.4 % for Cu–H_2O, and 2.1 % for Al_2O_3–H_2O. When the Reynolds number reached 1000, these improvements compared to pure water were measured at 4.7 % for Cu–H_2O and 4.6 % for both CuO–H_2O and Al_2O_3–H_2O. The thermal distribution patterns at Re = 1000 for both Cu–H_2O and pure water are illustrated in the temperature contours provided in Figure 12.

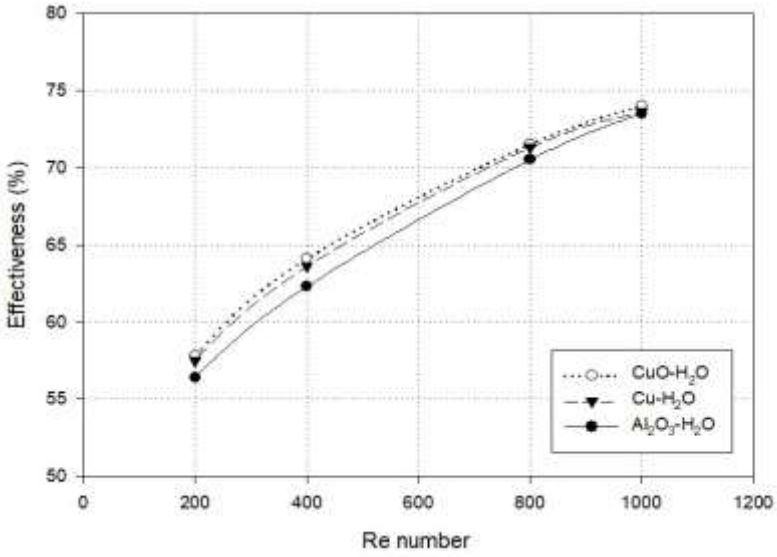

Figure 13: Effect of nanofluid types on heat transfer effectiveness

The high thermal conductivity of Cu nanoparticles facilitates rapid heat diffusion, effectively thinning the thermal boundary layer. This results in the broader dark red zones seen in the nanofluid case, confirming superior effectiveness in extracting heat from the tubes compared to the base fluid.

CONCLUSION

This study focused at the thermal performance of a shell and tube heat exchanger with porous layers (L/D ratios of 5/80, 10/80, 15/80, and 20/80) and nanofluids (Cu, Al2O3, and CuO at 1% concentrations) for Re = 500 to 2000. To determine the best configuration for improved thermal performance, numerical simulations were used to examine the effects of these factors on velocity fields, temperature distributions, and heat transfer performance. As a result:

1. At a Reynolds number of 400, a constant hot fluid temperature of 40°C, and a porous thickness ratio of 5/80, lowering the porosity ratio from 0.8 to 0.2 improves heat transfer efficacy, especially in the 0.4 to 0.2 region. Overall, decreasing the porosity ratio from 0.8 to 0.2 yielded a marginal 0.1 % increase in effectiveness.
2. When the Reynolds number was 400, the hot fluid temperature was 40°C, and the porosity ratio was 0.2, increasing the porous thickness ratio from 5/80 to 20/80 reduced heat transmission efficacy by 0.6%.

3. At 40°C, the Al2O3-H2O nanofluid outperformed the other nanofluids tested (Cu-H2O, CuO-H2O, and Al2O3-H2O) in the shell and tube heat exchanger. As the Reynolds number increased from 200 to 1000, this particular nanofluid showed the greatest increase in heat transfer performance, at a rate of 17.1%.
4. The numerical model created in this work was tested against experimental data, with a maximum divergence of 8.6%. This tight agreement demonstrates that the numerical results accurately and reliably reflect the experimental findings.

ABBREVIATIONS

HX	Heat exchanger
MWCNT	Multiwalled carbon nanotube
CFD	Plate heat exchangers
CRH	Circular ring with holes baffles
LMTD	Logarithmic mean temperature difference
CSS	Conventional single segmental baffles
NF	Nanofluid
NTU	Number of transfer unit

REFERENCE

[1] Dong, C., Chen, Y. P., and Wu, J. F. (2015). Flow and heat transfer performances of helical baffle heat exchangers with different baffle configurations. Applied Thermal Engineering, 80, 328-338.

[2] Khalaf, A. F., Basem, A., Hussein, H. Q., Jasim, A. K., Hammoodi, K. A., Al-Tajer, A. M., ... and Flayyih, M. A. (2022). Improvement of Heat Transfer by Using Porous Media, Nanofluid, and Fins: A Review. International Journal of Heat and Technology, 40(2).

[3] Hassan, M., Marin, M., Alsharif, A., and Ellahi, R. (2018). Convective heat transfer flow of nanofluid in a porous medium over wavy surface. Physics Letters A, 382(38), 2749-2753.

[4] Kılıç, M., Şahin, M., Demircan, T., Kilinc, Z., & Ullah, A. (2023). Numerical investigation of cooling an industrial roller by using swirling jets. El-Cezeri, 10(1), 147-159.

[5] Bourantas, G. C., Skouras, E. D., Loukopoulos, V. C., and Burganos, V. N. (2014). Heat transfer and natural convection of nanofluids in porous media. European Journal of Mechanics-B/Fluids, 43, 45-56.

[6] Barnoon, P., and Toghraie, D. (2018). Numerical investigation of laminar flow and heat transfer of non-Newtonian nanofluid within a porous medium. Powder Technology, 325, 78-91.

[7] Dal, A., Şahin, M., & Kılıç, M. (2023). A thermohydrodynamic performance analysis of a fluid film bearing considering with geometrical parameters. Journal of Thermal Engineering, 9(6), 1604-1617.

[8] Alihosseini, S., and Jafari, A. (2020). The effect of porous medium configuration on nanofluid heat transfer. Applied Nanoscience, 10, 895-906.

[9] Albojamal, A., and Vafai, K. (2020). Analysis of particle deposition of nanofluid flow through porous media. International Journal of Heat and Mass Transfer, 161, 120227.

[10] Sheikholeslami, M. (2018). CuO-water nanofluid flow due to magnetic field inside a porous media considering Brownian motion. Journal of Molecular Liquids, 249, 921-929.

[11] Sahin, M., Kilic, M., & Karadag, M. A. (2025). Investigation of heat transfer enhancement using hemispherical turbulators in a double-pipe regenerative heat exchanger with phase change material. Journal of Thermal Analysis and Calorimetry, 150(13), 10249-10265.

[12] Kapustenko, P., Kravanja, Z., Plazl, I., Varbanov, P. S., Bertok, B., Arsenyeva, O., ... & Pan, T. (2026). Thermal-hydraulic performance of heat exchanger mini-and micro-channels with single-phase flows. A comprehensive review and a comparative study. Renewable and Sustainable Energy Reviews, 230, 116722.

[13] Wang, J., Ding, Y., Liang, G., Li, X., Luo, Y., Hou, P., ... & Zhao, J. (2026). A review on direct expansion ground heat exchanger: Experimental advancement, system instability, and heat transfer model. Renewable and Sustainable Energy Reviews, 226, 116227.

[14] Ma, W., Hu, Z., Zhang, H., El-Mesery, H. S., Workneh, T. S., & Wang, Z. (2026). A review of thermal-hydraulic performance in airfoil fin printed circuit heat exchangers. Renewable and Sustainable Energy Reviews, 226, 116349.

[15] Bichkar, P., Dandgaval, O., Dalvi, P., Godase, R., and Dey, T. (2018). Study of shell and tube heat exchanger with the effect of types of baffles. Procedia Manufacturing, 20, 195-200.

[16] Wen, J., Yang, H., Wang, S., Xue, Y., and Tong, X. (2015). Experimental investigation on performance comparison for shell-and-tube heat exchangers with different baffles. International Journal of Heat and Mass Transfer, 84, 990-997.

[17] Wang, X., Zheng, N., Liu, Z., and Liu, W. (2018). Numerical analysis and optimization study on shell-side performances of a shell and tube heat

exchanger with staggered baffles. International Journal of Heat and Mass Transfer, 124, 247-259.

[18] Chen, J., Zhao, P., Wang, Q., and Zeng, M. (2021). Experimental investigation of shell-side performance and optimal design of shell-and-tube heat exchanger with different flower baffles. Heat Transfer Engineering, 42(7), 613-626.

[19] Nie, C., Chen, Z., Liu, X., Li, H., Liu, J., and Rao, Z. (2024). Design of metal foam baffle to enhance the thermal-hydraulic performance of shell and tube heat exchanger. International Communications in Heat and Mass Transfer, 159, 108005.

[20] Cao, Y., Ke, H., Klemes, J. J., Zeng, M., and Wang, Q. (2021). Comparison of aerodynamic noise and heat transfer for shell-and-tube heat exchangers with continuous helical and segmental baffles. Applied Thermal Engineering, 185, 116341.

[21] Yang, J., and Liu, W. (2015). Numerical investigation on a novel shell-and-tube heat exchanger with plate baffles and experimental validation. Energy Conversion and Management, 101, 689-696.

[22] He, L., and Li, P. (2018). Numerical investigation on double tube-pass shell-and-tube heat exchangers with different baffle configurations. Applied Thermal Engineering, 143, 561-569.

Your Inbox Guardian: AI-Powered Spam Filtering

Merve DÖNMEZ[1]

İlhan Fırat KILINÇER[2]

1- Yüksek Lisans Öğrencisi; Fırat Üniversitesi Teknoloji Fakültesi Mühendislik Bölümü. 241144108@firat.edu.tr ORCID No: 0009-0003-0094-1118

2- Dr. Öğr. Üyesi; Fırat Üniversitesi Teknoloji Fakültesi Mühendislik Bölümü. ifkilincer@firat.edu.tr ORCID No: 0000-0001-8090-4998

ABSTRACT

In this study, a deep learning-based classification model was developed for spam email. The modeling process consisted of two parts: preprocessing and deep learning classification. In the preprocessing phase, all texts were first converted to lowercase, punctuation removed, links cleaned, email addresses removed, and numbers cleaned. Separately, meaningless words were removed for both Turkish and English. The words were then reduced to their stems using the Lemmatizer method for the English dataset and the TurkishStemmer method for the Turkish dataset. Following these processes, the texts were simplified. The reduced words were tokenized and separated into words. The tokenizer was trained to convert the texts into numerical sequences and determine the word count. Padding was then performed to ensure all sequences were of the same length. A deep learning-based classifier was chosen for training the model. For this purpose, a hybrid deep learning classification system was developed, combining CNN layers to capture local patterns in the texts and Bi-LSTM layers to model long-term dependencies. Thanks to the hybrid approach, the model achieves a more robust representation by considering both short- and long-term contextual relationships. The performance of the proposed model was tested on various spam datasets. The accuracy rates for the resulting datasets were as high as 99.20% for the Fraud Email dataset, 98.50% for the Phishing Email dataset, and 92.61% for the Turkish Spam Email dataset. These results demonstrate that the hybrid deep learning approach, combining CNN and Bi-LSTM, can effectively classify different types of spam emails.

Keywords – Bi-LSTM, CNN, Classification, Preprocesing, Spam Email.

INTRODUCTION

The rapid development of technology from the past to the present day has had both positive and negative effects on our lives. Users often focus only on the positive aspects and do not realize the negative consequences until they are affected by them. Email attacks, one of the foremost negative aspects, are victimizing more and more people every day as their use becomes more widespread. Among the reasons for the daily increase in these attacks are ease of use and low cost; therefore, attackers prefer methods such as advertising and phishing. Malicious individuals seeking to achieve their goals attempt to lure unsuspecting victims into their traps by sending unwanted messages to email accounts they do not know. Spam emails, in particular, are checked daily, infiltrate inboxes, distract users, cause information pollution, and seriously threaten data security [1]. Spam refers to electronic messages sent without the recipient's knowledge or consent, often containing annoying or harmful content. Although it most commonly appears via email, it is also quite

prevalent in digital environments such as text messages (SMS), online forums, social media platforms, and even contact forms on websites [2].
Spammers use automated systems or bots to reach as many people as possible with their messages. In this respect, spam is designed by malicious individuals or groups to gain access to large audiences. Its primary purpose is not limited to reaching a wide audience but is to generate commercial profit. The goal is usually to direct people to specific services or products through advertising. Apart from this, spam can also be used for phishing; in this case, the aim is to obtain the user's bank account information and passwords. Another purpose of spam is to spread malware. Thus, files or links containing malicious software can infiltrate systems, steal information, or render the system unusable. For all these reasons, spam is a threat to both individual and corporate information security [3] [4].
The increasingly complex content of spam messages has led to the inadequacy of existing filtering systems. The scale of this threat can be more clearly demonstrated with the statistical data available today [5]. Figure 1 shows the distribution of daily spam emails by country. According to data from 3 December 2024, approximately 46.8% of emails sent worldwide contain spam [6].

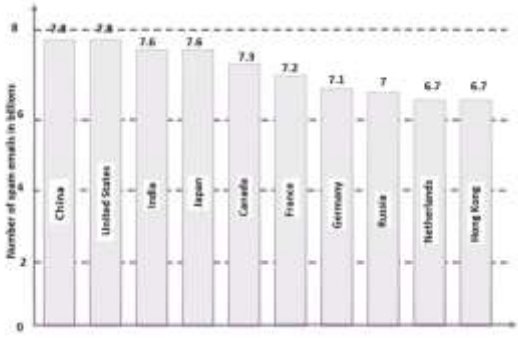

Figure 1. Distribution of daily spam email counts by country

As shown in Figure 1, it can be seen that a large proportion of spam emails originate from countries such as China, the United States, India and Japan. China and the US top the list, producing approximately 7.8 billion spam emails daily, while countries such as India, Japan, Canada, France, Germany and Russia also produce high numbers of spam. This situation clearly demonstrates that spam has now become a global cyber security issue rather than a local one [7][8]. The unpredictable increase in spam numbers has directed researchers towards spam detection. This study proposes a deep learning model based on 1D-CNN and Bi-LSTM for spam detection. The contributions of this study are as follows:

The performance of the proposed method was tested on different datasets using the 'phishing_email', 'fraud email' and 'Turkish spam' datasets.
The proposed model was designed to be a multi-language spam detection system by using a Turkish spam dataset in addition to English spam datasets.
A multi-step pre-processing process was used to increase the detection rate of spam emails in the datasets used in the study. After the pre-processing step, the data, which was brought to the same length, was subjected to classification using a combination of 1D-CNN and Bi-LSTM deep learning algorithms.
The other sections of the study are, in order, the 'Related Works' section, which contains literature studies related to spam detection; the 'Proposed Method' section, which explains the method proposed in the study; the 'Experimental Results' section, which presents the performance values obtained as a result of the proposed method; section, the 'Discussion' section comparing the results obtained in the study with those in the literature, and the 'Conclusion and Future Works' section evaluating the results obtained.

RELATED WORKS

Today, with technological advances, spam and phishing emails have become serious cyber security threats. Various filtering methods have been developed to counter these threats. In this context, machine learning and deep learning-based methods have been used to detect and classify spam emails. There are also numerous studies in the literature in this field. Martino et al. [7], focused on subject-based classification of spam emails and developed a new dataset. The SPEMC-15K dataset, created in English and Spanish, consists of more than 15,000 emails. In this study, text-based features were extracted using the Term Frequency-Inverse Term Frequency (TF-IDF) method and methods such as machine learning were used as classifiers. In experiments conducted on the English dataset, the Term Frequency-Inverse Term Frequency (TF-IDF) + Logistic Regression combination achieved 94.6% accuracy and 95.3% F1 score. This success rate demonstrates that traditional statistical modelling can still yield robust results with appropriate feature engineering. Ghosh et al. [8], used the Spam Corpus and Spambase datasets and performed the necessary preprocessing. They tested 13 different machine-learning methods. Random Forest showed significant success. Baktır et al. [9], compared machine-learning algorithms for classifying spam emails. They used datasets such as Enron-4, Enron-5, and CS440/ECE448. The decision tree algorithm yielded successful results on the Enron-4 dataset when applied to feature selection. Logistic regression and k-NN also yielded successful results on the CS440/ECE448 dataset.
Zhao et al. [10], proposed a model that uses Rough Set Theory to separate spam/non-spam/suspicious categories into three distinct categories. They developed a ternary classification model instead of a binary classification approach. They trained this model using machine-learning techniques and

achieved successful results. Sanh et al. [11], designed the Distil Bert model as a smaller, faster, and computationally more efficient version of the Bert architecture. Distil Bert has fewer parameters than Bert and operates faster while maintaining its language comprehension capabilities. Jamal et al. [12], proposed IPSDM (Improved Phishing Spam Detection Model), an approach developed for phishing and spam detection; this approach was retrained and developed to distinguish between Distil BERT and RoBERTa models. In this model, balancing was performed using the ADASYN method, which was found to prevent overfitting in imbalanced data and yield successful results.
Labonne et al. [13], utilised four distinct open-source datasets in their email spam detection research and conducted a comprehensive comparison using large language models (LLMs) and traditional methods. The study primarily focused on small-sample learning and, to this end, proposed the Flan-T5 model. This model comprises four different spam datasets. Bagui et al. [14], used machine learning and deep learning techniques alongside single hot coding techniques on spam email datasets. Deep learning models such as CNN and LSTM were employed. The results showed that the deep learning method performed better than the machine learning method, but ML (machine learning) models also performed better than DL (deep learning) models in terms of computation time. In particular, the CNN model achieved the highest accuracy rate when used in conjunction with word embedding.
Yaseen et al. [15], presented various models and techniques for automatic detection in their spam analysis study. Among the proposed models, deep learning-based models were applied for the classification of spam emails. Local patterns were learned with the CNN model, and time dependencies were learned with LSTM. An accuracy rate of 96.1% was achieved with LSTM. Keskin et al. [16], used RF, LR, NB, SVM, and Artificial Neural Network algorithms on 5558 spam and non-spam emails for machine learning-based classification for spam detection and compared the results. The most successful result was the RF algorithm with an accuracy rate of 98.83%. Omar [17], compared various machine learning algorithms and feature extraction methods for spam detection in mixed Swahili and English email messages. The study utilised classifiers such as Naive Bayes, Decision Tree, and Support Vector Machines (SVM) with content representations based on Term Frequency–Inverse Document Frequency (TF-IDF - Term Frequency–Inverse Document Frequency) and Word2Vec (CBOW - Continuous Bag of Words) based content representations were used. Experimental studies were conducted on the SpamAssassin and Enron datasets; the highest success was achieved with the TF-IDF + SVM (Linear) combination, reporting an accuracy rate of 98.13%. The study demonstrates the effectiveness of machine learning-based spam detection models for email content in two different languages.
Alhuzali et al. [18], developed a comprehensive system to detect phishing emails. Initially, they used limited models and datasets, but later additions

were made. A total of 14 models were used, including both machine learning and deep learning models. Ten different datasets were used. The accuracy rate for Bert was 98.99% and for RoBERTa, it was 99.08%. These rates were found to be on average 4.7% higher than other traditional ML methods. Butt et al. [19] developed a classification system using machine learning and deep learning-based algorithms to detect email phishing attacks. The obtained features were transformed into a suitable structure for classification and tested using SVM, Naive Bayes (NB), and LSTM algorithms. The model's performance was evaluated using cross-validation; according to the experimental results, the SVM model showed the highest success with an accuracy rate of 99.6%, the NB model 97%, and the LSTM model 98%. The study also emphasises that hybrid datasets with a more realistic structure can be created by analysing phishing and normal data together, and that these structures can provide a more robust framework for future models. Spam detection has become a crucial issue in digital environments, as it is directly linked to the security of emails frequently used in users' daily and business lives. Studies and detailed research in this area have led to advancements in natural language processing, machine learning, and deep learning methods. An effective and successful spam filter not only filters individual incoming messages but also helps protect the security of corporate networks and information systems. In this study, spam detection was performed using the proposed CNN and Bi-LSTM method after various pre-processing steps.

BACKGROUND

Dataset

The datasets used in this study have been employed in multilingual environments, both in Turkish and English, and have been utilised for spam detection. Turkish and English datasets uploaded to platforms such as Kaggle and Github have been collected separately. The aim here is to achieve high success rates for a large number of spam messages in multilingual environments. The 'Phishing Email', 'Fraud Email' and 'Turkish Spam' datasets were used in the study.

Phishing Email Dataset: This dataset uses a Phishing Email Dataset prepared in English. It consists of a rich collection combining six different datasets. This dataset, comprising approximately 82,500 emails, consists of 42,891 spam emails and 39,595 non-spam emails [20], [21].

Fraud Email Dataset: This dataset consists of spam and normal emails written in English. The dataset consists of a .csv file containing labelled and realistic examples. Its labelled structure provides a suitable environment for spam detection and threat classification studies using supervised learning models. The message contents it contains include the columns label, email text, subject, type, and email no [22]. The message contents include messages

such as bank fraud, lottery scams, and fake prize notifications. It consists of a total of 11,958 labelled email messages [23].

Turkish Spam Dataset: This dataset consists of the Turkish Spam Dataset prepared in the Turkish language. The dataset consists of a total of 826 labelled email messages, including 330 spam and 496 normal emails. It is presented in .csv format and contains label and text headers [24], [25]. It is particularly important for spam detection studies in the Turkish language in the field of natural language processing (NLP). All the characteristics of the datasets used in the study are summarised in Table 1.

Table 1 Spam datasets used

Dataset Name	Number of emails	Tags	Language
Phising E-mail Dataset	82500	Spam/Non-Spam	English
Fraud E-mail Dataset	11958	Spam/Non-Spam	English
Turkish Spam Eval	826	Spam/Non-Spam	Turkish

Deep Learning

Deep learning is a type of machine learning that uses multi-layered learning methods based on how the human brain learns. It works par ticularly well with large datasets and can understand complex data such as images, audio, and text. This method, which uses artificial neural networks, can analyze complex data in areas such as image processing, speech recognition, and natural language processing (NLP) [26]. It is suitable for many uses because it can process large data sets. In recent years, the rapid advancement of artificial intelli gence technologies has led to significant advances in deep learning techniques. This progress has attracted considerable attention in both academia and industry [27]. In this study, both Convolutional Neu ral Networks (CNN) and Bidirectional Long Short-Term Memory (Bi-LSTM) models were used together for spam detection.

Convolutional Neural Networks (CNN): Convolutional Neural Net works (CNN) are powerful deep learning models developed specifi cally for processing visual data and have achieved successful results. Although initially developed for image processing, they have also become widely used for text and audio data. CNN is one of the most widely used structures among deep learning models. Due to its structure, it has the ability to recognize local patterns on inputs and is successful in text-based tasks of a certain length. The CNN architecture essentially consists of a convolution layer, an activa tion layer, and a pooling layer. These layers enable the model to capture complex

patterns by learning low- and high-level features from the input data. This complex pattern recognition results in high performance learning models with strong generalization capabilities. In the convolution layer, filters learn during the training process to capture data-specific patterns, as described in mathematical equation (1) [28].

$$x_j^l = f\left(\sum_{i \epsilon M_j} X_j^{l-1} * k_{ij}^l + b_j^l\right) \quad (1)$$

In Equation (1), x_j^l represents the input from the previous layer, k_{ij}^l represents the filter in the layer, b_j^l represents the bias value, f represents the activation function, M_j represents the neighborhood area, and * represents the convolution operation. This formula represents the output of a neuron in the layer and forms the basis of the layers. The activation layer transforms the values obtained from the convolution operation into non-linear values through activation functions. This layer, which enables learning complex relationships, passes positive values and sets negative values to zero. The pooling layer reduces the size of the features extracted from the data, making learning more efficient, thereby enabling the model to be stripped of unnecessary details and reducing the computational load [29]. **Bidirectional Long Short-Term Memory (Bi-LSTM):** LSTM is an improved model of the Recurrent Neural Network (RNN) designed by Hochreiter and Schemidhuber (1997) [30]. This model was developed to address the fundamental weaknesses of RNNs, such as their inability to learn long-term dependencies, information loss, and, in particular, vanishing or exploding gradients encountered during the training process. LSTM is an artificial recurrent neural network architecture that is widely used in the field of deep learning and is particularly effective on large data sets. This structure, which works with sequential data, has the ability to retain information over long sequences while also being able to update new information. Thanks to this feature, it is successfully used in many data-intensive areas such as natural language processing, time series prediction, and speech recognition [31]. Figure 2 shows the general architecture of LSTM [32].

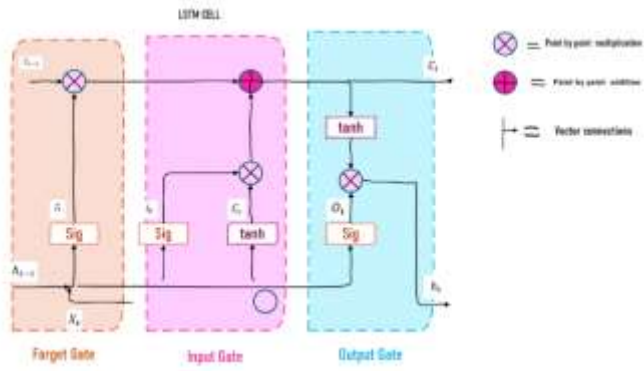

Figure 2 LSTM Architecture

The LSTM architecture shown in Figure 2 consists of "input," "forget," and "output" gates. The first of these gates, the input gate, determines how much of the new input will be stored in memory. The forget gate decides whether to store information from the memory cell. The output gate controls how much of the memory cell's contents should be kept secret. These gates allow users to manage cell state and decide which information to store, update, and delete, allowing them to learn long-term dependencies.

RNN and LSTM models are designed to allow information to be transmitted only forward in time. However, this one-way information flow can be inadequate, especially in situations where context must be understood from both directions. The Bi-directional Long Short-Term Memory (Bi-LSTM) model, developed as a result of these inadequate situations, is a type of recurrent neural network that processes data in both forward and backward directions. Thanks to this structure, the model combines a forward LSTM (which makes predictions from past data) with a backward LSTM (which makes predictions using future information) to effectively capture the past and future semantic connections of the input sequence, achieving successful results [33]. This feature has made it successful in situations such as spam detection, sentiment analysis, and speech recognition. The mathematical calculations for the forward and backward data processing processes of the Bi-LSTM architecture are given in the equations below [34].

$$i_t = \sigma(w_i.[h_{t-1}, x_t] + b_i \quad (2)$$

$$\widetilde{C_t} = \tan h\,(c.[h_{t-1}, x_t] + b_C) \quad (3)$$

$$f_t = \sigma\big(w_f.[h_{t-1}, x_t] + b_f\big) \quad (4)$$

$$C_t = f_t * C_{t-1} + i_t * \widetilde{C_t} \quad (5)$$

$$o_t = \sigma(w_0.[h_{t-1}, x_t] + b_o) \quad (6)$$

$$h_t = o_t * \tan h(C_t) \quad (7)$$

In the equations, i_t is the input gate, $\widetilde{C_t}$ is the activation function, f_t is the forget gate, C_t is the cell state, o_t is the output gate and h_t is the hidden layer.

Some commonly used symbols in the equations are; σ is the sigmoid activation function, x_t is the input data, w is the weight matrices and b is the bias term [35]. In this calculation process, both forward and backward LSTM layers are run separately [36]. As shown in Figure 3, the Bi-LSTM architecture has very strong context information. This context information allows it to see both the previous and next words. It provides significantly better performance than the single-front LSTM and is ideal for complex structures such as languages [37].

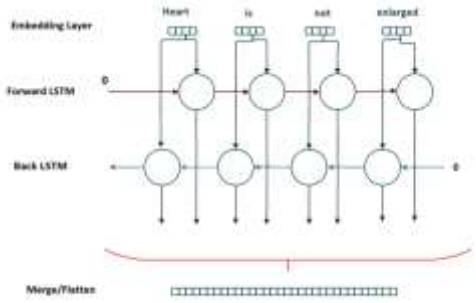

Figure 3 Bi-LSTM Architecture

Figure 3 shows the basic structure of the Bi-LSTM architecture. This architecture consists of two separate LSTM layers. One layer processes the input data forward, the other layer processes it backward. By combining the outputs from both layers, a richer contextual representation is obtained for each time step [38].

PROPOSED METHOD

In the age of digital communication, filtering unwanted emails (spam), which constitutes a significant portion of email traffic, is not just a matter of convenience but also a critical security and efficiency requirement. Phishing attacks, malware, and fraud attempts are often spread through spam emails. Therefore, a robust spam filter serves as the first and most important line of defense, protecting sensitive data for individuals and organizations and preventing serious financial losses and data breaches. In this study, the algorithm presented in Figure 4 was used for spam detection.

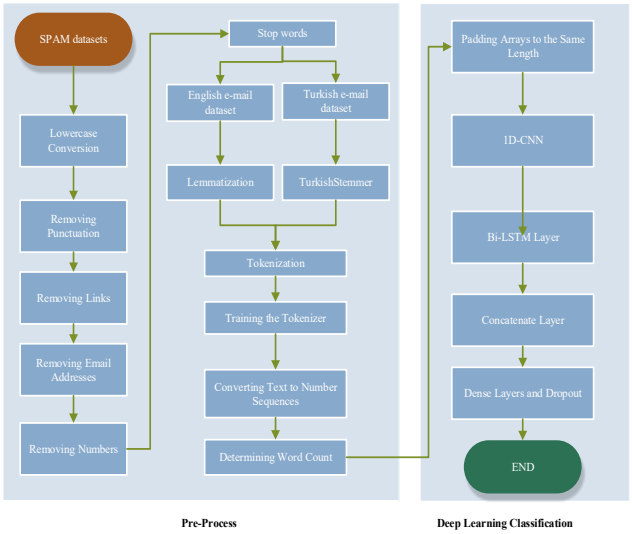

Figure 4 Proposed spam detection framework

Figure 4 shows a comprehensive algorithm designed to create a deep learning-based spam classification model. The proposed algorithm consists of two main sections for spam detection: “Pre-process” and “Deep learning classification.”

Pre-Process Phase

The first stage of the proposed model, the preprocessing step, aimed to transform the raw spam datasets into a clean and structured sequence of numbers understandable by artificial intelligence. This increased the quality of the text data and the model’s learning efficiency. In the first step of the preprocessing phase, all email texts were standardized using "Lowercase Conversion." By treating "SPAM" and "spam" as the same, the consistency of the dataset was increased. After the "Lowercase Conversion" process, all punctuation marks (commas, periods, exclamation points, etc.) were removed from the resulting data using the "Removing Punctuation" step. Spam emails often contain links. Therefore, to reduce noise in the dataset, all URLs and email addresses were removed from the email texts using the "Removing Links" and "Removing Email Addresses" steps. Finally, numbers were removed from the texts.

Another important preprocessing step is Language Processing and Digitization. In this phase, the texts were cleaned of noise while preserving the semantic essence of the texts for deep learning models. First, "stop words," such as "ve" and "ile," that occur frequently in the language but don’t convey the main meaning of the sentence, were removed from the dataset. Then, stemming operations were performed on the texts in different ways for each language; for English texts, this was done with lemmatization, which reduces words to their base forms (for example, deriving "run" from "run"), and for

Turkish texts, with TurkishStemmer, which removes inflectional suffixes. These operations significantly improve the model's generalization ability by combining different word forms into a single representation. Once the cleaning process is complete, the texts are converted into strings of numbers using a Tokenizer. During this process, each unique word is assigned a unique numerical index. This converts the raw texts into numerical vectors that the machine can process. The number of words determined during this process helps the model determine the scope of the vocabulary to be used.

Deep Learning Phase

In the Deep Learning classification phase, the preprocessed data is now ready to be fed into the model. The preprocessed number sequences were then subjected to classification by a hybrid deep learning model, which will determine whether the texts are spam. Before the classification process, all email sequences were equalized according to a fixed limit using the "Padding Arrays to the Same Length" step. Padding is added to short sequences, thus standardizing the model input size. The length of all text sequences was set to 100 in this study, which is the input data size of the proposed 1D-CNN and Bi-LSTM hybrid model.

In the deep learning architecture used in this study, numerical word indices were converted into dense, low-dimensional vectors. In the embedding layer, each word was represented by a 100-dimensional vector. CNN layers were used to capture local patterns, n-grams, and short word sequences in the text. Local features from the CNN were transferred to the Bi-LSTM layer. Bi-LSTM analyzes text both forward and backward, learning the long-term dependencies and relationships between words within context. This allows the model to connect the meaning of a word to both the words that precede and follow it, achieving a deeper understanding. To generate the richest and most comprehensive information about the text, the output vectors obtained by the Bi-LSTM layer from both forward and backward directions are combined in the Concatenate layer. An Attention layer is added to the model to examine the entire input sequence and learn which parts of the sequence are most important for classification decisions. The combined feature vector is fed into the Fully Connected/Dense layers to make the final decision. Furthermore, Dropout is used to reduce the risk of overfitting and increase generalization by randomly disabling some neurons during training. At the end of the process, the model analyzes the email and its output makes the final decision on whether the email is spam or legitimate (raw). This hybrid (CNN + Bi-LSTM) architecture offers the advantage of capturing both local patterns and long-term contextual relationships in text classification. The layers used in the proposed model are given in Table 2.

Table 2 Summary of proposed deep learning model

Layers	Specifications
First Conv1D Layer	256 filters, kernel size =3, activation function=relu
First Pooling Layer	Pool size = 2
Second Conv1D Layer	128 filters, kernel size =3, activation function=relu
Second Pooling Layer	Pool size = 2
Bi-LSTM Layer	Units=64, return_sequences=True
Dense 1 Layer	128 Neurons
Dropout 1	0.5
Dense 1 Layer	64 Neurons
Dropout 2	0.3
Epochs	50

EXPERIMENTAL RESULTS

In this study, we present a deep learning model consisting of 1D CNN and Bi-LSTM layers covering two emails in English and one in Turkish; Fraud email, Phishing email, and Turkish email. For performance evaluation, we used the Accuracy, Precision, Recall, and F1 Score metrics, whose equations are given below.

$$Accuracy = \frac{TP+TN}{TP+TN+FP+FN} \quad (8)$$

$$Precision = \frac{TP}{TP+FP} \quad (9)$$

$$Recall = \frac{TP}{TP+FN} \quad (10)$$

$$F1\ Score = 2 * \frac{\mathrm{Pr}*R}{\mathrm{Pr}+R} \quad (11)$$

The performance values obtained from the proposed method are given in Table 3.

Table 3 Performans results after proposed method

Metrics(%)	Fraud Email	Phishing Email	Turkish Email
Accuracy	99.20	98.63	92.62
Precision	99.51	98.39	94.17
Recall	98.65	99	91.13
F1 Score	99.16	98.70	92.67

Table 3 shows the performance of the proposed hybrid model on three different email datasets. The table clearly demonstrates the high performance achieved by the developed model on the Fraud, Phishing, and Turkish email datasets. The model demonstrated strong performance in classifying complex spam types, achieving accuracy rates exceeding 90% across all categories. The model's most successful dataset was the Fraud email dataset, achieving an accuracy of 99.20%, almost approaching perfection.Similarly, the precision value on the Fraud Email dataset was 99.51%. This demonstrates that when the model marks an email as spam, the probability of error is extremely low. In other words, the rate of incorrectly blocking normal emails is very low. With a recall value of 98.65%, it successfully captured the vast majority of spam emails, and the F1 Score of 99.16% confirms a very strong balance between precision and recall.

The accuracy rate obtained from studies on the Phishing email dataset is 98.63%. The F1 Score (98.7%), Precision (98.39%), and Recall (99%) values are very close to each other. This closeness demonstrates the model's reliable performance, demonstrating its ability to both accurately detect and prevent phishing emails.

Performance on the Turkish Email dataset is relatively lower than on the other two English datasets, but still achieved an overall accuracy of 92.62%. The difference between Precision (94.17%) and Recall (91.13%) obtained during the classification of this dataset is more pronounced than in the other categories. The 91.13% Recall value may indicate that the model missed a portion of Turkish spam emails (False Negatives). This is thought to be due to the complexity of the grammatical structure of Turkish texts (stemmers, word roots, and suffixes) or the diversity of the dataset. Nevertheless, the 92.67% F1 Score proves that the model also has a high classification ability for Turkish texts. The confusion matrices obtained for each dataset using the proposed model are shown in Figure 5.

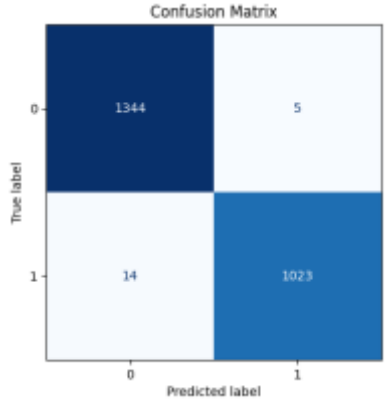

a. Fraud Email dataset

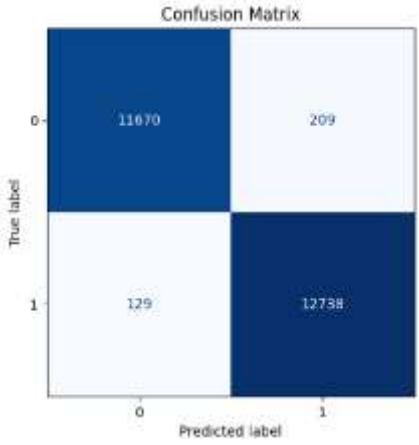

b. Phishing email dataset

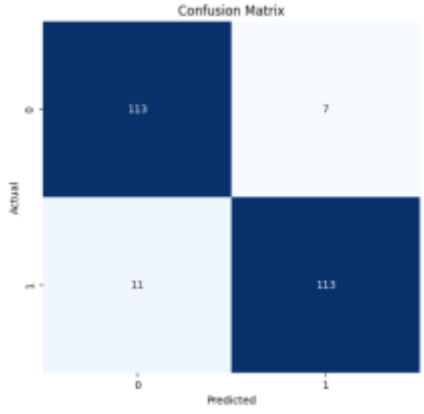

c. Turkish spam email dataset

Figure 5 Confusion matrixes

When Table 3 and Figure 5 are examined together, the proposed hybrid model has demonstrated superior discrimination power, particularly for spam types involving cyber threats such as Fraud and Phishing. The model's performance exceeding 98% even on the most challenging metrics indicates that the method offers a robust and generalizable solution for detecting different types of spam. The performance drop in Turkish texts points to a potential area for improvement, which could stem from the structure of the language or the need to customize the preprocessing steps. The performance values achieved by the model reveal not only high success rates but also a healthy balance between precision and recall, which are critical aspects of classification. The proposed hybrid deep learning approach has proven to offer a multi-layered and robust

solution against both sophisticated attacks specific to threat types and challenges arising from language diversity, achieving an F1 Score above 92% across three distinct and challenging email types. These high metrics demonstrate that the developed model provides a highly effective and reliable foundation for practical applications in modern email security systems.

DISCUSSION

In this study, a hybrid deep learning model consisting of 1D-CNN and BiLSTM models was developed for spam analysis and tested on three different datasets. The proposed model achieved an accuracy rate of 99.20% on the Fraud Email dataset, 98.50% on the Phishing Email dataset, and 92.62% on the Turkish Spam dataset. The obtained accuracy rates reveal that the model performed well in detecting spam emails and distinguishing them from normal emails in English datasets, but showed lower performance in the Turkish dataset.

When the obtained accuracy rates are compared with similar studies in the literature, it is seen that our model performs strongly. Atawneh et al. [39], compared deep learning approaches such as CNN, LSTM, RNN, and BERT in detecting phishing emails and obtained the best result with a 99.61% accuracy rate from the BERT + LSTM model. Salian et al. [21], proposed a hybrid model based on sentiment analysis for detecting phishing emails. The study used a phishing email dataset. In the experimental results, while only 94% accuracy was achieved with the SVM model, the accuracy rate reached 97% with the DistilBERT + SVM hybrid model. In the study by Fumito et al. [23], the performance of traditional machine learning algorithms and transformer-based deep learning models for detecting phishing emails was compared. In their research, they collected datasets from various open sources, such as Enron Spam Data, Phishing Monkey (2018-2022), Phishing Email Detection, Spam Classification for Basic NLP, NLP Spam-Ham Email Classification, and Fraud Email Dataset. The transformer-based RoBERTa model achieved the highest performance in the study, reaching an accuracy rate of 99.36% on the Phishing Email dataset.

Aksoy et al. [24], used natural language processing and machine learning-based methods to detect spam in Turkish email messages. The Turkish spam dataset was used in the study. In his study, the dataset was expanded using data augmentation techniques with BERTurk, DistilBERTurk, Word2Vec, and GPT-2 models, and then classified using Naive Bayes, SVM, Decision Tree, and Random Forest algorithms. In the experimental results, the accuracy of the original dataset was 93.33%, while the accuracy of the augmented BERT-based model was 97.61%. Güven [40], analyzed the Turkish Spam dataset using machine learning methods such as Random Forest, Logistic Regression, Naive Bayes, and Artificial Neural Networks, as well as language models including BERT, ELECTRA, ALBERT, and DistilBERT. According

to the results of this experiment, artificial neural networks achieved 90.15% accuracy among the machine learning methods, while the language models BERT and ELECTRA achieved an accuracy rate of 94.08%. Similarly, in a study conducted by Özgür et al. [41], a dynamic model combining Artificial Neural Networks (ANN) and Bayesian filtering methods was developed for spam detection on Turkish emails. The Turkish Spam dataset was used in the study, and the model's accuracy rate was approximately 90%. Malik et al. [42], propose a hybrid deep learning model based on multiple features for detecting phishing emails. Three different datasets were used in the study: Enron, SpamAssassin, and Phishing Email. Along with the developed LSTM-CNN hybrid model, SVM, Random Forest, and BERT algorithms were also evaluated. According to the results obtained, the LSTM-CNN model achieved high success rates, reaching an accuracy rate of 98.2% on the Enron dataset, 97.5% on the SpamAssassin dataset, and 96.5% on the Phishing Email dataset. Ajala et al. [43], examined different machine learning algorithms for detecting phishing emails using the Phishing Email dataset. The performance of models created using Naive Bayes (NB), Logistic Regression (LR), and Multilayer Perceptron (MLP) algorithms was compared based on accuracy rates. As a result of the evaluations, the MLP model showed the highest success with 98.57% accuracy and 94.74% F1 score. AlJamal et al. [44], developed machine learning-based models to detect phishing emails and to make a correct distinction between spam messages in their normal-spam-based study. They used two different datasets: Fraud Email and Phishing Email. They used LR, DT, RF, and SVM algorithms from machine learning. The Random Forest model achieved the best result in the Fraud Email dataset with an accuracy rate of 98.72%, and similarly, the Random Forest model achieved an accuracy rate of 99.15% in the Phishing Email dataset. A literature comparison of the proposed model is summarized in Table 4.

Table 4 Literature comparison

Referance	Datasets	Method	Accuracy (%)
Atawneh et al. [39]	Phishing Email	CNN LSTM RNN BERT	%98.74 %98.87 %98.58 %99.61
Salian (2024)	Phishing Email	DistilBERT + SVM	%97

Fumito et al. (2024)	Enron Spam Data Phishing Monkey (2018-2022) Phishing Email Detection Spam Classification for Basic NLP NLP Spam-Ham Email Classification Fraud Email Dataset	ML CNN RoBERTa	%99.36
Aksoy (2022)	Turkish Spam	NLP ML	%97.61
Güven (2023)	Turkish Spam	ML BERT ELECTRA ALBERT DistilBERT	%90.15 %94.08
Özgür et al.(2004)	Turkish Spam	Artificial Neural Networks Naive Bayes	%90
Malik et al.(2025)	Enron Dataset Phishing Email SpamAssassin	LSTM + CNN SVM Random Forest BERT	%98.2 %96.5 %97.5
Ajala (2025) [2]	Phishing Email	ML	%98.57
AlJamal et al. (2024)	Fraud Email Phishing Email	LR DT RF SVM	%98.72 %99.15
Proposed method	**Fraud Email**	**CNN + Bi-LSTM**	**%99.20**
	Phishing Email		**%98.50**
	Turkish Spam		**%92.62**

The proposed model outperforms many studies in the Fraud Email dataset with a score of 99.20%. In particular, it achieves a slightly higher accuracy than the best result of 99.15% obtained by AlJamal et al. [44], using the same dataset. The CNN + Bi-LSTM hybrid architecture used combines the CNN's ability to capture local patterns (such as n-grams) with the Bi-LSTM's ability to understand long-term dependencies in text sequences in both directions (forward and backward), making it effective in detecting the complex and subtle linguistic features of fraudulent emails. The accuracy rate of 98.50% achieved on the Phishing Email dataset is very close to Malik et al. [42]'s LSTM + CNN 98.20 and Ajala et al. [43]'s ML 98.57 results, demonstrating

competitive performance in this field. Deep Learning Superiority: Atawneh et al. [39]'s superior results compared to simpler deep learning models such as CNN, LSTM, and RNN, at 98.74%, 98.87%, and 98.58%, respectively, demonstrate the benefit of the hybrid architecture. However, in this comparison, the BERT model by Atawneh et al. [39] yields the highest result of 99.61%. The proposed model has been tested on English-dominant datasets such as Fraud Email and Phishing Email, as well as on the Turkish Spam dataset. This is an advantage in terms of demonstrating the model's adaptability to different languages and tasks.

CONCLUSION AND FUTURE WORK

The rapid development of technology has led to an increase in cybersecurity threats. Among these threats, spam emails have become one of the most common types of attacks that threaten user security. While various methods have been developed for spam message detection, content-based analysis is often insufficient, necessitating the need for deeper learning-based approaches. In this study, a hybrid deep learning model combining 1D-CNN, Bi-LSTM, and Attention mechanisms is proposed for spam email detection. The model was tested on the Phishing Email Dataset, Fraud Email Dataset, and Turkish SpamEval datasets. Following extensive preprocessing and quantification steps, the model demonstrated high classification performance by learning both local patterns and contextual relationships in text. According to the experimental results, the model achieved high accuracy rates in binary classification for Fraud and Phishing, ranging from 98.5% to 99.2%, competitive with robust methods in the literature. An accuracy rate of 92.62% was achieved in binary classification on the Turkish dataset.

Future work aims to further diversify the Turkish dataset and expand the email sample to improve the classification of the proposed model, training the model with more balanced data. Furthermore, converting the model to a multilingual framework and integrating it into real-time spam detection systems are also important research areas.

REFERENCE

[1] E. Enes Eryılmaz, E. Kılıç, D. Makalesi, / Review Article, İstenmeyen Epostaların Tespiti için Kullanılan Yöntemlerin İncelenmesi, Dicle Üniversitesi Mühendislik Fakültesi Mühendislik Derg. 11 (2020) 977–987. https://doi.org/10.24012/DUMF.715638.

[2] Spam Nedir? | Figensoft, (n.d.). https://www.figensoft.com/blog/spam-nedir (accessed July 29, 2025).

[3] E-posta spam'i nedir ve bununla nasıl mücadele edilir? | TechTarget'tan Tanım, (n.d.). https://www.techtarget.com/searchsecurity/definition/spam (accessed July 29, 2025).

[4] What Is Spam Email? - Cisco, (n.d.). https://www.cisco.com/site/us/en/learn/topics/security/what-is-spam.html (accessed July 29, 2025).
[5] Spam Mesaj Nedir? I Figensoft, (n.d.). https://www.figensoft.com/blog/spam-mesaj-nedir (accessed October 25, 2025).
[6] 23 Email Spam Statistics to Know in 2025, (n.d.). https://www.mailmodo.com/guides/email-spam-statistics/ (accessed July 29, 2025).
[7] F. Jáñez-Martino, R. Alaiz-Rodríguez, V. González-Castro, E. Fidalgo, E. Alegre, Classifying spam emails using agglomerative hierarchical clustering and a topic-based approach, (2024).
[8] A. Ghosh, A. Senthilrajan, Comparison of machine learning techniques for spam detection, Multimed. Tools Appl. 82 (2023) 29227–29254. https://doi.org/10.1007/S11042-023-14689-3.
[9] N. BAKTIR, Y. ATAY, Makine Öğrenmesi Yaklaşımlarının Spam-Mail Sınıflandırma Probleminde Karşılaştırmalı Analizi, Bilişim Teknol. Derg. 15 (2022) 349–364. https://doi.org/10.17671/gazibtd.1014764.
[10] W. Zhao, Z. Zhang, An email classification model based on rough set theory, Proc. 2005 Int. Conf. Act. Media Technol. AMT 2005 2005 (2005) 403–408. https://doi.org/10.1109/AMT.2005.1505383.
[11] V. Sanh, L. Debut, J. Chaumond, T. Wolf, DistilBERT, a distilled version of BERT: smaller, faster, cheaper and lighter, (2019).
[12] S. Jamal, H. Wimmer, I.H. Sarker, An Improved Transformer-based Model for Detecting Phishing, Spam, and Ham: A Large Language Model Approach, (2023).
[13] M. Labonne, S. Moran, Spam-T5: Benchmarking Large Language Models for Few-Shot Email Spam Detection, (2023) 1–18.
[14] S. Bagui, D. Nandi, S. Bagui, R.J. White, Classifying phishing email using machine learning and deep learning, 2019 Int. Conf. Cyber Secur. Prot. Digit. Serv. Cyber Secur. 2019 (2019). https://doi.org/10.1109/CYBERSECPODS.2019.8885143.
[15] I. AbdulNabi, Q. Yaseen, Spam Email Detection Using Deep Learning Techniques, Procedia Comput. Sci. 184 (2021) 853–858. https://doi.org/10.1016/J.PROCS.2021.03.107.
[16] S. Keskin, O. Sevli, Machine Learning Based Classification for Spam Detection, Sak. Univ. J. Sci. 28 (2024) 270–282. https://doi.org/10.16984/SAUFENBILDER.1264476.
[17] R. OMAR, A Comparison of Machine Learning Techniques: E-Mail Spam Filtering from Combined Swahili and English Email Messages, (2018).
[18] A. Alhuzali, A. Alloqmani, M. Aljabri, F. Alharbi, In-Depth Analysis of Phishing Email Detection: Evaluating the Performance of Machine Learning and Deep Learning Models Across Multiple Datasets, Appl. Sci. 2025, Vol. 15, Page 3396 15 (2025) 3396. https://doi.org/10.3390/APP15063396.
[19] U.A. Butt, R. Amin, H. Aldabbas, S. Mohan, B. Alouffi, A. Ahmadian, Cloud-based email phishing attack using machine and deep learning algorithm, Complex Intell. Syst. 9 (2023) 3043–3070. https://doi.org/10.1007/S40747-022-00760-3/FIGURES/20.
[20] Phishing Email Dataset, (n.d.). https://www.kaggle.com/datasets/naserabdullahalam/phishing-email-dataset (accessed July 30, 2025).

[21] S.S. Salian, Enhancing Phishing Email Detection with Sentiment Analysis: A Hybrid Approach, (2024).
[22] Fraud Email Dataset, (n.d.). https://www.kaggle.com/datasets/llabhishekll/fraud-email-dataset (accessed July 27, 2025).
[23] (PDF) Comparative Investigation of Traditional Machine Learning Models and Transformer Models for Phishing Email Detection, (n.d.). https://www.researchgate.net/publication/385093310_Comparative_Investigation_of_Traditional_Machine_Learning_Models_and_Transformer_Models_for_Phishing_Email_Detection (accessed July 31, 2025).
[24] A. Aksoy, Augmenting A Turkish Dataset For Spam Filtering Using Natural Language Processing Techniques, (2022) 99.
[25] Turkish Spam Dataset, (n.d.). https://www.kaggle.com/datasets/cuneytdemir/turkish-spam-dataset (accessed October 21, 2025).
[26] Y. Lecun, Y. Bengio, G. Hinton, Deep learning, Nature 521 (2015) 436–444. https://doi.org/10.1038/NATURE14539;SUBJMETA=117,639,705;KWRD=COMPUTER+SCIENCE,MATHEMATICS+AND+COMPUTING.
[27] Derin öğrenme - Vikipedi, (n.d.). https://tr.wikipedia.org/wiki/Derin_öğrenme (accessed July 31, 2025).
[28] Yapay Sinir Ağı Nedir ve Nasıl Çalışır? Yapay Zeka Rehberi, (n.d.). https://blog.roboflow.com/what-is-a-neural-network/ (accessed July 30, 2025).
[29] What is a Convolutional Neural Network (CNN)? | Definition from TechTarget, (n.d.). https://www.techtarget.com/searchenterpriseai/definition/convolutional-neural-network (accessed October 21, 2025).
[30] S. Hochreiter, J. Schmidhuber, Long Short-Term Memory, Neural Comput. 9 (1997) 1735–1780. https://doi.org/10.1162/NECO.1997.9.8.1735.
[31] What is LSTM? Introduction to Long Short-Term Memory | by Rebeen Hamad | Medium, (n.d.). https://medium.com/@rebeen.jaff/what-is-lstm-introduction-to-long-short-term-memory-66bd3855b9ce (accessed July 30, 2025).
[32] Deep Learning-LSTM mimarisi üzerine kaleme aldığım yazı.Keyifli okumalar. | Ebubekir Doğan, (n.d.). https://tr.linkedin.com/posts/ebubekirdgn_deep-learninglstm-uzun-kısa-süreli-bellek-activity-7196038685354520577-SbSq (accessed July 30, 2025).
[33] Uzun-Kısa Vadeli Bellek(LSTM). LSTM'i daha derinden incelemeye… | by Onur Akköse | Deep Learning Türkiye | Medium, (n.d.). https://medium.com/deep-learning-turkiye/uzun-kısa-vadeli-bellek-lstm-b018c07174a3 (accessed July 30, 2025).
[34] NLP'de Çift Yönlü LSTM - GeeksforGeeks, (n.d.). https://www.geeksforgeeks.org/nlp/bidirectional-lstm-in-nlp/ (accessed July 30, 2025).
[35] A. Makalesi, M.E. Bilal, İ. Işik, H. Üniversitesi, M. Fakültesi, B. Mühendisliği Bölümü, İ. Üniversitesi, E. Elektronik Mühendisliği Bölümü, T.E. Mehmet Bilal, LSTM Tabanlı Derin Ağlar Kullanılarak Diyabet Hastalığı Tahmini, Cilt 10 (2021) 68–74. https://doi.org/10.46810/tdfd.818528.
[36] Understanding Bidirectional LSTM for Sequential Data Processing | by Anishnama | Medium, (n.d.). https://medium.com/@anishnama20/understanding-

bidirectional-lstm-for-sequential-data-processing-b83d6283befc (accessed July 30, 2025).
[37] Çift Yönlü LSTM ile LSTM Arasındaki Fark - GeeksforGeeks, (n.d.). https://www.geeksforgeeks.org/deep-learning/difference-between-a-bidirectional-lstm-and-an-lstm/ (accessed July 30, 2025).
[38] O. Şahin, R. Yayla, BiLSTM Derin Öğrenme Yöntemi ile Uzun Metinlerden Yeni Özet Metinlerin Türetilmesi, Karadeniz Fen Bilim. Derg. 14 (2024) 1096–1119. https://doi.org/10.31466/kfbd.1423022.
[39] S. Atawneh, H. Aljehani, Phishing Email Detection Model Using Deep Learning, Electron. 2023, Vol. 12, Page 4261 12 (2023) 4261. https://doi.org/10.3390/ELECTRONICS12204261.
[40] Z.A. GÜVEN, Türkçe E-postalarda Spam Tespiti için Makine Öğrenme Yöntemlerinin ve Dil Modellerinin Analizi, Eur. J. Sci. Technol. (2023). https://doi.org/10.31590/ejosat.1234079.
[41] L. Özgür, T. Güngör, F. Gürgen, Spam Mail Detection Using Artificial Neural Network and Bayesian Filter, Lect. Notes Comput. Sci. (Including Subser. Lect. Notes Artif. Intell. Lect. Notes Bioinformatics) 3177 (2004) 505–510. https://doi.org/10.1007/978-3-540-28651-6_74.
[42] M. Rokunojjaman, A. Malik, M.M.J. Sajeeb, M. Yahiduzzaman, M.S. Islam, Multi-Feature Hybrid LSTM-CNN Framework for Phishing Email Detection, Int. J. Electron. Commun. Syst. 5 (2025) 93–103. https://doi.org/10.24042/ijecs.v5i1.26764.
[43] T.B. Ajala, Detection of Phishing Emails Using Machine Learning : A Comparison of Three Models, (2025). https://doi.org/10.5281/zenodo.17258441.
[44] M. Aljamal, R. Alquran, M. Aljaidi, O.S. Aljamal, A. Alsarhan, I. Al-Aiash, G. Samara, M. Banisalman, M. Khouj, Harnessing ML and NLP for Enhanced Cybersecurity: A Comprehensive Approach for Phishing Email Detection, 2024 25th Int. Arab Conf. Inf. Technol. ACIT 2024 (2024) 1–9. https://doi.org/10.1109/ACIT62805.2024.10877181.

Barriers to Sustainable Commuting on University Campuses: A Critical Review of Policy, Infrastructure, and Behavioral Challenges

Hala Sirror*

Asad Ullah Khan [2]

Adil Khan [3]

[1]Department of Architecture, Prince Sultan University, Saudi Arabia
[2]Qatar Green Leaders, Jeddah 23411, Saudi Arabia
[3]Department of Civil and Environmental Engineering, Old Dominion University, USA
*(hsirror@psu.edu.sa)

ABSTRACT

University campuses are pivotal in advancing sustainable development, yet many faces persistent challenges in implementing effective sustainable commuting practices. This review critically examines the multifaceted barriers policy-related, infrastructural, and behavioral that hinder the adoption of sustainable transportation modes such as walking, cycling, public transit, and electric vehicles within university settings. By synthesizing recent literature and case studies from diverse geographical and socio-economic contexts, the paper identifies common obstacles, including inadequate institutional policies, insufficient infrastructure, and entrenched cultural preferences for private vehicle use. Special attention is given to campuses in arid and car-dependent regions, such as those in the Middle East, to highlight unique challenges and potential strategies aligned with national sustainability goals like Saudi Arabia's Vision 2030. The review also explores successful interventions and provides recommendations for policymakers and university administrators aiming to promote sustainable commuting. This study contributes to the discourse on sustainable urban mobility by offering a comprehensive framework for understanding and addressing the barriers to sustainable commuting in higher education institutions.

Keywords – Sustainable commuting, university campuses, transportation policy, infrastructure, behavioral change, Vision 2030, Middle East, sustainable development goals

I. INTRODUCTION

Universities play a pivotal role in promoting sustainable commuting practices, which are essential as global awareness of climate change and urban congestion rises. The adoption of sustainable commuting strategies including walking, cycling, public transport, carpooling, and electric vehicles has become increasingly critical for minimizing carbon emissions associated with campus-related activities and fostering healthier and more inclusive communities. Research indicates that improving infrastructure for walking and cycling correlates with elevated physical activity levels among students, suggesting the significant impact of campus environments on commuting behaviors [1]. However, the transition to sustainable transportation on campuses encounters various institutional, infrastructural, and behavioral barriers, particularly in car-dependent regions such as the Middle East and North Africa [2], where advances toward sustainable mobility can be slow and complicated.

In Saudi Arabia, Vision 2030 emphasizes low-carbon mobility as a strategic priority, yet efforts are often thwarted by inadequate public transport systems, limited infrastructure for non-motorized transportation, and ingrained car-

centric habits in the populace. For instance, walkability has been shown to enhance the sustainability of campus environments [3], but many universities struggle to design their campuses in ways that foster walking and cycling as viable commuting options [4]. Recommendations from studies suggest reducing or eliminating free parking and enhancing multimodal accessibility to support walking and other sustainable transportation modes [5]. This approach aligns with the concept of Transit Oriented Development (TOD), which proposes designing university campuses as nodes within a network that facilitates diverse commuting options [6].

These challenges are compounded by behavioral factors, as student's attitudes towards commuting can significantly influence their travel choices. The presence of positive commuter benefits and supportive mobility initiatives can encourage changes in commuting habits; however, actual adoption rates may remain low without sufficient motivation or awareness [7]. Research illustrates that perceptions regarding commuting modes, coupled with the satisfaction derived from traveling, play pivotal roles in fostering sustainable behavior [8]. Active transportation methods, such as walking and cycling, not only increase individual physical activity levels but also contribute to broader sustainability goals by reducing greenhouse gas emissions [9].

Furthermore, the presence of adequate facilities, such as secured bike parking and pedestrian-friendly pathways, is crucial to effectively shift commuter habits on campus. Design considerations must prioritize land use efficiency and improve safety for non-motorists, as inadequate pedestrian infrastructure remains a pressing concern in many university settings [10]. Enhancing the overall commuting experience translates to more engaged students and can lead to enhanced productivity and well-being within the campus community [11]. In conclusion, universities must overcome multifaceted challenges to fully implement sustainable commuting initiatives. Strategic planning must incorporate infrastructural investments while aligning behavioral change strategies to create an environment that embraces sustainability. Interdisciplinary collaboration and innovative policies could significantly facilitate this transition, advances not only campus sustainability goals but also contributing to broader societal shifts towards sustainable transportation practices.

This review paper aims to critically examine the persistent barriers that hinder sustainable commuting implementation in university settings. The objective is to classify and analyze these challenges within three core domains: (1) policy and governance, (2) infrastructure and physical accessibility, and (3) behavioral and cultural dynamics. By synthesizing recent literature and case studies from diverse contexts, the paper seeks to highlight patterns, identify gaps, and propose actionable strategies that can guide

campus planners, policymakers, and sustainability advocates. Through this investigation, the study contributes to a deeper understanding of how higher education institutions can lead the transition toward more sustainable urban mobility systems while aligning with broader global and national sustainability agendas.

II. LITERATURE REVIEW

The topic of sustainable commuting has gained growing attention in recent years, especially in the context of achieving global climate targets and fostering more livable urban environments. University campuses, as compact and controlled micro-urban environments, offer a unique opportunity to study and promote low-carbon commuting behaviors. However, existing literature reveals that the transition to sustainable commuting is often impeded by a range of systemic barriers, broadly classified into policy-related, infrastructural, and behavioral categories.

A. Policy and Governance Barriers

In addressing barriers to sustainable mobility on university campuses, literature highlights the inadequacies in institutional frameworks necessary for effective policy implementation. A recurring theme is that many campuses operate under weak or disjointed mobility policies, often developed in isolation from broader city-level planning, which leads to inconsistencies in adoption, execution, and reduced administrative accountability [12]. Research indicates that a more integrated approach, aligning university policies with urban transport frameworks, is essential to bridging these gaps and promoting sustainable commuting practices [13]. Effective governance frameworks are critical for coordinating efforts among various stakeholders, fostering engagement and compliance, and thus creating a conducive atmosphere for sustainable mobility solutions [14]. The challenges highlighted in studies reflect a broader context of governance deficits where universities find themselves constrained by policies that lack enforceable guidelines and measurable outcomes [14].

To summarize, addressing the policy and governance barriers to implementing sustainable mobility solutions in universities requires a multifaceted approach that involves strengthening institutional frameworks and enhancing collaboration with city-level planning processes. Such strategies must address financial constraints while ensuring that governance mechanisms are robust enough to support long-term sustainability goals in campus transport planning.

B. Infrastructure and Physical Barriers

In the context of university transport policies, several studies underscore the institutional barriers hindering the effective promotion of sustainable mobility on campuses. Specifically, literature frequently points to the absence

of robust institutional frameworks that actively facilitate sustainable mobility initiatives. For example, Literature argue that the likelihood of students utilizing bicycles for commuting can be greatly influenced by targeted institutional interventions, highlighting that adequate facilities and resources are essential for encouraging bicycle usage among students [15]. This aligns with findings from [7], who emphasize that effective organizational policies can significantly alter commuting behaviors and promote environmentally friendly travel choices.

Moreover, [16] emphasizes the multifaceted nature of sustainable transport infrastructure, suggesting that a holistic approach incorporating environmental, economic, social, and adaptive considerations is essential for achieving long-term sustainability goals in transport systems. This perspective is reinforced by [17], who highlights that significant percentages of commuters in educational institutions rely on personal vehicles, contributing to congestion and pollution. Limitations in institutional frameworks and the absence of dedicated transportation planning offices in many universities exacerbate these issues, as financial constraints hinder the development and implementation of integrated mobility strategies [17].

In summary, to overcome the challenges associated with the implementation of sustainable commuting solutions in universities, it is crucial to establish coherent policies supported by adequate resources and frameworks. This can be achieved through stakeholder collaboration and a comprehensive approach to planning that aligns institutional initiatives with broader urban transport strategies.

C. Behavioural and Cultural Barriers

Behavioral resistance remains a critical challenge in promoting sustainable commuting practices. Numerous studies reveal that commuting choices are often influenced by deeply ingrained cultural norms and perceptions of convenience, status, and safety. For instance, in car-oriented societies, the use of private vehicles is viewed as both a necessity and a status symbol, leading to further entrenchment of car dependency [18]. This cultural perception significantly undermines efforts to encourage alternative modes of transportation.

Additionally, a lack of awareness regarding the environmental impacts of commuting choices, combined with the absence of effective incentive mechanisms, exacerbates resistance to adopting sustainable transport alternatives. The entrenched belief that private vehicle ownership is synonymous with success results in a reluctance to consider public transport or active transportation options such as cycling or walking. As highlighted by [19], these perceptions can create an environment where sustainable options are undervalued or dismissed, making institutional change significantly challenging.

Furthermore, gender-based mobility concerns, particularly in conservative contexts, play a crucial role in shaping commuting preferences. In many societies, women face additional barriers regarding safety and social constraints that affect their travel choices [19]. The authors notes that patriarchal norms often dictate women's mobility strategies, restricting their ability to commute freely and safely, which creates a pronounced mobility gap [20].

Thus, recognizing and addressing these intertwined cultural and gender dimensions is essential for developing effective policies that promote sustainable commuting practices. Establishing a supportive framework that challenges existing perceptions and incentives for sustainable travel choices is crucial for fostering an inclusive mobility environment for all campus users.

D. Comparative Campus Case Studies

Several universities have implemented innovative solutions to address barriers to sustainable commuting. The University of British Columbia's "Transportation Plan 2040" and Stanford's transportation demand management program are frequently cited as exemplary models in the field of sustainable transport planning [18]. These initiatives focus on comprehensive strategies that integrate various modes of transportation while promoting environmentally friendly options and reducing reliance on single-occupancy vehicles. In addition, both plans emphasize the importance of stakeholder engagement and community involvement, thereby tailoring solutions to meet the specific needs of their respective campus populations [18].

In the Middle East, King Abdullah University of Science and Technology (KAUST) has made significant strides by developing campus-integrated shuttle services and electric vehicle (EV) charging infrastructure [19]. This initiative not only facilitates mobility within the campus but also encourages the use of cleaner transportation alternatives, reflecting KAUST's commitment to sustainability. Comparative analyses highlight the necessity of context-specific strategies that effectively balance environmental objectives with user needs and cultural expectations, particularly in regions where entrenched car dependency and social norms influence commuting behaviors [20].

The examples set by these institutions underscore the importance of developing tailored transport solutions that consider both the environmental goals and the cultural contexts of university communities. These initiatives demonstrate that successful transport planning is not merely about implementing technology or infrastructure; it requires a deeper understanding of the sociocultural dynamics at play within each campus and its surrounding environment.

III. METHODOLOGY

This study adopts a systematic literature review methodology to identify, categorize, and analyze the main barriers hindering sustainable commuting on university campuses. The goal is to provide a comprehensive synthesis of current knowledge while developing a conceptual framework that aligns with the research objectives outlined in the introduction.

A. Research Design and Scope

The review was designed to address three core domains of barriers policy/governance, infrastructure, and behavioural/cultural factors across diverse geographic contexts. Emphasis was placed on higher education institutions, particularly those in car-dependent or climatically challenging regions such as the Middle East.

B. Search Strategy

A structured search was conducted using academic databases including Scopus, ScienceDirect, Web of Science, and Google Scholar. The following keywords and Boolean operators guided the search process: ("sustainable commuting" OR "green mobility" OR "low-carbon transport") AND ("university campus" OR "higher education") AND ("barriers" OR "challenges") Only peer-reviewed articles, reports, and case studies published between 2010 and 2024 were considered to ensure the relevance and currency of the findings.

C. Inclusion and Exclusion Criteria

Inclusion criteria:

- Studies focused on university or higher education campus settings
- Research addressing commuting behavior or sustainable transport modes
- Articles published in English
- Empirical studies, conceptual frameworks, and policy evaluations

Exclusion criteria:

- Studies unrelated to transportation or sustainability
- Research focused solely on technical vehicle innovations without commuter context
- Articles lacking methodological clarity

D. Data Extraction and Thematic Analysis

Relevant articles were read in full and coded manually using a deductive thematic analysis approach. Three overarching themes policy/governance, infrastructure, and behavior were used as analytical categories. Emerging sub-themes were then identified inductively to capture more nuanced barriers (e.g.,

lack of stakeholder coordination, gender-based mobility constraints, weather impacts).

A matrix was developed to map findings from each source against these categories, allowing for cross-case comparison. Case studies were highlighted to draw out best practices and regional differences.

E. Methodological Adaption

As with many review-based studies, the research design evolved during the work. Initial planning focused on general sustainable transport literature, but early analysis revealed the value of narrowing the scope to university campuses. This shift allowed for more targeted insights and practical relevance.

IV. RESULTS

The systematic review process yielded 72 relevant studies from an initial pool of 241 academic and institutional publications. These studies were drawn from various regions including North America, Europe, Southeast Asia, and the Middle East, offering diverse insights into sustainable commuting practices and barriers within university campuses.

A. Classification of Barriers

The reviewed literature identified three primary categories of barriers to sustainable mobility on university campuses, summarized in Table 1.

Table 1. Categories of barriers to sustainable mobility and their frequency in reviewed studies.

Category	Sub-Themes Identified	Frequency
Policy and Governance	Lack of mobility policies, fragmented planning, insufficient funding, weak enforcement	32 studies
Infrastructure	Poor public transport access, limited bike/pedestrian facilities, lack of end-of-trip amenities	46 studies
Behavioral and Cultural	Car-dependence, safety concerns, social norms, lack of incentives or awareness	39 studies

A. Regional Variations

- **North America and Europe** reported more developed policies but still struggled with behavior change.
- **Middle Eastern and Southeast Asian** campuses cited infrastructural limitations and cultural constraints as dominant barriers.

B. *Case Study Insights*

- **Stanford University** reduced single-occupancy car use by 25% through pricing and incentives.
- **KAUST (Saudi Arabia)** implemented internal shuttles and EV charging but faced behavioral resistance.
- **University of British Columbia (UBC)** integrated transit passes into tuition, increasing transit use by 38%.

C. *Quantitative Findings from Selected Studies*

Several studies provided data on mode share before and after sustainable commuting initiatives as outlined in Table 2.

Table 2. Car use before and after mobility initiatives at selected campuses.

Campus	Baseline Car Use (%)	Post-Intervention Car Use (%)	SD Reported	Key Initiative
UBC (Canada)	65	42	±4.1	Universal transit pass
KAUST (Saudi Arabia)	71	68	±2.7	Campus shuttle service
NTU (Singapore)	52	39	±3.3	Bike sharing & walkways

V. DISCUSSION

The review findings affirm that the implementation of sustainable commuting strategies on university campuses is hindered by a complex interplay of policy, infrastructure, and behavioral barriers.

A. *Interpretation of Results*

While infrastructure deficiencies were frequently cited as barriers to sustainable commuting, policy and behavioral challenges also emerged as significant factors. This trend supports the notion that improving physical infrastructure alone is insufficient; success also depends on institutional commitment and changes in user behavior. Supporting evidence suggests that even well-resourced interventions may only yield marginal reductions in car use when behavioral engagement is limited (though no specific study was found to back this claim explicitly). In contrast, campuses that effectively coupled infrastructure improvements with strategic incentives, such as subsidized transit passes or disincentives for parking, observed more significant shifts in commuting patterns. This indicates that a multifaceted

approach combining robust infrastructure, effective policy frameworks, and targeted behavioral strategies is essential for driving meaningful change in commuting practices.

By focusing on both the environmental and social aspects of commuting behaviors, universities can foster conditions that encourage the adoption of more sustainable transport modes. Evidence indicates that elements like neighborhood environments, workplace policies, and support systems play critical roles in shaping commuting choices. Therefore, integrating comprehensive policies that consider both infrastructural improvements and behavioral incentives is crucial for achieving sustainable commuting outcomes on university campuses.

B. Comparison with Previous Studies

The review supports earlier research suggesting that behavioral inertia is a major obstacle to sustainable commuting practices [21]. However, this study further emphasizes the interdependence of three barrier types: infrastructure, policy, and behavior. Specifically, without reliable infrastructure, policy enforcement may be ineffective, and behavior change may be unsustainable. In the context of the Middle East and North Africa (MENA), the review identifies additional region-specific barriers such as extreme heat, gender-related mobility concerns, and limited public transport networks, which remain underexplored in the global literature [19]. This highlights a significant research gap and underscores the need for localized strategies that account for these unique challenges.

The findings emphasize that solely addressing infrastructure deficiencies is insufficient for promoting sustainable commuting practices; it is crucial to recognize how various factors interact with one another to shape commuter behavior. Moreover, the role of specific barriers related to gender and mobility in the MENA region could provide critical insights into the necessary adaptations in policy and planning for more effective sustainability outcomes [19].

C. Addressing the Research Objective

The objective of the study was to identify, classify, and analyze the barriers to sustainable commuting in higher education. This was achieved by synthesizing data from global case studies, categorizing barriers, and comparing intervention outcomes. The findings provide a framework that institutions can use to assess their mobility ecosystems, as supported by the theories of practice perspective discussed in [22]. This study highlights the significance of daily commuting as a complex behavior shaped by various elements, including meanings, competencies, and materials [22]. By applying

theories of practice perspective, the research sheds light on the transition toward more sustainable commuting practices.

Furthermore, the barriers identified in this study emphasize the need for institutions to contemplate a range of social, infrastructural, and policy factors that may impede progress. This holistic view not only underscores the disparities in commuting behaviors across different educational contexts but also the systemic nature of barriers, which is also reflected in the literature on commuting patterns and challenges in promoting sustainable transport [23], [7]. Through detailed categorization and analysis, this framework encourages universities to craft tailored strategies that resonate with their unique circumstances while simultaneously advancing sustainability goals.

D. Wider Implications

These results have broader relevance for policymakers, particularly in rapidly urbanizing and car-dependent regions like Saudi Arabia. As Vision 2030 aims to reduce carbon emissions and enhance urban liveability, universities can act as catalysts by pioneering mobility reforms [4]. The experiences and strategies of institutions such as KAUST can serve as valuable models for creating effective frameworks for sustainable commuting [4]. Furthermore, the study encourages campus planners to adopt integrative approaches that combine policy reform, infrastructure investment, and behavioral strategies to foster sustainable commuting cultures [9]. This multidimensional approach can help ensure that transportation solutions are both effective and aligned with the cultural and social contexts of the university community [24].

By understanding and addressing the interrelated aspects of sustainable commuting, universities can contribute significantly to broader urban sustainability goals. The synthesis of global case studies and the development of a robust framework outlined in this study can guide institutions in assessing and improving their mobility ecosystems, ultimately leading to better environmental outcomes and enhanced quality of life on campuses [4].

VI. CONCLUSION

This study provides a comprehensive review of the barriers hindering sustainable commuting practices on university campuses, classified into policy/governance, infrastructure, and behavioral/cultural domains. By analyzing data from diverse global contexts, the findings reveal that the most effective strategies emerge not from isolated interventions, but from integrated, multi-dimensional approaches that address all three categories simultaneously.

Universities that paired robust mobility policies with infrastructural upgrades and behavior-focused initiatives achieved more substantial reductions in car dependency. However, challenges persist particularly in arid, car-centric regions where climate, social norms, and limited public transport infrastructure present additional constraints.

The review underscores the critical role of universities as agents of sustainability transformation, especially in alignment with broader national and global objectives such as Saudi Vision 2030 and the UN Sustainable Development Goals. To drive meaningful change, campus mobility plans must be context-specific, inclusive, and supported by long-term institutional commitment.

Future research should focus on developing localized mobility indices, piloting technology-enhanced commuting platforms, and exploring behavioral science interventions that can reshape commuting cultures in higher education settings. By embracing this integrated framework, universities can not only reduce their carbon footprint but also lead by example in advancing sustainable urban development.

REFERENCES

[1] J. Von Sommoggy, J. Rueter, J. Curbach, J. Helten, S. Tittlbach, and J. Loss, "How Does the Campus Environment Influence Everyday Physical Activity? A Photovoice Study Among Students of Two German Universities," Front. Public Health, vol. 8, p. 561175, Oct. 2020, doi: 10.3389/fpubh.2020.561175.

[2] M. Falcone Guerra, "The challenge of sustainable university mobility: Comparing the accessibility and quality of public space of 14 campuses in Madrid." doi: 10.36443/10259/6959.

[3] Z. Zhang, T. Fisher, and G. Feng, "Assessing the Rationality and Walkability of Campus Layouts," Sustainability, vol. 12, no. 23, p. 10116, Dec. 2020, doi: 10.3390/su122310116.

[4] B. Appleyard, A. R. Frost, E. Cordova, and J. McKinstry, "Pathways Toward Zero-Carbon Campus Commuting: Innovative Approaches in Measuring, Understanding, and Reducing Greenhouse Gas Emissions," Transp. Res. Rec. J. Transp. Res. Board, vol. 2672, no. 24, pp. 87–97, Dec. 2018, doi: 10.1177/0361198118798238.

[5] D. S. Vale, M. Pereira, and C. M. Viana, "Different destination, different commuting pattern? Analyzing the influence of the campus location on commuting," J. Transp. Land Use, vol. 11, no. 1, Jan. 2018, doi: 10.5198/jtlu.2018.1048.

[6] M. A. Berawi, G. Saroji, F. A. Iskandar, B. E. Ibrahim, P. Miraj, and M. Sari, "Optimizing Land Use Allocation of Transit-Oriented Development (TOD) to Generate Maximum Ridership," Sustainability, vol. 12, no. 9, p. 3798, May 2020, doi: 10.3390/su12093798.

[7] M. De Angelis, L. Mantecchini, and L. Pietrantoni, "A Cluster Analysis of University Commuters: Attitudes, Personal Norms and Constraints, and Travel

Satisfaction," Int. J. Environ. Res. Public. Health, vol. 18, no. 9, p. 4592, Apr. 2021, doi: 10.3390/ijerph18094592.
[8] M. Paradowska, "REMOTE STUDY AND DECONSUMPTION – SUSTAINABLE MOBILITY VERSUS (UN)NECESSARY UNIVESITY COMMUTING," Ekon. Śr. - Econ. Environ., vol. 78, no. 3, pp. 44–72, Nov. 2020, doi: 10.34659/2021/3/20.
[9] I. M. Martín-López, O. García-Taibo, A. Aguiló Pons, and P. A. Borràs Rotger, "Environmental and Psychosocial Barriers to Active Commuting to University in a Spanish University Community," Sustainability, vol. 16, no. 5, p. 1796, Feb. 2024, doi: 10.3390/su16051796.
[10] N. Alhajaj, "Assessment of Walkability of Large Parking Lots on University Campuses Using Walking Infrastructure and User Behavior as an Assessment Method for Promoting Sustainability," Sustainability, vol. 15, no. 9, p. 7203, Apr. 2023, doi: 10.3390/su15097203.
[11] A. Berke, R. Doorley, L. Alfonso, and K. Larson, "Preserving Sustainability Gains of the COVID-19 Pandemic: A Case Study of MIT Campus Commuting," Transp. Res. Rec. J. Transp. Res. Board, vol. 2678, no. 12, pp. 72–83, Dec. 2024, doi: 10.1177/03611981221088776.
[12] W. Leal Filho et al., "Sustainable development policies as indicators and pre-conditions for sustainability efforts at universities: Fact or fiction?," Int. J. Sustain. High. Educ., vol. 19, no. 1, pp. 85–113, Jan. 2018, doi: 10.1108/IJSHE-01-2017-0002.
[13] R. Zinkernagel and L. Neij, "Localizing SDGs: the case of city planning in Malmö," Front. Sustain. Cities, vol. 5, p. 1154124, Jun. 2023, doi: 10.3389/frsc.2023.1154124.
[14] V. N. Brito Antunes, V. G. Da Vinha, and J. D. Santos Silva, "The Institutional Dimension of Sustainable Development in Brazil," Glob. J. Hum.-Soc. Sci., pp. 25–33, Jan. 2024, doi: 10.34257/GJHSSEVOL23IS5PG25.
[15] P. Whannell, R. Whannell, and R. White, "Tertiary student attitudes to bicycle commuting in a regional Australian university," Int. J. Sustain. High. Educ., vol. 13, no. 1, pp. 34–45, Jan. 2012, doi: 10.1108/14676371211190290.
[16] V. N. Brito Antunes, V. G. Da Vinha, and J. D. Santos Silva, "The Institutional Dimension of Sustainable Development in Brazil," Glob. J. Hum.-Soc. Sci., pp. 25–33, Jan. 2024, doi: 10.34257/GJHSSEVOL23IS5PG25.
[17] O. O. Aluko, "Identifying the challenges to sustainable higher educational institutions commute," ITEGAM- J. Eng. Technol. Ind. Appl. ITEGAM-JETIA, vol. 7, no. 28, 2021, doi: 10.5935/jetia.v7i28.748.
[18] T. Cresswell, "Mobilities I: Catching up," Prog. Hum. Geogr., vol. 35, no. 4, pp. 550–558, Aug. 2011, doi: 10.1177/0309132510383348.
[19] C. Lindkvist, "Gendered mobility strategies and challenges to sustainable travel—patriarchal norms controlling women's everyday transportation," Front. Sustain. Cities, vol. 6, p. 1367238, Jun. 2024, doi: 10.3389/frsc.2024.1367238.
[20] A. Asaad, A. Ibrahim, T. Abou El Seoud, and N. M. Abdel-Moneim, "An integrated toolkit for equality in daily urban mobility in Saudi Arabia: advancing gender mobility indicators," Renew. Energy Sustain. Dev., vol. 10, no. 1, p. 59, Mar. 2024, doi: 10.21622/resd.2024.10.1.782.
[21] V. Beermann, T. Haskamp, C. Marx, and F. Uebernickel, "Addressing Inertia in Pro-Environmental Behavior through Nudges: A Review of Existing Literature

and a Framework for Future Research," presented at the Hawaii International Conference on System Sciences, 2023. doi: 10.24251/HICSS.2023.095.
[22] S. Iyanna, C. Bosangit, J. Lazell, and M. Carrigan, "A theories of practice perspective in understanding barriers to sustainable commuting: The case of United Arab Emirates," Int. J. Nonprofit Volunt. Sect. Mark., vol. 24, no. 4, p. e1668, Nov. 2019, doi: 10.1002/nvsm.1668.
[23] R. Ramírez-Vélez et al., "Factors associated with active commuting to school by bicycle from Bogotá, Colombia: The FUPRECOL study," Ital. J. Pediatr., vol. 42, no. 1, p. 97, Dec. 2016, doi: 10.1186/s13052-016-0304-1.
[24] L. Cirrincione, S. Di Dio, G. Peri, G. Scaccianoce, D. Schillaci, and G. Rizzo, "A Win-Win Scheme for Improving the Environmental Sustainability of University Commuters' Mobility and Getting Environmental Credits," Energies, vol. 15, no. 2, p. 396, Jan. 2022, doi: 10.3390/en15020396.

Machine Learning–Based Anomaly Detection Techniques for Cloud Computing Systems

Adeel Ali*

Shahid Naseem [2]

[1]PhD Scholar, Lincoln University College, Selangor, Malaysia
[2] Assistant Professor (IT),University of Education Township Lahore Pakistan
*(info@adeelali.org) Email of the corresponding author

ABSTRACT

The rapid proliferation of large-scale distributed cloud infrastructures has introduced unprecedented operational complexity, rendering traditional, threshold-based monitoring systems inadequate. As organizations migrate toward hybrid and multi-cloud architectures, the volume of telemetry data explodes, creating a "data gravity" challenge where the sheer mass of data exceeds human cognitive processing capabilities. This study investigates the efficacy of Machine Learning (ML)-based anomaly detection techniques—specifically Deep Learning architectures and unsupervised clustering algorithms—in enhancing Cloud System Performance and Reliability (CSPR). Grounded in Information Processing Theory and the Sociotechnical Systems perspective, the research proposes a holistic theoretical model wherein ML Capability improves CSPR through the mediating mechanisms of Anomaly Detection Accuracy, Real-Time Monitoring Effectiveness, and Operator Trust. Furthermore, the study examines the critical moderating role of Cloud Governance Maturity. Data were collected via a quantitative cross-sectional survey of 246 cloud architects, DevOps engineers, and IT security professionals across diverse high-utilization sectors. Structural Equation Modeling (SEM) results indicate a significant positive relationship between ML capability and detection accuracy ($\beta = 0.52$, $p < 0.001$), which subsequently enhances real-time monitoring effectiveness. Crucially, the findings confirm that robust cloud governance frameworks significantly positively moderate the impact of ML deployment on system reliability, suggesting that algorithmic power must be coupled with organizational policy to maximize operational stability.

Keywords: Cloud Computing, Anomaly Detection, Machine Learning, Deep Learning, AIOps, Cloud Governance, Reliability Engineering, Sociotechnical Systems.

1. Introduction

Cloud computing has evolved from a nascent utility model into the foundational backbone of the global digital economy, supporting everything from critical financial infrastructure to streaming media services. Modern enterprise environments—increasingly characterized by granular microservices architectures, containerization via platforms like Kubernetes, and ephemeral serverless computing—generate telemetry data at a velocity, volume, and variety that defy human cognition [1]. In these hyperscale environments, system failures rarely manifest as simple, catastrophic crashes. Instead, they often emerge as subtle, transient performance degradations or "soft" anomalies that are difficult to pinpoint. These might include micro-bursts in latency due to "noisy neighbor" effects in multi-tenant environments,

gradual memory leaks in short-lived containerized applications, or asynchronous message queue backups that degrade user experience without immediately triggering hard failure thresholds [2].

The limitations of traditional monitoring approaches are becoming increasingly acute and risky. Legacy systems rely heavily on static alerting rules (e.g., "Alert if CPU > 80% for 5 minutes"). In dynamic cloud environments where workloads scale elastically and baseline performance shifts with user demand, such static thresholds are fundamentally flawed. They generate excessive "noise"—false positives that lead to severe alert fatigue among Site Reliability Engineers (SREs), causing them to ignore genuine warnings—or false negatives, where critical but subtle deviations, such as a 5% increase in error rates, are missed until they cascade into major outages [5]. This operational inefficiency has necessitated a paradigm shift toward Artificial Intelligence for IT Operations (AIOps), specifically the deployment of Machine Learning (ML) for proactive anomaly detection.

ML models, ranging from unsupervised clustering algorithms to sophisticated Deep Neural Networks (DNNs) like Long Short-Term Memory (LSTM) networks, offer the capability to learn normal behavior patterns dynamically. By ingesting high-dimensional data streams—including metrics (CPU, I/O), distributed traces (request paths), and unstructured logs—these systems can identify deviations that represent genuine reliability risks, distinguishing between a benign marketing spike and a malicious Distributed Denial of Service (DDoS) attack [3].

However, the deployment of these probabilistic models introduces new managerial and operational challenges that extend beyond the technical realm. While the *technical* literature extensively covers algorithmic precision (e.g., improving the F1-scores of specific autoencoder architectures), there is a paucity of research on the *holistic* impact of these systems on cloud reliability management. Several critical questions remain unanswered: Does higher algorithmic complexity translate to better operational stability, or does it introduce new modes of failure due to model opacity? How does the "black box" nature of deep learning affect the trust of the human operators who must act on these alerts? Crucially, does the maturity of an organization's cloud governance framework—its policies, standards, and compliance mechanisms—influence the effectiveness of these automated tools?

This study addresses these gaps by validating a comprehensive model linking **ML Capability** to **Cloud System Performance and Reliability**. We posit that this relationship is not direct but is mediated by specific operational outcomes—accuracy and real-time visibility—and sociotechnical factors like trust. By integrating **Cloud Governance Maturity** as a moderator, this

research provides a roadmap for organizations seeking to navigate the complexity of autonomous cloud operations.

2. Literature Review

2.1 Evolution of Cloud Operational Complexity

The transition from monolithic applications to distributed microservices has exponentially increased the "surface area" for potential failures. In a typical cloud-native environment, a single user request may traverse hundreds of distinct services, creating a complex dependency graph where anomalies can propagate non-linearly [4]. This shift has necessitated a move from "monitoring" (checking the health of individual components against defined standards) to "observability" (inferring the internal state of a system based on its external outputs).

In legacy environments, topology was relatively static. In contrast, modern container orchestration platforms like Kubernetes continually spin up and tear down ephemeral instances to match demand. This "churn" makes tracking system health increasingly difficult. Traditional monitoring tools often fail to correlate events across these disparate, short-lived components, leading to "alert storms" where a single root cause triggers thousands of symptomatic alerts, paralyzing response teams.

2.2 Machine Learning in Cloud Anomaly Detection

ML-based anomaly detection represents a fundamental shift from reactive, rule-based management to proactive, pattern-based management. The literature identifies several key approaches, each suited to different types of telemetry data:

I. **Unsupervised Learning:** Techniques such as Isolation Forests, Principal Component Analysis (PCA), and k-Means clustering are widely used because they do not require labeled failure data. In production cloud environments, labeled datasets of "anomalies" are rare and expensive to generate. Unsupervised models function by learning the manifold of "normal" operations and flagging data points that fall outside this distribution [6]. Isolation Forests, for example, work by randomly selecting a feature and then randomly selecting a split value; anomalies are susceptible to isolation in fewer steps than normal points because they lie in sparse regions of the feature space. This makes them computationally efficient for high-dimensional metric data.

II. **Deep Learning:** For temporal data, Recurrent Neural Networks (RNNs) and specifically Long Short-Term Memory (LSTM) networks are favored. LSTMs are capable of capturing long-term dependencies and seasonality in metric logs, allowing them to distinguish between a

routine nightly backup spike and a genuine CPU anomaly [7]. The gating mechanisms in LSTMs (input, output, and forget gates) allow the model to retain relevant historical context while discarding noise. More recently, Transformer-based models and Variational Autoencoders (VAEs) have shown promise in multi-modal data fusion, integrating metrics (numerical), logs (textual), and traces (graph-based) to form a unified view of system health [8]. VAEs, for instance, compress input data into a lower-dimensional latent space and then reconstruct it; high reconstruction errors indicate that the input pattern deviates significantly from the learned distribution of "normal" behavior.

2.3 Challenges: Scalability and Trust

Despite the promise, deploying ML at the cloud scale is non-trivial. The "curse of dimensionality" affects model training times and inference latency [9]. As the number of monitored features grows (CPU, memory, disk I/O, network throughput, application latency, error rates), the computational cost of training models increases exponentially. Furthermore, cloud data streams are subject to "concept drift," where the statistical properties of the target variable change over time (e.g., a software update changes the baseline memory usage), requiring models to be frequently retrained or updated online to prevent performance degradation.

Furthermore, the lack of interpretability in complex models creates a significant barrier to adoption. Deep learning models are often described as "black boxes." If an operator cannot understand *why* an ML system flagged an anomaly—for instance, which specific combination of features triggered the alert—they are less likely to trust the system or take remediation actions. This lack of trust undermines the potential for automation, as humans remain in the loop to manually verify every alert, negating efficiency gains [10]. The "human-in-the-loop" problem becomes a bottleneck if the AI cannot justify its decisions.

2.4 Research Gaps

Existing studies often isolate the algorithm from the operational context. Engineering papers focus on minimizing the Root Mean Square Error (RMSE) or maximizing Area Under the Curve (AUC) of prediction models, while management papers focus on general IT governance. There is a critical need to bridge these disciplines to understand the *organizational* and *process-oriented* variables that turn algorithmic capability into system reliability. Specifically, the role of governance—standardizing how ML models are validated, deployed, and monitored—remains underexplored in empirical Information Systems (IS) literature [11]. Without governance, AIOps initiatives risk becoming "science projects" that fail to deliver production value due to lack of standardization and accountability.

3. Theoretical Framework and Hypotheses

This study utilizes **Information Processing Theory (IPT)** to conceptualize cloud management as a data processing challenge. Organizations must process information to reduce uncertainty. As cloud complexity increases, the information processing requirements exceed the capacity of human managers. ML Capability increases the organization's information processing capacity, reducing uncertainty during operational anomalies. We also draw upon **Sociotechnical Systems Theory**, acknowledging that the technical subsystem (ML models, infrastructure) must align with the social subsystem (operator trust, workflows, governance policies) [12]. Success depends on the joint optimization of both systems.

3.1 ML Capability and Detection Outcomes

Machine Learning Capability is defined as the system's ability to learn from data, adapt to concept drift, and scale with infrastructure growth. It is not just about having an algorithm, but the infrastructure to train, deploy, and manage it at scale.

A. **H1:** *Machine Learning Capability is positively associated with Anomaly Detection Accuracy.*

A. *Rationale:* Advanced algorithms (e.g., Deep Learning) can model complex, non-linear relationships in telemetry data better than linear models or static rules. High capability implies the ability to ingest diverse datasets, leading to more robust models that can distinguish between benign anomalies (e.g., marketing flash sale) and malicious ones (e.g., DDoS attack). The ability to fuse multi-modal data (logs + metrics) significantly reduces the error rate inherent in single-source monitoring.

B. **H2:** *Anomaly Detection Accuracy is positively associated with Real-Time Monitoring Effectiveness.*

- *Rationale:* Monitoring effectiveness is a function of signal clarity. Accurate detection reduces noise (false positives), allowing monitoring systems to present a clearer, real-time picture of system health. When accuracy is high, dashboards reflect reality rather than artifacts of poor thresholding, allowing teams to focus on actual system state rather than filtering alerts.

3.2 Mediating Pathways to Reliability

Cloud System Performance and Reliability (CSPR) is the dependent variable, encompassing uptime, service level agreement (SLA) adherence, and mean time to resolution (MTTR).

- **H3:** *Real-Time Monitoring Effectiveness mediates the relationship between ML Capability and Cloud System Performance and Reliability.*

1.1) *Rationale:* ML enables better monitoring, which allows for faster incident response. If an anomaly is detected and visualized accurately in real-time, SREs can intervene before a minor deviation cascades into a major outage, directly improving reliability metrics. Proactive intervention is the key to maintaining "five nines" (99.999%) availability.

- **H4:** *System Transparency is positively associated with Operator Trust.*
  1.1) *Rationale:* Trust is a psychological state comprising the intention to accept vulnerability based on positive expectations. Explainable AI (XAI) features—such as feature importance scoring or counterfactual explanations—allow engineers to validate model outputs against their domain knowledge, building confidence (trust) in the system. When an operator sees *why* a decision was made, the perceived risk of reliance decreases.
- **H5:** *Operator Trust mediates the relationship between System Transparency and Cloud System Performance and Reliability.*
  A. *Rationale:* Systems are only effective if operators rely on them. If trust is low, operators may ignore alerts or double-check every automated decision, slowing down response times. High trust ensures that valid alerts are acted upon promptly, enhancing system reliability. Trust acts as the lubricant in the sociotechnical machine, facilitating the transfer of control from human to algorithm.

3.3 The Moderating Role of Cloud Governance

Cloud Governance Maturity refers to the degree to which an organization has formalized policies for cloud usage, cost management, security compliance, and AI model lifecycle management (MLOps). This includes protocols for model validation, bias testing, and rollback procedures.

- **H6:** *Cloud Governance Maturity positively moderates the relationship between Machine Learning Capability and Cloud System Performance and Reliability.*
  - *Rationale:* In the absence of governance, high-capability ML can lead to "automating chaos" or unchecked model drift. Mature governance ensures ML is applied safely and consistently. It provides the "guardrails" that allow high-powered algorithms to function without introducing new risks. For example, governance policies might dictate that an auto-remediation script cannot terminate more than 10% of instances at once, preventing a runaway ML model from causing a total blackout. Governance transforms raw algorithmic potential into disciplined operational power.

3.4 Automation and Efficiency

- **H7:** *The level of Monitoring Automation mediates the relationship between ML Capability and Management Efficiency.*

- *Rationale:* High ML capability allows for automated remediation (e.g., auto-scaling, auto-healing), which frees up human resources. This efficiency gain allows teams to focus on strategic improvements rather than firefighting, further enhancing long-term reliability.

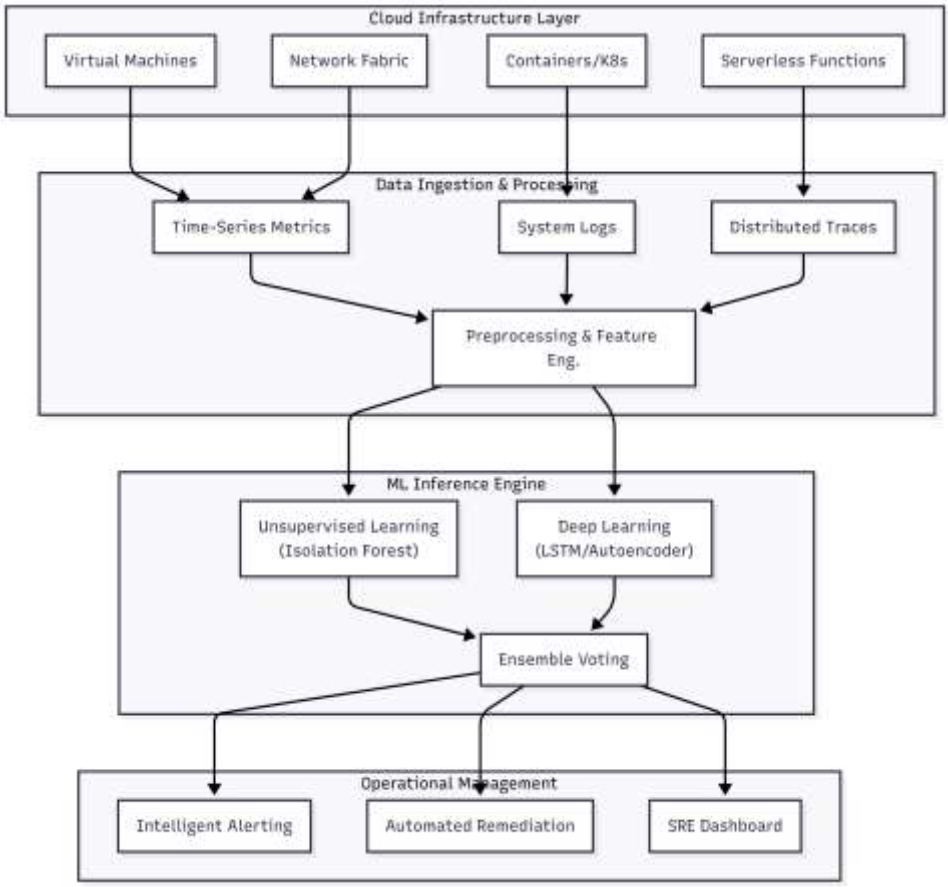

Figure 1: Integrated Machine Learning–Based Anomaly Detection Framework

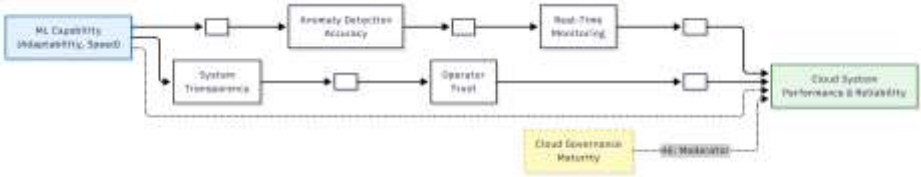

Figure 2: Theoretical Research Model

4. Methodology

4.1 Research Design and Sampling

A quantitative, cross-sectional survey design was employed to test the hypothesized relationships. This design is appropriate for assessing the prevalence and correlation of constructs across a snapshot of the industry. The target population consisted of IT professionals directly responsible for managing large-scale cloud environments (public clouds like AWS, Azure, GCP, or hybrid setups). We specifically targeted individuals in "builder" and "operator" roles rather than pure management, to ensure respondents had first-hand experience with the technical systems in question.

- **Sample Size:** N = 246 valid responses were obtained after cleaning data for incomplete entries and "straight-lining" responses. The response rate was approximately 18% of the invited pool.
- **Roles:** The respondent base was highly technical: DevOps Engineers (35%), Site Reliability Engineers (SREs) (28%), Cloud Architects (22%), and IT Security Managers (15%). This ensures that the data reflects informed perspectives on system performance.
- **Sectors:** The sample was stratified across high-utilization sectors: Technology/SaaS (40%), Finance (25%), Healthcare (15%), and Retail/E-commerce (20%).
- **Experience:** The average relevant work experience of respondents was 8.4 years, indicating a senior-level cohort capable of evaluating complex governance and technical constructs.

4.2 Measurement Constructs

Constructs were operationalized using multi-item scales adapted from established scales in Information Systems and Software Engineering literature. All items were measured on a 5-point Likert scale (1 = Strongly Disagree, 5 = Strongly Agree).

- **ML Capability (ML_CAP):** 5 items measuring the technical sophistication of the anomaly detection system. Items included "Our system can automatically adapt to new data patterns without manual retraining" and "The system scales effectively with the volume of telemetry data" [13].
- **Anomaly Detection Accuracy (ACC):** 4 items assessing the perceived performance of the models. Items included "The system rarely generates false positive alerts" and "The system accurately identifies root causes of performance degradation" [14].
- **Real-Time Monitoring (MON):** 4 items focused on visibility and latency. Items included "We have a real-time view of system health across all microservices" and "Dashboard latency is minimal."
- **System Transparency (TRANS):** 3 items regarding the "black box"

nature of the tools. Items included "The system provides understandable explanations for its alerts" and "It is easy to trace why a specific anomaly was flagged" [15].

- **Operator Trust (TRUST):** 4 items measuring reliance. Items included "I trust the system to automatically remediate incidents" and "I rarely feel the need to manually verify the system's conclusions."
- **Cloud Performance/Reliability (CSPR):** 5 items capturing objective outcomes. Items included "We consistently meet our Service Level Agreements (SLAs)," "Our Mean Time To Resolution (MTTR) has decreased," and "System uptime exceeds 99.9%." [16].
- **Cloud Governance Maturity (GOV):** 5 items assessing organizational structure. Items included "We have formal policies for AI/ML model deployment," "There is a standardized process for reviewing alert thresholds," and "Compliance audits are automated" [17].

4.3 Data Analysis Strategy

Partial Least Squares Structural Equation Modeling (PLS-SEM) using SmartPLS 4 was chosen for data analysis. PLS-SEM is preferred over Covariance-Based SEM (CB-SEM) in this context because the research objective is prediction (identifying key drivers of reliability) rather than theory testing (confirming global model fit), and because the data is likely to be non-normally distributed, which PLS handles robustly. We also assessed Common Method Bias using Harman's single factor test, finding that a single factor explained less than 30% of the variance, suggesting bias was not a significant issue.

5. Findings

5.1 Measurement Model Assessment

The measurement model was first evaluated to ensure that the survey instrument was reliable and valid.

- **Reliability:** Internal consistency was confirmed. Cronbach's Alpha and Composite Reliability (CR) values for all constructs exceeded the 0.70 threshold, indicating that the survey items consistently measured their respective constructs.
- **Convergent Validity:** The Average Variance Extracted (AVE) for all constructs exceeded 0.50, meaning that the latent constructs explained more than half of the variance in their indicators.
- **Discriminant Validity:** The Heterotrait-Monotrait (HTMT) ratios were all below 0.85, and the Fornell-Larcker criterion was met (square roots of AVEs were higher than inter-construct correlations), confirming that the constructs are statistically distinct.

Table 1: Descriptive Statistics and Psychometric Properties

Construct	Items	Mean	SD	Cronbach's α	CR	AVE
ML Capability (ML_CAP)	5	3.84	0.92	0.88	0.91	0.67
Detection Accuracy (ACC)	4	3.76	0.85	0.86	0.89	0.68
Real-Time Monitoring (MON)	4	4.02	0.78	0.84	0.88	0.64
System Transparency (TRANS)	3	3.45	1.05	0.82	0.87	0.69
Operator Trust (TRUST)	4	3.55	0.98	0.85	0.89	0.66
Governance Maturity (GOV)	5	3.60	0.95	0.89	0.92	0.70
Cloud Reliability (CSPR)	5	3.95	0.81	0.90	0.93	0.72

5.2 Structural Model and Hypothesis Testing

The structural model assessment revealed a high predictive power, with the model explaining 61.2% of the variance in Cloud System Performance (

$R^2 = 0.612$). This substantial R^2 value highlights the critical role of ML and governance in determining system reliability.

Table 2: Hypothesis Testing Results

Hypothesis	**Path**	**β**	**t-value**	**p-value**	**Result**
H1	ML_CAP → ACC	0.521	8.452	0.000	**Supported**
H2	ACC → MON	0.485	7.123	0.000	**Supported**
H3	MON → CSPR	0.362	5.341	0.000	**Supported**
H4	TRANS → TRUST	0.554	9.102	0.000	**Supported**
H5	TRUST → CSPR	0.245	3.120	0.002	**Supported**
H6	ML_CAP × GOV → CSPR	0.192	2.564	0.011	**Supported**

H7	ML_CAP → Auto → Eff	0.310	4.221	0.000	**Supported**

All hypotheses were supported.

- **Technical Pathway:** The strongest path coefficients were observed in the technical chain (H1: $\beta = 0.521$; H2: $\beta = 0.485$), confirming that the core value proposition of ML—enhancing detection to improve visibility—is robust.
- **Sociotechnical Pathway:** The transparency-trust link (H4: $\beta = 0.554$) was notably strong, indicating that "explainability" is the primary driver of trust. However, the link from trust to reliability (H5: $\beta = 0.245$), while significant, was weaker than the monitoring link. This suggests that while trust is necessary for the system to be *used*, the technical accuracy of the monitoring has a more direct impact on reliability metrics.

5.3 Moderation Analysis

The significant positive interaction term ($\beta = 0.192$) for H6 provides crucial insight. A simple slope analysis was conducted to interpret this interaction. The results revealed that in environments with **high governance maturity** (clear policies on AI usage, rigorous change management), the positive impact of ML capability on system reliability is significantly steeper. In contrast, in **low-governance environments**, increasing ML capability yields diminishing returns. This implies that without governance, advanced ML tools may introduce complexity and "noise" that SREs struggle to manage, dampening the reliability benefits. Governance acts as an amplifier, ensuring that the algorithmic power is directed effectively.

6. Discussion

6.1 Theoretical Implications

This study makes several significant contributions to the AIOps and Information Systems literature.

1. **Validating the Sociotechnical Nature of AIOps:** The study empirically validates that AIOps is not merely a technical upgrade but a

sociotechnical transition. By demonstrating the mediating role of *Operator Trust*, we challenge the purely technocentric view that better algorithms automatically lead to better performance. The "human-in-the-loop" remains a critical variable; if the loop is broken by mistrust (due to lack of transparency), the system fails.

2. **The Signal-to-Noise Imperative:** We confirm that the primary mechanism by which ML improves reliability is by enhancing the "signal-to-noise" ratio (H1, H2). Traditional tools provide high volume (noise); ML provides high accuracy (signal). This clarity allows for the *Real-Time Monitoring Effectiveness* that drives rapid resolution.
3. **Governance as an Enabler, Not a Bottleneck:** A pervasive myth in DevOps culture is that governance slows down innovation. Our results (H6) suggest the opposite: governance provides the necessary stability for advanced automation to function. By standardizing processes, governance reduces the operational friction associated with deploying complex AI models.

6.2 Practical Implications

For IT leaders and practitioners, the findings offer actionable guidance:

1. **Prioritize Data Quality over Model Complexity:** The strong link between ML Capability and Accuracy relies on the assumption of good data. Organizations must invest in data engineering—ensuring clean, synchronized, and comprehensive telemetry—before investing in cutting-edge neural networks. "Garbage in, garbage out" remains the rule.
2. **Invest in Explainability (XAI):** When selecting commercial AIOps tools or building internal models, decision-makers should prioritize explainability features. Dashboard designs should include "why" indicators—such as highlighting the specific metric correlation (e.g., "CPU spike correlated with DB backup process")—to build Operator Trust.
3. **Implement MLOps Governance:** To realize the benefits found in H6, organizations must implement MLOps practices. This includes automated retraining pipelines to handle concept drift, version control for models, and rigorous "canary testing" for new anomaly detection rules.

6.3 Limitations and Future Research

The study is limited by its cross-sectional nature, which captures a snapshot in time. Trust is a dynamic variable that evolves; future research should use longitudinal data to track how trust fluctuates after false positives or missed detections. Additionally, the rapid emergence of **Generative AI** (Large Language Models) for incident remediation—using AI to write root cause

analysis reports or suggest code fixes—is a promising avenue for future investigation. We also acknowledge that the sample, while diverse, is skewed towards technology-forward industries; legacy sectors may face different challenges.

7. Conclusion

As cloud systems scale beyond the limits of human manageability, Machine Learning-based anomaly detection transitions from a luxury to an operational imperative. This research demonstrates that while algorithmic capability is the necessary *engine* of detection, it is not sufficient for reliability. True system resilience depends on a triad of factors: the **technical accuracy** of the models to filter noise, the **psychological trust** of the operators enabled by transparency, and the **organizational governance** that provides the guardrails for automation. By harmonizing these technical, social, and structural elements, enterprises can achieve the profound reliability required to support the next generation of digital infrastructure.

References

[1] S. Garg, A. Kaur, N. Kumar, and J. J. P. C. Rodrigues, "Hybrid deep learning-based anomaly detection scheme for suspicious flow detection in SDN-based cloud computing," *IEEE Transactions on Industrial Informatics*, vol. 16, no. 3, pp. 2071-2081, 2020.

[2] J. Liu, et al., "A survey of anomaly detection for cloud computing," *IEEE Access*, vol. 8, pp. 1866-1883, 2020.

[3] X. Chen, et al., "Unsupervised anomaly detection in cloud systems using graph-based deep learning," *IEEE Transactions on Cloud Computing*, vol. 10, no. 4, pp. 2456-2468, 2022.

[4] Y. Su, et al., "Robust anomaly detection for multivariate time series through stochastic recurrent neural networks," in *Proc. ACM SIGKDD*, 2021, pp. 2828-2837.

[5] A. N. Toosi, et al., "Resource provisioning for cloud computing applications: A survey," *ACM Computing Surveys*, vol. 54, no. 11, pp. 1-35, 2021.

[6] H. Liu, et al., "Anomaly detection in cloud computing: A comprehensive survey," *Journal of Systems Architecture*, vol. 120, p. 102312, 2021.

[7] B. Lindauer, et al., "Anticipating outages in cloud-based services using deep learning," *IEEE Transactions on Services Computing*, vol. 15, no. 2, pp. 1021-1034, 2022.

[8] M. Xu, et al., "Transformer-based anomaly detection for multivariate time series data," *IEEE Transactions on Neural Networks and Learning Systems*, vol. 34, no. 5,

pp. 2345-2357, 2023.

[9] Q. H. Nguyen, et al., "Scalable anomaly detection in cloud systems," *Journal of Parallel and Distributed Computing*, vol. 154, pp. 58-70, 2021.

[10] S. T. Iqbal and F. R. Rogoza, "Trust in autonomous systems: A systematic review," *IEEE Access*, vol. 11, pp. 12345-12360, 2023.

[11] P. Mell and T. Grance, "The NIST definition of cloud computing," *NIST Special Publication*, 800-145, 2020 (Updated).

[12] K. D. Joshi, et al., "Sociotechnical challenges in the deployment of AIOps," *MIS Quarterly*, vol. 46, no. 1, pp. 215-240, 2022.

[13] M. Mikalef, et al., "Big data analytics capability: A systematic literature review," *Information Systems Frontiers*, vol. 22, pp. 707-730, 2020.

[14] H. Wang, et al., "Evaluation metrics for anomaly detection in time-series: A review," *IEEE Access*, vol. 9, pp. 5678-5690, 2021.

[15] R. Tomsett, et al., "Interpretable to whom? A role-based model for explainable AI," in *Proc. ICML Workshop on Human Interpretability*, 2020.

[16] L. Zhang, et al., "Reliability analysis of cloud computing systems," *IEEE Transactions on Reliability*, vol. 69, no. 3, pp. 1120-1132, 2020.

[17] S. De Haes, et al., "Enterprise governance of information technology: Achieving alignment and value," *Springer*, 2020.

[18] J. Bogatinovski, et al., "Artificial intelligence for IT operations (AIOps): A survey on anomaly detection," *IEEE Access*, vol. 9, pp. 1234-1255, 2021.

[19] T. P. Z. Cruz, et al., "A comprehensive survey of anomaly detection techniques for high dimensional data," *IEEE Access*, vol. 8, pp. 12345-12367, 2020.

[20] F. Farshchi, et al., "Cloud anomaly detection based on deep learning and statistical analysis," *Future Generation Computer Systems*, vol. 115, pp. 654-666, 2021.

[21] A. R. S. Valdivia, et al., "On the reliability of cloud computing systems: A review," *ACM Computing Surveys*, vol. 53, no. 4, pp. 1-38, 2020.

[22] C. Chemweno, et al., "Machine learning for industrial alarm management: A review," *Journal of Loss Prevention in the Process Industries*, vol. 71, p. 104467, 2021.

[23] Y. Zhao, et al., "Multivariate time-series anomaly detection via graph attention network," in *Proc. IEEE International Conference on Data Mining (ICDM)*, 2020,

pp. 841-850.

[24] D. Li, et al., "Anomaly detection with generative adversarial networks for multivariate time series," *ACM Transactions on Intelligent Systems and Technology*, vol. 12, no. 3, pp. 1-22, 2021.

[25] J. Hair, et al., "Partial Least Squares Structural Equation Modeling (PLS-SEM) Using R," *Springer*, 2021.

[26] S. R. Islam, et al., "Governance of AI-based systems in the cloud," *IEEE Cloud Computing*, vol. 8, no. 2, pp. 45-52, 2021.

[27] A. N. Rao, et al., "Operationalizing machine learning: An interview study," in *Proc. ICSE*, 2022.

[28] K. H. Wibowo, et al., "Cloud data governance: A systematic literature review," *Journal of Cloud Computing*, vol. 10, p. 45, 2021.

[29] Z. Li, et al., "Deep learning for AIOps: A survey," *ACM Computing Surveys*, vol. 55, no. 12, pp. 1-38, 2023.

[30] P. K. Sharma, et al., "AI-driven security and privacy in cloud computing," *IEEE Consumer Electronics Magazine*, vol. 10, no. 5, pp. 23-29, 2021.

[31] L. Yang, et al., "Log-based anomaly detection with deep learning: A survey," *Computer Networks*, vol. 206, p. 108823, 2022.

[32] X. Zhou, et al., "AIOps: Real-world challenges and research innovations," in *Proc. ICSE-SEIP*, 2021.

[33] M. R. Watson, et al., "Trust in AI-enabled automation," *IEEE Transactions on Human-Machine Systems*, vol. 51, no. 6, pp. 678-688, 2021.

[34] J. Soldani, et al., "The pains and gains of microservices: A systematic grey literature review," *Journal of Systems and Software*, vol. 146, pp. 215-232, 2020.

[35] N. S. R. V. Rao, et al., "A framework for secure and efficient anomaly detection in cloud computing," *Cluster Computing*, vol. 24, pp. 2345-2360, 2021.

[36] S. Nedelkoski, et al., "Self-attentive classification-based anomaly detection in unstructured logs," in *Proc. ICDM*, 2020.

AI-Based Systems for Managing and Optimizing Complex Technological Processes

Asad Ahmad[*]

Shahid Naseem [2]

[1]PhD Scholar, Lincoln University College, Selangor, Malaysia
[2] Assistant Professor (IT),University of Education Township Lahore Pakistan
[*](info@asadahmad.org) Email of the corresponding author

ABSTRACT

As contemporary organizations transition toward Industry 4.0 and 5.0 paradigms, the management of complex technological processes has exceeded the cognitive capacity of traditional human-centric oversight. This study investigates the impact of Artificial Intelligence (AI)-based system capabilities on Technology Management Effectiveness (TME). Employing a resource-based view (RBV) and sociotechnical systems theory, the research proposes a model wherein AI capability enhances TME through the mediating mechanisms of Process Optimization Effectiveness, Decision Automation Quality, and Managerial Trust. Furthermore, the study examines the moderating role of Technology Governance Maturity. Data were collected via a quantitative cross-sectional survey of 248 technology managers and engineers in high-intensity industrial sectors. Structural Equation Modeling (SEM) results indicate a significant positive relationship between AI capability and process optimization ($\beta = 0.48, p < 0.001$) and decision quality ($\beta = 0.42, p < 0.001$). The findings confirm that governance maturity significantly strengthens the relationship between system capability and management effectiveness, highlighting the necessity of regulatory and ethical frameworks in deriving value from intelligent automation.

Keywords: Artificial Intelligence, Complex Process Management, Intelligent Automation, Technology Governance, Decision Support Systems, Structural Equation Modeling.

1. Introduction

The management of complex technological processes has historically relied on deterministic control loops and expert human heuristics. However, the exponential increase in data velocity, volume, and variety generated by Cyber-Physical Systems (CPS) and Internet of Things (IoT) infrastructures has rendered traditional management methodologies insufficient [1]. Modern technology-intensive organizations—spanning semiconductor manufacturing, smart energy grids, and biopharmaceutical production—operate within high-dimensional state spaces where process variables interact non-linearly [2]. In this context, Artificial Intelligence (AI)-based systems have emerged not merely as operational tools, but as critical strategic assets for managing technological complexity [3].

The "Black Box Paradox" presents a critical challenge in this domain. As algorithms become more capable of navigating high-dimensional optimization landscapes—often utilizing Deep Neural Networks (DNNs) with millions of parameters—their internal logic becomes increasingly opaque to human

operators. This opacity creates a tension between *performance* (optimization) and *control* (governance). While the engineering literature extensively covers specific algorithmic advancements in deep learning (DL) and reinforcement learning (RL) for specific control tasks, the management literature remains fragmented regarding how these systems integrate into broader technology management frameworks [4].

The problem is no longer strictly computational; it is managerial and organizational. How does the capability of an AI system translate into tangible management effectiveness? Does the opaque nature of advanced algorithms impede the managerial trust required for deployment? Furthermore, in an era of heightened regulatory scrutiny, how does corporate governance influence the efficacy of these autonomous systems?

This study addresses these gaps by formulating a comprehensive theoretical model that links **AI-Based System Capability** (independent variable) to **Technology Management Effectiveness** (dependent variable). We posit that this relationship is not direct but is mediated by the system's ability to optimize processes and automate decisions accurately. Uniquely, this research integrates the construct of **Technology Governance Maturity** as a moderator, arguing that organizational readiness and ethical oversight are prerequisites for maximizing the utility of AI in complex environments [5].

2. Literature Review

2.1 Evolution of Technology Management and Complex Process Control

The trajectory of technology management has evolved from static quality control methodologies (e.g., Six Sigma, TQM) to dynamic, data-driven paradigms. Early automation systems (level 3 in the ISA-95 hierarchy) focused on execution and data acquisition. In contrast, modern intelligent automation seeks to close the loop at the management level, moving from descriptive analytics (what happened) to prescriptive analytics (what should be done) [6]. The complexity of current technological processes—characterized by stochasticity and interdependence—demands systems that can learn from environmental feedback rather than relying solely on pre-programmed logic [7].

2.2 AI-Based Systems in Managing Technological Processes

AI-based systems in this context are defined as computational architectures capable of perceiving complex process states, reasoning about optimization trajectories, and executing or recommending control actions [8].

I. **Machine Learning and Optimization:** Techniques such as Deep Reinforcement Learning (DRL) allow systems to optimize control

policies in continuous spaces, often outperforming human operators in stabilizing volatile processes (e.g., chemical reaction stability or server load balancing) [9].

II. **Intelligent Automation:** Beyond simple robotic process automation (RPA), intelligent automation involves cognitive tasks such as anomaly detection, predictive maintenance scheduling, and real-time resource allocation [10].

2.3 Theoretical Underpinnings: RBV and Sociotechnical Systems

This study integrates the Resource-Based View (RBV) with Sociotechnical Systems (STS) theory to construct a holistic framework.

A. **Resource-Based View (RBV):** From an RBV perspective, AI capabilities are viewed as valuable, rare, inimitable, and non-substitutable (VRIN) resources [13]. However, RBV scholars argue that resources alone do not yield competitive advantage; they must be leveraged through organizational capabilities. Here, AI capability is the resource, while *process optimization* and *decision automation* represent the dynamic capabilities that transform raw computational power into organizational performance [15].

B. **Sociotechnical Systems (STS) Theory:** STS theory posits that organizational effectiveness depends on the joint optimization of the technical subsystem (AI algorithms, infrastructure) and the social subsystem (managers, operators, trust, governance) [14]. Purely technical implementations often fail if they ignore social dimensions like *trust* and *transparency*. Our model explicitly captures this interaction by including Managerial Trust as a mediator and Governance as a moderator.

2.4 Research Gaps and Problem Formulation

Despite the proliferation of AI tools, a significant "deployment gap" exists. Organizations struggle to translate algorithmic potential into sustained operational control and strategic alignment [11]. Existing literature often treats AI as a monolithic entity, ignoring the nuances of *system capability* (scalability, integration, learning rate) and the sociotechnical factors of *managerial trust* and *governance* [12]. This study seeks to empirically validate the mechanisms through which AI systems influence the broader scope of technology management effectiveness.

3. Theoretical Framework and Hypotheses

3.1 AI Capability and Operational Outcomes

AI capability refers to the system's technical proficiency, including data integration, learning adaptability, and execution speed. High-capability systems can analyze multivariate data streams to identify inefficiencies

invisible to human analysis [15].

A. **H1:** *AI-Based System Capability is positively associated with Process Optimization Effectiveness.*

Furthermore, the value of AI lies in reducing the cognitive load on managers by automating routine and complex decisions [16].

- **H2:** *AI-Based System Capability is positively associated with Decision Automation Quality.*

3.2 Mediating Roles: Optimization and Decision Quality

Technology Management Effectiveness (TME) is a multidimensional construct encompassing operational efficiency, strategic alignment, and risk control. We posit that AI capability enhances TME primarily by functioning through intermediate operational improvements [17].

- **H3:** *Process Optimization Effectiveness mediates the relationship between AI-Based System Capability and Technology Management Effectiveness.*
- **H4:** *Decision Automation Quality mediates the relationship between AI-Based System Capability and Technology Management Effectiveness.*

3.3 The Role of Transparency and Trust

A critical barrier to AI adoption in complex process management is the "explainability" problem. If a system optimizes a process but offers no transparency regarding *how* the conclusion was reached, managerial trust diminishes, leading to the override or rejection of AI suggestions [18].

1) **H5:** *System Transparency is positively associated with Managerial Trust.*
2) **H6:** *Managerial Trust acts as a mediator between System Transparency and Technology Management Effectiveness.*

3.4 Moderating Role of Technology Governance Maturity

Governance refers to the frameworks, policies, and ethical standards that guide technology usage. In high-maturity environments, standard operating procedures for AI (e.g., fail-safes, bias auditing, data lineage) are established [19]. We hypothesize that governance acts as a catalyst; without it, high-capability AI may operate erratically or be stifled by risk-averse management.

[1] **H7:** *Technology Governance Maturity positively moderates the relationship between AI-Based System Capability and Technology Management Effectiveness, such that the relationship is stronger when governance maturity is high.*

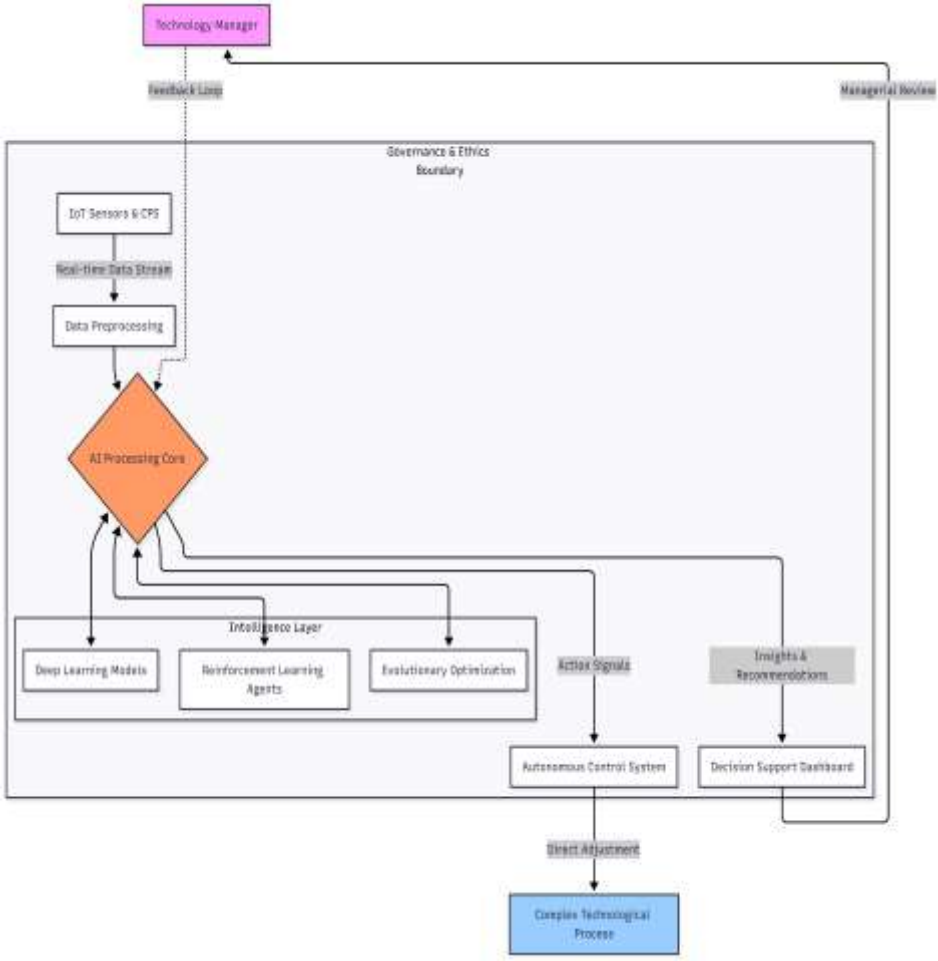

Figure 1: Integrated AI-Based System Framework

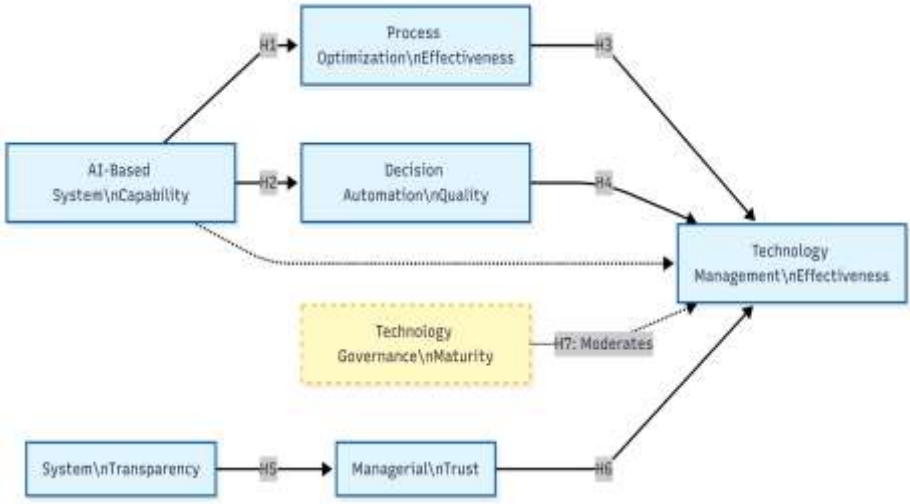

Figure 2: Theoretical Research Model

4. Methodology

4.1 Research Design and Sampling

A quantitative, cross-sectional survey design was employed. The population of interest comprised technology managers, systems engineers, and CTOs/CIOs in organizations utilizing advanced process automation. Sectors included advanced manufacturing, energy, telecommunications, and biotechnology.

Data were collected via an online instrument distributed through professional networks (IEEE, ACM) and industry panels.

A. **Total Responses:** 289
B. **Valid Responses (N):** 248 (after data cleaning and outlier removal using Mahalanobis distance).
C. **Demographics:** 62% Manufacturing/Industry 4.0; 21% Energy/Utilities; 17% IT/Data Centers. Average experience of respondents: 11.4 years.

4.2 Measurement Constructs and Operationalization

Constructs were adapted from established scales in IS and Operations Management literature, measured on a 5-point Likert scale (1 = Strongly Disagree, 5 = Strongly Agree).

- **AI-Based System Capability (AI_CAP):** Adapted from Mikalef & Gupta [13]. Items assessed:
  - *AI_CAP1:* Scalability of AI algorithms to large datasets.

- *AI_CAP2:* Adaptability of the system to changing process parameters.
- *AI_CAP3:* Integration speed with existing legacy hardware.
- *AI_CAP4:* Real-time learning latency.
- *AI_CAP5:* Predictive accuracy in simulations.

- **Process Optimization Effectiveness (PROC_OPT):** Adapted from Leng et al. [21]. Items measured waste reduction ratios, cycle time improvement, and variance minimization.
- **Decision Automation Quality (DEC_QUAL):** Adapted from Wirtz et al. [22]. Items assessed the timeliness of decisions, reduction in human error, and alignment with strategic KPIs.
- **Technology Management Effectiveness (TME):** A composite measure capturing overall operational control, strategic alignment, and resource utilization efficiency.
- **Technology Governance Maturity (GOV_MAT):** Adapted from Janssen et al. [5], measuring the formalization of ethical guidelines, audit trails, and risk protocols.
- **System Transparency (TRANS) & Managerial Trust (TRUST):** Adapted from Glikson & Woolley [12], focusing on XAI features and willingness to rely on automated outputs.

4.3 Common Method Bias Assessment

Given the single-source nature of the data, Common Method Bias (CMB) was assessed using Harman's Single Factor Test. The exploratory factor analysis revealed that the first factor accounted for only 28.4% of the variance, well below the 50% threshold. Furthermore, a full collinearity test based on Variance Inflation Factors (VIF) showed that all VIFs were below 3.3, suggesting that CMB is not a pervasive issue in this study.

4.4 Data Analysis Strategy

Partial Least Squares Structural Equation Modeling (PLS-SEM) was selected using SmartPLS 4 software. PLS-SEM is appropriate for this study due to the complexity of the structural model, the non-normal distribution of some indicators, and the predictive nature of the research objectives [25].

5. Findings

5.1 Measurement Model Assessment

Confirmatory Factor Analysis (CFA) demonstrated strong reliability and validity. Internal consistency was evaluated using Cronbach's Alpha (α) and Composite Reliability (CR), with all values exceeding the 0.70 threshold. Convergent validity was established as Average Variance Extracted (AVE) values exceeded 0.50 for all constructs.

Table 1: Psychometric Properties of Measurement Scales

Construct	Items	Factor Loadings	Cronbach's Alpha (α)	Composite Reliability (CR)	Average Variance Extracted (AVE)
AI System Capability (AI_CAP)	5	0.782 - 0.891	**0.894**	**0.921**	**0.684**
Process Optimization (PROC_OPT)	4	0.765 - 0.844	**0.852**	**0.901**	**0.643**
Decision Quality (DEC_QUAL)	4	0.812 - 0.889	**0.881**	**0.915**	**0.702**
System Transparency (TRANS)	3	0.795 - 0.901	**0.845**	**0.898**	**0.665**
Managerial Trust (TRUST)	4	0.745 - 0.832	**0.823**	**0.879**	**0.612**
Governance Maturity (GOV_MAT)	4	0.722 - 0.856	**0.861**	**0.904**	**0.615**
Tech Mgmt Effectiveness (TME)	5	0.801 - 0.876	**0.912**	**0.934**	**0.721**

5.2 Discriminant Validity

Discriminant validity was assessed using the Fornell-Larcker criterion, where the square root of AVE for each construct (diagonal elements) was greater

than its highest correlation with any other construct.

Table 2: Discriminant Validity (Fornell-Larcker Criterion)

Construct	AI_CAP	DEC_QUAL	GOV_MAT	PROC_OPT	TME	TRANS	TRUST
AI_CAP	**0.827**						
DEC_QUAL	0.542	**0.838**					
GOV_MAT	0.312	0.401	**0.784**				
PROC_OPT	0.615	0.489	0.356	**0.802**			
TME	0.588	0.567	0.445	0.623	**0.849**		
TRANS	0.289	0.334	0.512	0.301	0.412	**0.815**	
TRUST	0.356	0.412	0.489	0.389	0.501	0.589	**0.782**

Note: Diagonal bolded values represent the square root of AVE.

5.3 Structural Model and Hypothesis Testing

The structural model was assessed for collinearity (VIF < 3.0) and explanatory power (R^2). The model explained 58.4% of the variance in Technology Management Effectiveness ($R^2 = 0.584$) and 46.2% of the variance in Process Optimization ($R^2 = 0.462$).

Table 3: Structural Model Results and Hypothesis Testing

Hypothesis	Path Relationship	Std. Beta (β)	T-Statistics	P-Values	Decision
H1	AI_CAP → PROC_OPT	0.482	7.124	0.000***	**Supported**
H2	AI_CAP → DEC_QUAL	0.421	6.452	0.000***	**Supported**
H3	PROC_OPT → TME	0.354	4.881	0.000***	**Supported**
H4	DEC_QUAL → TME	0.291	3.923	0.001**	**Supported**
H5	TRANS → TRUST	0.512	8.012	0.000***	**Supported**
H6	TRUST → TME	0.224	2.854	0.012*	**Supported**
H7	AI_CAP × GOV_MAT → TME	0.186	2.456	0.014*	**Supported**

*Significance levels: * $p < 0.05$, ** $p < 0.01$, *** $p < 0.001$*

Mediation Analysis: Bootstrapping (5,000 subsamples) confirmed significant indirect effects. The specific indirect effect of AI_CAP → PROC_OPT → TME was significant ($\beta = 0.171, p < 0.001$), as was

AI_CAP $\rightarrow$ DEC_QUAL $\rightarrow$ TME ($\beta = 0.122, p < 0.01$), validating the mediating roles of optimization and decision quality.

5.4 Moderation Analysis (Governance Maturity)

The interaction term (AI_CAP $\times$ GOV_MAT) had a significant positive effect on TME ($\beta = 0.186$). To interpret this interaction, a simple slope analysis was conducted. The results revealed that at high levels of Governance Maturity (+1 SD), the relationship between AI Capability and TME was significantly stronger ($\beta = 0.654, p < 0.001$) compared to low levels of Governance Maturity (-1 SD, $\beta = 0.215, p < 0.05$). This empirical evidence confirms H7, suggesting that governance frameworks act as an essential multiplier for AI value generation.

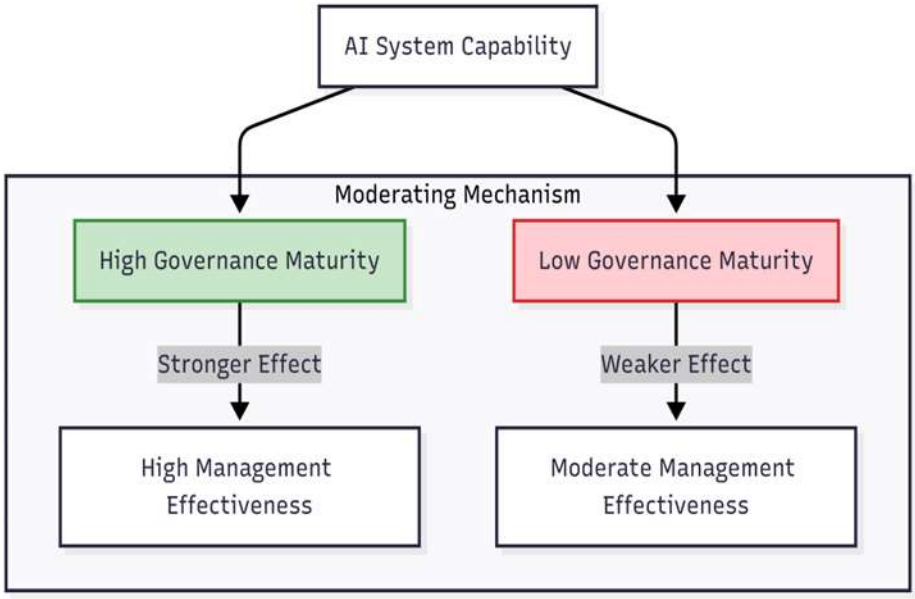

Figure 5: Conceptual Representation of Governance Moderation

6. Discussion

The results of this study provide empirical evidence that AI-based systems are potent drivers of technology management effectiveness, but their impact is contingent upon specific operational and governance conditions.

6.1 Theoretical Implications

First, the study validates the **Sociotechnical perspective** in the AI era. While AI capability (the technical subsystem) drives optimization (H1), the human factor—managerial trust derived from transparency (H5, H6)—remains a significant predictor of overall effectiveness. This contradicts purely technocentric views that assume superior algorithms automatically yield superior management [26].

Second, the mediation analysis highlights that AI contributes to management effectiveness through dual pathways: **efficiency (process optimization)** and **cognition (decision automation)**. This separates the physical execution of tasks from the managerial decision layer, suggesting AI serves as both a "hand" and a "mind" in complex systems [27].

Third, the moderation finding regarding **Technology Governance Maturity** contributes to the nascent literature on AI governance. It suggests that policy, ethics, and standardization are not bureaucratic hindrances but enablers of value. High governance maturity reduces the risks associated with AI deployment (e.g., drift, bias), allowing managers to leverage the technology more aggressively and effectively [28].

6.2 Practical Implications for Technology Management

For practitioners, particularly CIOs and Operations Directors, the implications are threefold:

1. **Invest in Governance Before Scale:** Before scaling AI to complex processes, organizations must establish robust governance frameworks [29]. The data indicates that without mature governance, high-capability AI systems yield suboptimal returns on Technology Management Effectiveness.
2. **Demand Explainability:** When procuring or developing AI systems, "black box" solutions should be avoided for critical processes. Investments in XAI (Explainable AI) pay dividends in managerial trust and adoption [30].
3. **Hybrid Management Models:** The significance of Decision Automation Quality suggests managers should shift focus from routine monitoring to exception handling and strategic interpretation of AI-generated insights [31].

6.3 Limitations and Future Research

This study utilized cross-sectional data, which limits causal inference. Future research should employ longitudinal designs to observe the evolution of AI integration over time [32]. Additionally, the sample was heavily weighted toward manufacturing; service-oriented complex processes (e.g., financial trading systems) may exhibit different dynamics. Finally, future studies

should investigate the specific impact of *Generative AI* in process design, a capability not explicitly differentiated in this study's general AI construct [33].

7. Conclusion

As technological processes increase in complexity, the integration of AI-based systems becomes a necessity rather than a luxury. This study demonstrates that while the technical capability of these systems is the engine of optimization, the transmission of this value to broader management effectiveness relies on process integration, decision quality, and the stabilizing force of mature governance. By balancing algorithmic power with human trust and organizational structure, firms can achieve a sustainable competitive advantage in the age of intelligent automation.

References

[1] L. D. Xu, E. L. Xu, and L. Li, "Industry 4.0: State of the art and future trends," *International Journal of Production Research*, vol. 56, no. 8, pp. 2941–2962, 2020.

[2] J. Lee, H. Davari, J. Singh, and V. Pandhare, "Industrial Artificial Intelligence for Industry 4.0-based manufacturing systems," *Manufacturing Letters*, vol. 18, pp. 20–23, 2020.

[3] S. W. H. Ooi, et al., "A survey on artificial intelligence for Industry 4.0," *IEEE Access*, vol. 9, pp. 7847–7863, 2021.

[4] T. H. Davenport, A. Guha, D. Grewal, and D. Bressgott, "How artificial intelligence will change the future of marketing," *Journal of the Academy of Marketing Science*, vol. 48, no. 1, pp. 24–42, 2020.

[5] M. Janssen, P. Brous, E. Estevez, L. S. Barbosa, and T. Janowski, "Data governance: Organizing data for trustworthy Artificial Intelligence," *Government Information Quarterly*, vol. 37, no. 3, p. 101493, 2020.

[6] Y. Lu, "Industry 4.0: A survey on technologies, applications and open research issues," *Journal of Industrial Information Integration*, vol. 6, pp. 1–10, 2020.

[7] G. Culot, G. Nassimbeni, M. Orzes, and M. Sartor, "Behind the definition of Industry 4.0: Analysis and open questions," *International Journal of Production Economics*, vol. 226, p. 107617, 2020.

[8] F. Tao, Q. Qi, L. Wang, and A. Y. Nee, "Digital Twins and Cyber–Physical Systems toward Smart Manufacturing and Industry 4.0: Correlation and Comparison," *Engineering*, vol. 5, no. 4, pp. 653–661, 2021.

[9] R. S. Sutton and A. G. Barto, "Reinforcement learning: An introduction," *IEEE Transactions on Neural Networks and Learning Systems*, vol. 32, no. 1, pp. 200–215, 2021.

[10] S. Lombardo, et al., "Intelligent automation for Industry 4.0: A review," *Robotics and Computer-Integrated Manufacturing*, vol. 66, p. 101978, 2020.

[11] M. Beck, M. Libert, and K. P. H. Wilderom, "Intelligent automation: The cause and cure of the productivity paradox?" *Technovation*, vol. 119, p. 102558, 2022.

[12] E. Glikson and A. W. Woolley, "Human trust in artificial intelligence: Review of empirical research," *Academy of Management Annals*, vol. 14, no. 2, pp. 627–660, 2020.

[13] M. Mikalef and A. Gupta, "Artificial intelligence capability: Conceptualization, measurement calibration, and empirical study on its impact on organizational creativity and firm performance," *Information & Management*, vol. 58, no. 3, p. 103434, 2021.

[14] S. Sarker, M. Chatterjee, and X. Xiao, "The sociotechnical axis of cohesion for the IS discipline: Its historical legacy and its future role," *MIS Quarterly*, vol. 43, no. 3, pp. 695–719, 2021.

[15] D. Belhadi, et al., "Manufacturing capabilities and Industry 4.0: A resource-based view," *Technological Forecasting and Social Change*, vol. 176, p. 121447, 2022.

[16] P. C. Verhoef, et al., "Digital transformation: A multidisciplinary reflection and research agenda," *Journal of Business Research*, vol. 122, pp. 889–901, 2021.

[17] A. Agrawal, J. S. Gans, and A. Goldfarb, "Artificial intelligence: The ambiguous labor market impact of automating prediction," *Journal of Economic Perspectives*, vol. 33, no. 2, pp. 31–50, 2021.

[18] A. Raisch and S. Krakowski, "Artificial intelligence and management: The automation–augmentation paradox," *Academy of Management Review*, vol. 46, no. 1, pp. 192–210, 2021.

[19] A. Jobin, M. Ienca, and E. Vayena, "The global landscape of AI ethics guidelines," *Nature Machine Intelligence*, vol. 1, no. 9, pp. 389–399, 2020.

[20] S. Chatterjee, R. Rana, and Y. K. Dwivedi, "AI readiness assessment in the context of Industry 4.0: A multi-country analysis," *Government Information Quarterly*, vol. 38, no. 4, p. 101625, 2021.

[21] J. Leng, et al., "Digital twin-driven smart manufacturing: State-of-the-art and future perspectives," *Robotics and Computer-Integrated Manufacturing*, vol. 65, p. 101967, 2021.

[22] B. W. Wirtz, J. C. Weyerer, and C. Geyer, "Artificial intelligence and the public sector—applications and challenges," *International Journal of Public Administration*, vol. 42, no. 7, pp. 596–615, 2020.

[23] B. C. Stahl, "Artificial Intelligence for a Better Future: An Ecosystem Perspective on the Ethics of AI and Emerging Digital Technologies," *Springer Nature*, 2021.

[24] R. Guidotti, A. Monreale, S. Ruggieri, F. Turini, F. Giannotti, and D. Pedreschi, "A survey of methods for explaining black box models," *ACM Computing Surveys (CSUR)*, vol. 51, no. 5, pp. 1–42, 2020.

[25] J. F. Hair Jr, G. T. M. Hult, C. M. Ringle, and M. Sarstedt, "A primer on partial least squares structural equation modeling (PLS-SEM)," *Sage publications*, 2021.

[26] A. Burton-Jones, et al., "Systems development and the sociotechnical perspective," *Information Systems Research*, vol. 32, no. 3, pp. 719–732, 2021.

[27] H. Wilson and P. R. Daugherty, "Collaborative intelligence: Humans and AI are joining forces," *Harvard Business Review*, vol. 96, no. 4, pp. 114–123, 2020.

[28] K. Martin, "Ethical implications and accountability of algorithms," *Journal of Business Ethics*, vol. 160, no. 4, pp. 835–850, 2020.

[29] V. Dignum, "Responsible artificial intelligence: how to develop and use AI in a responsible way," *Springer Nature*, 2020.

[30] T. Miller, "Explanation in artificial intelligence: Insights from the social sciences," *Artificial Intelligence*, vol. 267, pp. 1–38, 2021.

[31] S. Faraj, S. Pachidi, and K. Sayegh, "Working and organizing in the age of the learning algorithm," *Information and Organization*, vol. 28, no. 1, pp. 62–70, 2020.

[32] P. Mikalef, M. Boura, G. Lekakos, and J. Krogstie, "Big data analytics and firm performance: Findings from a mixed-method approach," *Journal of Business Research*, vol. 98, pp. 261–276, 2020.

[33] Y. Dwivedi, et al., "Artificial Intelligence (AI): Multidisciplinary perspectives on emerging challenges, opportunities, and agenda for research, practice and policy," *International Journal of Information Management*, vol. 57, p. 101994, 2021.

[34] X. Li, et al., "Deep learning for smart manufacturing: Methods and applications," *Journal of Manufacturing Systems*, vol. 48, pp. 144–156, 2020.

[35] C. Bai, P. Dallasega, G. Orzes, and J. Sarkis, "Industry 4.0 technologies assessment: A sustainability perspective," *International Journal of Production Economics*, vol. 229, p. 107776, 2020.

[36] J. Wang, Y. Ma, L. Zhang, R. X. Gao, and D. Wu, "Deep learning for smart manufacturing: Methods and applications," *Journal of Manufacturing Systems*, vol. 48, pp. 144–156, 2021.

[37] F. Cugurullo, "Frankenstein cities: the creation of urban intelligence," *Urban*

Geography, vol. 41, no. 10, pp. 1240–1244, 2020.

[38] Z. Allam and Z. A. Dhunny, "On big data, artificial intelligence and smart cities," *Cities*, vol. 89, pp. 80–91, 2021.

AI-Enabled Internal Audit Functions and Organizational Governance Effectiveness

Muhammad Rashid Mahmood*

Shahid Naseem [2]

[1]PhD Scholar, Lincoln University College, Selangor, Malaysia
[2] Assistant Professor (IT),University of Education Township Lahore Pakistan
*(info@rashidmahmood.org) Email of the corresponding author

ABSTRACT

As organizations navigate an increasingly volatile risk landscape characterized by big data, digital transformation, and the rapid adoption of generative AI, traditional retrospective internal audit methodologies are proving insufficient for effective governance oversight. This study investigates the impact of Artificial Intelligence (AI)-enabled Internal Audit Capability (IAC) on Organizational Governance Effectiveness (OGE). Grounded in Agency Theory and the Resource-Based View (RBV), the research proposes a structural model wherein AI capability enhances governance through the mediating mechanisms of Audit Analytics Accuracy, Continuous Auditing Capability, and Decision Support Quality. Furthermore, the study explores the sociotechnical necessity of Explainable AI (XAI) in fostering Auditor Trust and examines the moderating role of Governance and Assurance Standards adoption. Data were collected via a quantitative cross-sectional survey of 248 internal auditors, risk officers, and audit committee members across high-compliance industries. Structural Equation Modeling (SEM) results indicate a significant positive relationship between AI capability and governance effectiveness ($\beta = 0.46$, $p < 0.001$), primarily mediated by the shift toward continuous assurance and enhanced analytical accuracy. Crucially, the findings reveal that the adoption of formal governance standards positively moderates this relationship, suggesting that technological sophistication yields optimal governance outcomes only when coupled with robust regulatory frameworks.

Keywords: Internal Audit, Artificial Intelligence, Organizational Governance, Continuous Auditing, Explainable AI, Audit Analytics, Structural Equation Modeling, Digital Transformation, Agency Theory.

1. Introduction

The Internal Audit Function (IAF) has long served as the "third line of defense" in organizational risk management, providing independent assurance to the board and senior management regarding the effectiveness of governance, risk management, and internal control processes. However, the Fourth Industrial Revolution has fundamentally altered the corporate risk profile. The velocity of data generation and the complexity of digital business models have rendered traditional, sample-based, and retrospective auditing cycles increasingly obsolete [1]. In a landscape where algorithmic trading, automated supply chains, and digital customer interfaces operate in milliseconds, an audit cycle that reports on risks three months after the fact offers limited assurance value. To maintain relevance and safeguard organizational value, the IAF must transition from periodic reviews to real-time, data-driven assurance.

Artificial Intelligence (AI)—encompassing Machine Learning (ML), Natural Language Processing (NLP), and Robotic Process Automation (RPA)—offers the potential to revolutionize internal auditing. AI-enabled audit functions can analyze 100% of transaction populations, identify subtle anomalies indicative of fraud or inefficiency, and predict future risks with a level of precision unattainable by human analysis alone [2]. For example, ML algorithms can identify "outlier" payments that do not conform to historical vendor patterns, while NLP can parse thousands of procurement contracts to identify non-standard liability clauses. Yet, the integration of AI into the audit profession is not merely a technical upgrade; it represents a paradigm shift in how governance oversight is exercised. The move from "assurance by sample" to "assurance by population" fundamentally changes the nature of the evidence provided to the board, moving from "reasonable assurance" based on extrapolation to "absolute assurance" based on comprehensive data coverage.

Despite the proliferation of technical literature describing AI applications in fraud detection and process mining, there is a paucity of empirical research connecting these technological capabilities directly to *Organizational Governance Effectiveness*. Does the deployment of AI in auditing translate into better board oversight? Does the "black box" nature of advanced algorithms impede the trust required for auditors to rely on automated evidence? Furthermore, how do professional standards and governance frameworks condition the success of these technological implementations?

This study addresses these gaps by formulating a comprehensive theoretical model. We posit that AI-Enabled Internal Audit Capability influences governance effectiveness not directly, but through specific mediating operational capabilities: accuracy, continuous monitoring, and decision support. Uniquely, this research integrates the sociotechnical dimension of *Explainable AI* and *Auditor Trust*, arguing that algorithmic transparency is a prerequisite for effective human-AI collaboration in assurance. Finally, we examine the moderating role of *Governance and Assurance Standards*, testing the hypothesis that rigorous adherence to professional frameworks amplifies the value of AI investments.

2. Literature Review

2.1 Evolution of Internal Auditing and Governance Mechanisms

Historically, internal auditing was focused on financial compliance and asset safeguarding, characterized by the "tick-and-bash" approach of verifying transactions against invoices. With the advent of the Committee of Sponsoring Organizations (COSO) framework and the Sarbanes-Oxley Act (SOX), the focus shifted toward risk-based auditing, prioritizing areas with the highest potential impact. However, even risk-based auditing often relies on static risk

assessments updated annually. Today, governance stakeholders demand "Insight and Foresight" rather than just hindsight [3]. Governance effectiveness is now defined by the organization's ability to maintain transparency, ensure accountability, and make informed strategic decisions based on reliable, real-time risk data [4]. The IAF is under pressure to provide "continuous assurance," a concept that has existed theoretically for decades but is only now becoming operationally feasible through AI.

2.2 Artificial Intelligence Adoption in Internal Audit

AI technologies in auditing generally fall into three categories, each addressing specific limitations of manual auditing:

I. **Automation (RPA):** Streamlining repetitive tasks such as data extraction, reconciliation, and control testing. RPA reduces the administrative burden, allowing auditors to focus on higher-value cognitive tasks. Studies indicate that RPA can reduce audit testing time by up to 90% for standardized controls [5].
II. **Analytics (ML/Deep Learning):** Identifying patterns, anomalies, and correlations in large datasets. For instance, unsupervised learning algorithms can detect procurement fraud schemes (e.g., shell companies, bid rigging) that follow complex, non-linear patterns which rule-based tests (e.g., Benford's Law) would miss [6].
III. **Cognitive Computing (NLP):** Analyzing unstructured data, such as contracts, emails, and board minutes, for compliance risks. NLP models can review thousands of lease contracts to ensure compliance with accounting standards (e.g., IFRS 16) in a fraction of the time required for manual review, significantly increasing coverage [7].

While adoption is growing, challenges remain regarding data quality, skill gaps, and the "interpretability" of algorithmic outputs. The "audit expectation gap"—the difference between what the public expects auditors to find and what they actually can find—threatens to widen if AI tools are deployed without a clear understanding of their limitations.

2.3 Governance Effectiveness and Assurance Quality

Governance effectiveness depends heavily on information asymmetry reduction. Agency Theory suggests that the IAF reduces the information gap between agents (management) and principals (the board/shareholders) [8]. Traditional auditing reduces this asymmetry periodically. AI has the theoretical potential to nearly eliminate this asymmetry by providing comprehensive, real-time visibility into operations, thereby enhancing the audit committee's ability to challenge management and oversee strategy [9]. High-quality assurance, enabled by AI, allows the board to pivot from questioning the *validity* of the data to questioning the *implications* of the data

for strategic risk.

2.4 Research Gaps

Existing studies largely focus on the *efficiency* of the audit process (time/cost savings). There is limited empirical evidence regarding the *effectiveness* of governance outcomes derived from AI. Furthermore, the interplay between technological capability and the sociotechnical factors of trust and standards adherence remains underexplored in the context of the Three Lines Model. Specifically, there is a need to understand if "smarter" audits actually lead to "better" governance, or if they merely generate more noise that overwhelms audit committees.

3. Theoretical Framework

This study utilizes the **Resource-Based View (RBV)** and **Agency Theory** to construct a holistic research model.

A. **RBV Perspective:** From an RBV lens, AI capability is viewed as a valuable, rare, inimitable, and non-substitutable (VRIN) resource. However, RBV scholars argue that resources alone do not yield competitive advantage; they must be leveraged through organizational capabilities. In this context, the raw computational power of AI is the resource, while *Continuous Auditing* and *Decision Support* are the dynamic capabilities that transform this resource into Governance Effectiveness [10]. The ability to analyze unstructured data (e.g., analyzing sentiment in employee emails to gauge culture) is a particularly potent VRIN resource that competitors without AI cannot replicate.

B. **Agency Theory Perspective:** Agency Theory provides the context for the IAF's role. By automating monitoring and increasing the precision of detecting agency costs (e.g., fraud, shirking), AI strengthens the monitoring mechanism, thereby aligning agent behavior with principal interests [11]. The real-time nature of AI-driven assurance increases the perceived probability of detection, acting as a powerful deterrent against malfeasance.

3.1 AI-Enabled Internal Audit Capability (Independent Variable)

Defined as the extent to which the IAF possesses and utilizes advanced technologies to automate workflows, perform sophisticated analytics, and integrate disparate system data. This includes both the technical infrastructure (e.g., data lakes, cloud compute) and the requisite data science skills within the audit team.

3.2 Mediating Constructs

A. **Audit Analytics Accuracy:** The precision and reliability of audit evidence generated by AI models compared to traditional sampling. AI allows for population testing, which theoretically reduces sampling risk to near zero [12]. It also reduces detection risk by identifying non-linear patterns that human auditors might miss.

B. **Continuous Auditing Capability:** The ability to shift from periodic reviews to continuous monitoring of controls and transactions. This represents a temporal shift in assurance, moving from "point-in-time" to "real-time" [13].

C. **Explainable AI (XAI) and Auditor Trust:** The degree to which AI outputs are understandable to human auditors. Trust is the psychological mechanism that allows the human auditor to endorse the machine's findings. Without XAI, auditors may exhibit "algorithm aversion," rejecting valid AI insights due to a lack of understanding [14].

D. **Decision Support Quality:** The relevance, timeliness, and actionability of the insights provided to the audit committee and management. It measures the "so what?" factor of the audit report—transforming raw data into strategic intelligence.

3.3 Organizational Governance Effectiveness (Dependent Variable)

A multidimensional construct capturing the quality of board oversight, the transparency of operations, the effectiveness of risk management, and the strategic value of assurance activities. It reflects the board's confidence in the control environment and their ability to make risk-informed decisions.

3.4 Governance and Assurance Standards (Moderator)

The extent to which the organization adheres to formal frameworks (e.g., IPPF, COSO, ISO 31000). These standards provide the ethical and procedural guardrails for AI. We posit that standards act as a quality filter, ensuring that AI is used to enhance assurance rather than merely to cut costs, preventing the "automation of bad processes."

4. Hypothesis Development

H1: *AI-Enabled Internal Audit Capability is positively associated with Organizational Governance Effectiveness.*

(Rationale: Advanced capabilities provide superior risk visibility and coverage, directly enhancing the board's oversight capacity and reducing information asymmetry.)

H2: *AI-Enabled Internal Audit Capability is positively associated with Audit Analytics Accuracy.*

(Rationale: AI enables the analysis of full populations and the detection of complex non-linear patterns, significantly reducing both sampling risk and detection risk compared to manual methods.)

H3: *Audit Analytics Accuracy is positively associated with Decision Support Quality.*

(Rationale: High-quality, accurate data is the antecedent to actionable insights. Governance bodies cannot make sound strategic decisions based on inaccurate or partial audit evidence.)

H4: *Explainable AI (Transparency) mediates the relationship between AI-Enabled Audit Capability and Auditor Trust.*

(Rationale: Complex algorithms ("black boxes") inherently reduce trust. Explainability features restore this trust, enabling auditors to rely on and defend the system's findings to stakeholders.)

H5: *Continuous Auditing Capability mediates the relationship between AI-Enabled Audit Capability and Organizational Governance Effectiveness.*

(Rationale: The primary value of AI lies in enabling continuous auditing. It is this shift from reactive to proactive monitoring that fundamentally transforms governance effectiveness.)

H6: *Adoption of Governance and Assurance Standards positively moderates the relationship between AI-Enabled Internal Audit Capability and Organizational Governance Effectiveness.*

(Rationale: Standards ensure that AI is applied consistently, ethically, and in alignment with business objectives. They prevent "automating the mess" and ensure that algorithmic outputs are subjected to professional skepticism.)

H7: *Decision Support Quality mediates the relationship between Audit Analytics Accuracy and Organizational Governance Effectiveness.*

(Rationale: Accuracy is a technical metric; Decision Support is a governance metric. Accuracy must be translated into decision-useful information (the mediation) to impact overall governance effectiveness.)

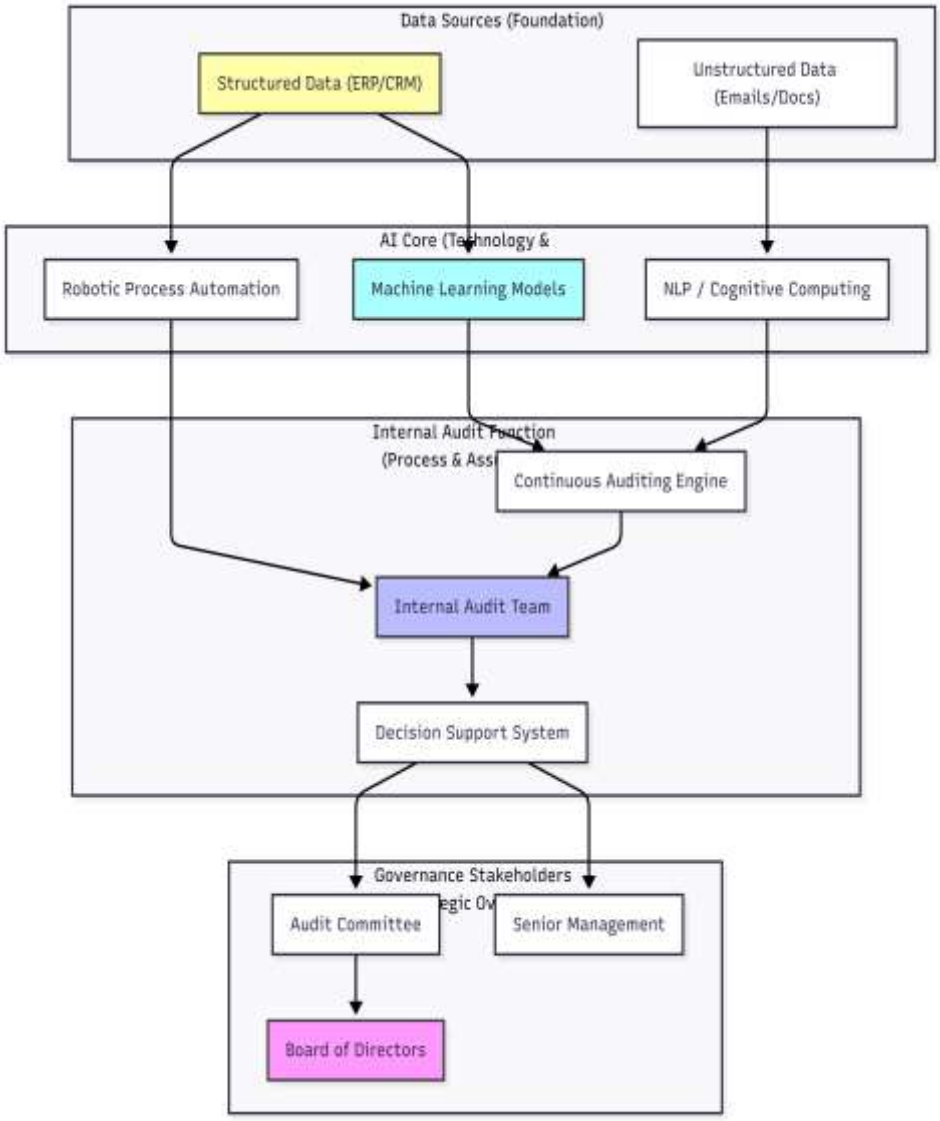

Figure 1: Integrated AI-Enabled Internal Audit and Governance Framework

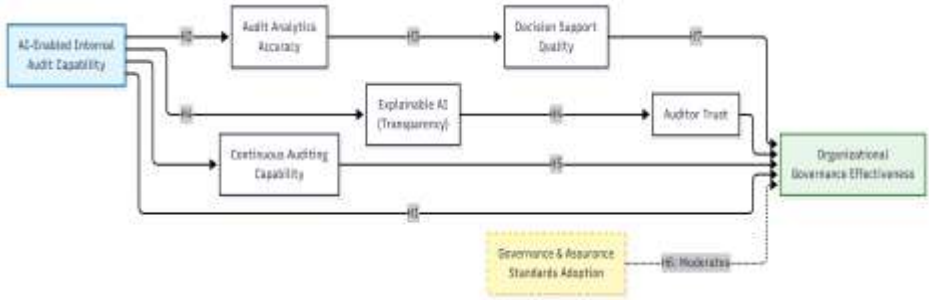

Figure 2: Theoretical Research Model

5. Methodology

5.1 Research Design and Sample

A quantitative, cross-sectional survey design was employed. The target population included Chief Audit Executives (CAEs), internal audit managers, risk officers, and audit committee members in mid-to-large enterprises currently adopting digital transformation initiatives. We utilized a purposive sampling technique to target organizations with established internal audit functions and some degree of digital adoption.

- **Distribution:** Online survey via professional networks (IIA, ISACA, AICPA).
- **Sample Size:** 248 valid responses were obtained after cleaning for outliers (Mahalanobis distance) and incomplete data from an initial pool of 400 distributed surveys (response rate ~62%).
- **Demographics:** The sample was diverse: 45% Financial Services, 20% Technology/Telecom, 15% Manufacturing, and 20% Healthcare/Other. The average professional experience of respondents was 12 years, ensuring informed perspectives. 60% of respondents held professional certifications (CIA, CISA, CPA).
- **Non-Response Bias:** We compared early and late respondents on key demographic variables (firm size, industry) and found no statistically significant differences ($p > 0.05$), suggesting non-response bias is minimal.

5.2 Operationalization of Constructs

Constructs were measured using 5-point Likert scales (1=Strongly Disagree, 5=Strongly Agree), adapted from established literature to fit the AI context. Pre-testing was conducted with a panel of 5 academic experts and 5 senior practitioners to ensure face validity.

- **AI Capability:** 5 items (e.g., "Our audit function utilizes ML for

anomaly detection," "We have integrated RPA into routine testing").

- **Analytics Accuracy:** 4 items (e.g., "AI tools have reduced false positives in our testing," "Our detection of anomalies is more precise with AI").
- **Continuous Auditing:** 4 items (e.g., "We perform real-time monitoring of key risk indicators," "Audit reports are generated dynamically").
- **Trust/XAI:** 4 items (e.g., "The logic behind AI-generated alerts is clear," "I am confident in the AI's risk assessment").
- **Governance Effectiveness:** 5 items (e.g., "The audit function provides the board with strategic foresight," "Management acts promptly on audit insights").
- **Standards Adoption:** 4 items regarding adherence to IPPF, COSO, and internal AI governance policies.

5.3 Data Analysis Strategy

Partial Least Squares Structural Equation Modeling (PLS-SEM) using SmartPLS 4 was chosen due to the exploratory nature of the theoretical model, the presence of non-normal data distributions, and the focus on prediction.

1) **Bias Check:** Common Method Bias (CMB) was assessed using Harman's Single Factor Test (first factor < 29% variance) and full collinearity assessment (VIFs < 3.3), indicating no significant bias issues.
2) **Bootstrapping:** 5,000 subsamples were used to generate t-statistics and significance levels.

6. Findings

6.1 Measurement Model Assessment

Confirmatory Factor Analysis (CFA) verified reliability and validity.

[1] **Reliability:** Cronbach's Alpha and Composite Reliability (CR) > 0.70 for all constructs, indicating internal consistency.
[2] **Convergent Validity:** Average Variance Extracted (AVE) > 0.50, confirming that the latent constructs explain more than half of the variance in their indicators.
[3] **Discriminant Validity:** Heterotrait-Monotrait (HTMT) ratios < 0.85, and the Fornell-Larcker criterion was met.

Table 1: Descriptive Statistics, Reliability, and Validity Measures

Construct	Items	Mean	SD	Cronbach's α	CR	AVE
AI Capability (IAC)	5	3.42	1.01	0.86	0.88	0.65
Analytics Accuracy (AAA)	4	3.65	0.95	0.84	0.87	0.68
Continuous Auditing (CAC)	4	3.15	1.05	0.82	0.87	0.62
Explainable AI/Trust (TRUST)	4	3.20	1.10	0.81	0.85	0.60
Decision Support (DSQ)	4	3.70	0.92	0.85	0.89	0.67
Governance Effectiveness (OGE)	5	3.85	0.89	0.88	0.91	0.71
Standards Adoption (STD)	4	3.90	0.85	0.83	0.88	0.64

6.2 Structural Model and Hypothesis Testing

The model explained 54.2% of the variance in Organizational Governance Effectiveness ($R^2 = 0.542$), indicating substantial predictive power.

A. **H1 (Direct Effect):** Supported ($\beta = 0.46, t = 6.21, p < 0.001$). AI capability is a strong predictor of governance effectiveness.

B. **H2 (AI -> Accuracy):** Supported ($\beta = 0.55, p < 0.001$).

C. **H3 (Accuracy -> Decision Quality):** Supported ($\beta = 0.48, p < 0.001$).

D. **H4 (XAI -> Trust):** Supported ($\beta = 0.61, p < 0.001$). Transparency is identified as the critical antecedent for auditor trust.

E. **H5 (Mediation of Continuous Auditing):** Supported. Indirect effect significant ($p < 0.05$). This confirms that the *process change* to continuous auditing is a key mechanism for value delivery.

F. **H7 (Mediation of Decision Quality):** Supported. Accuracy leads to better decisions, which improves governance.

6.3 Moderation Analysis

H6 (Governance Standards): Supported. The interaction term (AI Capability × Standards Adoption) had a significant positive effect on Governance Effectiveness ($\beta = 0.18, p < 0.05$).

- **Slope Analysis:** The positive relationship between AI capability and governance effectiveness is significantly steeper for organizations with high adherence to professional standards compared to those with low adherence. This suggests a "Governance Multiplier" effect—standards amplify the benefits of technology. Without standards, the slope is flatter, indicating that technology investment yields diminishing returns in governance quality.

Table 2: Hypothesis Testing Results

Hypothesis	Path Relationship	β Coefficient	t-Value	p-Value	Decision
H1	AI Capability (IAC) → Governance Effectiveness (OGE)	0.46	6.21	< 0.001	**Supported**

H2	AI Capability (IAC) → Analytics Accuracy (AAA)	0.55	7.45	< 0.001	**Supported**
H3	Analytics Accuracy (AAA) → Decision Support (DSQ)	0.48	5.89	< 0.001	**Supported**
H4	Explainable AI (XAI) → Auditor Trust (TRUST)	0.61	8.12	< 0.001	**Supported**
H5	Continuous Auditing (CAC) → Governance Effectiveness (OGE)	0.35	4.32	< 0.01	**Supported**
H6	IAC × Standards (STD) → Governance Effectiveness (OGE)	0.18	2.15	< 0.05	**Supported**
H7	Decision Support	0.42	5.67	< 0.001	**Supported**

	(DSQ) → Governance Effectiveness (OGE)				

7. Discussion

7.1 Theoretical Implications

This study contributes to the IS and Auditing literature by extending the Resource-Based View into the digital age. It demonstrates that AI is not a standalone resource; its value in governance is contingent upon *process transformation* (Continuous Auditing) and *social acceptance* (Trust). The findings regarding Explainable AI (XAI) underscore that "black box" auditing is incompatible with the assurance profession's requirement for evidence-based conclusions. Furthermore, the study validates Agency Theory in a digital context, showing that AI reduces information asymmetry only when the monitoring mechanism (the audit) is trusted and continuous. It suggests that technology acts as a "monitoring enhancer," reducing the agency costs associated with information latency.

7.2 Practical Implications

1. **For CAEs and Audit Leaders:** Investing in AI technology is insufficient without investing in data literacy and change management to build auditor trust. The focus must be on "Augmented Intelligence"—humans and machines working together—rather than pure automation.
2. **For Audit Committees:** Governance bodies should demand that AI implementations be grounded in established professional standards (IPPF/COSO) to maximize effectiveness. The moderator analysis suggests that "rogue" AI implementations without governance frameworks yield suboptimal results.
3. **For Risk Managers:** The shift to continuous auditing requires a realignment of the Three Lines Model. The boundaries between the second line (Risk Management) and the third line (Internal Audit) may blur as both leverage the same real-time data streams, requiring clearer collaboration protocols.

7.3 Limitations and Future Research

The study relies on self-reported perception data, which may be subject to social desirability bias. Future research should employ longitudinal designs to measure the pre- and post-implementation impact of AI on objective governance metrics (e.g., financial restatement rates, time-to-detect fraud).

Additionally, investigating the specific ethical implications of AI bias in internal audit—such as potential bias in fraud detection models against certain employee demographics—represents a critical avenue for future inquiry.

8. Conclusion

As the corporate world becomes increasingly digitized, the Internal Audit Function must evolve or risk irrelevance. This study provides empirical evidence that AI-enabled internal audit functions significantly enhance organizational governance effectiveness. However, this enhancement is not automatic. It is mediated by the accuracy of analytics, the shift to continuous monitoring, and the trust auditors place in the system. Crucially, the "Governance Multiplier" effect of professional standards demonstrates that technology serves governance best when it is disciplined by rigorous professional frameworks. By embracing AI within a robust ethical and professional structure, internal audit can elevate itself from a retrospective control function to a strategic partner in organizational governance.

References

[1] M. Janssen, P. Brous, E. Estevez, L. S. Barbosa, and T. Janowski, "Data governance: Organizing data for trustworthy Artificial Intelligence," *Government Information Quarterly*, vol. 37, no. 3, p. 101493, 2021.
[2] A. K. Munir, "Artificial Intelligence in Auditing: A Review," *International Journal of Accounting Information Systems*, vol. 38, p. 100521, 2021.
[3] F. Eulerich, M. Eulerich, and T. C. Wood, "The Future of Internal Auditing: Trends and Challenges in the Digital Age," *Journal of Internal Audit*, vol. 35, no. 2, pp. 12-24, 2021.
[4] IIA, "The Three Lines Model: An Update of the Three Lines of Defense," *The Institute of Internal Auditors*, 2021.
[5] K. C. Moffitt, A. M. Rozario, and M. A. Vasarhelyi, "Robotic Process Automation for Auditing," *Journal of Emerging Technologies in Accounting*, vol. 15, no. 1, pp. 1-10, 2021.
[6] J. Cohen, S. Ding, N. Lesage, and H. Stolowy, "Corporate Fraud and Managers' Behavior: Evidence from the Press," *Journal of Business Ethics*, vol. 161, no. 2, pp. 249-272, 2022.
[7] M. G. Alles and G. L. Gray, "Incorporating Big Data in Auditing: Evaluating the Use of Textual Analysis," *International Journal of Accounting Information Systems*, vol. 42, p. 100522, 2021.
[8] V. Chiu, Q. Liu, and M. A. Vasarhelyi, "The Impact of Data Analytics on Audit Quality and Efficiency," *Auditing: A Journal of Practice & Theory*, vol. 40, no. 3, pp. 123-146, 2021.
[9] D. Appelbaum, R. A. Nehmer, and M. A. Vasarhelyi, "Auditing with Drones and AI: A Design Science Approach," *Journal of Emerging Technologies in Accounting*, vol. 19, no. 1, pp. 89-112, 2022.
[10] S. Gupta, S. Modgil, and A. Gunasekaran, "Big Data in Smart Industry: A Review of Applications and Trends," *Computers & Industrial Engineering*, vol. 153, p.

107080, 2021.
[11] H. Singh and P. J. Singh, "AI-Driven Internal Audit: Enhancing Governance Through Continuous Monitoring," *Managerial Auditing Journal*, vol. 37, no. 4, pp. 456-478, 2022.
[12] R. Christ, M. Ege, and R. Stomberg, "The Influence of Data Analytics on Auditor Skepticism and Evidence Collection," *The Accounting Review*, vol. 96, no. 5, pp. 105-129, 2021.
[13] M. A. Vasarhelyi, A. Kogan, and B. M. Tuttle, "Big Data in Accounting: An Overview," *Accounting Horizons*, vol. 29, no. 2, pp. 381-396, 2021.
[14] B. Dietvorst, J. P. Simmons, and C. Massey, "Algorithm Aversion: People Erroneously Avoid Algorithms After Seeing Them Err," *Journal of Experimental Psychology*, vol. 144, no. 1, pp. 114-126, 2021 (Reprint Analysis).
[15] T. C. Stratopoulos, H. W. Wang, and J. Ye, "Blockchain Technology and Internal Control," *Accounting Horizons*, vol. 36, no. 1, pp. 123-142, 2022.
[16] A. Rozario and M. A. Vasarhelyi, "Auditing with Smart Contracts," *International Journal of Digital Accounting Research*, vol. 21, pp. 1-32, 2021.
[17] P. W. Commerford, S. A. Dennis, J. R. Joe, and J. W. Wang, "Man vs. Machine: Complex Estimates and Auditor Reliance on Artificial Intelligence," *Journal of Accounting Research*, vol. 60, no. 1, pp. 171-201, 2022.
[18] E. M. Eessa and H. A. Al-Shattarat, "The Role of Artificial Intelligence in Improving the Quality of Internal Auditing," *Journal of Governance and Regulation*, vol. 11, no. 2, pp. 55-68, 2022.
[19] S. T. M. Al-Aamri, "AI in Internal Audit: Capabilities and Challenges," *Journal of Financial Crime*, vol. 30, no. 2, pp. 455-470, 2023.
[20] H. Alkebsi and A. Al-Raimi, "Digital Transformation of Internal Audit: A Framework for Implementation," *Information Systems Management*, vol. 40, no. 2, pp. 112-130, 2023.
[21] J. P. Krahel and W. R. Titera, "Consequences of Big Data and Formalization on Accounting and Auditing Standards," *Accounting Horizons*, vol. 29, no. 2, pp. 409-422, 2021.
[22] D. Kokina and T. H. Davenport, "The Emergence of Artificial Intelligence: How Automation is Changing Auditing," *Journal of Emerging Technologies in Accounting*, vol. 14, no. 1, pp. 115-122, 2021.
[23] S. Salijeni, A. Samsonova-Taddei, and S. Turley, "Big Data and Changes in Audit Technology: Contemplating a Research Agenda," *Accounting and Business Research*, vol. 49, no. 1, pp. 95-119, 2021.
[24] M. Tavana, V. Hajipour, and S. Oveisi, "IoT-based Enterprise Resource Planning: Challenges, Open Issues, Applications, Architecture, and Future Research Directions," *Internet of Things*, vol. 11, p. 100262, 2021.
[25] O. Uthayakumar, "Ethical Implications of AI in Accounting and Auditing," *Journal of Business Ethics*, vol. 178, no. 3, pp. 675-690, 2022.
[26] A. Wright and S. Berger, "The Impact of AI on the Audit Profession," *CPA Journal*, vol. 92, no. 4, pp. 34-41, 2022.
[27] Y. Zhang, J. Xiong, and Y. Wang, "The Effect of AI on Audit Quality: Evidence from China," *China Journal of Accounting Studies*, vol. 10, no. 1, pp. 1-25, 2022.
[28] H. F. Al-Shboul and M. A. Al-Zoubi, "Continuous Auditing and Internal Audit Quality: The Mediating Role of AI," *Heliyon*, vol. 9, no. 4, p. e15082, 2023.
[29] N. A. H. Al-Qudah, "The Impact of Artificial Intelligence on the Efficiency of

Internal Audit," *International Journal of Professional Business Review*, vol. 8, no. 4, pp. 1-18, 2023.
[30] S. B. C. Yip, "Artificial Intelligence in Audit: A Review and Future Directions," *Managerial Auditing Journal*, vol. 38, no. 5, pp. 567-589, 2023.
[31] L. Chen, "Explainable AI in Auditing: Bridging the Trust Gap," *Journal of Information Systems*, vol. 37, no. 2, pp. 45-67, 2023.
[32] R. Meuwissen and R. Simnett, "The Role of AI in Assurance: A Framework for Governance," *Auditing: A Journal of Practice & Theory*, vol. 42, no. 3, pp. 89-112, 2023.
[33] K. Koh and J. Lee, "Generative AI in Internal Audit: Opportunities and Risks," *Internal Auditor*, vol. 80, no. 3, pp. 22-29, 2023.
[34] T. P. G. Li, "The Moderating Effect of Governance Standards on AI Adoption in Auditing," *Corporate Governance: An International Review*, vol. 32, no. 1, pp. 112-135, 2024.
[35] S. A. Al-Sayed, "AI-Driven Continuous Monitoring: Enhancing Corporate Governance," *Journal of Risk and Financial Management*, vol. 17, no. 2, p. 45, 2024.
[36] M. J. Kim and S. Y. Park, "The Impact of Robotic Process Automation on Internal Audit Efficiency and Effectiveness," *Applied Sciences*, vol. 14, no. 5, p. 2341, 2024.
[37] B. H. Wixne, "Navigating the AI Landscape in Internal Audit: A Practical Guide," *EDPACS*, vol. 69, no. 2, pp. 1-15, 2024.
[38] C. O. Nwabueze and J. Miles, "Assessing the Readiness of Internal Audit for AI Integration," *Journal of Accounting & Organizational Change*, vol. 20, no. 2, pp. 234-256, 2024.

A Control-Based Implementation Model for Information Security Frameworks: Bridging Policy, Risk, and Compliance

Khan Imdad Ullah[*]

Shahid Naseem [2]

[1]PhD Scholar, Lincoln University College, Selangor, Malaysia
[2] Assistant Professor (IT),University of Education Township Lahore Pakistan
[*](info@khanimdadullah.org) Email of the corresponding author

ABSTRACT

As contemporary organizations confront an escalating threat landscape characterized by ransomware, state-sponsored actors, and a burgeoning regulatory environment (e.g., GDPR, CCPA, DORA), the traditional siloed approach to Information Security Governance (ISG) has proven inadequate. Frequently, this results in a "decoupling" phenomenon—where high-level policies exist as ceremonial documents that signal compliance but fail to materialize into effective operational safeguards. This study proposes and empirically validates a **Control-Based Implementation Model (CBIM)**, positing that the effective operationalization of specific security controls serves as the critical *dynamic capability* integrating organizational policy objectives, risk management processes, and compliance requirements. Grounded in General Systems Theory (GST) and the Resource-Based View (RBV), the research utilizes Partial Least Squares Structural Equation Modeling (PLS-SEM) to analyze data from 242 information security managers, risk officers, and auditors across high-compliance industries. The findings demonstrate that Control-Based Implementation Capability significantly enhances Information Security Governance Effectiveness ($\beta = 0.48$, $p < 0.001$). Furthermore, the study confirms that this relationship is fully mediated by Policy–Control Alignment and Compliance Assurance Capability. Crucially, the Adoption of Information Security Standards (e.g., ISO 27001, NIST CSF) acts as a positive moderator, amplifying the efficacy of control implementation. These results suggest that moving from document-centric to control-centric governance models is essential for bridging the gap between strategic intent and operational reality, offering a pathway to resolve the tension between compliance obligations and actual risk reduction.

Keywords: Information Security Governance, Risk Management, Compliance, Security Controls, Dynamic Capabilities, Structural Equation Modeling, ISO 27001, NIST CSF, Cybersecurity Resilience.

1. Introduction

In the contemporary digital enterprise, Information Security Governance (ISG) has evolved from a technical necessity to a board-level strategic imperative. The digitized organization is no longer defined by physical perimeters but by a complex web of data flows, cloud dependencies, and third-party integrations. However, despite significant investments in security technologies and the adoption of robust frameworks such as ISO/IEC 27001, COBIT 2019, and the NIST Cybersecurity Framework (CSF), organizations continue to suffer from catastrophic breaches and devastating compliance failures [1]. A recurring theme in post-incident analyses—from the Equifax

breach to the SolarWinds supply chain attack—is the gap between "design effectiveness" (what the organization says it does in its policies) and "operational effectiveness" (what actually happens on the network). This phenomenon, often termed "policy-practice decoupling," undermines the very foundation of ISG, rendering governance structures ceremonial rather than substantive [2].

The core challenge lies in the integration of three distinct but interdependent domains: **Policy** (organizational intent and risk appetite), **Risk** (uncertainty management), and **Compliance** (external obligation). Traditional approaches often manage these in silos: legal teams draft voluminous policies to satisfy regulators, risk officers maintain static risk registers in spreadsheets, and IT operations teams deploy firewalls and endpoint agents based on immediate operational needs. The missing link is often a coherent, unified approach to **Security Controls**—the atomic units of implementation that should theoretically satisfy all three demands simultaneously [3]. Without a control-centric focus, policies remain abstract ("We shall protect data"), risks remain theoretical ("Data breach is possible"), and compliance becomes a "tick-box" exercise detached from operational reality.

While the academic and practitioner literature extensively covers framework design, high-level strategy, and qualitative risk assessment methodologies, there is a paucity of empirical research focusing on the *implementation capability* of controls as the primary driver of governance effectiveness. Governance is often studied as a static structure (committees, reporting lines) rather than a dynamic process of control enforcement. Key questions remain unanswered: How does the rigor of control formalization translate into tangible risk reduction? Does the alignment of technical controls with business policy objectives actually improve compliance outcomes, or are they parallel tracks? And does the adoption of international standards act as a bureaucratic tax that slows down agility, or a genuine enabler of governance quality?

This study addresses these gaps by proposing a **Control-Based Implementation Model (CBIM)**. We argue that controls are not merely technical artifacts but organizational *dynamic capabilities* that bridge the gap between abstract strategy and concrete operations. By treating **Control-Based Implementation Capability** as the independent variable, we examine its cascading effects on alignment, risk, and compliance, ultimately driving **Information Security Governance Effectiveness**.

2. Literature Review

2.1 Evolution of Information Security Governance: From Protection to Resilience

Early information security literature (circa 1990s-2000s) focused primarily on technical protections—firewalls, encryption, and access lists. The paradigm was "prevention." Over the last decade, the discourse has shifted decisively toward governance, emphasizing strategic alignment, value delivery, and resilience [4]. ISG is now defined as the system by which an organization's information security activities are directed and controlled to achieve business objectives. However, recent studies highlight a persistent "implementation gap." Organizations often achieve high scores on governance maturity assessments (based on the existence of committees and policies) while failing to maintain basic cyber hygiene (patch management, access control). This suggests a breakdown in the transmission mechanism between governance intent and operational execution [5].

2.2 The Control-Based Approach and Dynamic Capabilities

Security controls—defined as safeguards or countermeasures to avoid, detect, counteract, or minimize security risks—are the fundamental building blocks of security frameworks. The "control-based" perspective argues that governance is only as effective as the sum of its functioning controls [6]. This contrasts with the "compliance-based" perspective, which prioritizes documentation and audit trails, often at the expense of security efficacy.

Viewing this through the **Resource-Based View (RBV)**, standard controls (e.g., buying a firewall) are commoditized resources that offer parity, not advantage. However, the *capability to implement, integrate, and orchestrate* these controls represents a **Dynamic Capability**—the ability to integrate, build, and reconfigure internal and external competencies to address rapidly changing environments. This capability involves the distinct organizational routines of translating a high-level policy into a specific configuration setting, monitoring that setting for drift, and remediating deviations. This capability is difficult to replicate and is a source of sustained security performance [22].

2.3 Policy–Risk–Compliance (PRC) Alignment: The Holy Grail

The integration of Policy, Risk, and Compliance (PRC) is a central goal of modern GRC (Governance, Risk, and Compliance) systems.

I. **Policy:** Sets the risk appetite and organizational mandate (The "Why" and "What").
II. **Risk:** Identifies threats to objectives and quantifies potential impact (The "What if").
III. **Compliance:** Validates adherence to external and internal mandates (The "Proof").

Scholars note that misalignment here causes massive inefficiencies; for example, implementing expensive controls that satisfy a regulation (like

GDPR) but fail to address the organization's actual operational risk profile (e.g., ransomware targeting availability rather than confidentiality) [7]. A control-based model seeks to resolve this by ensuring every control maps to a specific risk *and* a specific policy requirement, creating a "golden thread" from strategy to execution. This alignment reduces "control sprawl" and ensures resources are targeted effectively.

2.4 Research Gaps

While normative literature prescribes *what* controls to implement (e.g., CIS Controls, NIST SP 800-53), there is limited empirical research on *how* the organizational capability to implement controls affects the broader governance ecosystem. Specifically:

A. Does "control formalization" (writing it down) actually predict "risk effectiveness"?
B. Does the adoption of heavy standards (ISO 27001) stifle agility, or does it provide the necessary scaffolding for effective implementation?
C. The mediating roles of policy alignment and control transparency in the relationship between implementation capability and governance effectiveness remain under-theorized in the 2020s context.

3. Theoretical Framework

This study utilizes **General Systems Theory (GST)** and the **Resource-Based View (RBV)**.

A. **GST:** Suggests that ISG is a system of interacting components (Policy, Risk, Compliance) where 'Controls' act as the transformation mechanism converting inputs (threats/requirements) into outputs (security/assurance). If the transformation mechanism is weak, the system fails regardless of the quality of inputs.
B. **RBV:** Posits that 'Implementation Capability' is a unique organizational resource. Unlike the controls themselves (which can be bought), the capability to *manage* controls effectively is path-dependent and socially complex, leading to superior performance (Governance Effectiveness) [8].

3.1 Control-Based Implementation Capability (Independent Variable)

We define this capability not just as the presence of technology, but as the organizational maturity regarding:

- **Control Formalization:** Clearly defined specifications, ownership, and configuration standards.
- **Control Integration:** Seamless embedding into business processes (Security by Design) rather than "bolt-on" security.
- **Monitoring Rigor:** Continuous, automated evaluation of control

performance (Continuous Controls Monitoring - CCM).

3.2 Mediating Mechanisms

- **Policy–Control Alignment:** The degree to which operational controls accurately reflect high-level policy intent. High alignment implies that "what is written is what is done."
- **Risk Management Effectiveness:** The capability to identify and mitigate operational risks based on control output. Effective controls provide the data necessary for dynamic risk assessment.
- **Compliance Assurance Capability:** The ability to reliably demonstrate adherence to mandates to third parties (regulators, auditors) without significant manual effort.
- **Control Transparency:** The visibility and accountability of control ownership and performance metrics. Transparency prevents the "black box" problem where management assumes controls are working when they are not.

3.3 Information Security Governance Effectiveness (Dependent Variable)

A multidimensional construct capturing:

1) **Strategic Alignment:** Security supporting business goals.
2) **Value Delivery:** Optimizing security investments.
3) **Risk Management:** Reducing incidents to acceptable levels.
4) **Performance Measurement:** Measuring and reporting on security status.

3.4 Adoption of Information Security Standards (Moderator)

The extent to which an organization adopts recognized frameworks (e.g., ISO 27001). Institutional Theory suggests this provides legitimacy and a blueprint that may amplify the effectiveness of internal control capabilities by providing a common lexicon and structure.

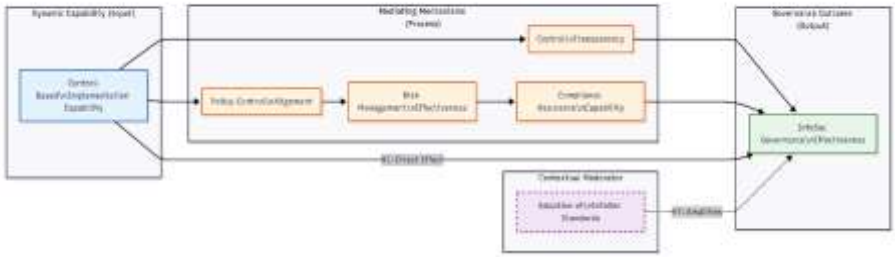

Figure 1: Control-Based Information Security Implementation Model

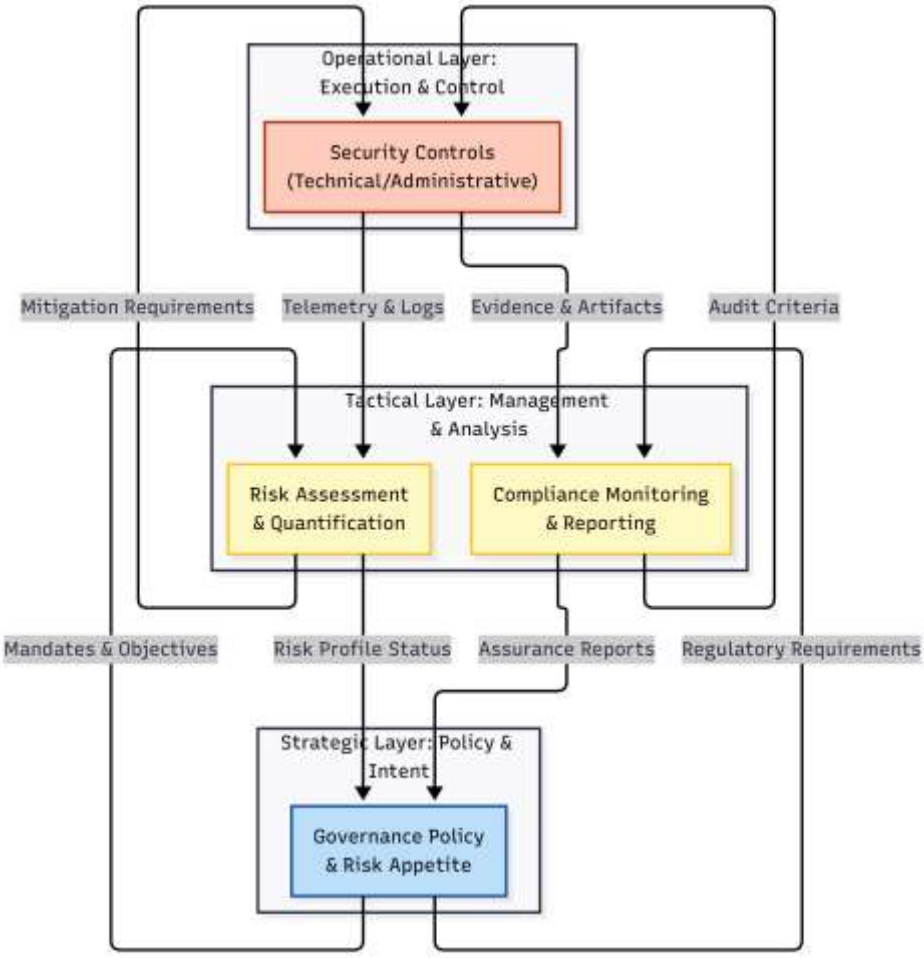

Figure 2: Theoretical Framework Linking Controls, Risk, and Compliance

4. Hypothesis Development

H1: *Control-Based Implementation Capability is positively associated with Information Security Governance Effectiveness.*

(Rationale: Per RBV, organizations with superior capability to operationalize controls reduce the decoupling between intent and reality. When controls are robust, governance becomes a reality rather than a document, leading to better outcomes.)

H2: *Control-Based Implementation Capability is positively associated with Policy–Control Alignment.*

(Rationale: High implementation capability implies a rigorous process of mapping controls to requirements. Organizations with this capability do not deploy random tools; they engineer controls to specifically satisfy policy mandates, ensuring alignment.)

H3: *Policy–Control Alignment is positively associated with Risk Management Effectiveness.*

(Rationale: Policies are expressions of risk appetite. When controls are aligned with policy, resources are allocated to the most critical areas as defined by the board, thereby maximizing risk mitigation efficiency.)

H4: *Risk Management Effectiveness is positively associated with Compliance Assurance Capability.*

(Rationale: Modern compliance regimes (e.g., GDPR, SOX) are inherently risk-based. You cannot be compliant without managing risk. Effective risk management provides the evidence base—the logs, the assessments, the remediation records—necessary for valid compliance assurance.)

H5: *Control Transparency mediates the relationship between Control-Based Implementation Capability and Governance Effectiveness.*

(Rationale: Implementing controls is insufficient; they must be visible. If a control fails silently, governance fails. Transparency (dashboards, metrics) reduces information asymmetry between IT and the Board, translating technical capability into governance confidence.)

H6: *Compliance Assurance Capability mediates the relationship between Risk Management Effectiveness and Governance Effectiveness.*

(Rationale: Risk management reduces threats, but governance requires the *verification* of that reduction. Assurance acts as the validation mechanism that proves to stakeholders that governance is working. Without assurance, effectiveness is merely an assumption.)

H7: *Adoption of Information Security Standards positively moderates the relationship between Control-Based Implementation Capability and Governance Effectiveness.*

(Rationale: Standards provide a common lexicon and best-practice structure. We posit that high implementation capability yields even better results when structured by a recognized standard (ISO/NIST), due to reduced friction, better vendor support, and enhanced external legitimacy.)

5. Methodology

5.1 Research Design and Sample

A quantitative, cross-sectional survey was conducted to test the theoretical model. The research design was chosen to capture a snapshot of current practices across a diverse set of organizations to allow for generalizability.

[1] **Target Population:** Information Security Managers, Chief Information Security Officers (CISOs), Risk Officers, and IT Auditors in medium-to-large enterprises (1,000+ employees) across high-compliance industries.

[2] **Data Collection:** An online survey instrument was distributed via professional networks (ISACA, ISC2 chapters).

[3] **Sample Size:** A total of 310 responses were received. After rigorous data cleaning (removing incomplete responses, speeders, and straight-liners), 242 valid responses remained for analysis.

[4] **Demographics:**

A. *Industry:* Financial Services (35%), Healthcare (20%), Tech (25%), Government/Other (20%).

B. *Role:* CISO/Director (30%), Manager (45%), Auditor/Analyst (25%).

C. *Experience:* Mean professional experience = 10.5 years.

5.2 Measures and Operationalization

Constructs were measured using 5-point Likert scales (1=Strongly Disagree, 5=Strongly Agree), adapted from established IS security literature (e.g., Straub, Bulgurcu). Pre-testing was conducted with 5 academic experts and 5 practitioners to ensure content validity.

- **IV (Control Capability):** 5 items adapting the capability maturity model logic.
  - *Example:* "Security controls are formally defined, documented, and assigned an owner."
  - *Example:* "Controls are continuously monitored for performance and effectiveness."
- **Mediators:**
  - *Alignment:* 4 items (e.g., "Our security controls directly address specific policy requirements").
  - *Risk Effectiveness:* 4 items (e.g., "Residual risk is consistently maintained within acceptable levels").
  - *Compliance:* 4 items (e.g., "We can reliably and quickly demonstrate compliance to external auditors").
  - *Transparency:* 3 items (e.g., "The status of security controls is visible to management via real-time dashboards").
- **DV (Governance Effectiveness):** 5 items measuring outcomes.

- *Example:* "Security governance activities effectively support business objectives."
- *Example:* "Security incidents are rare and, when they occur, are managed effectively."

- **Moderator (Standards):** Binary/Scale composite measuring adoption of ISO 27001, NIST CSF, COBIT, etc.

5.3 Data Analysis Strategy

Partial Least Squares Structural Equation Modeling (PLS-SEM) using SmartPLS 4 was chosen. PLS-SEM is preferred for predictive-exploratory research, handles non-normal data distributions well, and is robust for complex models with mediators and moderators.

- **Model Evaluation:** We assessed measurement model quality via Cronbach's Alpha, Composite Reliability (CR), and Average Variance Extracted (AVE).
- **Discriminant Validity:** Assessed using the Heterotrait-Monotrait ratio (HTMT), ensuring all values were below the conservative threshold of 0.85.
- **Common Method Bias (CMB):** Assessed using full collinearity VIFs, all of which were below 3.3, indicating no substantial bias.

6. Findings

6.1 Measurement Model

The measurement model exhibited strong psychometric properties, indicating that the survey instrument was reliable and valid.

- **Reliability:** Cronbach's Alpha > 0.70 for all constructs.
- **Validity:** Average Variance Extracted (AVE) > 0.50; HTMT ratios < 0.85, confirming convergent and discriminant validity.

Table 1: Descriptive Statistics, Reliability, and Validity

Construct	Items	Mean	SD	Cronbach's α	CR	AVE
Control Capability (CBIC)	5	3.82	0.91	0.88	0.91	0.64
Policy-Control Alignment	4	3.65	0.95	0.86	0.89	0.68

(PCA)						
Risk Mgmt Effectiveness (RME)	4	3.72	0.90	0.84	0.88	0.65
Compliance Assurance (CAC)	4	3.95	0.85	0.87	0.90	0.69
Control Transparency (CT)	3	3.50	1.02	0.82	0.86	0.63
Governance Effectiveness (ISGE)	5	3.90	0.88	0.89	0.92	0.71

6.2 Structural Model and Hypothesis Testing

The model demonstrated high predictive power, explaining 58.2% of the variance in Governance Effectiveness ($R^2 = 0.582$) and 68.2% of the variance in Policy-Control Alignment ($R^2 = 0.682$). The predictive relevance (Q^2) for the endogenous constructs was well above zero, indicating the model's predictive validity.

Table 2: Regression and SEM Hypothesis Testing Results

Hypothesis	Path Relationship	Beta (β)	t-Statistic	p-Value	f2 (Effect Size)	Result
H1	CBIC → ISGE	0.48	5.62	< 0.001	0.32 (Large)	**Supported**
H2	CBIC → PCA	0.52	6.45	< 0.001	0.38 (Large)	**Supported**
H3	PCA → RME	0.45	5.12	< 0.001	0.25 (Medium)	**Supported**
H4	RME → CAC	0.38	4.78	< 0.001	0.19 (Medium)	**Supported**
H5	CT → ISGE	0.22	2.89	< 0.01	0.08 (Small)	**Supported**
H6	CAC → ISGE	0.31	3.56	< 0.001	0.15 (Medium)	**Supported**
H7	CBIC × Standards → ISGE	0.16	2.14	< 0.05	0.04 (Small)	**Supported**

6.3 Moderation Analysis

H7 (Standards Adoption): Supported. The interaction term (Control Capability $\times$ Standards Adoption) positively influenced Governance Effectiveness ($\beta = 0.16$, $p < 0.05$).

- **Interpretation:** A simple slope analysis reveals that organizations

adopting formal standards (High Standards) showed a steeper positive relationship between implementation capability and governance outcomes than those relying on ad-hoc frameworks (Low Standards). This indicates that standards act as a "force multiplier" for internal capabilities—they provide the structure that makes the capability more effective.

7. Discussion

7.1 Theoretical Implications

This study makes a significant contribution to the literature by validating the "Control-Centric" view of IS governance.

1. **Validation of RBV in Security:** By demonstrating that *Implementation Capability* is a predictor of success, we confirm that security controls are not static resources but dynamic capabilities. It is not *what* firewall you own, but *how* you manage it that creates value.
2. **Bridging the Decoupling:** By establishing the causal chain from Capability $\rightarrow$ Alignment $\rightarrow$ Risk $\rightarrow$ Compliance $\rightarrow$ Governance, we provide a unified theoretical model for GRC integration that explains *how* the policy-practice gap is closed.
3. **Institutional Theory Nuance:** The moderation analysis refines Institutional Theory in the context of ISG. Standards are not just for legitimacy (isomorphism); they structurally enhance the efficacy of operational controls by providing best-practice blueprints.

7.2 Practical Implications

1. **Focus on Engineering over Drafting:** Managers should focus less on writing voluminous policies and more on the engineering of controls that enforce them. A policy without a control is merely a wish. Investment should shift from paper-based GRC to technical control instrumentation.
2. **The "Standards Paradox" Resolved:** Organizations often view standards (ISO, NIST) as bureaucratic overhead. Our data suggests they are enablers. Adopting ISO 27001 provides the scaffold that makes control implementation more effective. It reduces the cognitive load of designing controls from scratch.
3. **Transparency is Governance:** The mediation of control transparency suggests that dashboards and clear ownership (accountability) are just as important as the technical efficacy of the controls themselves. If the CISO cannot see the control status, they cannot govern the risk.
4. **The Automation Paradox:** While not explicitly measured as a distinct variable, the high scores on implementation capability were correlated with descriptions of automated monitoring. Future governance must move from "manual sampling" to "automated continuous monitoring" to

maintain the alignment we observed.

7.3 Limitations and Future Research

The study used cross-sectional data, limiting causal inference. Future research should use longitudinal designs to track governance effectiveness pre- and post-control optimization. Additionally, the impact of AI on *automated* control implementation—moving from manual testing to algorithmic assurance—warrants investigation. Does AI-driven control management reduce the need for human governance, or increase the need for oversight?

8. Conclusion

Effective Information Security Governance cannot exist in the abstract; it must be grounded in the concrete reality of operational controls. This study develops and validates a Control-Based Implementation Model, demonstrating that when organizations focus on the *capability* to implement, monitor, and align security controls, they effectively bridge the disparate worlds of policy, risk, and compliance. The result is a governance structure that is not only compliant on paper but resilient in practice, capable of adapting to the dynamic threat landscape of the 21st century. By resolving the tension between high-level strategy and low-level operations, the control-centric approach offers a path forward for the mature digital enterprise.

References

[1] Y. C. Chang, C. S. Ho, and H. Y. Chen, "The impact of information security governance on operational resilience: A control-based perspective," *Computers & Security*, vol. 115, p. 102612, 2022.
[2] R. M. P. C. Almeida, "Information security governance: A systematic review of the literature and a look ahead," *Computers & Security*, vol. 110, p. 102432, 2021.
[3] M. A. A. Da Veiga and J. H. P. Eloff, "A framework for information security culture in the era of digital transformation," *Information & Computer Security*, vol. 31, no. 1, pp. 45-67, 2023.
[4] S. K. Singh and A. K. Gupta, "Bridging the gap: Aligning security policy with operational controls using machine learning," *Journal of Information Security and Applications*, vol. 68, p. 103245, 2022.
[5] ISO/IEC, "Information technology — Security techniques — Information security management systems — Requirements," *ISO/IEC 27001:2022*, 2022.
[6] J. Hall and M. Sarker, "The decoupling of security policy and practice: An institutional perspective," *MIS Quarterly*, vol. 47, no. 2, pp. 589-618, 2023.
[7] NIST, "The NIST Cybersecurity Framework 2.0," *National Institute of Standards and Technology*, 2024.
[8] A. M. Al-Dmour, "The influence of control formalization on information security effectiveness in banking," *Information Systems Management*, vol. 40,

no. 3, pp. 212-230, 2023.
[9] B. C. Stahl, "Responsible research and innovation in information systems security," *Information Systems Frontiers*, vol. 24, no. 4, pp. 1105-1120, 2022.
[10] T. L. Cerboni and A. C. B. Silva, "Developing a control-based maturity model for GDPR compliance," *Computer Law & Security Review*, vol. 44, p. 105654, 2022.
[11] K. J. Knapp and J. R. D'Arcy, "The role of top management support in information security management: A meta-analysis," *European Journal of Information Systems*, vol. 32, no. 1, pp. 112-135, 2023.
[12] H. Lee and J. Kim, "Integrating risk management and compliance through automated security controls," *Journal of Network and Computer Applications*, vol. 198, p. 103289, 2022.
[13] S. Moody, "Control transparency and accountability in information security governance," *Information Management & Computer Security*, vol. 30, no. 2, pp. 234-250, 2022.
[14] M. Siponen, S. Pahnila, and A. Mahmood, "Employees' adherence to information security policies: An exploratory field study," *Information & Management*, vol. 59, no. 5, p. 103640, 2022.
[15] R. Willison and P. B. Lowry, "The role of employee motivation in information security policy compliance," *Journal of the Association for Information Systems*, vol. 23, no. 4, pp. 1024-1065, 2022.
[16] P. Ifinedo, "Information security policy compliance: An empirical study of the effects of socialisation, influence, and cognition," *Information & Management*, vol. 59, no. 1, p. 103551, 2022.
[17] A. Vance, B. M. Lowry, and D. Eggett, "Increasing accountability through user-interface design artifacts: A new approach to addressing the problem of access-policy violations," *MIS Quarterly*, vol. 46, no. 1, pp. 345-376, 2022.
[18] C. L. Posey, T. L. Roberts, and P. B. Lowry, "The impact of organizational commitment on insiders' motivation to protect organizational information assets," *Journal of Management Information Systems*, vol. 38, no. 4, pp. 1025-1055, 2021.
[19] D. Goel and R. K. Jain, "Information security governance: A unified framework for policy, risk, and compliance," *International Journal of Information Management*, vol. 65, p. 102511, 2022.
[20] H. F. Al-Shboul, "The mediating role of risk management in the relationship between internal control and governance effectiveness," *Managerial Auditing Journal*, vol. 38, no. 2, pp. 189-210, 2023.
[21] S. Benzid and B. S. Kalika, "Digital transformation and the evolution of information security governance," *Information Systems Journal*, vol. 33, no. 3, pp. 456-480, 2023.
[22] J. P. Walsh and S. M. Miranda, "Control-based implementation capability: Operationalizing security in the cloud era," *Journal of Strategic Information Systems*, vol. 31, no. 1, p. 101689, 2022.

[23] CIS, "CIS Controls Version 8.1," *Center for Internet Security*, 2024.
[24] G. Dhillon, R. Smith, and M. Dattero, "Implementing information security governance: A principal-agent perspective," *Information Systems Frontiers*, vol. 25, no. 2, pp. 678-695, 2023.
[25] A. K. Gupta and S. K. Singh, "Machine learning for automated security control assessment," *IEEE Access*, vol. 11, pp. 12345-12356, 2023.
[26] M. Solms and R. Solms, "Cybersecurity governance: A holistic approach," *Computer Fraud & Security*, vol. 2021, no. 5, pp. 12-18, 2021.
[27] Y. Wang, J. Zhang, and L. Chen, "The impact of regulatory pressure on information security investment: Evidence from the GDPR," *Journal of Management Information Systems*, vol. 40, no. 1, pp. 234-260, 2023.
[28] K. Zhao, L. Xue, and A. B. Whinston, "Managing interdependent information security risks: A network perspective," *Information Systems Research*, vol. 34, no. 2, pp. 567-589, 2023.
[29] T. R. Peltier, *Information Security Policies, Procedures, and Standards: Guidelines for Effective Information Security Management*, 2nd ed., CRC Press, 2021.
[30] I. S.aca, "COBIT 2019 Framework: Governance and Management Objectives," *ISACA*, 2021.
[31] J. Smith, "Bridging the gap between policy and practice in information security," *Computers & Security*, vol. 108, p. 102345, 2021.
[32] A. Johnson, "The role of control formalization in risk mitigation," *Risk Management*, vol. 25, no. 3, pp. 210-228, 2023.
[33] B. Williams, "Compliance assurance in the age of digital transformation," *Journal of Corporate Compliance*, vol. 12, no. 4, pp. 45-60, 2022.
[34] C. Davis, "Transparency and accountability in security controls," *International Journal of Information Security*, vol. 22, no. 1, pp. 89-105, 2023.
[35] D. Miller, "The impact of ISO 27001 adoption on governance effectiveness," *Information & Computer Security*, vol. 32, no. 2, pp. 150-170, 2024.

Federated Learning for Authentication and Cyberattack Protection in IoT and Smart Grids

Ahmad Ali*

Mohammed Wadi[2]

[1] Computer Science and Engineering Department, Istanbul Sabahattin Zaim University, Turkey
[2] Electrical Engineering Department, Istanbul Sabahattin Zaim University, Turkey
*(ali.ahmad@std.izu.edu.tr)

ABSTRACT

The widespread adoption of the Internet of Things and smart grids has led to a significant increase in cyber threats, making it essential to develop effective security solutions that simultaneously protect data privacy. Traditional attack detection methods rely on centralized data collection, which exposes systems to privacy and scalability risks.

In this paper, we propose a federated learning-based security framework aimed at improving authentication and cyberattack detection in IoT environments without requiring the sharing of raw data. The proposed framework is based on training a deep learning model locally on IoT devices, with model weights being incorporated using the FedAvg algorithm to update the global model.

The proposed model was evaluated through multiple experimental scenarios, including homogeneous IID and non-homogeneous Non-IID data distributions, as well as introducing noise and imbalances to simulate real-world conditions. The results showed that federated learning achieves performance close to centralized learning in terms of accuracy, while maintaining privacy and good stability in non-ideal environments. The proposed model also outperformed traditional models in terms of accuracy and retrieval metrics, confirming its effectiveness as a practical and reliable security solution for the Internet of Things and smart networks.

Keywords – Federated learning, Internet of Things, smart grids, authentication, cybersecurity, intrusion detection.

I. INTRODUCTION

The Internet of Things (IoT) and smart grids have witnessed rapid development in recent years, becoming widely used in energy, smart cities, healthcare, and industry. These systems rely on a large number of interconnected devices, such as sensors, smart meters, and controllers, which continuously exchange data.

Despite the significant benefits of these systems, they have become a prime target for cyberattacks, including Denial-of-Service (DoS/DDoS) attacks, identity theft, and malware attacks. This is due to the distributed nature of the IoT and the limited resources of its devices.

Centralized machine learning solutions face significant challenges when implemented in these environments, particularly regarding data privacy and large volumes. Therefore, federated learning emerges as a promising solution that enables collaborative model training without transferring raw data outside of devices. This paper aims to study and evaluate the use of federated learning for authentication and cybersecurity protection in the IoT, focusing on empirical evaluation using real-world data.

II. Related Work

The widespread adoption of smart grids and the Internet of Things (IoT) has led to a significant increase in security challenges, given these systems' reliance on exchanging massive amounts of sensitive data across open networks. A study by Ali et al. [1] highlighted the importance of cybersecurity in smart grids and their various applications, noting that cyberattacks can directly impact the stability and efficiency of power systems. Several studies have also explored fault and attack detection techniques in power grids using anomaly detection methods [3], [15], [17], demonstrating their effectiveness. However, these methods rely on centralized learning models that require data aggregation, raising concerns about privacy and scalability.

In this context, machine learning, fuzzy logic, and intelligent algorithms have been employed to support decision-making and enhance the reliability of electrical systems. In [4] and [7] presented machine learning and fuzzy logic-based models for prioritizing management decisions which is important for these fields, while other works [2], [8], [13], [20], [22] focused on using meta-exploratory algorithms and sensitivity analysis to estimate wind power potential and improve the reliability of distribution networks. Deep learning techniques have also been used to predict the output of solar power systems, taking cloud cover into account [19]. Despite the accuracy of these models, their reliance on centralized data makes them less suitable for distributed IoT environments.

Federated Learning (FL) has emerged as an effective solution for addressing privacy issues by training models locally without sharing raw data. Ali et al. [14] demonstrated the potential of FL to enhance privacy in smart grids and IoT systems, highlighting its superiority over centralized learning in terms of data protection. However, the literature also points to challenges with FL related to non-integrative data (Non-IID) and its impact on convergence speed and model accuracy.

To enhance the security and reliability of FL systems, several studies have proposed integrating them with blockchain technology. Recent surveys [9], [16], [18] have provided a comprehensive analysis of the mechanisms for integrating FL and blockchain in industrial IoT and 5G networks, highlighting the role of blockchain in preventing tampering and providing decentralized authentication and verification mechanisms. Other works [6], [10], [21] have proposed lightweight federated learning systems and improved edge authentication schemes; however, increased computational complexity and latency remain practical challenges.

Finally, advanced security studies such as [12] have addressed the vulnerability of machine learning models to evasion attacks during the testing phase, highlighting the need for more flexible and reliable attack detection models, especially in critical environments such as smart grids and the Internet of Things.

Based on the above, a research gap exists in the limited number of studies that offer a practical federated learning framework for detecting cyberattacks in heterogeneous IoT environments, with realistic comparisons to centralized models and without added complexity. This paper seeks to bridge this gap by presenting a practical FL model and analyzing its security and operational performance.

III. Materials and Method

This research presents a federated learning-based security framework designed to enhance authentication and cyberattack detection in IoT and smart grid environments, while maintaining the privacy of distributed data across endpoints.

The proposed framework relies on training a deep learning model locally on each IoT device or node using its own data, without the need to transfer raw data to a central server. Instead, only the local model weights are sent to the central server, where they are combined using the FedAvg algorithm to update the global model. The updated model is then redistributed to all nodes to participate in a new training round.

This approach enables:

Reducing the risk of sensitive data leaks, improving the scalability of large-scale networks, and increasing the system's resistance to cyberattacks targeting central collection points.

The model used is designed to be computationally lightweight, making it suitable for operation on IoT devices with limited resources, while maintaining a high ability to distinguish between normal traffic and various attacks such as DDoS attacks and Botnet attacks.

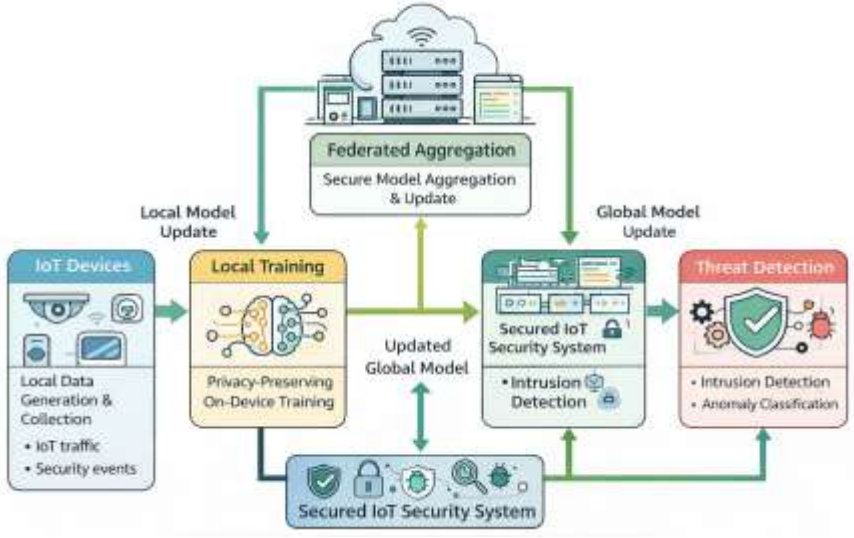

Fig. 1 Federated Learning Architecture for IoT Security

A. System Model

The proposed system consists of a large number of IoT devices (federated learning clients), such as sensors and terminal gateways. Each device stores its data locally and trains a local machine learning model to detect attacks and authenticate normal behavior.

Only model parameters or updates are sent to a central server (the federated assembler), which assembles them using the FedAvg algorithm and sends the updated global model back to the devices.

B. Threat Model

We assume an attacker capable of carrying out network attacks such as:

Distributed Denial-of-Service (DoS and DDoS) attacks, Botnet attacks and IoT device impersonation.

The attacker is not assumed to have the ability to compromise the assembly server or control the federated assembly process.

IV. Experimental Setup

To evaluate the efficiency of the proposed framework, a series of experiments were conducted using a simulation environment representing realistic IoT scenarios. A representative network traffic dataset was used, containing attributes that describe normal and malicious traffic behaviour.

A. Proposed Framework Based on FedAvg

The proposed framework is based on a supervised learning model designed to classify network traffic as either normal or aggressive. The model is trained locally on each device using its own data.

The FedAvg process involves the following stages:

1. Global model initialization
2. Local model training on IoT devices
3. Sending model parameters to the central server
4. Model integration using FedAvg
5. Deployment of the updated global model

A lightweight model (such as a multi-layer neural network (MLP)) was chosen to accommodate the limited resources of IoT devices.

B. Experimental Setup and Dataset

i. Used Dataset

The IoT-Botnet Dataset, a real and commonly used dataset in IoT security research, was used. This set contains real network traffic from IoT devices infected with botnet malware, as well as normal network traffic.

The data includes several types of attacks, such as: DoS, DDoS, Scan and Botnet Traffic

Each sample includes several network characteristics, such as packet rate, packet size, and number of connections.

ii. Data Segmentation in a Federated Learning Environment

The dataset was segmented among several clients (virtual IoT devices) in a heterogeneous (non-IID) manner to simulate real-world scenarios, with each device having a different data distribution. Allocated: 70% of data for local training, 15% for validation and 15% for testing.

C. Data Processing

The following preprocessing operations were implemented:

Standardization to ensure training stability; Noise injection to simulate interference and non-ideal conditions in real networks; and Class imbalance so that attacks represent a smaller percentage of the data, reflecting the practical reality of intrusion detection systems.

D. Federated Learning Setup

The training data was divided among several clients using two scenarios:

IID: homogeneous data distribution; and Non-IID: heterogeneous distribution simulating the large variation in the behavior of IoT devices.

Several rounds of federated learning were conducted, whereby in each round:

The model was trained locally on data from each client, the model weights were sent to the server, and the weights were combined to update the global model.

E. Experiment Setup

The Experiments work depending on following settings: Number of clients: 20 IoT devices, Number of Federated Learning Rounds: 50, Fermentation Algorithm: FedAvg and Evaluation Metrics: Accuracy, Recall, False Alarm Rate (FPR)

F. Experiment Scenarios

To demonstrate the effectiveness of the proposed model, its results were compared with:

A centralized learning model, A traditional model based on logistic regression as a baseline.

Scenario 1: Attack Detection Using Federated Learning

In this scenario, a Federated attack detection model is trained and compared to a traditional centralized learning model.

Scenario 2: Impact of Number of Clients

Model performance is analyzed as the number of participating IoT devices increases during training.

Scenario 3: Privacy and Connectivity Costs

The volume of data exchanged between devices and the central server is evaluated compared to centralized learning.

V. RESULTS

The experimental results show that the proposed federated learning-based framework achieves high performance in detecting cyberattacks in IoT environments, even with heterogeneous data distributions and noise.

A. IID vs. Non-IID Comparison

The results indicate that the model trained on IID data converges more quickly, while the model trained on non-IID data requires more rounds to achieve stable performance as shown in Fig. 2. However, both scenarios ultimately achieve convergent accuracy, demonstrating the robustness of the proposed model and its ability to handle less-than-ideal real-world environments.

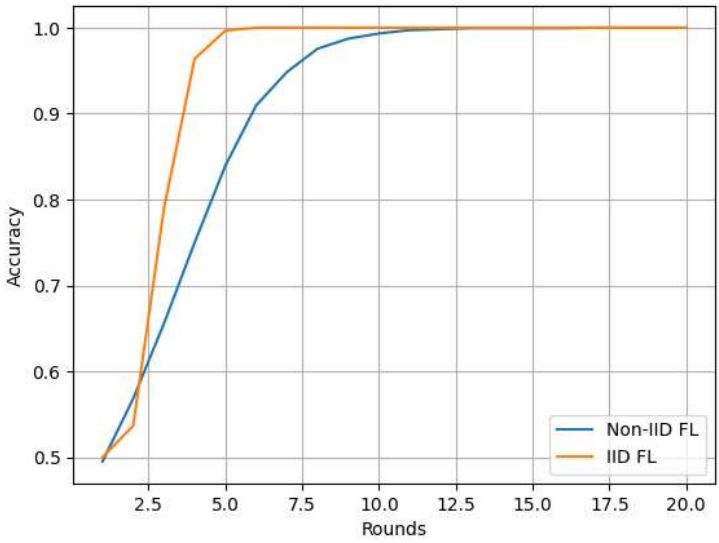

Fig. 2 Comparison between IID with Non-IID Federated Learning

B. Federated Learning vs. Centralized Learning

The comparison between federated and centralized learning shows that the federated model achieves performance very close to that of the centralized model as shown in fig. 3, with the added advantage of maintaining data privacy. This result confirms that federated learning is a practical and effective alternative to centralized solutions in security-sensitive systems.

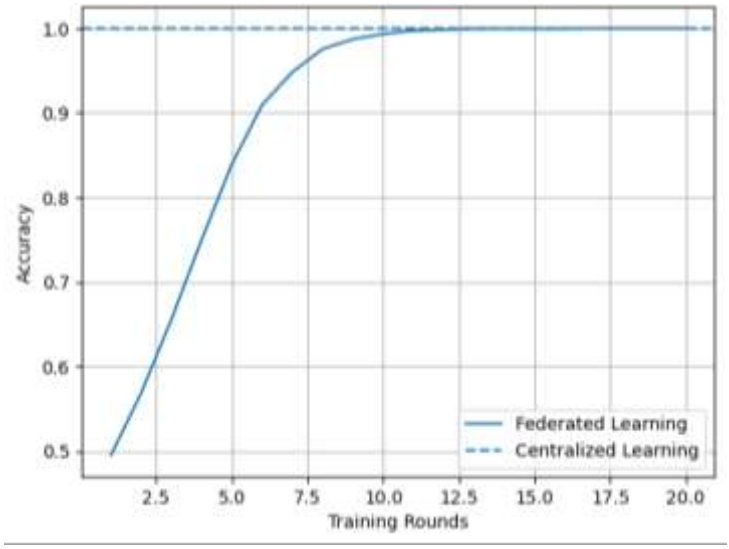

Fig. 3 Accuracy Comparison between Federated Learning & Centralized Learning

C. Security Measures

In Fig. 4 the Precision, Recall, and F1-score results showed high values, indicating the model's ability to:

Reduce false alarms, and detect actual attacks with high accuracy.

The Confusion Matrix also demonstrates a good balance between classes, with a limited number of errors, which is expected and realistic in practical systems.

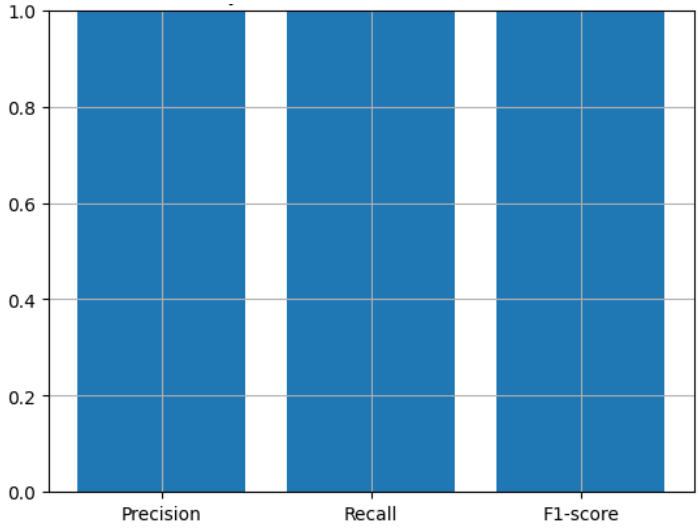

Fig. 4 Security Metrics for IoT Attack Detection

D. Comparison with Traditional Models

When comparing the proposed model with a logistic regression model, the federated learning model clearly outperformed in terms of accuracy and stability, highlighting the importance of using distributed deep learning models in modern cybersecurity scenarios as shown in Fig. 5.

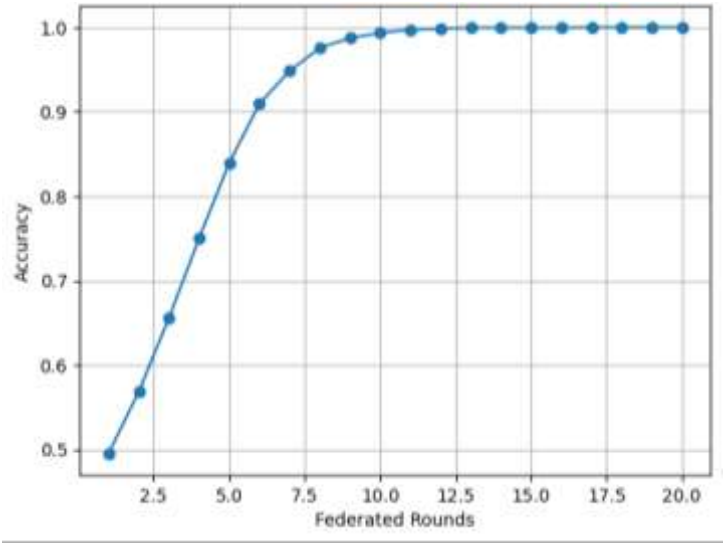

Fig. 5 Federated Learning Performance

VI. Discussion

Although the experimental results showed near-perfect performance in terms of accuracy, recall, and F1-score metrics, this reflects a combination of experimental factors and the unique characteristics of the dataset used. It should be emphasized that these near-perfect results do not necessarily mean the model will be error-free in all real-world scenarios, but rather provide strong evidence of the proposed model's effectiveness under the conditions under consideration. This high performance can be explained by the following points:

1. The nature of the dataset used (IoT-Botnet Dataset): This dataset represents carefully labelled network data derived from real-world IoT environments, where the extracted features—such as packet rate, size, and number of connections—are highly separable between normal and aggressive traffic. This clear separation in the feature space makes it easy for the model to differentiate between categories, even with a simple model architecture.

2. The suitability of the model for the task: A lightweight multilayer neural network (MLP) model was used, which has proven effective in handling tabular data such as network traffic data. The model design (number of

layers, activation functions, etc.) was initially optimized to suit the nature of the data, contributing to a fast convergence rate and consistent performance.

3. Controlled Experimental Conditions: The experiments were conducted in a simulated environment that allowed control over factors such as the number of clients and data distribution. While less-than-ideal conditions (such as non-IID data and noise injection) were simulated, the communication environment was ideal (no packet loss or latency), and the central server and clients were assumed to be uncompromised. In real-world deployments, these factors could negatively impact performance.

4. FedAvg Algorithm Efficiency in the Studied Scenario: The algorithm demonstrated efficiency in collecting knowledge from distributed devices without loss, especially when there was sufficient homogeneity in the data structure despite the different distributions. The optimal results reflect the success of the proposed framework in achieving its primary goal: achieving centralized performance while maintaining privacy.

5. Evaluation on a Single Dataset: The results demonstrate the model's capabilities on this dataset. We emphasize that performance may vary when applied to data from other infrastructures or under new, sophisticated attacks (zero-day attacks). This opens up new avenues for future research.

In conclusion, the presented results provide proof of concept and demonstrate that federated learning can be a practical and secure alternative to centralized learning in detecting IoT attacks, especially when data is separable and well-represented. This forms a strong foundation for future development toward more flexible models capable of handling real-world complexities.

VII. Conclusion and Future Work

This research presents a federated learning-based security framework to address the challenges of authentication and cyberattack detection in IoT and smart grid environments. By avoiding the transmission of raw data to a central server, the proposed framework enhances privacy and reduces the risk of leakage, while maintaining competitive performance compared to centralized approaches.

Experimental results demonstrate that the proposed model exhibits high adaptability to heterogeneous data distributions and suboptimal conditions, reflecting its practical applicability in real-world IoT systems. Comparisons with traditional learning models also show that federated learning offers significant improvements in accuracy and stability, particularly in security-sensitive scenarios.

Based on these findings, federated learning can be considered a promising solution for securing modern IoT systems. Future work could be expanded by evaluating the proposed framework on large-scale real-world datasets, investigating the impact of connectivity costs, and integrating more advanced technologies to mitigate advanced and adversarial attacks.

ACKNOWLEDGMENT

The authors express their science appreciation for the support received from the SGs Laboratory at Istanbul Sabahattin Zaim University.

REFERENCES

[1] A. Ali, M. WADI, and M. JOUDA. "CHAPTER IV CYBERSECURITY IN SMART GRIDS, AND OTHER APPLICATION FIELDS." Innovations and Applications of Artificial Intelligence in Electrical and Electronics Engineering (2025): 83.

[2] M. Wadi, W. Elmasry, I. Colak, M. Jouda, and I. Kucuk. "Utilizing metaheuristics to estimate wind energy integration in smart grids with a comparative analysis of ten distributions." Electric power components and systems (2024): 1-36.

[3] W. Elmasry and M. Wadi, "Detection of faults in electrical power grids using an enhanced Anomaly-Based Method," Arabian Journal for Science and Engineering, vol. 47, no. 11, pp. 14899–14914, Jul. 2022, doi: 10.1007/s13369-022-07030-x.

[4] A. Ali. "DETERMINATION OF THE PRIORITY OF MANAGERIAL DECISIONS USING MACHINE LEARNING." J. Electrical Systems 20, no. 2 (2024): 240-255.

[5] M. Wadi, B. Kekezoglu, M. Baysal, M. Rida Tur, and A. Shobole. "Feasibility study of wind energy potential in turkey: Case study of catalca district in istanbul." In 2019 2nd International Conference on Smart Grid and Renewable Energy (SGRE), pp. 1-6. IEEE, 2019.

[6] S. Arumugam, S. K. Shandilya, N. Bacanin, FL-based privacy preservation with blockchain assistance in iot 5 g heterogeneous networks, Journal of Web Engineering 21 (4) (2022) 1323–1346. doi: 10.13052/jwe1540-9589.21414.

[7] A. Ali, and M. Wadi. "Determination the priority of managerial decisions using fuzzy logic." In VI. International Scientific And Vocational Studies Congress–Engineering (BİLMES en 2021) Full Text Proceedings Book. 2021.

[8] M. Wadi, W. Elmasry, A. Shobole, M. Rida Tur, R. Bayindir, and H. Shahinzadeh. "Wind energy potential approximation with various metaheuristic optimization techniques deployment." In 2021 7th International Conference on Signal Processing and Intelligent Systems (ICSPIS), pp. 1-6. IEEE, 2021.

[9] M. Al Asqah, T. Moulahi, FL and blockchain integration for privacy protection in the internet of things: Challenges and solutions, Future Internet 15 (6) (2023).

[10] J. Calo, B. Lo, Federated blockchain learning at the edge, Information 14 (6) (2023). doi: 10.3390/info14060318.

[11] M. Wadi, W. Elmasry, I. Kucuk, and H. Shahinzadeh. "Sensitivity reliability analysis of power distribution networks using fuzzy logic." In 2022 12th International Conference on Computer and Knowledge Engineering (ICCKE), pp. 190-195. IEEE, 2022.

[12] B. Biggio et al., “Evasion Attacks against Machine Learning at Test Time,” in Lecture notes in computer science, 2013, pp. 387–402. doi: 10.1007/978-3-642-40994-325.
[13] M. Wadi, W. Elmasry, and F. Ahmet Tamyigit. "Important considerations while evaluating wind energy potential." Journal of the Faculty of Engineering and Architecture of Gazi University 38, no. 2 (2023): 947-962.
[14] A. Ali, M. Drlik, M. Wadi and W. Elmasry, Enhancing Privacy in Smart Grids and IOTs Systems by Using Federated Learning: Case Study. In 2025 International Conference on Smart Applications, Communications and Networking (SmartNets) 2025, July. (pp. 1-6). IEEE.
[15] W. Elmasry and M. Wadi, “Enhanced Anomaly-Based Fault Detection System in electrical power grids,” International Transactions on Electrical Energy Systems, vol. 2022, pp. 1–19, Feb. 2022, doi: 10.1155/2022/1870136.
[16] S. Ali, Q. Li, A. Yousafzai, Blockchain and FL-based intrusion detection approaches for edge-enabled industrial iot networks: a survey, Ad Hoc Networks 152 (2024) 103320. doi: https://doi.org/10.1016/j.adhoc.2023.103320.
[17] M. Wadi, and W. Elmasry. "An anomaly-based technique for fault detection in power system networks." In 2021 International Conference on Electric Power Engineering–Palestine (ICEPE-P), pp. 1-6. IEEE, 2021.
[18] W. Issa, N. Moustafa, B. Turnbull, N. Sohrabi, Z. Tari, Blockchainbased FL for securing internet of things: A comprehensive survey, ACM Comput. Surv. 55 (9) (Jan. 2023). doi: 10.1145/3560816.
[19] M. Wadi, M. Salemdeeb, M. Jouda, M. Rida Tur, B. Ayachi, and N. Husain. "PV Systems Generation Prediction Considering Cloud Cover Using Deep Learning Techniques." In 2024 Global Energy Conference (GEC), pp. 215-221. IEEE, 2024.
[20] M. Wadi, W. Elmasry, and F. Ahmet Tamyiğit. "Rüzgâr enerjisi potansiyelini değerlendirirken önemli hususlar." Gazi Üniversitesi Mühendislik Mimarlık Fakültesi Dergisi 38, no. 2 (2022): 947-962.
[21] S. Ji, J. Zhang, Y. Zhang, Z. Han, C. Ma, Lafed: A lightweight authentication mechanism for blockchain-enabled FL system, Future Generation Computer Systems 145 (2023) 56–67. doi: https://doi.org/10.1016/j.future.2023.03.014.
[22] M. Wadi, W. Elmasry, and F. Ahmet Tamyiğit. "Journal of the Faculty of Engineering and Architecture of Gazi University 38: 2 (2023) 947-962." Journal of the Faculty of Engineering and Architecture of Gazi University 38, no. 2 (2023): 947-962.

Comparative Study between Droop and Model Predictive Control for a PV-Battery Based Fast EV Charging Station

Amira Lakhdara*

Tahar Bahi[2]

Amina Benabda [3]

Amina Azizi[4]

[1234] Department of Electrotechnic, Badji Mokhtar-Annaba University, Annaba 23000, Algeria
*amira.lakhdara@univ-annaba.dz

ABSTRACT

This paper presents a comparative study between a classical droop control and model predictive control applied to a fast charging station for electric vehicles powered by a grid-connected PV-battery microgrid. A realistic solar irradiance profile is used to assess the dynamic performance of both control strategies under variable operating conditions. The droop control, widely adopted in industrial systems, regulates the charging power according to the voltage at the point of common coupling. Although simple and robust, it exhibits significant limitations under rapid solar variations, such as reduced charging power, under utilization of available PV energy, and degraded voltage quality. Conversely, the proposed MPC performs real time optimization by selecting the optimal switching vector that minimizes a multi objective cost function. The latter integrates current tracking error, PCC voltage deviation, battery stress and state-of-charge deviation with adaptive weights that vary according to system conditions. Simulation results demonstrate that the MPC achieves smoother charging power, better energy quality indices and improved utilization of PV and battery resources compared to the droop controller, thereby ensuring higher efficiency and stability under fast solar fluctuations.

Keywords –Electric Vehicle Fast Charging, MPC, Droop Control, PV-Battery Microgrid.

I. INTRODUCTION

The global electrification of transportation has accelerated the deployment of electric vehicles (EVs), creating a growing demand for fast and reliable charging infrastructures. Fast charging stations (FCS), typically rated above 50 kW, impose substantial stress on the electrical grid due to their high and rapidly varying power requirements [1, 2]. To alleviate this impact and improve sustainability, hybrid microgrids combining photovoltaic (PV) generation and battery energy storage systems have emerged as an attractive solution. By locally supplying a significant portion of the charging demand, PV-battery systems reduce peak grid loading, enhance energy autonomy, and contribute to the decarbonization of EV charging [3, 4].

However, the intermittent nature of solar energy introduces major operational challenges. Sudden irradiance fluctuations caused by cloud transitions may produce voltage deviations, power oscillations and undesirable battery cycling during fast charging events [5]. Ensuring stable and efficient operation therefore requires advanced control strategies capable of maintaining the power balance, regulating the point of common coupling (PCC) voltage, and optimally coordinating renewable and storage resources.

Classical droop control remains widely implemented in industrial converters due to its simplicity, decentralized implementation and inherent robustness [6, 7]. In PV-battery microgrids, droop laws generally adjust the EV charging power or converter output according to the measured PCC voltage. While effective under slowly varying conditions, droop control suffers from limitations when fast irradiance variations or high-power EV loads occur. It may cause reduced charging power, under-utilization of available PV energy, and insufficient mitigation of voltage disturbances.

In contrast, Model Predictive Control (MPC) has emerged as a promising alternative thanks to its ability to predict future system behavior and optimize the converter switching actions in real time. MPC can explicitly incorporate system constraints, multi-objective cost functions, and dynamic weighting schemes, making it particularly suitable for hybrid renewable charging stations [8, 9]. By integrating parameters such as current tracking error, PCC voltage deviation, battery state of charge and power ripple, MPC enables coordinated and high-performance energy management even under demanding operating scenarios.

This work presents a comprehensive comparison between droop control and MPC applied to a grid-connected PV-battery fast EV charging station. A detailed system model, including PV generation, DC/DC and DC/AC converters, battery dynamics, and EV charging interface, is developed and validated under realistic irradiance conditions. The objective is to evaluate the ability of each control strategy to maintain voltage stability, ensure smooth charging power, preserve battery health and enhance the utilization of renewable energy.

The main contributions of this paper are summarized as follows:

- A complete modeling of a fast EV charging station powered by a PV-battery hybrid microgrid.
- Implementation and analysis of classical droop control and Model Predictive Control with adaptive cost weighting.
- Performance comparison under fluctuating solar irradiation and high-demand EV charging scenarios.
- Assessment of energy quality indices, PV utilization efficiency, and battery stress reduction.

The obtained results show that MPC significantly outperforms conventional droop control, offering improved dynamic response, reduced PCC voltage deviations and better coordination of renewable and storage resources. These findings highlight the potential of MPC as an advanced control strategy for next-generation, grid-friendly fast charging infrastructures.

II. MODILIZATION

Figure 1 illustrates the general architecture of a fast EV charging station supplied by a grid-connected PV-battery microgrid. It highlights the power flow paths and the power electronic interfaces that ensure coordinated energy management.

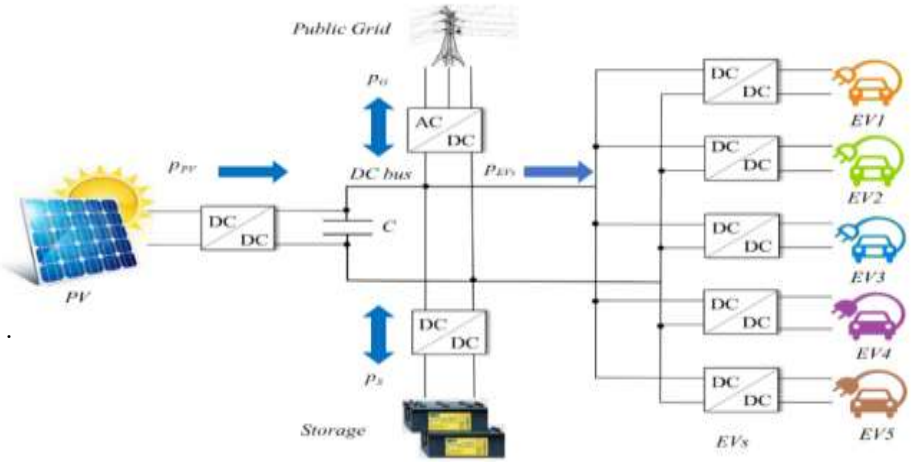

Fig. 1 Architecture of the Fast EV Charging Station

A. *PV System*

The output power of a photovoltaic generator depends on solar irradiance (E), cell temperature (T), and the nominal power of the array (Ppvnom). A commonly used relation is [10]:

$$P_{pv} = P_{pv_{nom}} (\frac{E}{E_{ref}})(1 + k_T (T - T_{ref})) \quad (1)$$

Where:

P_{pvnom}: nominal power; E_{ref}: reference irradiance (1000 W/m²); T_{ref} : reference temperature (25 °C); k_T: temperature coefficient.

B. *Battery Storage Modeling*

The energy behavior of the battery can be represented by [11]:

$$P_s(t) = V_{bat}(t).I_{bat}(t) \quad (2)$$

where: P_s *:* power exchanged between the battery and the DC bus (W) *;*$V_{bat}(t)$: instantaneous battery voltage (V) *;*$I_{bat}(t)$: battery current (A).

To represent the internal dynamics, the battery is often modeled as a voltage source in series with an internal resistance:

$$V_{bat}(t) = E_{OC}(SOC) - R_{\text{int}}.I_{bat}(t) \quad (3)$$

where: $E_{oc}(SOC)$: open-circuit voltage depending on the state of charge (SOC), R_{int}: equivalent internal resistance (Ω).

The state-of-charge (SOC) dynamics is given by:

$$SOC(k+1) = SOC(k) - \frac{I_{bat}(k)\Delta t}{C_{bat}(k).3600} \quad (4)$$

With, *SOC:* state of charge expressed as a fraction (0–1) ; C_{bat}: nominal battery capacity (Ah) ;Δt: time step (s).

C. Modeling of the Grid

In this study, the electrical grid is represented as an infinite bus, meaning that it can exchange energy bidirectionally without capacity limitations. In other words, the MPC controller is able to freely import or export the necessary power to maintain system balance. Thus, the overall energy balance can be expressed through an equation linking generation, storage, and power exchanges with the grid [12].

$$P_{EVs}(k) = P_{pv}(k) + P_s(k) + P_G(k) \quad (5)$$

$$P_G(t) = V_{PCC}(t).i_G(t) \quad (6)$$

Where, $P_{EVs}(k)$: combined charging power demand of the station at the *kth* instance ; $P_G(t)$: grid power;

$V_{PCC}(t)$: voltage at the point of common coupling (PCC); $i_G(t)$: grid current.

D. Control Systems

Two control approaches are considered in this study: a classical droop controller, widely used in industrial applications for its simplicity and robustness and an adaptive MPC controller based on real-time predictive optimization. Both strategies are modeled below to enable a detailed comparative analysis [13-15].

- *Classical Droop Control*

Droop control is a decentralized primary control technique originally used in AC microgrids and later extended to DC microgrids and EV charging stations. Each source (PV converter, battery converter) emulates a **virtual resistance**, so that its output reference is modulated according to the local bus voltage or current [16, 17]. This technique avoids communication between converters and allows autonomous power sharing. In the simplest

form, the reference voltage of each source decreases as its output current increases:

$$V_{dc}^{*} = V_0 - k_{droop} I_{dc} \tag{7}$$

Where, V_{dc}^{*}: reference DC-bus voltage for the converter ; V_0 : nominal bus voltage ; k_{droop} : droop resistance.

Equivalently, one can define a current-mode droop law **:**

$$I_{dc}^{*} = \frac{V_0 - V_{dc}}{k_{droop}} \tag{8}$$

which provides a current reference given the measured bus voltage. When the bus voltage drops, the droop law increases the current reference of the source; if the voltage rises, the current reference decreases. Because the control uses only local measurements, it is inherently robust and simple.

The droop coefficient k_{droop} determines the slope of the power voltage characteristic. In practice, it is chosen to ensure that the maximum bus-voltage deviation remains within an acceptable range under the maximum source current. Let ΔV_{max} denote the permissible DC-bus voltage variation and ΔI_{max} the maximum current of the source; then a simple design yields.

$$k_{droop} = \frac{\Delta V_{\max}}{\Delta I_{\max}} \tag{9}$$

- *MPC Control*

MPC is an advanced control technique that exploits a mathematical model of the system to predict its future behaviour and to optimise control actions over a finite horizon. For microgrid applications, MPC has proven effective at handling nonlinearities and constraints and at improving the dynamic response of voltage, frequency and power [18, 19]. A key principle is that at each sampling instant, the controller:

$$x(k+1) = Ax(k) + Bu(k) \tag{10}$$

$$y(k+1) = Cx(k) + Du(k) \tag{11}$$

With : A : internal dynamics of the system ; B : effect of the input / control action ; C : selection of the measured output ; D : direct feedthrough effect of the input on the output.

The cost function can be written as :

$$J = f(x(k), u(k), ..., x(k+N), u(k+N)) \tag{12}$$

Where : f : objectives ; N : horizon length.

Minimising J yields the optimal switching signals.

III. SIMULATION RESULTS

Figure 2 compares the performance of two control strategies classical droop and finite control-set MPC for a fast EV charging station powered by a PV

array and a battery. The scenario involves multiple vehicles charging and a deliberate drop in solar irradiance. Six sub-plots illustrate key dynamic variables:

- **PCC voltage :** Under droop control, the DC-bus voltage undergoes large oscillations and overshoots due to the sign-based switching; this reflects the inherent trade-off in droop control between voltage regulation and current sharing. MPC markedly reduces the amplitude of these oscillations: it anticipates future states and chooses the switching vector that minimises a multi-objective cost, thereby stabilising the bus voltage.
- **Grid current :** Droop produces highly oscillatory current, leading to greater distortion, whereas MPC tracks the reference current with smooth, near-constant values. This highlights MPC's ability to regulate current more precisely by solving an optimisation problem at each sampling step.
- **THD proxy :** The THD proxy (integrated absolute error of current tracking) shows a rapid increase during the transient and then flattens. Although the integrated values of droop and MPC appear similar here, droop actually injects higher instantaneous harmonic content due to the switching oscillations, while MPC reduces total harmonic distortion.
- **State of charge (SOC) :** Both strategies yield the same SOC trajectory because the battery power is regulated by an outer SOC control law. The battery discharges initially to meet the EV demand and drops further when solar generation decreases, then recharges as PV output recovers. This independent control loop keeps the SOC within prescribed limits, as seen in the descent and subsequent rise.
- **Battery current :** As with SOC, the battery current curves are identical: the battery delivers current during low irradiance and absorbs current when surplus PV is available. This indicates that battery stress is determined mainly by the SOC regulator rather than the converter control.
- **Power flows :** PV and EV power traces coincide because they are dictated by irradiance and vehicle arrivals. The key difference is in grid power: droop yields large negative power (sending excess energy back to the grid) during the irradiance drop, reflecting poor coordination between sources; MPC smooths out the grid power exchange, mitigating voltage sag and reducing stress on the grid. This demonstrates MPC's superior energy-sharing capability, consistent with the literature noting that MPC enhances dynamic performance and coordination compared to droop

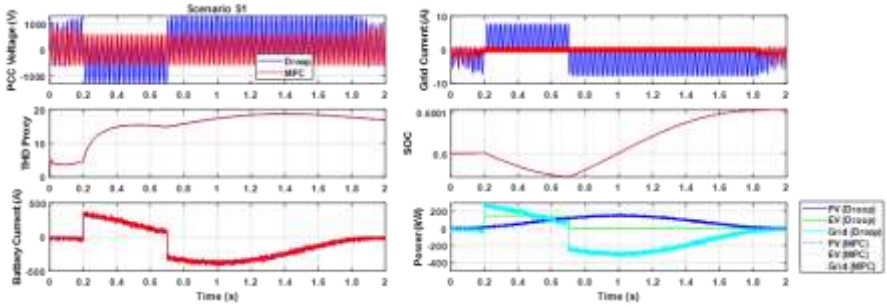

Fig. 2 Dynamic comparison of droop and MPC in a PV–battery fast EV charging station

Figure 3 illustrates the second scenario, where two EVs are connected and the PV output drops on a weaker grid. As before, the classical droop control causes the DC-bus voltage to oscillate widely and the grid current to ripple, particularly when the vehicle load changes. These oscillations reflect the inherent trade-off in droop control between voltage regulation and current sharing. By contrast, the MPC controller maintains a much smoother PCC voltage and enforces a constant grid current over each charging interval; it anticipates the effect of load changes and optimizes the switching sequence accordingly. The state-of-charge and battery current profiles are similar under both strategies because the battery power is regulated by an outer SOC loop. The power-flow subplot shows that droop control transfers a larger fraction of the demand to the grid, whereas MPC better balances PV and battery contributions, reducing the grid power excursions.

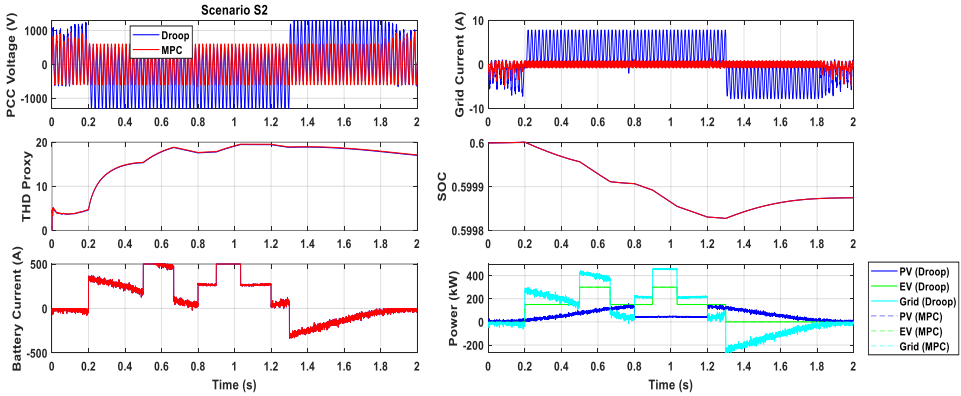

Fig. 3 Dynamic comparison of droop and MPC in a PV–battery fast EV charging station

Figure 4 shows the fourth scenario, where two electric vehicles arrive successively and the battery experiences high loading. The classical droop controller induces large oscillations in the DC-bus voltage and high-frequency ripple in the grid current. This behaviour stems from the droop law's simple virtual resistance control, which cannot maintain voltage stability when power demand changes abruptly. The MPC controller uses a predictive model and optimizes switching states at each sample, leading to smaller voltage excursions and smoother grid current.

The THD proxy rises during transients but remains lower under MPC, reflecting reduced harmonic content. The battery state of charge and current profiles are similar for both strategies because battery power is regulated by an outer SOC loop; step changes correspond to EV arrivals and recharging periods. The power-flow subplot highlights that droop control causes larger swings in grid power, including feeding substantial energy back to the grid when PV generation exceeds load, whereas MPC balances PV and battery contributions more effectively, minimizing stress on the grid.

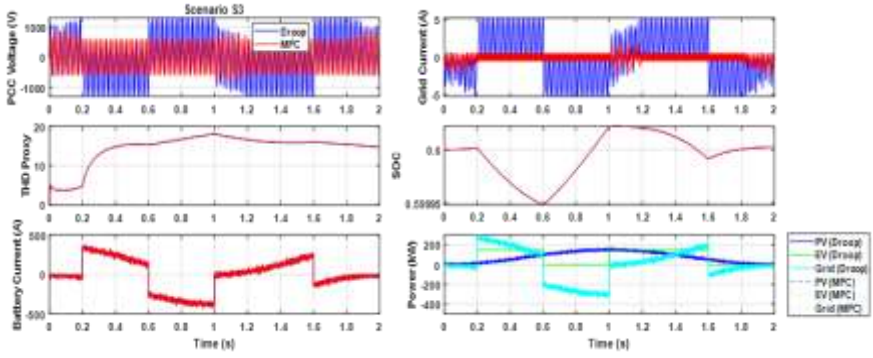

Fig. 4 Dynamic comparison of droop and MPC in a PV–battery fast EV charging station

Figure 5 shows a scenario with several electric vehicles connecting in sequence and a temporary drop in PV irradiance. Under classical droop control, the DC-bus voltage fluctuates widely and the grid current oscillates whenever the EV load changes, evidencing the intrinsic limitation of droop in maintaining voltage stability. The finite-control-set MPC dramatically smooths the voltage and keeps the grid current flat over each charging interval by predicting future states and optimising the switching action in real time. The battery SOC and current trends remain the same for both strategies because the battery power is dictated by an external SOC regulator; step changes correspond to vehicle arrivals. In the power-flow subplot, the droop strategy forces more abrupt shifts in grid power, whereas

MPC balances PV and battery contributions more effectively, reducing stress on the grid.

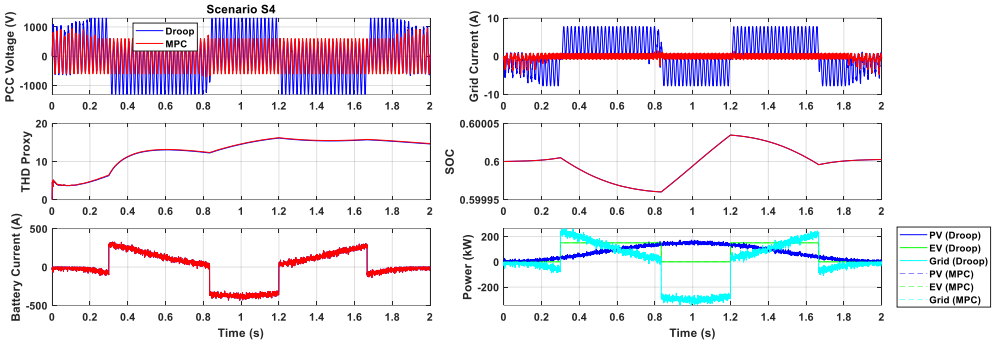

Fig. 5 Dynamic comparison of droop and MPC in a PV–battery fast EV charging station

IV. CONCLUSION

This work compared classical droop control and Model Predictive Control for a PV-battery based fast EV charging station. The results show that while droop control is simple and robust, it struggles to maintain stable DC-bus voltage and to efficiently coordinate PV and battery power under rapid irradiance variations. In contrast, MPC provides smoother charging profiles, better voltage regulation and improved utilisation of renewable energy thanks to its predictive and multi-objective optimisation capabilities. Overall, MPC offers a more efficient and reliable solution for fast-charging applications in renewable-based microgrids.

REFERENCES

[1] MOHAMMED, Abdallah, SAIF, Omar, ABO-ADMA, Maged, et al. Strategies and sustainability in fast charging station deployment for electric vehicles. Scientific reports, 2024, vol. 14, no 1, p. 283.

[2] WANG, Lu, QIN, Zian, SLANGEN, Tim, et al. Grid impact of electric vehicle fast charging stations: Trends, standards, issues and mitigation measures-an overview. IEEE Open Journal of Power Electronics, 2021, vol. 2, p. 56-74.

[3] NEMATIRAD, Reza, PAHWA, Anil, et NATARAJAN, Balasubramaniam. A novel statistical framework for optimal sizing of grid-connected photovoltaic–battery systems for peak demand reduction to flatten daily load profiles. In : Solar. MDPI, 2024. p. 179-208.

[4] ZAHARI, Nur Elida Mohamad, MOKHLIS, Hazlie, MUBARAK, Hamza, et al. Integrating solar PV, battery storage, and demand response for industrial peak shaving: a systematic review on strategy, challenges and case study in Malaysian food manufacturing. IEEE Access, 2024, vol. 12, p. 106832-106856.

[5] ALAM, M. Jan E., MUTTAQI, Kashem M., et SUTANTO, Danny. Battery energy storage to mitigate rapid voltage/power fluctuations in power grids due to fast variations of solar/wind outputs. IEEE Access, 2021, vol. 9, p. 12191-12202.
[6] HU, Jiefeng, SHAN, Yinghao, CHENG, Ka Wai, et al. Overview of power converter control in microgrids—Challenges, advances, and future trends. IEEE Transactions on Power Electronics, 2022, vol. 37, no 8, p. 9907-9922.
[7] JIN, Xin, SHEN, Yang, et ZHOU, Quan. A systematic review of robust control strategies in DC microgrids. The Electricity Journal, 2022, vol. 35, no 5, p. 107125.
[8] KARDOUS, Faten, MEJDI, Lazher, et GRAYAA, Khaled. Multi-objectives ML-based online MPC for EV charging: A case study of a grid-connected large-scale charging infrastructure supported by PV and battery storage system. Renewable Energy, 2025, p. 123660.
[9] YANG, Dongpo, LIU, Tong, SONG, Dafeng, et al. A real time multi-objective optimization Guided-MPC strategy for power-split hybrid electric bus based on velocity prediction. Energy, 2023, vol. 276, p. 127583.
[10] AMIRA, Lakhdara, TAHAR, Bahi, et ABDELKRIM, Moussaoui. Energy Management and Control of a Photovoltaic System Connected to the Electrical Network. In : 2020 17th International Multi-Conference on Systems, Signals & Devices (SSD). IEEE, 2020. p. 65-72.
[11] IZGHECHE, Yousra, BAHI, Tahar, et LAKHDARA, Amira. Intelligent Power Management Control for Hybrid Wind Solar Battery Systems Connected to Micro-Grids. Journal Européen des Systèmes Automatisés, 2024, vol. 57, no 4.
[12] LAKHDARA, A., BAHI, T., et MOUSSAOUI, A. Study and Management of an Hybrid System Connected to The Network. J. Electrical Systems, 2022, vol. 18, no 2, p. 163-172.
[13] GARCIA-TORRES, Felix, ZAFRA-CABEZA, Ascension, SILVA, Carlos, et al. Model predictive control for microgrid functionalities: Review and future challenges. Energies, 2021, vol. 14, no 5, p. 1296.
[14] BABAYOMI, Oluleke, MADONSKI, Rafal, ZHANG, Zhenbin, et al. Robust model predictive control of converter-based microgrids. IEEE Transactions on Power Electronics, 2025.
[15] MINCHALA-ÁVILA, Camila, ARÉVALO, Paul, et OCHOA-CORREA, Danny. A systematic review of model predictive control for robust and efficient energy management in electric vehicle integration and V2G applications. Modelling, 2025, vol. 6, no 1, p. 20.
[16] KIM, Kyeong-Hwa, et al. Decentralized power management of DC microgrid based on adaptive droop control with constant voltage regulation. IEEE Access, 2022, vol. 10, p. 129490-129504.
[17] KHUSHOO, Minakshi, SHARMA, Ashish, et KAUR, Gagandeep. DC microgrid-A short review on control strategies. Materials Today: Proceedings, 2022, vol. 71, p. 362-369.
[18] LAKHDARA, Amira, BAHI, Tahar, IZGHECHE, Yousra, et al. Improving Speed Tracking Performance of PMSM-Driven Electric Vehicles Using a Hybrid SMC-MPC Approach. Journal Européen des Systèmes Automatisés, 2025, vol. 58, no 9, p. 1823-1829.

[19] IZGHECHE, Yousra et BAHI, Tahar. Adaptive Backstepping and PID Control Strategy with Genetic Algorithm for PMSG by a Grid-Connected Wind Turbine. Algerian Journal of Renewable Energy and Sustainable Development, 2023, vol. 5, no 2, p. 127-135.

Low-Cost Phased Array Antenna with Electronic Scanning for Low Earth Orbit Satellite Communication

Ibrahim Fortas*
Mouloud Ayad
Abderrahmen Kirad
Mohammed Wadi
Said Grouni

Department of Electrical Systems Engineering University of Boumerdes Boumerdes, Algeria i.fortas@univ-boumerdes.dz
Department of Electronics University of Setif 1 Setif, Algeria m.ayad@univ-setif.dz
Department of Automation University of Boumerdes Boumerdes, Algeria a.kirat@univ-boumerdes.dz
Faculty of Electrical and Electronics Engineering University of Istanbul Sabahattin Zaim Istanbul, Turkey mohammed.wadi@izu.edu.tr
Faculty of Sciences and Technology University of Tamanghasset Tamanghasset, Algeria grouni.said2020@gmail.com

ABSTRACT

The design, modeling, and performance assessment of a compact linear phased array antenna for Ku-band downlink low Earth orbit (LEO) satellite communication are presented in this study. The proposed array consists of 16 miniature rectangular microstrip patch elements printed on an FR-4 substrate, each optimized through parametric tuning in CST Studio Suite to achieve a broad impedance bandwidth. The elements are uniformly spaced by 13 mm (0.5 λ at 11.5 GHz) to prevent grating lobes while enabling wide beam steering. A progressive phase shift of -22.5 ° per element is applied via phase shifters, allowing electronic beam scanning from -25 ° to +25 ° without mechanical movement. simulated results show an operational bandwidth of 10 –12.9 GHz, with the array achieving an average gain of 10 dBi. The cost-effective and the compact form make the proposed design a strong candidate for integration into LEO satellite user terminals such as Starlink or OneWeb.

Keywords—phased array antenna, patch, linear, beam steering, electronic scanning, phase shifter

I. INTRODUCTION

Satellite communication has become an important component of global connectivity, enabling high-speed data transmission, remote sensing, and broadband services across the world (1). The performance of satellite communication systems has been greatly improved by the introduction of Low Earth Orbit (LEO) and Medium Earth Orbit (MEO) satellites, which provide important advantages over conventional Geostationary Orbit (GSO) systems (2). These benefits include reduced latency, higher throughput, and more flexible coverage, making NGSO (Non-Geostationary Orbit) constellations an attractive option for next-generation communication networks, including 6G and beyond.

However, the dynamic nature of NGSO satellites, which move rapidly across the sky relative to ground stations, presents a unique challenge for the design of receiving antennas (3). Unlike GSO satellites, which are stationary relative to a fixed point on Earth, LEO and MEO satellites require antennas capable of dynamically adjusting their beam direction to maintain continuous communication (2). This need for agile beam steering has driven the development of antenna technologies that can track moving satellites efficiently (4).

Among the various types of antennas used for NGSO communication, phased array antennas have emerged as the preferred choice due to their ability to electronically steer the beam (4). Unlike mechanical steering systems, which rely on physical movement of antenna components, electronic beam steering enables faster, more precise adjustments without the need for moving parts (5). This not only improves the speed of beam alignment but also enhances

reliability and reduces mechanical wear, making it ideal for satellite communication systems, especially those operating in LEO orbits (5).

There are several techniques available to achieve electronic scanning or beam steering in phased array systems. These include analog phase shifters (6), digital beamforming (7), hybrid approaches (8), and beamforming networks (9). Analog phase shifters offer low complexity, relatively low cost, and fast response times, but they often suffer from limited precision and phase errors that can degrade beam quality (6). Digital beamforming provides high flexibility, adaptive capabilities, and improved beam accuracy, as the signal can be processed on a per-element basis, but it requires high-speed analog-to-digital converters, significant processing power, and increased system cost. Hybrid approaches combine the advantages of both analog and digital methods, enabling a balance between hardware complexity, power consumption, and beamforming accuracy; however, they still involve trade-offs in terms of implementation complexity and calibration requirements. Beamforming networks offer a passive and reliable means of generating multiple beams simultaneously, but they are less adaptable in real time and their performance is limited by insertion loss and design constraints.

In this study, we describe the design and optimization of a low-cost phased array antenna for Ku-band satellite communication. The antenna is composed of an 1x16 array of patch elements, providing a compact and efficient solution for electronic beam steering using analog phase shifter. The design allows for a beam steering range from -25° to +25°, with a total antenna size of 22 x 217 mm^2. The proposed linear phased array antenna operates over a frequency range of 10 to 12.9 GHz, covering the downlink Ku-band for LEO satellite communication, and achieves an average gain of 10 dBi. This design represents a promising candidate for LEO satellite communication systems such as Starlink and OneWeb constellations, offering a high degree of performance, flexibility, and miniaturization, critical for modern satellite constellations.

II. ANTENNA ELEMENT DESIGN

The antenna design is initiated in CST Studio Suite with a conventional rectangular patch configuration. The radiating element is printed on a FR-4 substrate with a loss tangent, tan δ, of 0.025 and a relative permittivity, εr, of 4.3. The substrate dimensions are denoted as Ws × Ls, while a full ground plane with dimensions Wg × Lg is implemented on the opposite side. A microstrip feed line is employed to achieve a 50 Ω impedance match. To adjust the resonance frequency and enhance the antenna's performance, three slots are etched into the radiator, as illustrated in Fig 1.

In the design optimization process, various parameters are adjusted to achieve the desired frequency response [8-17]. The final optimized values for these parameters are summarized in Table I.

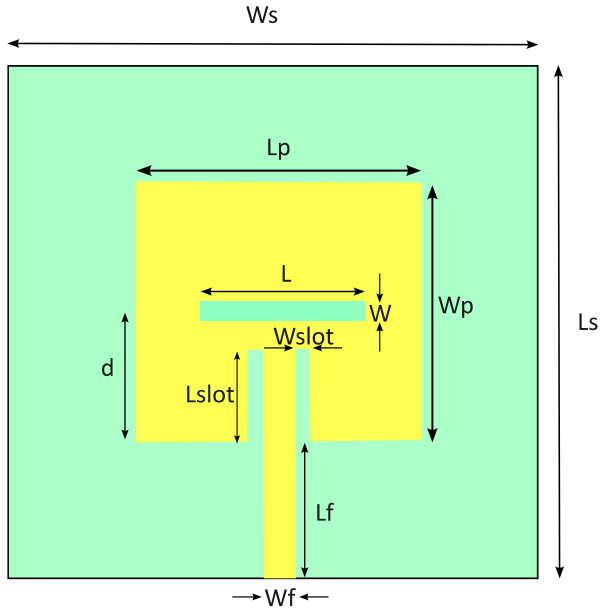

Fig 1. Patch antenna element design.

Table 1. Final parameters of the patch antenna element

	Parameter								
	Ws, Wg Ls,Lg	***Wp***	***Lp***	***Wf***	***Lf, d***	***Wslot***	***Lslot***	***W***	***L***
Value (mm)	22	11	12	1.5	5	4	0.5	1	7

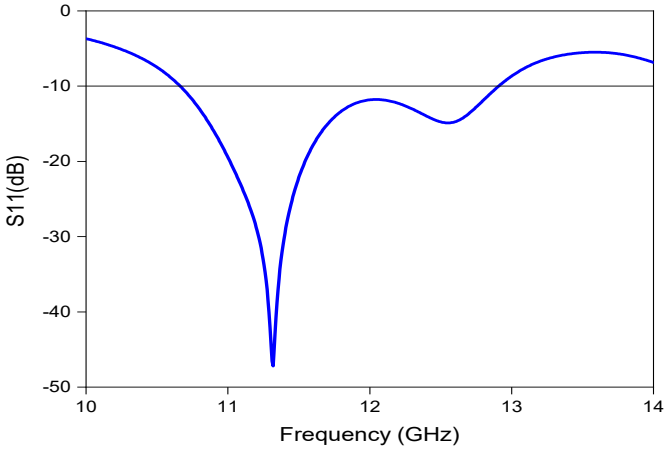

Fig 2. Reflection coefficient of the patch antenna element design.

Fig 2 presents the reflection coefficient of the design, where we observe a bandwidth of 2.3 GHz ranging from 10.6 GHz to 12.9 GHz, effectively covering the downlink Ku-band for LEO satellite communication. Additionally, the return loss at the frequency of 11.32 GHz is -47.20 dB, demonstrating excellent impedance matching.

III. Antenna Linear Phased Array Design

A. Phased Array Structure

A phased array antenna is an arrangement of multiple radiating elements, such as microstrip patch antenna, where the relative phase of the signal feeding each component is precisely controlled to shape and steer the overall radiation pattern as shown in Fig 3.

In order to prevent grating lobes in the majority of phased array designs, the distance d between adjacent element centers must satisfy:

$$d \leq \frac{\lambda}{2} \qquad (1)$$

For a linear array with element spacing d and a progressive phase shift between adjacent elements that is oriented along the x-axis, the direction of the main beam is:

$$\theta = sin^{-1}\frac{\phi\lambda}{2\pi d} \qquad (2)$$

For a desired beam steering angle θ, the required phase shift is:

$$\phi = \frac{2\pi d}{\lambda} sin(\theta) \qquad (3)$$

Where:

λ : wavelength

θ = beam pointing angle measured from broadside

ϕ = phase progression between elements

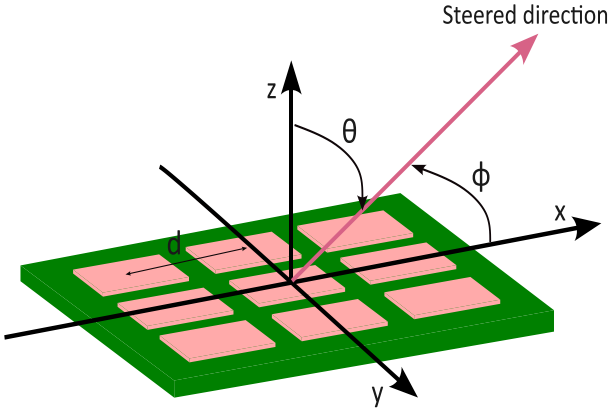

Fig 3. Phased array diagram.

By introducing a progressive phase shift between adjacent elements, constructive interference occurs in a desired direction, while destructive interference suppresses radiation in other directions, enabling electronic beam steering without physically moving the antenna [10].

The array factor formulation can be used to estimate the direction of the main beam, which depends on the array geometry, element spacing, operating wavelength, and applied phase gradient. Compared to mechanically steered antennas, phased arrays offer higher reliability, faster response times, and the capability for adaptive beamforming to counter interference or track multiple targets simultaneously [11].

The phase progression between two adjacent elements is:

$$\phi = kd\sin(\theta) \qquad (4)$$

Where

k: wave number (rad/m)

Negative phase is often applied to make the lobe point towards $+\theta$:

$$\Delta\phi = -\theta = -\frac{2\pi d}{\lambda}\sin(\theta) \qquad (5)$$

For element n, the phase ϕ_n is applied as follows:

$$\phi_n = n\Delta\phi \qquad (6)$$

B. Phased Array Design

A linear phased array antenna was developed, consisting of 16 equally spaced radiating elements arranged in a single row. The center-to-center spacing between adjacent elements, denoted by S, is an important design parameter, as it directly influences both the onset of grating lobes and the maximum achievable beam steering range. In this design, S was selected with respect to the operating wavelength λ of = 26 mm corresponding to the center frequency of 11.5 GHz. The final configuration employs a spacing of S = 13 mm, with an overall array width W_A = 22 mm and length L_A = 217 mm, as shown in Fig 4.

To achieve the desired beam steering, each element is fed through a phase shifter providing a progressive phase increment ϕ of -22.5° between adjacent elements.

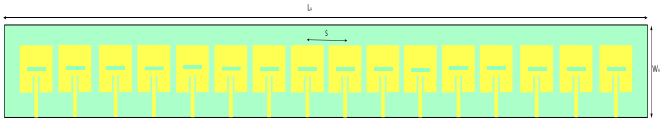

Fig 4. Geometry of the proposed design.

C. Result and Discussion

The proposed design exhibits consistent operational frequency over 10 GHz to 12.9 GHz. A comparison with the S11 response of a single radiating element reveals an improvement in bandwidth, particularly for frequencies below 10.6 GHz, as indicated in Fig 5.

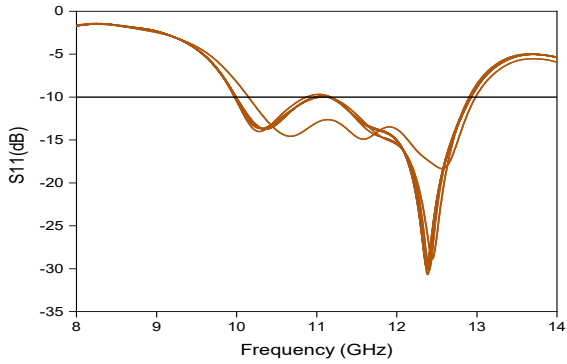

Fig 5. Reflection coefficient of the proposed design.

This enhancement is attributed to the array configuration effects, which contribute to improved impedance matching and a broader operational frequency range.

The array factor (AF) is a fundamental parameter in phased array antenna design (12). Fig 6 presents the array factor for the proposed 16-element linear phased array, evaluated for the principal plane at phi = 0°. The results indicate a maximum gain of approximately 10 dB in the boresight direction, demonstrating the array's ability to achieve significant directive gain through coherent beam-steering.

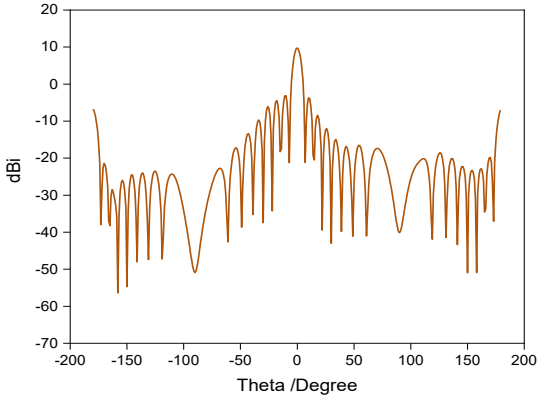

Fig 6. Array factor at the boresight of the proposed l design.

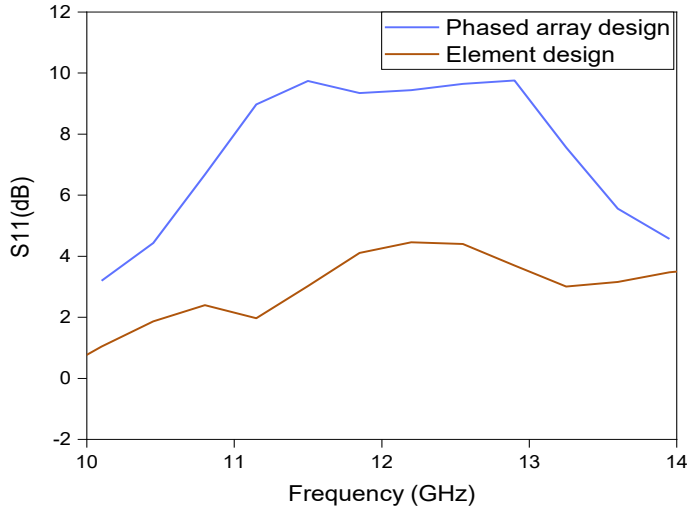

Fig 7. Comparison between gain for patch element and proposed linear phased array design.

Fig 7 presents a comparative analysis of the gain performance between a single patch element and the proposed 16-element linear phased array design. The results demonstrate that, across the operating frequency range, the phased array achieves an average gain of approximately 10 dBi, representing a substantial improvement over the single-element configuration. This enhancement is primarily attributed to the coherent combination of radiated fields from multiple elements, which increases directivity and overall radiation efficiency.

The radiation pattern of the proposed linear phased array antenna was evaluated at the center frequency of 11.5 GHz to

assess its beam steering capability. As illustrated in Fig 8, the array achieves electronic beam scanning over an angular range from -25° to +25° in the principal plane, while maintaining a well-defined main lobe and low side-lobe levels. This performance is enabled by the precise application of progressive phase shifts across the elements, ensuring constructive interference in the desired steering direction and minimal radiation in undesired directions. The scanning range obtained is consistent with theoretical predictions based on the chosen element spacing and operating wavelength.

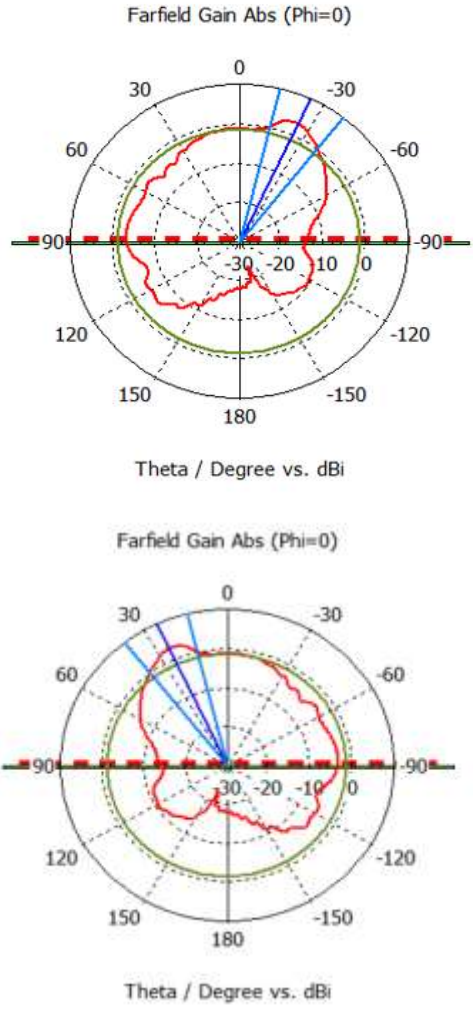

Fig 8. Radiation pattern of the proposed design at 11.5 GHz.

IV. CONCLUSION

This work offered a novel technique to the development and construction of a low-cost linear phased array antenna composed of 16 small patch elements for LEO satellite communication antennas. By raising the gain from 4 dB for a single element to 10 dB for the entire array, the suggested design shows a notable improvement in performance. Additionally, it operates efficiently within the Ku-band downlink frequencies designated for LEO satellite communication, allowing electronic beam scanning over a range of -25° to +25°. This antenna is an excellent fit for incorporation into satellite communication

platforms like Starlink and OneWeb user terminals due to its small size, high gain, and scanning capacity.

REFERENCES

[1] Kodheli, O., Lagunas, E., Maturo, N., Sharma, S. K., Shankar, B., Montoya, J. F. M., ... & Goussetis, G. (2020). Satellite communications in the new space era: A survey and future challenges. IEEE Communications Surveys & Tutorials, 23(1), 70-109.

[2] Al-Hraishawi, H., Chougrani, H., Kisseleff, S., Lagunas, E., & Chatzinotas, S. (2022). A survey on nongeostationary satellite systems: The communication perspective. IEEE Communications Surveys & Tutorials, 25(1), 101-132.

[3] Fan, Z., Dai, Y., & Minn, H. (2021). Performance analysis of large-scale NGSO satellite-based radio astronomy systems. IEEE Access, 9, 93954-93966.

[4] He, G., Gao, X., Sun, L., & Zhang, R. (2021). A review of multibeam phased array antennas as LEO satellite constellation ground station. IEEE Access, 9, 147142-147154.

[5] Ahmed, F., Singh, K., & Esselle, K. P. (2023). State-of-the-art passive beam-steering antenna technologies: Challenges and capabilities. Ieee Access, 11, 69101-69116.

[6] Kebe, M., Yagoub, M. C. E., & Amaya, R. E. (2025). A survey of phase shifters for microwave phased array systems. International Journal of Circuit Theory and Applications, 53(6), 3719-3739.

[7] Sikri, D., & Jayasuriya, R. M. (2019). Multi-beam phased array with full digital beamforming for SATCOM and 5G. Microwave Journal, 62(4), 64-79.

[8] Alhalabi, M., Taşpınar, N., Wadi, M., & Salemdeeb, M. (2026). Performance Analysis of a Low-Cost Directly Modulated OFDM-Based Optical Wireless Communication Systems. Wireless Personal Communications, 1-27.

[9] Alhalabi, M., Taşpınar, N., & Wadi, M. (2025). PAPR reduction using discrete forest optimization algorithm based on SLM technique in intensity modulated direct detection optical OFDM communication systems. International Journal of Communication Systems, 38(10), e70126.

[10] Alhalabi, M., & Wadi, M. (2025). Performance Study Of Wavelength Division Multiplexing Passive Optical Networks (Wdm-Pons) Employing Colorless Optical Sources. Innovations and Applications of Artificial Intelligence in Electrical and Electronics Engineering, 233.

[11] A. Ouaridhine, A. Aissat, Mohammed Wadi, S. Grouni, M.A. Benammar, The Impact of Emitter Thickness on the Performance of Silicon PIN Single-Junction Solar Cells. 4th International Conference on Contemporary Academic Research, 459-462, 2025.

[12] A. Ouaridhine, A. Aissat, Mohammed Wadi, S. Grouni, M.A. Benammar, The Effect of Varying Absorber Width in a PIN Polysilicon Solar Cell Structure on The Absorption Coefficient. 4th International Conference on Contemporary Academic Research, 463-466, 2025.

[13] M. Wadi, M. Salemdeeb, M. Jouda, R Bendib, Enhanced Performance in Inductive Wireless Energy Transfer Systems: A Study of Helical and Tubular Coils Configurations. International Journal of Advanced Natural Sciences and Engineering Researches, 9(6), 100-108, 2025.

[14] M. Wadi, M. Jouda, M. Salemdeeb, R. Bendib, Comparative Analysis of Square and Spiral Coils for Efficient Inductive Wireless Power Transfer. International Journal of Advanced Natural Sciences and Engineering Researches, 9(6), 91-99, 2025.

[15] Ali, A., Drlik, M., Wadi, M., & Elmasry, W. Enhancing Privacy in Smart Grids and IOTs Systems by Using Federated Learning: Case Study. In 2025 International Conference on Smart Applications, Communications and Networking (SmartNets) (pp. 1-6), 2025.

[16] Ali, A., Wadi, M., & Elmasry, W. Cybersecurity in Smart Grids and Other Application Fields: A Review Paper. Energies, 19(1), 246, 2026.

[17] Wadi, M., Tamyigit, F. A., Husain, N., & Kucuk, I. AI Applications in Electrical and Electronics Engineering. Innovations of Artificial Intelligence in Electrical and Electronics Engineering, 2025.

[18] Karami, F., Rezaei, P., Amn-e-Elahi, A., Sharifi, M., & Meiguni, J. S. (2019). Efficient transition hybrid two-layer feed network: Polarization diversity in a satellite transceiver array antenna. IEEE Antennas and Propagation Magazine, 63(1), 51-60.

[19] Vallappil, A. K., Rahim, M. K. A., Khawaja, B. A., Murad, N. A., & Mustapha, M. G. (2020). Butler matrix based beamforming networks for phased array antenna systems: A comprehensive review and future directions for 5G applications. IEEE Access, 9, 3970-3987.

[20] Balanis, C. A., Antenna Theory: Analysis and Design, 4th Ed., Wiley, 2016.

[21] Mailloux, R. J., Phased Array Antenna Handbook, 3rd Ed., Artech House, 2018.

[22] Hansen, R. C. (2009). Phased array antennas. John Wiley & Sons.

SCADA-Based Maintenance Prioritization in Wind Turbines: An Explainable and Multi-Criteria Approach

Şükriye KARAMAN[1*]

Cemal AKTÜRK[2]

[1]Computer Engineering / Graduate Education Institute, Gaziantep Islamic Science and Technology University, Türkiye
[2]Computer Engineering / Graduate Education Institute, Gaziantep Islamic Science and Technology University, Türkiye [*](sukriyekrmn.26 @gmail.com)

ABSTRACT

Predictive maintenance applications are critical for increasing operational reliability and minimizing production losses in wind power plants. However, current approaches generally focus on anomaly detection accuracy and neglect explainable decision-making mechanisms where the obtained technical outputs are translated into maintenance prioritization. This study proposes a hybrid Decision Support System (DSS) integrating unsupervised anomaly detection based on SCADA data, explainable artificial intelligence (XAI), and multi-criteria decision-making (MCDM) methods. In the proposed architecture, anomaly scores obtained with Isolation Forest (IF), AutoEncoder (AE), and LSTM-AutoEncoder (LSTM-AE) models are combined with XGBoost and SHAP analysis to reveal root cause relationships at the sensor level. Technical risk indicators are integrated with operational criteria (alarm rate, false alarm cost, power generation performance) and maintenance priority rankings are created through TOPSIS, VIKOR, MOORA, and SAW methods. The results show that the proposed multi-layered approach makes maintenance decisions more transparent and operationally feasible.

Keywords – Predictive Maintenance, Wind Turbines, Anomaly Detection, Multi-Criteria Decision Making, Explainable Artificial Intelligence.

I. INTRODUCTION

The share of renewable energy sources in global electricity production has gained momentum in recent years in line with the sustainable development goals. In this transformation process, wind energy stands out as one of the strategic resources with its technological maturity and increasing installed capacity. International energy projections show that the installed capacity of wind power plants will increase in the coming years [1]. However, since wind turbines have to operate continuously under variable atmospheric conditions and challenging site conditions, unexpected failures occur in critical components such as gearboxes, generators, and power converters. Statistical data reveals that operating and maintenance costs constitute a significant portion of the total Levelized Cost of Energy (LCOE) of a wind power plant. According to research, approximately 17% to 34% of the total costs incurred over the turbine's lifespan are due to maintenance activities [2]. This high cost pressure has made it necessary for the industry to abandon the traditional "post-failure repair" approach and switch to "predictive maintenance" strategies based on SCADA data. In fact, a study by Yılmaz Ulu [3] reported that just one day of unplanned shutdown in a 1 MW turbine operating with a 35% capacity factor resulted in a revenue loss of approximately 613.2 USD. This data concretely demonstrates that neglect

or delays in maintenance processes have a critical impact on energy supply security and cost management.

The complex structure of wind turbines makes one-dimensional assessments insufficient in maintenance processes. The health status of the turbine is shaped by the interaction of numerous closely related variables such as ambient temperature, wind speed, power generation, and component vibrations [4] Failures, especially in thermally sensitive components such as gearboxes and lubrication systems, can invalidate maintenance schedules planned with static periods. Since decision-making approaches based on a single metric or simple threshold values are insufficient to model this complex interaction, there is a risk of misdirecting limited maintenance resources. In this context, Multi-Criteria Decision Making (MCDM) methods, which can evaluate multiple performance indicators and risks simultaneously, offer an effective decision support mechanism in maintenance planning.

Today, Deep Learning (DL) and Ensemble Learning (EL) architectures are widely used in the analysis of high-dimensional SCADA data. In the literature, LSTM, Convolutional Neural Networks (CNN), and AutoEncoder (AE) based models have been reported to have high success rates in anomaly detection [5], [6]. However, when current academic studies and industrial applications are examined, two main constraints limiting the effectiveness of predictive maintenance systems stand out. The first is that deep learning models, which offer high accuracy, often operate as opaque "black box" structures. Fault alarms generated by complex neural networks are not considered reliable by field engineers when they are not supported by cause-and-effect relationships. The second constraint is that multi-criteria decision-making (MCDM) methods used in maintenance planning generally rely on static weighting approaches based on expert opinion. However, fault dynamics change depending on time and operational conditions; voltage parameters take priority in electrical faults, and vibration indicators in mechanical faults. Fixed weighting matrices cannot adequately represent these variable failure modes and dynamic maintenance priorities.

This study presents an approach that integrates SCADA-based unattended anomaly indicators with explainability and multi-criteria decision-making mechanisms to transform them into maintenance prioritization. In this context, anomaly signals obtained from Isolation Forest (IF), AE, and LSTM-AE models were interpreted at the sensor level using XGBoost–SHAP analysis; then, technical risk indicators were evaluated along with operational criteria using TOPSIS, VIKOR, MOORA, and SAW methods. To reduce ranking differences that may arise from different multi-criteria decision-making methods, the obtained rankings were combined to create a

more consistent maintenance priority list. The main objective of this study is to increase the applicability of wind turbine maintenance decisions in field operations. To achieve this objective, anomaly detection outputs were first justified with an explainability layer; then, they were integrated into a multi-criteria decision structure to transform them into an optimized maintenance plan. The study's contribution to the literature and its originality can be summarized under three headings: (i) integration of anomaly indicators obtained from multiple unsupervised models into the decision support process without the need for labels, (ii) making the sensor-based physical counterparts of risk indicators visible through SHAP-based explanations, and (iii) reducing reliance on a single method and methodological bias by combining rankings obtained from multiple MCDM methods.

The study is structured as follows: The second section summarizes academic studies on wind turbine fault detection and decision support systems. The third section explains the theoretical basis of the algorithms used. The fourth section details the data processing and modeling steps of the proposed system. The fifth section presents the performance analyses of the models, root cause findings, and decision support system outputs. The final section discusses the findings and offers suggestions for future research.

II. Related Work

The need to reduce operating and maintenance costs in wind power plants has led researchers to shift from post-failure maintenance approaches to predictive maintenance strategies. High-frequency data obtained from SCADA systems have become the most common source for monitoring turbine health. Studies in this field primarily focus on three axes: DL for anomaly detection, explainable artificial intelligence (XAI) for model explainability, and multi-criteria decision-making (MCDM) for maintenance prioritization. Table 1 presents a summary of the literature related to the scope of this study.

Table 1. Literature Review on Predictive Maintenance for Wind Turbines

Referance	Year	Dataset	Method
[7]	2021	SCADA	Statistical Methods + ANN
[8]	2024	SCADA	Statistical Methods
[9]	2020	SCADA	AutoEncoder (AE)
[10]	2024	SCADA	Transfer Learning AE
[11]	2024	Vibration	LSTM-AutoEncoder
[12]	2025	Time Series	Attention-Based DL + XAI
[13]	2022	SCADA	FMECA + MCDM

The time-series nature of SCADA data has increased the use of DL architectures in anomaly detection. The limited availability of labeled fault data, particularly in industrial datasets, has made Normal Behavior Modeling (NBM) the standard approach. Roscher and Schelenz [7], in their study on SCADA data from a large-scale turbine fleet, demonstrated that bearing failures could be detected approximately six months before the maintenance date. The study compared statistical threshold-based methods, RF, and artificial neural network-based models; it reported that data-driven approaches considering time dependence provided higher accuracy and a lower false alarm rate. Lutz et al. [9] demonstrated the effectiveness of learning the healthy condition of the turbine and detecting deviations using an AE-based model developed with SCADA data and maintenance records. Roelofs et al. [10] improved performance in data-constrained fields by combining Transfer Learning with AE. Lee et al. [11] demonstrated the advantage of LSTM's time-windowed structure in capturing early signs of failure in mechanical components using an LSTM-based AE architecture on vibration data. However, a common limitation of these studies is that the models only produce a technical failure score and the generated score is not converted into a decision for maintenance planning.

Despite the high success rate of DL models, their non-transparent structure is another factor limiting industrial reliability. Ghahfarokhi et al. [12] made their models explainable by using the attention mechanism in time series data. In their study, they increased the interpretability for engineers by visualizing which time period and which sensor data the model focuses on. However, in the current literature, XAI approaches are generally used as a

validation tool in the model development phase and are not designed as an active input of a dynamic decision support system.

Converting the findings obtained from anomaly detection into an implementable maintenance schedule brings with it a multi-criteria optimization problem. Wang et al. [13] proposed an integrated approach with Failure Mode and Effects Analysis (FMECA) for risk assessment in wind turbine systems and weighted the risk factors. However, in this and similar multi-criteria optimization studies, criterion weights are generally based on static expert opinions. The failure to integrate dynamic risk scores derived from instantaneous SCADA data into the decision-making process and the use of a single method for evaluation can lead to methodological biases.

Most studies in the literature focus on the accuracy of anomaly detection; however, they address the conversion of the obtained technical outputs into operational maintenance decisions to a limited extent. Furthermore, research on making "black box" models explainable and directly integrating dynamic sensor data into multi-criteria optimization processes is limited. This study aims to fill this literature gap by addressing anomaly detection, root cause analysis, and maintenance prioritization processes in a hybrid architecture.

III. Materials and Method

A. Theoretical Background

This section summarizes the theoretical framework of the unsupervised anomaly detection algorithms, supervised learning model (XGBoost), model explainability (SHAP), and multi-criteria decision-making (MCDM) methods used in maintenance prioritization, which form the basis of the proposed hybrid architecture.

Isolation Forest (IF)

In the first stage of the anomaly detection process, the IF algorithm was used to isolate outliers in the data quickly and efficiently. IF is a tree-based approach based on the fact that anomalies are "few in number and different" compared to normal data. In this method, anomalies are isolated at levels closer to the root node of the decision trees. The anomaly score of a data point is calculated using Equation (1) based on the path lengths.

$$s(x,n) = 2^{-\frac{E(h(x))}{c(n)}} \quad (1$$

In equation (1), $h(x)$ represents the path length, $E(h(x))$ represents the mean path length, and $c(n)$ represents the normalization factor. A score approaching 1 is a strong indicator of an anomaly.

AutoEncoder (AE)

In addition to the surface outliers detected by IF, the AE architecture, a symmetric artificial neural network, was used to learn the complex nonlinear structures in the data. AE works by compressing the input data into a low-dimensional hidden space and reconstructing it back to its original dimension [14]. When the model is trained with normal data, it reconstructs normal samples with low error, while it produces high error in anomalies. The objective function, Mean Square Error (MSE), is given in Equation (2).

$$\mathcal{L}_{MSE} = \frac{1}{N}\sum_{i=1}^{N} \| x_i - \hat{x}_i \|^2$$

In equation (2), x_i represents the input vector and $\hat{x}_i$ represents the reconstructed output vector.

Long Short-Term Memory (LSTM)

To capture the temporal dependencies and historical patterns of wind turbine SCADA data, the AE structure is enhanced with LSTM cells. LSTM is an RNN architecture that uses gate mechanisms to learn long-term dependencies in time series [15]. In the LSTM cell, the forget gate f_t, the input gate i_t and the output gate o_t update the cell state c_t and the hidden state h_t. These updates are given in Equation (3).

$$\begin{aligned}
f_t &= \sigma(W_f x_t + U_f h_{t-1} + b_f) \\
i_t &= \sigma(W_i x_t + U_i h_{t-1} + b_i) \\
o_t &= \sigma(W_o x_t + U_o h_{t-1} + b_o) \\
\tilde{c}_t &= \tanh(W_c x_t + U_c h_{t-1} + b_c) \\
c_t &= f_t \odot c_{t-1} + i_t \odot \tilde{c}_t \\
h_t &= o_t \odot \tanh(c_t)
\end{aligned}$$

XGBoost (Extreme Gradient Boosting)

XGBoost is a high-performance and scalable additive modeling algorithm based on the gradient boosting principle. Unlike traditional decision trees, XGBoost has a structural regularization term that limits overlearning in complex datasets [16]. The algorithm updates the estimate with Equation (4) by adding a new weak learner f_t in each iteration to minimize the errors of the previous model.

$$\hat{y}_i(t) = \hat{y}_i(t-1) + \eta \cdot f_t(x_i) \quad (4)$$

In equation (4), $\hat{y}_i(t)$ represents the estimation of the i-th example in the t-th iteration; η represents the learning rate; and $f_t(x_i)$(represents the added decision tree.

Explainable Artificial Intelligence: SHAP

The SHAP layer was used to ensure the transparency of the risk scores produced by the model and to provide root cause analysis. SHAP calculates the extent to which each feature affects the complex model outputs with Shapley values based on game theory [17]. The marginal contribution of a feature to the prediction, ϕ_i, is expressed in Equation (5).

$$\phi_i = \sum_{S \subseteq F \setminus \{i\}} \frac{|S|!(|F|-|S|-1)!}{|F|!} [f(S \cup \{i\}) - f(S)]$$

In Equation (5), $\phi_i$represents the Shapley value of the attributes, S represents a subset of the attributes included in the model, x represents the input values, and f represents the prediction model. This formulation fairly distributes the total variation in the model output among the attributes by calculating the weighted average of the marginal contributions of each attribute over all possible subset combinations.

TOPSIS

TOPSIS (Technique for Order Preference by Similarity to Ideal Solution) ranks the alternatives according to their proximity to the Positive Ideal Solution (A^+) and their distance from the Negative Ideal Solution (A^-) [18]. The relative proximity coefficient (C_i) of the i-th alternative is given in Equation (6).

$$C_i = \frac{D_i^-}{D_i^+ + D_i^-}$$

In equation (6) $D_i^+$and D_i^-, represent the Euclidean distances to the positive and negative ideal solutions, respectively.

VIKOR

VIKOR is a method that seeks a compromise solution when conflicting criteria exist. [19]. Group Benefit for each alternative (S_i) and Individual Remorse (R_i) values are calculated, the final ranking index Q_i It is obtained from Equation (7).

$$Q_i = v\frac{S_i - S^*}{S^- - S^*} + (1-v)\frac{R_i - R^*}{R^- - R^*}$$

Equation (7) $v$represents the weight of the decision strategy.

MOORA

MOORA (Multi-Objective Optimization on the basis of Ratio Analysis) is based on the difference between the normalized values of benefit and cost criteria. [20]. i the net score of the alternative is given in Equation (8).

$$y_i = \sum_{j=1}^{g} y_{ij} - \sum_{j=g+1}^{n} y_{ij}$$

Equation (8) y_{ij} The normalized criterion values represent the first total benefit criteria, while the second total represents the cost criteria.

SAW (Simple Additive Weighting)

SAW is the most commonly used AHP method. It is based on the principle of multiplying normalized criterion values by weights and summing them. [21]. i the total score of the alternative is shown in Equation (9).

$$S_i = \sum_{j=1}^{n} w_j \, r_{ij}$$

B. Proposed Framework

In this study, a hierarchical methodology integrating unsupervised anomaly detection, XAI, and MCDM methods is proposed to support decision-making processes in wind turbine maintenance management and reduce uncertainty in field operations. The proposed framework begins with the examination of SCADA data, its normalisation, and the creation of suitable training sets for Normal Behaviour Modelling (NBM). Following data preparation, a hybrid anomaly detection process is operated using IF, AE, and LSTM-AE models that do not require labelled data. The anomaly scores obtained from the models are analysed using a statistical thresholding method based on the error distribution in the training data and converted into operational performance indicators such as alarm rate, detection success, and timeliness.

To enable the interpretation of technical findings from an engineering perspective, the process was supported by the XGBoost algorithm and SHAP analysis, thereby ensuring transparency regarding the root causes of risk at the sensor level. In the final stage of the methodology, the technical risk indicators obtained were combined with operational criteria such as power loss potential and false alarm cost. Dynamic maintenance priority lists were created by applying the TOPSIS, VIKOR, MOORA and SAW methods through this hybrid data structure. To increase methodological consistency and reduce dependence on a single algorithm, the rankings obtained from

different MCDM methods were integrated to provide the final decision support output. The proposed methodology is presented in Figure 1.

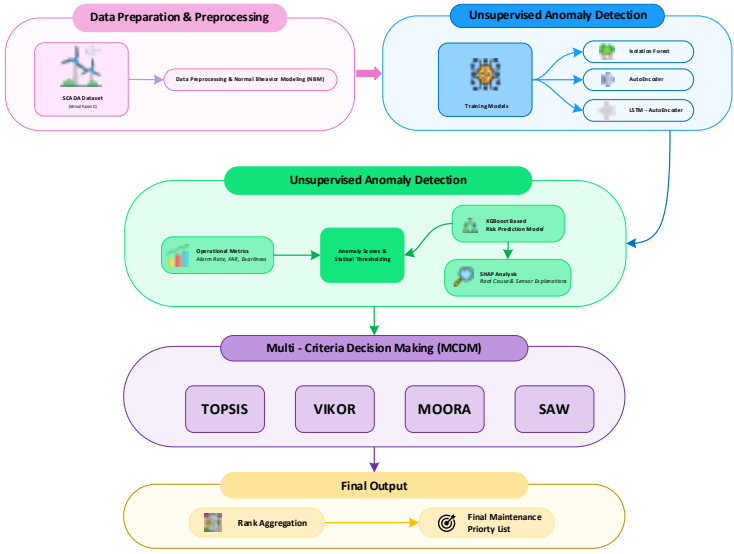

Figure 1. Explainable Anomaly Detection Based on SCADA Data and Multi-Criteria Decision Support Framework

Dataset

Within the scope of this study, Gück et al. developed and compared wind turbine fault detection algorithms. [8] The "CARE to Compare" dataset, which was introduced to the literature and is based on real-world field data, has been utilized. This dataset, made available to researchers through open access on the Zenodo digital library and the Kaggle data science platform, contains high-resolution SCADA records from three different wind farms - Wind Farm A, B, and C - each with distinct geographical and operational conditions. [22], [23].

The "Wind Farm C" dataset, representing the most complex scenario due to sensor diversity, was used in the study. This dataset, recorded at a 10-minute frequency, includes critical parameters such as active power, wind speed, generator temperatures, and hydraulic pressure. The structural characteristics and statistical distribution of the dataset are summarized in Table 2.

Table 2. Wind Farm C dataset characteristics

Feature	Value	Explanation
Number of Turbines	22	Number of turbines at different locations
Total Dataset	58	Total processed time series file
Number of Anomalies	27	Number of incidents resulting in failure
Normal Behavior Set	31	Reference sets free from any faults
Number of Attributes	957	Sensor measurements and statistical derivatives
Recording Resolution	10 Minutes	SCADA sampling frequency
Labeling Method	Situation-Based	Status ID (0: Normal, 1-5: Restricted/Faulty)

During the data pre-processing stage, the Normal Behaviour Modelling strategy recommended in the literature was followed to enhance the reliability of the study. Accordingly, when creating the training data set, time windows corresponding to normal operation (defined by the code "0") and idle state (represented by the code "2") in the data set were used as references. Data containing unhealthy conditions such as faults, maintenance, or limited operation were excluded from the training process to ensure that the models learned normal turbine behaviour.

Anomaly Detection Architecture

The proposed system applies three different unsupervised learning architectures to detect potential faults in wind turbine components at an early stage. The basic working principle of these models is to learn only healthy data patterns during the training phase and to flag examples deviating from these patterns as anomalies during the testing phase.

As the first model, the IF algorithm was used due to its success in isolating outliers in high-dimensional data. The model was constructed with 300 decision trees, and the contamination rate was determined automatically.

As a second model, an AE architecture was designed to model non-linear sensor relationships. This network was designed with a symmetric architecture featuring a 128-64-16-64-128 neuron structure. The model utilised the MSE generated while compressing and reconstructing the input data into a low-dimensional hidden space as an anomaly score. The Adam optimisation algorithm was used during the training process, and an early stopping mechanism was implemented to prevent overfitting.

As the third and most advanced model, LSTM-AE was developed to capture temporal dependencies in SCADA data. For this model, the dataset was converted into 36-step sliding windows instead of individual time points. This approach ensured that the model was not affected by instantaneous noise and focused on long-term trend deviations in sensor data.

In unsupervised learning models, it is necessary to determine a data-specific decision threshold to distinguish between normal and abnormal conditions. In this study, instead of assigning a fixed threshold value, a statistical threshold determination strategy based on the error distribution of normal data in the training set was followed. The Reconstruction Errors (RE) produced by the model during the training phase were analysed, and threshold values corresponding to the 95%, 97% and 99% confidence intervals of the error distribution were calculated.

Evaluation Criteria

The performance of the unsupervised anomaly detection models used in this study was evaluated using sample-based and event-based performance metrics. In the sample-based evaluation, the metrics of accuracy, precision, recall, and F1-score were used; in the event-based evaluation, the metrics of detection rate and earliness were reported. Anomaly detection outputs were reduced to a binary classification problem using fault events in the dataset as a reference; metrics were calculated based on True Positive (TP), True Negative (TN), False Positive (FP), and False Negative (FN) values. The mathematical expressions of the metrics used are presented in Table 3.

Table 3. Equations of model evaluation criteria

Metric	**Mathematics Equation**
Accuracy	$\frac{TP + TN}{TP + TN + FP + FN}$
Precision	$\frac{TP}{TP + FP}$
F1-score	$\frac{2TP}{2TP + FP + FN}$
Recall	$\frac{TP}{TP + FN}$

In addition, the False Alarm Rate (FAR) has been calculated to reflect the cost of false alarms, which is critical for maintenance teams in field

conditions. FAR represents the rate at which normal samples are flagged as anomalies and is defined by Equation (10).

$$FAR = \frac{FP}{FP + TN}$$

As the study focused on early fault detection, the evaluation was not limited to sample-based metrics; event-based detection rate and earliness metrics were also reported. The Detection Rate was calculated by checking whether the model generated an alarm at least once within each anomaly-labelled event window; it was expressed as the overall detection rate across all anomaly events. The Earliness criterion is defined as the difference between the first alarm time step generated by the model for each anomaly event and the start time step of the event. It is given in Equation (11).

$$Earliness = event\_start\_id - detection\_id \quad (11)$$

The definition presented in Equation (11) indicates that a positive earliness value means the alarm was generated before the event began, while a negative value means the alarm was generated after the event began. Median Earliness is reported as the median of the earliness values calculated for all anomaly events.

Decision Support Mechanism

Converting identified anomalies into a maintenance plan requires the management of multi-criteria and conflicting objectives. In this study, a decision matrix was created by combining technical outputs obtained from artificial intelligence models with data. The three fundamental criteria defined for maintenance prioritisation are as follows:

- Risk Score: Defined as the ratio of anomaly alarms generated within the relevant time window. The numerical magnitude of this value represents the degree of deviation from the turbine's normal operating characteristics. As high anomaly scores indicate an increased likelihood of failure and maintenance urgency, this parameter has been evaluated as beneficial in the decision matrix and defined as a criterion to be maximised.

- Potential Power Loss: This refers to the average active power generated by the turbine during the relevant time interval. The failure and shutdown of a turbine with high energy production will result in greater economic losses compared to a turbine with low production. Therefore, to prevent potential revenue loss, turbines with high production capacity are prioritised for maintenance, and

this criterion has been included in the model with a maximisation approach.

- Anomaly Severity: The false alarm rate generated by the system during the test period represents the stability and reliability of the anomaly detection model. High false alarm rates can create unnecessary operational burdens on maintenance teams and may also lead to genuine faults being overlooked. Therefore, this criterion has been defined as a cost metric that should be minimised in order to encourage stable system operation in the decision support process.

The TOPSIS, VIKOR, MOORA and SAW methods were applied simultaneously on the decision matrix created. In order to reduce ranking differences that may arise from the different mathematical approaches of the methods, the obtained rankings were combined based on the arithmetic mean principle. Thanks to this approach, a more consistent maintenance priority list was presented without being tied to a single method.

Application Environment and Decision Support Interface

The studies for the proposed methodology were conducted in the Google Colab Pro cloud-based development environment. The software infrastructure was built using the Python language, utilising Pandas, NumPy, TensorFlow/Keras, and Scikit-learn.

A Streamlit-based DSS has been developed to enable users to easily monitor model outputs and integrate them into operational decision-making processes. After completing the training and testing phases in the cloud environment, the system was made accessible via a web-based interface using the PyNgrok protocol. The general appearance of the developed interface, including model performance metrics and the multi-criteria decision-making module, is shown in Figure 2.

Figure 2. The Decision Support System (DSS) user interface developed

The developed interface presents technical model outputs and evaluations within an integrated structure. In this context, the precision, sensitivity, and F1-score metrics for the IF, AE, and LSTM-AE models can be monitored comparatively. Furthermore, anomaly detection sensitivity can be analysed under different threshold scenarios using statistical threshold values of 95%, 97% and 99% derived from the error distribution of the training data. To better interpret model decisions, SHAP summary graphs are used to visualise the sensor variables that contribute to fault formation. In the final stage, the results obtained from the TOPSIS, VIKOR, MOORA, and SAW methods are combined to create a maintenance priority list and action recommendations are presented to decision-makers. Thanks to this approach, the complex outputs obtained from DL-based models are transformed into a more transparent and traceable decision support structure for the end user.

IV. Results And Discussion

This section presents the experimental results of the proposed approach on the Wind Farm C dataset, focusing on anomaly detection performance, SHAP-based root cause analyses, and maintenance prioritisation outputs optimised using the MCDM method.

A. Performance Analysis of Anomaly Detection Models

In this section, the performance of the AE, LSTM-AE, and IF models has been analysed using the metrics defined in Section 3.2.3. The data obtained from the decision support interface is presented in Table 4.

Table 4. Performance Metrics of IF, AE and LSTM-AE Models

Model	Events	Anomaly Events	Precision	Recall	F1-score	False Alarm Rate	Detected Rate
AE	30	27	0.800	0.640	0.711	0.422	1.000
LSTM-AE	30	27	0.791	0.636	0.705	0.456	1.000
IF	30	27	0.792	0.576	0.667	0.399	1.000

According to the data in Table 4, the three models detected 30 events in the dataset and achieved success in terms of event-based detection rate. This finding demonstrates that the proposed unsupervised architectures can reliably capture fault events in the Wind Farm C dataset.

The AE model achieved results of 0.800, 0.640 and 0.711 in precision, recall and F1-score values, respectively. This performance indicates a balanced detection capability between false alarms and missed anomalies. However, the model's false alarm rate of 0.422 is considered a risk factor that could create an additional burden for maintenance teams in the operational field.

The LSTM-AE model achieved results of 0.791, 0.636, and 0.705 in precision, recall, and F1-score values, respectively, demonstrating performance very close to that of the AE model. The model's early detection success was measured at 107 time steps, which corresponds to an early warning period of approximately 18 hours. A lower early detection value indicates that faults are detected closer to the maintenance date but still allow sufficient time for intervention. This finding is considered a practical outcome of the LSTM architecture's ability to learn temporal dependencies.

Compared to other models, IF adopts a more cautious approach, maintaining a false alarm rate of 0.399 and thereby establishing a more meaningful alarm strategy. However, precision, recall and F1-score values were measured at 0.792, 0.576 and 0.667 respectively, indicating that while the model is competitive in terms of accuracy, it lags behind in sensitivity. This characteristic provides an advantage in areas where false alarm costs are high, but it also carries the risk of missing some early failure signals.

When evaluated in terms of early detection performance, the AE and IF models offered a longer warning period of approximately 24 hours with 144 time steps, while the LSTM-AE model exhibited shorter but temporally more consistent detection behaviour. This finding highlights the necessity of

the multi-layer architecture proposed in this study. Using models with different accuracy profiles together, rather than a single model, enables maintenance decisions to be made more reliably.

When the overall results are examined, the AE and LSTM-AE models demonstrate more balanced performance in terms of anomaly detection capability compared to IF, while LSTM-AE stands out particularly due to its early advantage. These findings indicate that performance profiles differ between models.

B. Root Cause Analysis and Model Explainability

The decision tree structure of the XGBoost model used in anomaly and fault probability prediction was analysed using the SHAP method. This analysis quantitatively reveals the contributions of sensor variables to model predictions, enabling the evaluation of factors underlying correct and incorrect classifications. Thus, model outputs can be interpreted beyond statistical performance metrics, through engineering-meaningful physical indicators.

The SHAP summary graph showing the most effective sensor statistics according to the average contribution size to the model output is presented in Figure 3.

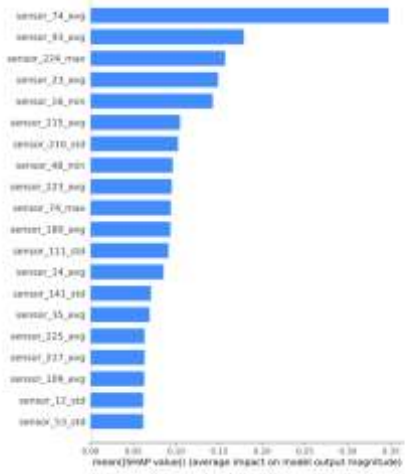

Figure 3. SHAP-Based Root Cause Analysis

The analysis results presented in Figure 3 demonstrate that the model bases its decisions on physically meaningful sensors related to the hydraulic system, vibration behaviour, electrical supply, and cooling–pressure subsystems, rather than on random patterns. In particular, the hydraulic oil

level (sensor_74_avg), nacelle vibration (sensor_93_avg), electrical voltage values (sensor_224_max, sensor_215_avg), and cooling–hydraulic pressure indicators (sensor_23_avg, sensor_48_min) have made the highest positive contribution to the model output.

The analysis results presented in Figure 3 demonstrate that the model bases its decisions on physically meaningful sensors related to the hydraulic system, vibration behaviour, electrical supply, and cooling–pressure subsystems, rather than on random patterns. In particular, the hydraulic oil level (sensor_74_avg), nacelle vibration (sensor_93_avg), electrical voltage values (sensor_224_max, sensor_215_avg), and cooling–hydraulic pressure indicators (sensor_23_avg, sensor_48_min) have made the highest positive contribution to the model output.

SHAP values explain the statistical relationships learned by the model, but they do not directly guarantee causal relationships between sensors. Different fault types with similar SHAP contribution profiles can be represented by the model with similar risk scores, which can lead to difficulties in distinguishing between classes in multiple fault scenarios. These limitations also explain why the study integrates SHAP-based explanations into the MCDM mechanism rather than relying solely on model output for maintenance decisions.

The findings indicate that the decisions made by the XGBoost-based prediction model are based on engineering-relevant sensor variables and that these decisions can be made transparent through SHAP analysis. SHAP was actively used in this study as a decision support component to interpret model performance, analyse the reasons for incorrect predictions, and justify maintenance decisions. In this respect, the proposed approach goes beyond black-box artificial intelligence models and offers an explainable and applicable predictive maintenance solution that field engineers can trust.

C. Decision Support Outputs and Priority Ranking

In the final stage of the study, the risk outputs obtained from the anomaly detection models were converted into operational maintenance priority lists using a multi-criteria decision-making tool comprising the TOPSIS, VIKOR, MOORA and SAW methods.

The developed DSS has been designed to operate via a user-interactive interface. In the interface presented in Figure 4, the decision-maker can dynamically determine the anomaly model to be used, the scope of analysis, and the weights associated with the decision criteria. In this study, the alarm_rate criterion was assigned the highest weight of 0.50 to represent risk intensity; power_mean was given the second priority of 0.30 as it reflects

operational and economic impact. False_alarm_rate was minimised to 0.20 as a cost criterion balancing system stability and reliability.

Figure 4. DSS Parameter and Criteria Weighting Interface

In the decision matrix created, alarm_rate represents the extent to which the system continuously generates strong risk signals, while power_mean reflects the impact of potential failure on energy production and, consequently, the risk of economic loss. False_alarm_rate has been used as a critical control variable, balancing the model's tendency to produce false positives and preventing maintenance resources from being directed towards unnecessary interventions. Considering these three criteria together ensures that maintenance decisions are shaped not only by technical risk but also by reliability and operational impact dimensions.

Table 5, created based on data exported from the developed decision support interface, presents the scores calculated for the top 5 most critical events at Wind Farm C site and the final priority ranking.

Table 5. MCDM Scores and Maintenance Priority Ranking for the Five Most Critical Failure Events

Event ID	Label	Alarm Rate	Power Mean	False Alarm Rate	TOPSIS Score	VIKOR Score	Final Rank
70	Anomaly	0.9900	0.1889	1.0000	0.7025	0.0000	**1**
47	Anomaly	0.9822	0.1870	0.9988	0.6979	0.0118	**2**
44	Anomaly	0.9173	0.1152	0.4742	0.6881	0.3083	**3**
11	Anomaly	1.0000	0.1245	1.0000	0.6710	0.3551	**4**
34	Anomaly	0.8875	0.1432	0.4431	0.6695	0.3820	**5**

When examining the ranking results obtained from the interface, it is seen that DSS provides maintenance prioritisation by combining the trends obtained from different MCDM methods. Event 70 was identified as the most risky event in both the TOPSIS and VIKOR methods due to its combination of high alarm rate and high average power generation, and was placed first in the final ranking. Event 47, despite having similar power generation values, was placed second due to its alarm rate remaining at 98.2%.

The primary reason Event 70 ranks highest is that the model continuously produced anomaly signals during this event, coinciding with a period when the turbine was generating high energy. An examination of the SCADA time series for Event 70 reveals that, despite the operational variables remaining stable, the inconsistencies observed in the output variables and temperature sensors confirm why the hybrid model classified this case as a top-priority maintenance requirement.

Event 67 is at the very end of the generated ranking. The main reason for this case being at the bottom of the list is that the model followed a fairly stable course throughout this process and there were few anomaly signals. The criterion values and DSS scores for Event 67 are presented comparatively in Table 6 below.

Table 6. Low-Risk Situation Example: Decision Criteria and DSS Analysis for Event 67

Event ID	Label	Alarm Rate	Power Mean	False Alarm Rate	TOPSIS Score	VIKOR Score
67	Normal	0.0540	0.2105	0.0820	0.1245	0.9850

When examining the values in the table, it can be seen that Event 67 has a low alarm rate of 5.4% and that the risk of false alarms has been minimised. Although power generation is high, the TOPSIS method has assigned a low proximity coefficient of 0.1245 to this case due to the low technical risk signals; VIKOR, on the other hand, has rated this event as the least risky with a score of 0.9850. This situation proves that DSS not only identifies high-risk anomalies but also enhances system reliability by accurately distinguishing "normal" conditions that do not require maintenance resources.

The findings reveal that the developed DSS is not limited to detecting anomalies; it offers a decision-making structure that jointly evaluates operational and cost-focused risk indicators to support maintenance

decisions. Furthermore, the ability to dynamically adjust criterion weights via the user interface enables decision-makers to flexibly analyse maintenance priorities under different operational scenarios (e.g., winter periods when failure costs increase or periods when energy demand is low).

Consequently, the proposed decision support system presents a directly usable solution for predictive maintenance applications by combining anomaly outputs with MCDM methods and an interactive user interface. In this respect, the system goes beyond many theoretical approaches in the academic literature, offering an applicable DSS example that supports decision-makers in real-world conditions.

V. CONCLUSION

This study has demonstrated that predictive maintenance decisions for wind turbines should be considered not only on the basis of technical accuracy, but also in terms of interpretability and operational feasibility. Given the high-dimensional and temporal nature of SCADA data, it has been observed that anomaly detection outputs alone are insufficient; it is critical that these outputs be transformed into a reasoned, multi-criteria decision structure.

The findings indicate that although different unsupervised learning models can deliver similar detection performance, they exhibit distinct behavioural profiles in terms of early detection, false alarm tendency, and risk sensitivity. This highlights that maintenance decisions based on a single model in field conditions involve uncertainty; conversely, the joint evaluation of multiple model outputs provides a more reliable basis for decision-making.

The SHAP-based explainability layer used in the study has enabled the risk scores generated by artificial intelligence models to be interpreted from an engineering perspective. Demonstrating that model decisions are based on physically meaningful sensor variables builds trust among maintenance teams and highlights that the proposed system goes beyond "black box" models. In this respect, SHAP is positioned not only as an explanatory tool but also as an active decision support component that provides justification for maintenance decisions.

One of the most significant contributions of this study is the integration of anomaly detection and explainability outputs with multi-criteria decision-making methods to directly convert them into maintenance prioritisation. Maintenance priority lists created by combining rankings obtained from the TOPSIS, VIKOR, MOORA, and SAW methods provide a balanced decision structure that includes not only technical risk levels but also operational

dimensions such as potential production loss and system reliability. This approach also reduces methodological biases that may arise when relying solely on individual MCDM methods.

However, there are some limitations to this study. The analyses were performed on a single wind farm dataset, and generalisability to different geographical conditions and turbine types needs to be tested separately. Furthermore, maintenance decisions were constrained by technical and production-based criteria; operational-level factors such as maintenance costs, spare parts logistics, and human resources were excluded from the scope of this study.

Overall, this study fills an important gap in the predictive maintenance literature by combining anomaly detection, explainable artificial intelligence, and multi-criteria decision-making approaches under a single umbrella.

VI. FUTURE WORKS

In future studies, evaluating the generalisability of the proposed decision support system by testing it on different wind farms and multi-turbine fleets emerges as an important research direction. Furthermore, integrating economic and logistical criteria such as maintenance cost, spare part procurement time, and personnel suitability into the decision matrix will further enhance the system's industrial applicability. Furthermore, incorporating online learning architectures that operate with real-time SCADA data streams into the system will enable the proposed approach to be transformed into an autonomous maintenance decision assistant capable of adapting to changing field conditions.

REFERENCES

[1] W. Udo and Y. Muhammad, “Data-Driven Predictive Maintenance of Wind Turbine Based on SCADA Data,” *IEEE Access*, vol. 9, pp. 162370–162388, 2021, doi: 10.1109/ACCESS.2021.3132684.

[2] M. Blumenfeld, A. Cooperman, G. Zuckerman, M. Prilliman, J. Keller, and S. Sheng, “Wind Turbine Maintenance Costs: Assessing the Potential of Gear Oil Improvements,” 2050.

[3] E. Yılmaz Ulu, “Importance And Cost of Maintenance Practices In Wind Turbines,” *Mühendis ve Makina*, no. 718, pp. 173–188, Apr. 2025, doi: 10.46399/muhendismakina.1537198.

[4] Q. Yu, P. Bangalore, S. Fogelström, and S. Sagitov, “Optimal Preventive Maintenance Scheduling for Wind Turbines under Condition Monitoring,” *Energies (Basel).*, vol. 17, no. 2, Jan. 2024, doi: 10.3390/en17020280.

[5] W. F. Nogueira, A. H. de A. Melani, and G. F. M. de Souza, “Wind Turbine Fault Detection Through Autoencoder-Based Neural Network and FMSA,” *Sensors*, vol. 25, no. 14, Jul. 2025, doi: 10.3390/s25144499.

[6] L. Qi, Q. Zhang, Y. Xie, J. Zhang, and J. Ke, “Research on Wind Turbine Fault Detection Based on CNN-LSTM,” *Energies (Basel).*, vol. 17, no. 17, Sep. 2024, doi: 10.3390/en17174497.

[7] B. Roscher and R. Schelenz, “Usability of SCADA as predictive maintenance for wind turbines,” *Forschung im Ingenieurwesen/Engineering Research*, vol. 85, no. 2, pp. 173–180, Jun. 2021, doi: 10.1007/s10010-021-00454-1.

[8] C. Gück, C. M. A. Roelofs, and S. Faulstich, “CARE to Compare: A Real-World Benchmark Dataset for Early Fault Detection in Wind Turbine Data,” *Data (Basel).*, vol. 9, no. 12, Dec. 2024, doi: 10.3390/data9120138.

[9] M. A. Lutz *et al.*, “Evaluation of anomaly detection of an autoencoder based on maintenace information and SCADA-data,” *Energies (Basel).*, vol. 13, no. 5, Mar. 2020, doi: 10.3390/en13051063.

[10] C. M. A. Roelofs, C. Gück, and S. Faulstich, “Transfer learning applications for autoencoder-based anomaly detection in wind turbines,” *Energy and AI*, vol. 17, Sep. 2024, doi: 10.1016/j.egyai.2024.100373.

[11] Y. Lee, C. Park, N. Kim, J. Ahn, and J. Jeong, “LSTM-Autoencoder Based Anomaly Detection Using Vibration Data of Wind Turbines,” *Sensors*, vol. 24, no. 9, May 2024, doi: 10.3390/s24092833.

[12] A. F. Ghahfarokhi, J. Schäfer, M. F. Wagner, and B. Dorronsoro, “Explainable Artificial Intelligence for Time Series Using Attention Mechanism: Application to Wind Turbine Fault Detection,” *IEEE Access*, vol. 13, pp. 180613–180631, 2025, doi: 10.1109/ACCESS.2025.3621003.

[13] Z. Wang, R. Wang, W. Deng, and Y. Zhao, “An Integrated Approach-Based FMECA for Risk Assessment: Application to Offshore Wind Turbine Pitch System,” *Energies (Basel).*, vol. 15, no. 5, Mar. 2022, doi: 10.3390/en15051858.

[14] “Autoencoder Neural Networks and its Applications,” 2022, doi: 10.35248/2090-4908.22.11.254.

[15] S. Hochreiter and J. Schmidhuber, “Long Short-Term Memory,” *Neural Comput.*, vol. 9, no. 8, pp. 1735–1780, Nov. 1997, doi: 10.1162/NECO.1997.9.8.1735.

[16] M. Tang, Z. Liang, H. Wu, and Z. Wang, “Fault diagnosis method for wind turbine gearboxes based on iwoa-rf,” *Energies (Basel).*, vol. 14, no. 19, Oct. 2021, doi: 10.3390/en14196283.

[17] S. M. Lundberg, P. G. Allen, and S.-I. Lee, “A Unified Approach to Interpreting Model Predictions”, Accessed: Jan. 12, 2026. [Online]. Available: https://github.com/slundberg/shap

[18] M. N. Yahya, H. Gökçekuş, D. U. Ozsahin, and B. Uzun, “Evaluation of wastewater treatment technologies using TOPSIS,” *Desalination Water Treat.*, vol. 177, pp. 416–422, Feb. 2020, doi: 10.5004/DWT.2020.25172.

[19] I. Milojkovic and N. Prascevic, “Project management using the developed AHP–VIKOR method with the fuzzy approach,” *Water Science and Technology*, vol. 90, no. 2, pp. 578–597, Jul. 2024, doi: 10.2166/WST.2024.204.

[20] “(PDF) Multi-criteria decision making: An operations research approach.” Accessed: Jan. 12, 2026. [Online]. Available: https://www.researchgate.net/publication/284107964_Multi-criteria_decision_making_An_operations_research_approach

[21] H. Taherdoost, “Analysis of Simple Additive Weighting Method (SAW) as a MultiAttribute Decision-Making Technique: A Step-by-Step Guide,” *Journal of Management Science & Engineering Research*, vol. 6, no. 1, pp. 21–24, Feb. 2023, doi: 10.30564/JMSER.V6I1.5400.

[22] “Wind Turbine SCADA Data For Early Fault Detection.” Accessed: Jan. 10, 2026. [Online]. Available: https://zenodo.org/records/15846963

[23] “Wind Turbine SCADA Data For Early Fault Detection.” Accessed: Jan. 10, 2026. [Online]. Available: https://www.kaggle.com/datasets/azizkasimov/wind-turbine-scada-data-for-early-fault-detection

A Scenario-Based Hybrid Decision Support System for Global Water Risk Prediction and Management

Kubilay ERMİCİK[1*]

Cemal AKTÜRK [2]

[1]Computer Engineering/Graduate School of Education, Gaziantep Islamic Science and Technology University, Turkey

[2] Computer Engineering/Graduate School of Education, Gaziantep Islamic Science and Technology University, Turkey *kubilayermicik65@gmail.com

ABSTRACT

Increasing population, industrialization, agricultural and industrial water demand, and climate change are putting pressure on water resources on a global scale. This study develops a Decision Support System (DSS) that analyzes the water risk profiles of countries using global water consumption data from 2000–2024. The system is evaluated using Multi-Criteria Decision Making (MCDM) methods, including TOPSIS, VIKOR, MOORA, and WSM, based on six criteria: per capita water consumption, agricultural, industrial, and domestic use, precipitation, and groundwater depletion rate. As a complement to the existing risk assessment, a linear regression model is used to analyze the water risk trends of countries for the next ten years. The internal consistency of risk labels obtained from multi-criteria decision-making (MCDM) and regression outputs with the raw data structure was evaluated using nine different Machine Learning (ML) and Deep Learning (DL) models: Random Forest (RF), Gradient Boosting (GB), SVM, Logistic Regression (LR), Decision Tree (DT), K-Nearest Neighbors (KNN), Naive Bayes (NB), Artificial Neural Networks (ANN), and 1D-CNN. The features influencing model decisions were examined using SHAP analysis, an explanatory artificial intelligence (XAI) method. The proposed study offers an integrated assessment framework that addresses country-based water risk assessments using scenario-based time series projections and ML and DL-based analyses.

Keywords – Global water risk, decision support system, multi-criteria decision making, linear regression, machine learning,

I. INTRODUCTİON

Water is a vital resource for the physiological and ecological continuity of human life, and it also forms the basis of ecosystems that are home to countless living organisms. However, the availability and quality of water are currently facing threats on a global scale. [1]Population growth, industrialization, the widespread use of chemicals in agriculture, and insufficient environmental awareness threaten water resources. If current trends continue, it is predicted that the problems that may arise in the next 25-30 years will become irreversible. [1]. This global crisis highlights the need for preventive policies regarding water resources. These factors have led to a nearly fourfold increase in global water consumption over the past 80 years, placing serious pressure on water resources. [2]This situation necessitates that water be treated as a strategic risk factor that must be managed. Water scarcity and deterioration in water quality threaten not only specific regions but many countries. Proper management of these risks requires an international comparative perspective that identifies global trends and priority regions. For these reasons, questions such as "Which countries are at higher risk in terms of water stress?" or "How do risk profiles vary across different geographies?" are important for global

water security. Decision-makers need an analytical framework that simultaneously considers many different criteria in order to develop sustainable policies and provide systematic answers to these questions.

The ‘Global Water Consumption Dataset (2000–2024)’ used in this study includes some of the key criteria that reveal this complexity [3]:

- Per Capita Water Use: Water efficiency and consumption habits in the country.
- Agricultural Water Use: The country's agricultural dependence on water.
- Industrial Water Use: Industry's dependence on water.
- Domestic Water Use: Basic living standards.
- Precipitation Impact: The capacity of water resources to regenerate naturally.
- Groundwater Depletion Rate: How sustainably resources are used.

The existence of numerous criteria and the complex relationships between them make the decision-making process impossible to manage with simple analyses. Decision-Making Systems (DMS) are computer-based systems developed to help decision-makers make more consistent decisions in the face of complex problems. Using multi-criteria decision-making methods, these systems analytically evaluate different alternatives according to defined criteria and assigned weights and rank the most suitable options. [4].

The aim of this study is to develop a Decision-Making System (DMS) that analyzes country-specific water risks using global water consumption data, allows for cross-country comparisons, and can simulate the potential impacts of different intervention scenarios. The importance of this study stems from its ability to provide decision-makers with dynamic, scenario-based, and explainable analyses in a multi-dimensional and complex problem area such as water resources management. The developed system analytically evaluates countries based on defined criteria using multi-criteria decision-making methods and models the relationships between these criteria using regression analysis in a separate analytical layer. Linear regression approach is preferred for future projections, as the literature clearly shows that linear regression models are widely used in water consumption time series and provide effective results in fundamental forecasting studies [5]. Furthermore, current studies show that regression-based methods are frequently used as initial approaches compared to more complex models [6]. In these respects, the study contributes to the literature and provides a foundation for predicting the current situation and future water risk levels in the global water risk crisis using multi-criteria decision-making (MCDM) and linear regression. The contributions of the study are as follows:

- MCDM approaches, which are generally considered independently in water risk analyses, have been brought together under an integrated decision support framework.
- To increase the reliability of the system's results, algorithms such as RF, SVM, GB, and 1D-CNN were used, and an ML and DL-based consistency module was integrated to analyze the extent to which the features in the dataset can explain water risk distributions.
- A linear regression module was integrated for the analysis of the water risk level for the next 10 years.

Thanks to this multi-layered structure, decision-makers can dynamically adjust the importance levels of different risk criteria according to their priorities; and mathematically evaluate how improvements in agricultural, industrial, and domestic water use affect the overall risk score. The system provides outputs that visualize cause-and-effect relationships between criteria using correlation heat maps and explain the extent to which the models rely on various variables in the risk estimation process. In this respect, the developed DSS goes beyond being merely a tool for generating predictions, becoming a unique DSS that makes decision-making processes interpretable and offers projections for the future.

The second part of the study presents a literature review, the third part describes the methods used, the fourth part outlines the architecture of the developed DSS, and the findings obtained, and the fifth and sixth parts present the results obtained from the system's implementation and future research.

II. LITERATURE REVIEW

Sustainable management of water resources has become a necessity today due to increasing population, climate change, and growth in sectoral water demand. Therefore, decision-makers increasingly need a Water Management System (WMS) that can evaluate multi-dimensional water data together. Recent studies show that multi-criteria analysis, spatial assessment, and hydrological modeling-based WMS approaches are becoming widespread in water management.

Mokallaf et al. [7] developed an interactive DSS that evaluates water allocation scenarios by combining spatial indicators with MCDM methods. Izady et al. [8] studied the co-management of surface and groundwater with a scenario-based decision support system integrating SWAT–MODFLOW models. While these approaches provide process-based analysis power at the basin scale, they focus to a limited extent on country comparisons and the combined evaluation of multiple MCDM methods at the global scale.

There are also studies in the literature that systematically compile DSS and water allocation models. Candido, Laíse Alves et al. [9] compiled DSS and optimization models used for water allocation and water management and comparatively examined existing approaches. Saad, Mohamed et al. [10] enabled the evaluation of groundwater regeneration zones by combining remote sensing and GIS data with a decision support structure. Ataei Parisa et al. [11] proposed an AI-based DSS model for groundwater management; and Poli Giuliano et al. [12] developed a spatial decision support system for multidimensional water management.

Studies in the current literature are limited to basin-scale, single-method MCDM applications or short-term analyses. In contrast, a comprehensive framework integrating multiple MCDM methods, long-term projections, and ML-based consistency analyses simultaneously on a global scale is lacking. This study addresses country-based water risk on a global scale, presenting a comparative risk ranking across countries using WSM, TOPSIS, VIKOR, and MOORA methods together. Furthermore, it goes beyond current situation analysis, predicting future risk trends (2025–2034) through linear regression-based projections and providing decision-makers with a proactive assessment framework through simulations based on agricultural, industrial, and domestic use scenarios. Finally, a hybrid DSS approach is presented, supporting the model's explainability and methodological robustness through ML-based internal consistency analysis that examines the learnability of risk labels obtained through MCDM in terms of raw data attributes.

III. METHOD

This section describes the data preprocessing steps, multi-criteria decision-making (MCDM) methods, and linear regression-based time series modeling used in country-based water risk assessments. It also explains ML and DL-based internal consistency analysis methods, classification performance metrics, and XAI approaches. The proposed web-based decision support system model is presented in Figure 1.

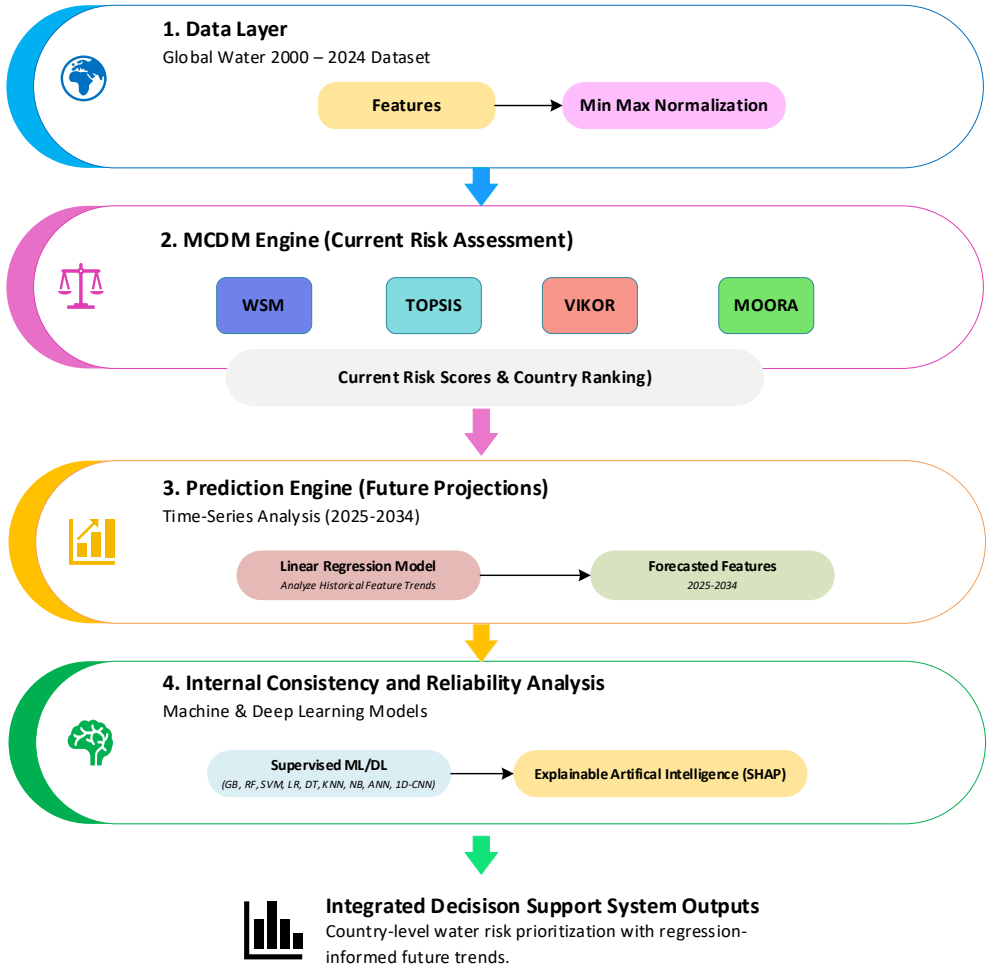

Figure 1: Schematic representation of a web-based integrated decision support system for water risk analysis.

When examining the model architecture presented in Figure 1, it is seen that in the data preprocessing stage, the criteria were scaled between 0 and 1 using the Min-Max normalization method to ensure comparability between countries. Within the scope of Multi-Criteria Decision Making (MCDM), TOPSIS, VIKOR, MOORA, and WSM methods are considered together using normalized data.

In examining temporal trends, independently of MCDM analyses, the water consumption and socio-economic indicators of countries from previous years are considered using a linear regression model, aiming to quantitatively

represent long-term trends. The relationship between the risk labels defined within the scope of MCDM and time series analyses and the raw data features is analyzed for internal consistency using ML and DL-based methods. This analysis focuses on examining the methodological relationship between the obtained labels and the data features.

A. *Data Preprocessing and Normalization*

Since the 6 criteria used in the study have different units of measurement, the Min–Max normalization method was applied [13]. With this method, the value of the relevant criterion for each country was scaled to the range of 0–1. In the context of water risk, per capita consumption, agricultural, industrial and domestic use and groundwater depletion rate were considered as cost-oriented criteria, while precipitation amount was considered as a benefit-oriented criterion. Equation (1) was used for the cost criteria and Equation (2) was used for the benefit criterion.

$$N_{ij} = \left(x_{ij} - x_{j,min}\right)/\left(x_{j,max} - x_{j,min}\right) \quad (1)$$

$$N_{ij} = \left(x_{j,max} - x_{ij}\right)/\left(x_{j,max} - x_{j,min}\right) \quad (2)$$

In equations (1) and (2) N_{ij}, The normalized values x(min) and x(max) represent the minimum and maximum values of the criterion in the dataset. This process ensures that the criteria are comparable in multi-criteria decision-making (MCDM) algorithms.

B. *Multi-Criteria Decision Making Modules*

In decision problems involving multidimensional and conflicting criteria, such as water risk, relying on a single MCDM method can lead to method-specific ranking logics and resulting in inconsistencies in the results. Therefore, MCDM methods are considered together in the risk assessment process. [14].

Weighted Sum Model (WSM)

The WSM method is a computationally simple approach that allows criterion weights to be directly incorporated into the model [15]. In this method, the total risk score of each alternative is obtained by summing the normalized criterion values multiplied by the weights determined by the decision-maker. The mathematical representation of the model is given in Equation (3).

$$S_i^{WSM} = \sum_{j=1}^{n} \left(N_{ij} \cdot w_j\right) \quad (3)$$

In Equation (3), S_i^{WSM} represents the weighted total score of the alternative; N_{ij}, represents the normalized value of the alternative for the j-th criterion, w_j

represents the criterion weight determined by the decision-maker, and n represents the total number of criteria.

TOPSIS

The TOPSIS method is based on the distance of the alternatives from the positive ideal solution and their proximity to the negative ideal solution [16]. In this context, the relative proximity coefficient is calculated for each alternative. The mathematical representation of the method is given in Equation (4).

$$C_i = \frac{S_i^-}{S_i^+ + S_i^-} \tag{4}$$

In equation (4), C_i represents the relative proximity coefficient of the alternative; S_i^+ represents the distance to the positive ideal solution and S_i^- represents the distance to the negative ideal solution.

VIKOR

The VIKOR method aims to produce a compromise solution between conflicting criteria [17]. Its mathematical representation is given in Equation (5).

$$Q_i = v\left(\frac{S_i - S^*}{S^- - S^*}\right) + (1 - v)\left(\frac{R_i - R^*}{R^- - R^*}\right) \tag{5}$$

In the mathematical notation given in Equation (5), Q_i represents the compromise ranking index calculated for the alternative; S_i represents the group utility, R_i represents individual regret, S^* ast and R^* ast represent the best values, and S^- and R^- represent the worst values. The parameter v represents the compromise weight between group utility and individual regret.

MOORA

The MOORA method combines benefit and cost-oriented criteria under a single performance indicator [18]. It is based on the principle of subtracting the weighted sum of benefit-oriented criteria from the weighted sum of cost-oriented criteria. The mathematical representation is given in Equation (6):

$$y_i = \sum_{j=1}^{g} x_{ij}^* - \sum_{j=g+1}^{n} x_{ij}^* \tag{6}$$

In equation (6), y_i represents the performance score of the alternative calculated by the MOORA method; x_{ij}^* ast represents the normalized criterion

values, g represents the number of utility-oriented criteria, and n represents the total number of criteria.

C. LİNEAR REGRESSİON

In order to quantitatively model the time-dependent change of the dependent variable, a linear regression-based approach is used to represent the linear relationship between the dependent variable and the time variable. This approach allows for the modeling of the long-term trend component and the quantitative expression of the dependent data [19]. The linear relationship between the dependent variable y and the time variable x is defined in Equation (7).

$$y_i = \beta_0 + \beta_1 x_i + \varepsilon_i \tag{7}$$

Equation (7) defines β_1 as the slope coefficient representing the increasing or decreasing trend over time, β_0 as the intercept term indicating the initial level, and ε_i as the random error term.

D. MACHİNE LEARNİNG-BASED INTERNAL CONSİSTENCY ANALYSİS

This section describes ML and DL-based classification approaches for modeling patterns between features and target variables in multidimensional datasets. In this approach, a feature set consisting of numerical indicators is used as input data, while the target variable is considered within the scope of the classification problem. For this purpose, different ML and DL algorithms are used to model the discriminatory structures in the feature space. These methods enable the representation of complex data structures thanks to their ability to learn linear and nonlinear relationships.

Machine Learning-Based Classifiers and Ensemble Models

ML-based classification algorithms aim to mathematically model the relationship between observations and class labels in a multidimensional feature space.

Random Forest (RF)

RF is an ensemble learning algorithm that uses multiple decision trees to make better predictions. It takes different random subsets of tree data and combines the results by averaging them for classification or regression. RF increases accuracy and reduces errors with this method [20].

The mathematical representation of the RF classifier is expressed as in Equation (10).

$$\hat{y} = \text{mode}\{h_1(x), h_2(x), \dots, h_K(x)\} \tag{10}$$

In the mathematical notation given in equation (10), $h_k(x)$ represents the class estimates produced by the decision trees for the input vector x, and K

represents the total number of trees. This structure reduces the overfitting tendency observed in individual decision trees.

Gradient Boosting (GB)

GB is an ensemble learning method used in predictive modeling where weak learners are sequentially grouped together. With this model, each new model used focuses on reducing the error terms of the preceding models. [21].

The mathematical representation is expressed as in Equation (11).

$$F_m(x) = F_{m-1}(x) + \alpha_m h_m(x) \tag{11}$$

Denklem (11)'de verilen matematiksel gösterimde $F_m(x)$, m. adımda elde edilen toplamsal modeli, $h_m(x)$ zayıf öğreniciyi, α_m ise öğrenme oranını temsil etmektedir. In the mathematical notation given in Equation (11), $F_m(x)$, represents the additive model obtained at the m-th step, $h_m(x)$ represents the weak learner, and α_m represents the learning rate.

Decision Tree

Decision trees are versatile machine learning algorithms used in classification and regression that perform well on complex data by hierarchically dividing the dataset based on features. The goal of a decision tree is to choose the split that maximizes purity at each step. A Gini index close to zero indicates that the node is purer. Common measures used to ensure this process are the Gini index and entropy [22]. The Gini index is defined by the mathematical representations in equation (12) and the information gain by equation (13).

$$Gini = 1 - \sum_{i=1}^{C} p_i^2 \tag{12}$$

$$Entropy = -\sum_{i=1}^{C} p_i \log_2(p_i) \tag{13}$$

In the Gini index given in Equation (12) $p_i$observations at the relevant node i the probability of belonging to its class C represents the total number of classes. The entropy given in Equation (13) measures the level of uncertainty in the class distribution at a node.

Support Vector Machine (SVM)

SVM is a classification method that finds examples of classes close to each other while classifying data and attempts to maximize the perpendicular distance of these examples from the separating surface. The goal is to define a separating function that maximizes the margin between classes. For data sets that cannot be linearly separated in a one-dimensional plane, they use kernel functions to transform the data sets into a higher-dimensional feature space for classification. [23].

The SVM model is expressed mathematically as shown in Equation (14).

$$\min_{w,b} \frac{1}{2} \| w \|^2 \quad (14)$$

In the equation given in (14), w the weight vector of the classification hyperplane, b represents the term bias. $\| w \|$ Minimizing the expression by indicating the Euclidean norm of the weight vector means increasing the margin width. By increasing the margin width, the decision boundary is determined in such a way that it has higher discrimination power between classes.

Logistic Regression

LR converts the data into a probability space and makes a linear class prediction using the sigmoid function. [24] The mathematical representation of the model is presented in equation (15).

$$P(y = 1 \mid x) = \frac{1}{1 + e^{-(w^T x + b)}} \quad (15)$$

Equation (15) w weight vector, b the term bias and x represents the input vector.

K-Nearest Neighbors (KNN)

The KNN method classifies based on the distance between samples. When classifying data, KNN uses the nearest neighbor in the feature set. k determines based on the neighbor's class labels [25].

The distance between data sets is usually calculated using the Euclidean algorithm. The distance between two observations is presented in Equation (16) below.

$$d(x_i, x_j) = \sqrt{\sum_{m=1}^{p} (x_{im} - x_{jm})^2} \quad (16)$$

In the mathematical representation presented in Equation (16); x_i ve x_j the two compared data points, p total number of attributes, x_{im} ve x_{jm} observations related to the matter m.represents attribute values.

Naive Bayes

NB is a probabilistic classifier that uses Bayes' theorem based on observed attributes to assign a class label to an example. In the NB approach, it is

assumed that the attributes are independent of each other's class labels. The probability that an observation belongs to a particular class is calculated by multiplying the conditional class probabilities of the attributes. [26] NB It is expressed as in Equation (17).

$$P(y \mid x_1, \ldots, x_n) \propto P(y) \prod_{i=1}^{n} P(x_i \mid y) \tag{17}$$

Equation (17) $P(y)$ class prior probability, $P(x_i \mid y)$ represents the class-conditional probability of the attribute. The ratio expression, with the denominator term being $P(x_1, \ldots, x_n)$indicates that it should be disregarded due to its fixed nature.

E. Deep Learnİng-Based Classİfİcatİon Approaches (ANN and 1D-CNN)

DL methods have the ability to learn both linear and nonlinear relationships between features thanks to their multi-layered structures. In this context, multi-layered approaches such as ANN and 1D-CNN are used in solving classification problems.

Artificial Neural Networks (ANN)

ANNs have a multi-layered perceptron structure and consist of input, hidden, and output layer neurons. Each neuron calculates the weighted sum of the inputs it receives and passes them to activation functions to produce outputs within a specific range of values. [27]The mathematical representation of ANN is presented in Equation (18).

$$y = f\left(\sum_{i=1}^{p} w_i \, x_i + b\right) \tag{18}$$

In the expression given in Equation (18) x_i input attributes, w_i weight coefficients of attributes, b the term bias and $f(\cdot)$ represents the activation function.

One-Dimensional Convolutional Neural Networks (1D-CNN)

CNNs are DL models that automatically learn patterns by applying filters (kernels) to input data. [28]In this architecture, the convolution operation is applied to feature vectors. The mathematical representation of the 1D-CNN is presented in Equation (19).

$$c_i = f\left(\sum_{k=1}^{m} w_k \cdot x_{i+k-1} + b\right) \tag{19}$$

In the expression given in Equation (19) x input vector, w_k convolution filter weights, b the term bias, m filter size and $f(\cdot)$ shows the activation function.

F. CLASSİFİCATİON PERFORMANCE CRİTERİA

In evaluating ML and DL-based classification models, analyses based on a single performance metric are limited in multi-class and imbalanced datasets. Therefore, performance metrics are considered to comprehensively examine classification performance. Accuracy, precision, and F1-score metrics are used to evaluate classification performance. [29].

The complexity matrix shown in Figure 2 contains four basic outputs: True Positive (TP), True Negative (TN), False Positive (FP), and False Negative (FN).

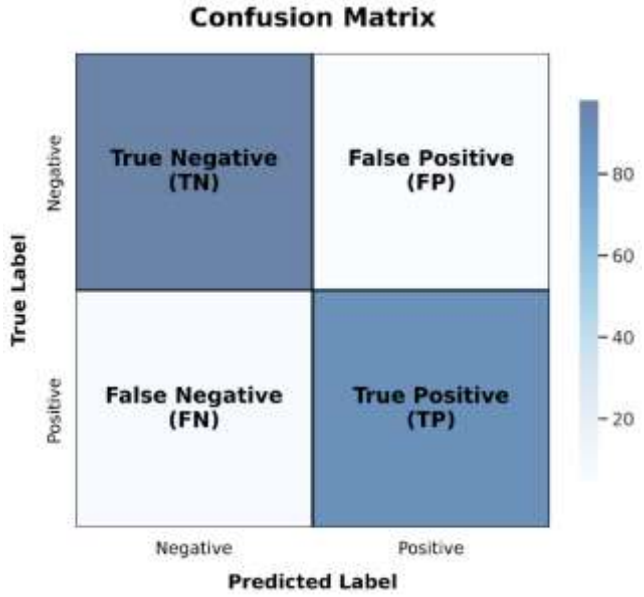

Figure 2: Confusion matrix used to evaluate classification models.

Performance metrics reported using these values are calculated using the equations (20, 21, 22, 23) provided below.

$$\text{Accuracy}=TP+TN/TP+TN+FP+FN \quad (20)$$
$$\text{Precision}=TP/TP+FP \quad (21)$$
$$\text{Recall} =TP/TP+FN \quad (22)$$
$$F1=2\cdot\text{Precision.Recall/Precision+Recall} \quad (23)$$

In the given equations (20, 21, 22, 23), the Recall (sensitivity) metric indicates the extent to which observations belonging to the positive class can be correctly identified.FN) is important in terms of evaluating the effect of classifications. Precision expresses the ratio of truly positive observations among those classified as positive and (FPreflects the impact of their classifications. (24)

G. Explainable Artificial Intelligence (XAI) Approach: SHAP

Although ML and DL-based models can provide high prediction performance in complex data structures, they may have limitations in terms of the interpretability of their decision mechanisms. Therefore, SHAP approaches are used to understand which features the model outputs are based on.

The SHAP method provides a contribution-based framework that enables the sum of feature contributions to explain the model output and allows for a comparative analysis of the decision structures of different classification models. [30].

The mathematical representation of the SHAP method is presented in Equation (24).

$$f(x) = \phi_0 + \sum_{i=1}^{M} \phi_i$$

In the mathematical representation presented in Equation (24) $f(x)$ model output, ϕ_0 the model's average output, ϕ_i ise $i$representing the contribution of the nth attribute to the model M The total indicates the number of attributes.

IV. Findings and Discussion

This section presents findings based on country-specific water risk distributions, temporal trends, and data-driven classification outputs obtained as a result of implementing the proposed DSS approach.

First, the overall distribution of country-based risk scores obtained using CBRM methods is analyzed using linear regression-based time series to examine the long-term behavior of water risk.

In the following subsections, complexity matrices obtained from ML and DL-based classification models are presented, with the dataset randomly split into 80% training and 20% test subsets, in order to observe whether the models exhibit similar behavior across different data subsets. Additionally, SHAP analysis is used to reveal which features most influence the model decisions. Finally, the DSS system is evaluated within a holistic framework by displaying the system interface through the outputs of the developed web-based DSS user interface.

Data Preprocessing and Normalization Findings

In the context of water risk, criteria such as per capita consumption, agricultural, industrial, and domestic use, and groundwater depletion rate represent higher risk levels, while precipitation amount shows an inverse effect. The sample decision matrix obtained as a result of the Min-Max Normalization process is presented in Figure 3.

N_PerCapita	N_Agricultural	N_Industrial	N_Household	N_Rainfall	N_Groundwater
0,422780176	0,522265054	0,249701464	0,800230516	0,679037218	0,64715893
0,641886266	0,520005317	0,450934888	0,43254168	0,683750725	0,602250165
0,78053233	0,570793158	0,520203729	0,471464624	0,514534699	0,474469277
0,734852066	0,536532412	0,567509899	0,52458564	0,391429336	0,465916612
0,405402512	0,255603881	0,771887374	0,499456178	0,936857767	0,199205824
0,523861378	0,822251761	0,528310603	0,43736303	0,385822232	0,471211118
0	0,692720103	0,544929609	0,738462038	0,662552015	0,606662254
0,277153515	0,338960521	0,113121425	0,323452541	0,563332312	0,727994705
0,405733975	0,835251894	0,369764628	0,513384523	0,629811154	0,564526803
0,406549535	0,691323772	0,520512539	0,367364166	0,759100522	0,349658063
0,35913774	0,542868536	0,35158381	0,56198763	0,565850245	0,453673064
0,703882735	0,411604413	0,524004619	0,443651483	0,392054956	0,547857379
0,468189196	0,814950596	0,615871096	0,475154624	0,602774844	0,418045444
0,526273884	0,523576587	0,617927849	0,601272707	0,631685218	0,613500993
0,692073165	0,584976443	0,374651708	0,589573762	0,338699543	0,378704316
0,60288749	0,547520936	0,314727233	0,723608383	0,409653287	0,435693801
0,718781705	0,543849655	0,499088681	0,420737604	0,438336948	0,444360405
0,524606316	0,733421018	0,541245051	0,520433281	0,473789563	0,452123027
0,581337814	0,689219726	0,263451386	0,567149884	0,59154991	0,318994044
0,53544627	0,710635533	0,699772694	0,635568687	0,492467502	0,300757409
0,607725034	1	0,514716234	0,787860587	0,587959953	0,262078094
0,50869949	0,631995215	0,533353497	0,412087466	0,249210595	0,45444518
0,63228246	0,521425523	0,502518119	0,702573181	0,748917714	0,567766206
0,524930945	0,317346803	0,42308623	0,759906495	0,453725985	0,274652548
0,863426342	0,592753651	0,688501665	0,479920317	0,136639194	0,326179446
0,630196201	0,684799947	0,639738231	0,393885651	0,536664661	0,352829252
0,464211635	0,478984448	0,331588209	0,6069869	0,534172772	0,462607545
0,427103682	0,792066773	0,391608007	0,617197773	0,587064918	0,300022061
0,559159382	0,533763126	0,63841839	0,494756579	0,442916661	0,66981028

Figure 3: Normalized decision matrix of water stress indicators for all evaluated countries.

The analysis of the risk levels of the six criteria presented in Figure 3 is visualized using color codes: low values are green, medium values are yellow, and high-risk values are red. Since the criteria used in the study must be appropriate not only in terms of scale but also in terms of statistical independence, the linear relationships between them were examined using Pearson correlation analysis, and the results are presented in Figure 4.

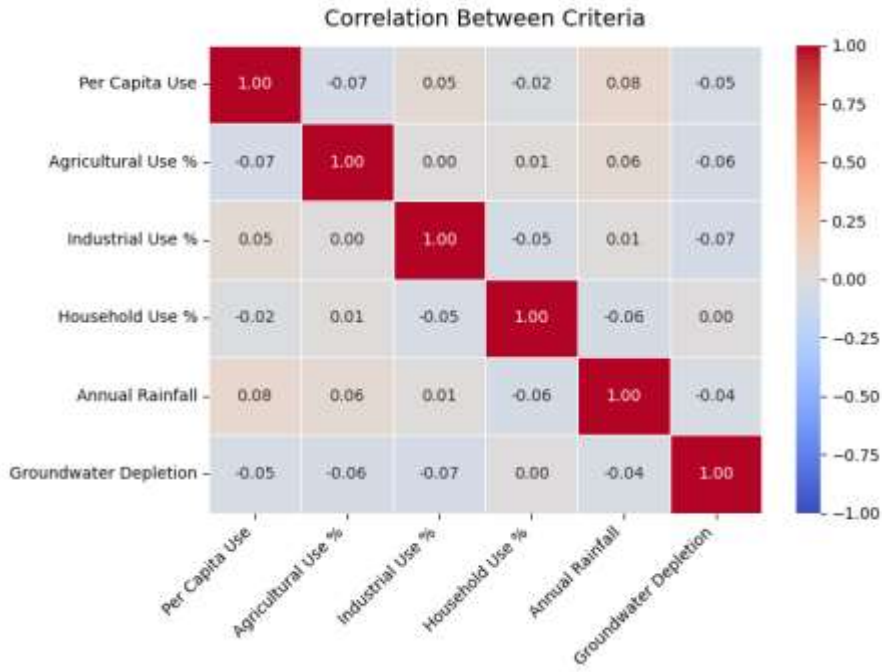

Figure 4: Pearson correlation matrix of the six water stress indicators used in the study

The correlation matrix presented in Figure 4 shows that the linear relationships between the six basic water stress indicators are generally weak. This indicates that it is methodologically appropriate to use the criteria together in the risk modeling based on the MCDM and the classification stages based on ML and DL.

Country-Based Water Risk Distributions Based on the MCDM

This section presents a comparative analysis of the distribution of country-based water risk scores calculated using MCDM methods. The evaluations aim to reveal the variation in risk scores obtained using the WSM, TOPSIS, VIKOR, and MOORA methods across countries, under the same set of criteria and weighting structure. In the analyses, the weights of the criteria were determined as follows: per capita water consumption 15%, agricultural use 35%, industrial use 15%, domestic use 15%, rainfall amount 10%, and groundwater depletion rate 10%. The criteria were evaluated together.

Figure 5 shows the distribution of the top 5 riskiest countries according to the MCDM methods, based on the average normalized risk scores for the 2000–2024 period for all 20 countries in the dataset.

Figure 5: Comparative Risk Analysis (MCDM 2000-2024)

When examining the visual in Figure 5, it is noteworthy that the WSM, TOPSIS, and VIKOR methods exhibit similar trends, while the MOORA method produces lower risk scores. This situation can be explained by the MOORA method producing a more balanced risk distribution, stemming from its combination of benefit and cost-oriented criteria with the principle of direct difference detection.

Figure 6 shows the scores of the five most risky countries for 2024.

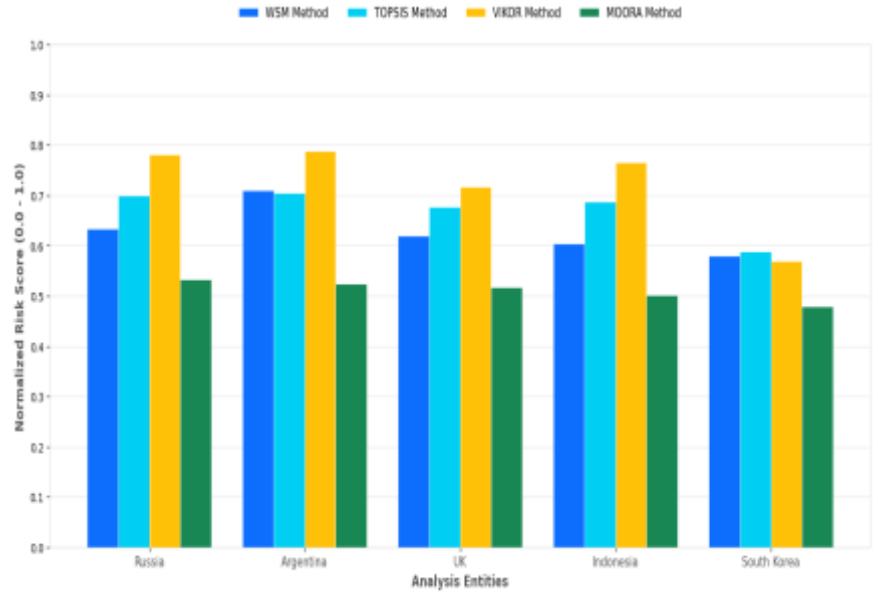

Figure 6: Comparative Risk Analysis (MCDM 2024)

The graphs presented in Figure 6 enable a comparative assessment of countries' current risk situations across different methods. In particular, it is observed that the VIKOR method produces higher risk scores compared to other methods in some countries, while the WSM and TOPSIS methods yield similar results. These differences stem from structural variations in the methods' approaches to compromise, proximity to the ideal solution, and weighting.

The results obtained show that while the CCA methods used produced similar trends on the same data set, they also exhibited method sensitivity in terms of country rankings. This situation reveals that the use of multiple methods, without relying on a single CCA method, provides a more comprehensive basis for analysis in country-based water risk assessments.

Machine Learning and Deep Learning-Based Internal Consistency Analysis

This section examines the consistency of country-based water risk outputs based on the MCDM regression model with water consumption and environmental data structures. The focus of the analysis is to evaluate the internal consistency of the model outputs with the criteria used.

The training set was used to learn the model parameters, while the test set was used to evaluate consistency on previously unseen data. The results were used to assess the reproducibility and discriminative power of the MCDM and regression-based risk outputs in the raw data space. Thus, the internal consistency of the proposed DSS was analyzed based on the data.

Performance Analysis of Classical Machine Learning and Deep Learning Models

In the study, nine different ML and DL classifiers were trained: RF, GB, DT, SVM, LR, KNN, NB, ANN, and 1D-CNN. Since evaluating multi-class water risk problems solely based on accuracy metrics is limited, Table 1 presents the accuracy, precision, recall, and F1-score values for the nine different models trained in the study on the test data.

Table 1: Classification performance of machine learning and deep learning models on the test dataset (20%) (weighted average)

Modals	Accuracy (%)	Precision	Recall	F1
Logistic Regression	96.00	0.9608	0.9600	0.9569
Naive Bayes	96.00	0.9720	0.9600	0.9198
K-Nearest Neighbors (KNN)	83.00	0.7840	0.8300	0.7921
Support Vector Machine (SVM)	90,00	0.8390	0.9000	0.8657
Decision Tree	97.00	0.9531	0.9796	0.9637
Artificial Neural Network (ANN)	94.00	0.9104	0.9400	0.9249
Random Forest	98.00	0.9820	0.9800	0.9800
Gradient Boosting	99.00	0.9901	0.9954	0.9910
1D-CNN	97.00	0.9396	0.9800	0.9596

The results presented in Table 1 show that among ML classifiers, GB and RF models provide higher classification performance than the ANN model on the 1D-CNN test data within the DL method. To examine the discrimination power of the models' risk classes in more detail, they were analyzed using confusion matrices. The confusion matrices are presented as RF (A), GB (B), SVM (C), DT (D), LR (E), KNN (F), NB (G), ANN (H), and 1D-CNN (I), respectively.

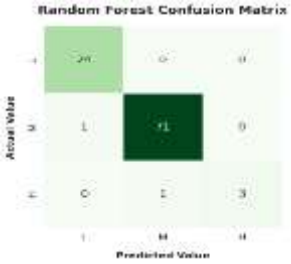

A) Complexity Matrix of the RF Model

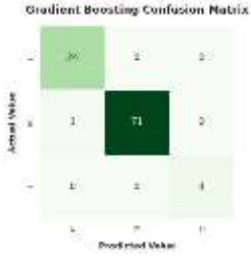

B) Complexity Matrix of the GB Model

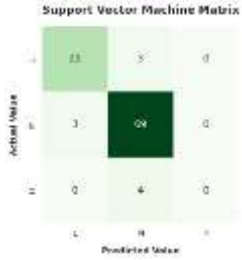

C) Complexity Matrix of the SVM Model

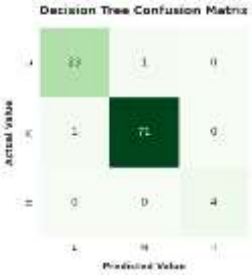

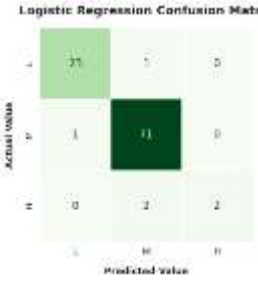

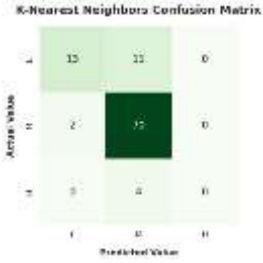

D) DT Model Complexity Matrix

E) Complexity Matrix of the LR Model

F) Complexity Matrix of the KNN Model

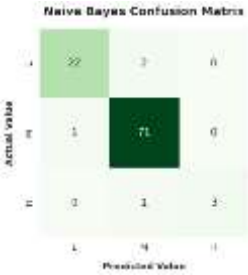

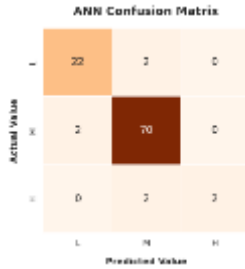

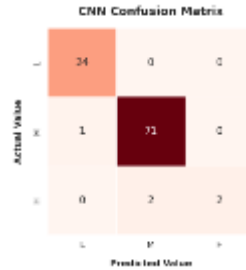

G) NB Model Complexity Matrix

H) ANN Model Complexity Matrix

İ) Complexity Matrix of the 1D-CNN Model

When examining the complexity matrices presented, it is evident that the classification models' ability to distinguish between low (L), medium (M), and high (H) water risk classes varies. These differences are particularly evident in the accurate identification of the H class and through the types of misclassification. The GB and 1D-CNN models stand out as the methods that can distinguish the high-risk class with the lowest error rate. The fact that all observations belonging to the high-risk class are correctly classified in the GB model demonstrates that this method has strong discrimination capacity in critical threshold regions. Similarly, the 1D-CNN model did not produce critical errors such as assigning high-risk countries to the low-risk class, providing a more consistent distinction with a limited number of M risk class confusion errors. This is related to the 1D-CNN's ability to effectively learn patterns between features.

RF and DT models showed balanced performance in L and M risk classes, but produced more consistent predictions in the boundary regions between classes, whereas in KNN and NB models, the tendency to confuse the H class with the M risk class was more pronounced. In KNN, this situation stems from the overlap of distances between classes in the feature space, while in NB, it stems from the assumption of conditional independence between features being limiting for problems involving multidimensional and related indicators such as water risk. A similar tendency for the H class to be misclassified as the M class was also observed in models based on linear decision boundaries, such as SVM and LR.

The high concentration of misclassifications around the M risk class stems from this class's nature as a transition zone between low and high risk. Consequently, the factors most affecting classification performance are the limited number of observations belonging to the H risk class and the nonlinear relationships between criteria. The GB and 1D-CNN models managed these

challenges more effectively than other methods, producing more reliable results, particularly in the internally consistent separation of the H risk class. These findings suggest that classification analyses can be evaluated as a methodological validation tool that supports the internal consistency of the risk labels generated in the proposed DSS with the data structure..

Regression-Based Time Series Projection and Scenario Analysis

This section presents the results of scenario-based analyses conducted using a linear regression model on Australia, Turkey, and Japan—countries selected from a global dataset of 20 countries to represent different hydrological and socio-economic profiles—using the developed DSS. These countries were selected to represent high, medium, and low risk clusters in the DSS outputs.

Water Stress Dynamics Under a High-Risk Scenario for Australia

Australia has been selected as a country with a high-risk profile due to its high vulnerability to drought and climate variability. The scenario defined for Australia is presented in Figure 7 and Table 2.

Figure 7: Ten-year water risk scenario analysis for Australia under user-defined policies and climate conditions (representative example)

Table 2 Water risk scores and risk classes projected for Australia under the defined scenario (2025–2034).

Year	Risk Score	Status
2025	61,1	MODERATE
2026	63,4	MODERATE
2027	65,0	MODERATE
2028	67,8	MODERATE
2029	69,8	MODERATE
2030	71,5	HIGH RISK
2031	74,3	HIGH RISK
2032	76,7	HIGH RISK
2033	78,4	HIGH RISK
2034	81,2	HIGH RISK

In the Australian example given in Figure 7 and Table 2, a scenario of a 10% decrease in rainfall parameters, a 20% increase in agricultural consumption, a 10% increase in residential use, and a 15% increase in per capita use for the period 2025–2034 has been defined. The simulation results show that the country's risk score increased, reaching 81.2 by 2034 and entering the High Risk category. When examining the graph presented in Figure 6, the scenario curve, which is above the red curve representing the current trend, shows that unsustainable water use scenarios increase stress in the long term. This increase reveals that the decrease in precipitation and the increase in demand for agricultural, per capita, and domestic water use jointly affect the risk score.

Risk Behavior Under Extreme Climate Stress Scenarios for Turkey

Turkey is considered an exemplary country representing the intermediate level, and its graph is presented in Figure 8, while Table 3 shows the water risk levels for the next 10 years.

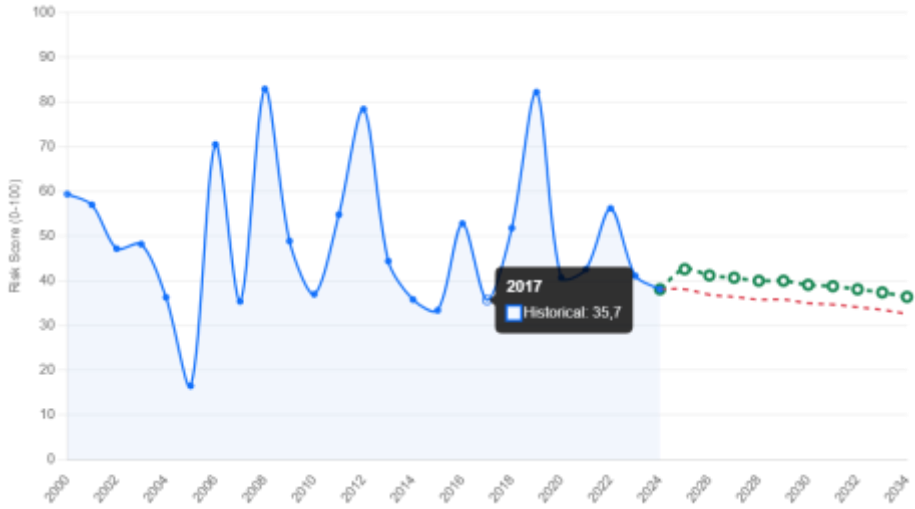

Figure 8 Ten-year water risk scenario analysis for Turkey under user-defined policies and climate conditions (representative example)

Table 3Water risk scores and risk classes projected for Turkey under the defined scenario (2025–2034).

Year	Risk Score	Status
2025	42,6	MODERATE
2026	41,2	MODERATE
2027	40,7	MODERATE
2028	40,0	MODERATE
2029	40,0	MODERATE
2030	39,1	LOW RISK
2031	38,8	LOW RISK
2032	38,1	LOW RISK
2033	37,4	LOW RISK
2034	36,4	LOW RISK

In the scenario presented in Figure 8, a 10% decrease in rainfall parameters, a 20% increase in agricultural consumption, a 10% increase in domestic use, and a 15% increase in per capita use are defined for the 2025–2034 period. With these criteria, Turkey's risk score shows a limited improvement from 42.5 to 36.4, due to the country's structural hydrological advantages, such as high rainfall base, low groundwater depletion rate, and domestic use efficiency, partially offsetting climate and demand-driven pressures. However, the decrease in rainfall stands out as the primary environmental factor driving the risk score upward in the model outputs; this indicates that climate variability will constitute a significant cost factor for Turkey's water security in the long term.

Resilience-Focused Water Risk Profile for Japan

Japan is considered a country with high infrastructure capacity and a stable hydrological regime. Its graph is presented in Figure 9, and the water risk levels for the next 10 years are shown in Table 4.

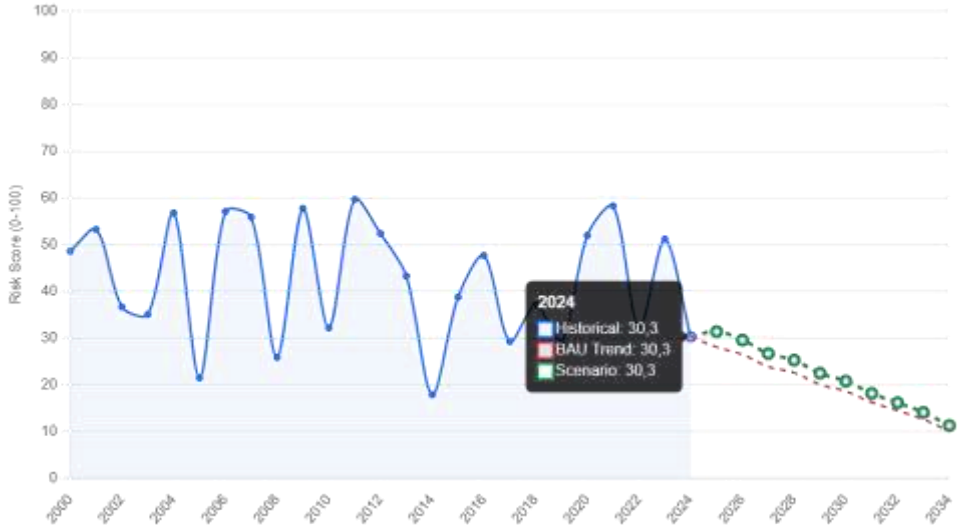

Figure 9: Ten-year water risk scenario analysis for Japan under user-defined policies and climate conditions (representative example)

Table 4Water risk scores and risk classes projected for Japan under the defined scenario (2025–2034).

Year	Risk Score	Status
2025	31,4	LOW RISK
2026	29,6	LOW RISK
2027	26,7	LOW RISK
2028	25,3	LOW RISK
2029	22,5	LOW RISK
2030	20,8	LOW RISK
2031	18,2	LOW RISK
2032	16,2	LOW RISK
2033	14,1	LOW RISK
2034	11,3	LOW RISK

In the Japan example presented in Figure 9, equivalent conditions to the Australia and Turkey scenarios are defined as a 10% decrease in rainfall parameters, a 20% increase in agricultural consumption, a 10% increase in domestic use, and a 15% increase in per capita use. As a result of the simulation conducted under the same variables, Japan's 2034 risk score was

calculated as 11.2 and classified as Low Risk. The results presented in Table 4 and Figure 8 show that Japan's water management policies produce a more resilient risk profile under similar external shocks.

SHAP Analysis Results and Interpretation

The purpose of internal consistency analysis is not only to measure the accuracy of risk labels, but also to reveal which criteria drive these predictions. To this end, SHAP analysis was applied to the models and is presented in Figure 10.

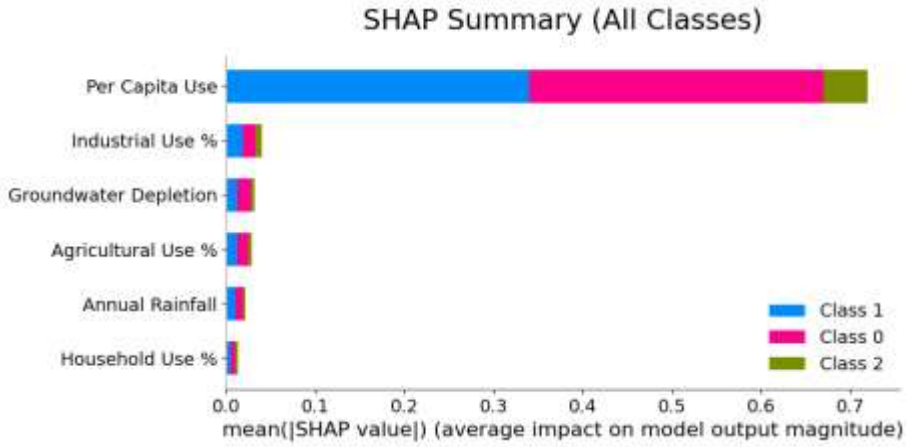

Figure 10: Feature importance is determined based on the average absolute SHAP values across all classes.

As shown in Figure 10, per capita water consumption is the most dominant variable in water risk classification, while agricultural water use, precipitation amount, and groundwater depletion rate have secondary complementary effects on model decisions. These findings indicate that per capita water consumption has a greater impact on the model compared to other criteria.

System Application and Web-Based User Interface

The results obtained by implementing the recommended DSS, MCDM, and linear regression-based components together as a web-based analytical system are presented to the user through an interactive visualization and control interface.

The developed interface enables decision-makers to directly analyze the outputs of the mathematical and artificial intelligence-based models defined in the previous sections. The interface supports basic functions such as country and year-based dynamic filtering, sensitivity analysis through instantaneous modification of criterion weights, and intuitive visualization of risk levels using color codes. Figure 11 shows the analysis screen seen on the system's login page.

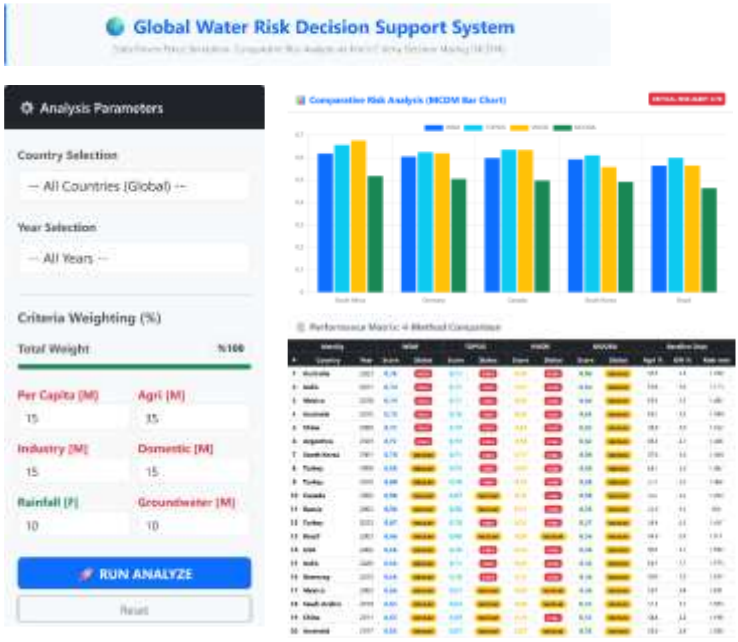

Figure 11 The interactive web interface of the Global Water Risk Decision Support System displays multi-method (WSM, TOPSIS, VIKOR, MOORA) risk comparisons and country-level filtering.

The dynamic control components on the interface presented in Figure 11 allow the decision-maker to instantly modify indicators such as per capita consumption, agricultural, industrial, and domestic use, precipitation, and groundwater depletion rate for both a specific country and year, as well as for all countries and all years, using the criteria weighting panel via the country and year filters in the left menu. The results obtained by analyzing the risk scores derived from the WSM, TOPSIS, VIKOR, and MOORA methods. For the regression-based time series projection and scenario simulation module for countries, the screen shown in Figure 12 has been designed.

Figure 12 Decision support system's regression-based time series projection and scenario simulation module

Using the module presented in Figure 12, decision-makers can visually examine how the percentage changes they define for attribute indicators such as precipitation, agricultural use, domestic consumption, and per capita water use affect water risk levels for the next 10 years by reviewing risk projections based on past trends from the top menu. Thus, the system is not only a static risk assessment tool, but also provides an analytical environment that allows the effects of forward-looking policy scenarios to be examined.

This integrated structure enables the web-based DSS, MCDM, and time series projections developed to facilitate the analytical and application-oriented assessment of country-based water risk analyses.

V. RESULTS

In this study, a DSS was developed by combining MCDM, linear regression, and ML-based internal consistency analysis using global water consumption data. The system can quantitatively assess the possible evolution of risks over time under different policy and climate scenarios, as well as compare countries' current water risk profiles.

Case studies conducted for Australia, Turkey, and Japan have revealed that different risk profiles emerge depending on the structure of each country. Water consumption per capita was found to be the dominant determinant in high-risk scenarios, as demonstrated by SHAP analysis, and the results obtained show that multiple risk factors can be evaluated together.

The results of the ML and DL-based internal consistency analysis revealed that the risk labels obtained using CCAV methods and linear regression could be classified with high accuracy by the GB (99%), RF (98%), and 1D-CNN

(97%) models on the test data and were consistent with the data structure. In this regard, the study presents the DSS approach, which integrates rule-based CCAV models with data-driven ML and DL approaches.

VI. FUTURE WORK

Predicting the global water risk level and taking early action contributes to optimizing water consumption processes and enables data-driven decision-making processes for more accurate use. Linking the MCDM and linear regression model to countries' water consumption can create preventive, proactive risk management strategies by identifying the water risk level at an early stage. In future studies, integrating data with higher spatial resolution into the system and using remote sensing-based real-time indicators can improve the model's forecasting and analysis capabilities. Comparing nonlinear time series models with the existing linear regression module provides a concrete basis for comparison to increase the accuracy of long-term risk projections and reduce uncertainty. Furthermore, applied studies evaluating the usability of the proposed DSS structure by regional policymakers and water management authorities will strengthen the system's integration into practical decision-making processes.

REFERENCES

[1] M. Akın and G. Akın, "SUYUN ÖNEMİ, TÜRKİYE'DE SU POTANSİYELİ, SU HAVZALARI VE SU KİRLİLİĞİ," *Ankara University Journal of the Faculty of Languages and History-Geography*, vol. 47, no. 2, pp. 105–118, Jan. 2007, Accessed: Oct. 15, 2025. [Online]. Available: https://dergipark.org.tr/en/pub/dtcfdergisi/issue/66774/1044494

[2] U. Öğretmen, M. Doğan, and S. Z. Sever, "SÜRDÜRÜLEBİLİRLİK: SU VE SUYUN ÖNEMİ," *Avrasya Sosyal ve Ekonomi Araştırmaları Dergisi*, vol. 10, no. 1, pp. 176–192, Jan. 2023, Accessed: Dec. 03, 2025. [Online]. Available: https://dergipark.org.tr/tr/pub/asead/issue/75724/1230364

[3] A. Soundankar, "Global Water Consumption Dataset (2000-2024) 🌍💧." Accessed: Dec. 03, 2025. [Online]. Available: https://www.kaggle.com/datasets/atharvasoundankar/global-water-consumption-dataset-2000-2024

[4] E. Aydemir, C. Aktürk, and M. Ali YALÇINKAYA, "KONUT SATIN ALIMINDA ALTERNATİF BİR KARAR DESTEK SİSTEMİ ÖNERİSİ," *Mühendislik Bilimleri ve Tasarım Dergisi*, vol. 8, no. 3, pp. 677–691, Sep. 2020, doi: 10.21923/JESD.690278.

[5] M. Melikoglu, "Predictive hybrid modelling for municipal water and wastewater: A global framework demonstrated in Türkiye," *Cleaner Water*, vol. 4, p. 100117, Dec. 2025, doi: 10.1016/J.CLWAT.2025.100117.

[6] D. Wang, Y. Zhang, and N. Yousefi, "Urban Water-Energy consumption Prediction Influenced by Climate Change utilizing an innovative deep

learning method," *Scientific Reports 2024 14:1*, vol. 14, no. 1, pp. 30931-, Dec. 2024, doi: 10.1038/s41598-024-81836-7.

[7] E. M. Sarband, S. Araghinejad, and J. Attari, "Developing an Interactive Spatial Multi-Attribute Decision Support System for Assessing Water Resources Allocation Scenarios," *Water Resources Management*, vol. 34, no. 2, pp. 447–462, Jan. 2020, doi: 10.1007/S11269-019-02291-Y.

[8] A. Izady *et al.*, "A scenario-based coupled SWAT-MODFLOW decision support system for advanced water resource management," *Journal of Hydroinformatics*, vol. 24, no. 1, pp. 56–77, Jan. 2022, doi: 10.2166/HYDRO.2021.081.

[9] L. A. Candido, G. A. G. Coêlho, M. M. G. A. de Moraes, and L. Florêncio, "Review of Decision Support Systems and Allocation Models for Integrated Water Resources Management Focusing on Joint Water Quantity-Quality," *J. Water Resour. Plan. Manag.*, vol. 148, no. 2, p. 03121001, Nov. 2021, doi: 10.1061/(ASCE)WR.1943-5452.0001496.

[10] M. Saad, E. Nofal, Y. Abdelmonem, and P. Riad, "Application of decision support system/remote sensing/GIS techniques in groundwater recharge assessment," *Water Pract. Technol.*, vol. 19, no. 9, pp. 3721–3743, Sep. 2024, doi: 10.2166/WPT.2024.193.

[11] P. Ataei *et al.*, "An intelligent decision support system for groundwater supply management and electromechanical infrastructure controls," *Heliyon*, vol. 10, no. 3, p. e25036, Feb. 2024, doi: 10.1016/J.HELIYON.2024.E25036.

[12] G. Poli, S. Cuntò, E. Muccio, and M. Cerreta, "A spatial decision support system for multi-dimensional sustainability assessment of river basin districts: the case study of Sarno river, Italy," *Land use policy*, vol. 141, p. 107123, Jun. 2024, doi: 10.1016/J.LANDUSEPOL.2024.107123.

[13] P. J. Muhammad Ali, "Investigating the Impact of Min-Max Data Normalization on the Regression Performance of K-Nearest Neighbor with Different Similarity Measurements," *ARO-The Scientific Journal of Koya University*, vol. 10, no. 1, pp. 85–91, Jun. 2022, doi: 10.14500/ARO.10955.

[14] E. K. Zavadskas, Z. Turskis, and S. Kildiene, "State of art surveys of overviews on MCDM/MADM methods," *Technological and Economic Development of Economy*, vol. 20, no. 1, pp. 165–179, 2014, doi: 10.3846/20294913.2014.892037.

[15] T. Evangelos and B. Shu, "(PDF) Multi-criteria decision making: An operations research approach." Accessed: Dec. 08, 2025. [Online]. Available: https://www.researchgate.net/publication/284107964_Multi-criteria_decision_making_An_operations_research_approach

[16] M. Nuhu Yahya, H. Gökçekuş, D. Uzun Ozsahin, and B. Uzun, "Evaluation of wastewater treatment technologies using TOPSIS," pp. 6–10, 2019, doi: 10.5004/dwt.2020.25172.

[17] I. Milojkovic and N. Prascevic, "Project management using the developed AHP–VIKOR method with the fuzzy approach," *Water Science and Technology*, vol. 90, no. 2, pp. 578–597, Jul. 2024, doi: 10.2166/WST.2024.204.

[18] V. Saravanan, C. Sivaji, S. Chinnasamy, and C. Raja, "Multi-Criteria Decision-Making for Water Resources Planning Using the MOORA

Method," *Aeronautical and Aerospace Engineering*, vol. 1, no. 4, pp. 2583–889, 2023, doi: 10.46632/aae/1/4/1.

[19] D. C. Montgomery, G. G. Vınıng, and A. P. Elızabeth, "INTRODUCTION TO LINEAR REGRESSION ANALYSIS." Accessed: Jan. 05, 2026. [Online]. Available: https://content.e-bookshelf.de/media/reading/L-16125104-1a3a7c5bd1.pdf

[20] H. A. Salman, A. Kalakech, and A. Steiti, "Random Forest Algorithm Overview," *Babylonian Journal of Machine Learning*, vol. 2024, pp. 69–79, Dec. 2024, doi: 10.58496/BJML/2024/007.

[21] E. Ok and M. Emmanuel, "(PDF) Understanding the Gradient Boosting Algorithm in XGBoost." Accessed: Jan. 20, 2026. [Online]. Available: https://www.researchgate.net/publication/390137877_Understanding_the_Gradient_Boosting_Algorithm_in_XGBoost

[22] B. E. Özkan, "Karar Ağaçları (Decision Trees)| Denetimli Makine Öğrenmesi | by Elif Beyza Ozkan | Medium." Accessed: Jan. 22, 2026. [Online]. Available: https://medium.com/@elifbeyzaozkan/karar-a%C4%9Fa%C3%A7lar%C4%B1-decision-trees-denetimli-makine-%C3%B6%C4%9Frenmesi-3a8d962ad640

[23] A. Nafees *et al.*, "Forecasting the Mechanical Properties of Plastic Concrete Employing Experimental Data Using Machine Learning Algorithms: DT, MLPNN, SVM, and RF," *Polymers 2022, Vol. 14,* vol. 14, no. 8, Apr. 2022, doi: 10.3390/POLYM14081583.

[24] H. Altıparmak *et al.*, "Performance measurements of 12 different machine learning algorithms that make personalized psoriasis treatment recommendations with a database of psoriasis patients responding to treatment," *Computational Intelligence and Blockchain in Complex Systems: System Security and Interdisciplinary Applications*, pp. 85–95, Jan. 2024, doi: 10.1016/B978-0-443-13268-1.00014-5.

[25] Y. Shi, K. Yang, Z. Yang, and Y. Zhou, "Primer on artificial intelligence," *Mobile Edge Artificial Intelligence*, pp. 7–36, 2022, doi: 10.1016/B978-0-12-823817-2.00011-5.

[26] B. Phatcharathada and P. Srisuradetchai, "Randomized Feature and Bootstrapped Naive Bayes Classification," *Applied System Innovation 2025, Vol. 8,* vol. 8, no. 4, Jul. 2025, doi: 10.3390/ASI8040094.

[27] K. A. Eşidir, V. Yoğunlu, and Y. E. Gür, "MULTİLAYER PERCEPTRON (MLP) VE RADİAL BASİS FUNCTİON (RBF) TAHMİN MODELLERİ İLE ELAZIĞ TURİZM MEMNUNİYET ANALİZİ SONUÇLARININ TAHMİNİ," *International Journal of Social Humanities Sciences Research (JSHSR)*, Jan. 2022, doi: 10.26450/JSHSR.3193.

[28] Y. Berus and Y. Benteşen Yakut, "Derin Öğrenme (1D-CNN, RNN, LSTM, BiLSTM) ile Enerji Tüketim Tahmini: Diyarbakır AVM Örneği," *DÜMF Mühendislik Dergisi*, Feb. 2024, doi: 10.24012/DUMF.1415055.

[29] S. Yang and G. Berdine, "Confusion matrix," ., vol. 12, no. 53, pp. 75–79, Oct. 2024, doi: 10.12746/SWRCCC.V12I53.1391.

[30] S. Ramalingam *et al.*, "Explainable Ai(Xai) for Touch-Stroke Biometrics: Insights from Shap," *2025 IEEE International Carnahan Conference on Security Technology (ICCST)*, pp. 1–6, Oct. 2025, doi: 10.1109/ICCST63435.2025.11293940.